University of São Paulo (USP)
Institute of Astronomy, Geophysics and Atmospheric Sciences
Department of Astronomy
&
University Nice-Sophia Antipolis (UNS)
UFR Sciences
Doctoral School in Fundamental and Applied Sciences

Daniel Moser Faes

An interferometric view of hot star disks

São Paulo
2015

UNIVERSITÉ NICE-SOPHIA ANTIPOLIS - UFR Sciences
École Doctorale de Sciences Fondamentales et Appliquées

THÈSE

pour obtenir le titre de

Docteur en Sciences

de l'UNIVERSITÉ Nice-Sophia Antipolis

Spécialité: SCIENCES DE L'UNIVERS

présentée et soutenue par

Daniel MOSER FAES

Une vue interférométrique des disques de étoiles chaudes

Thèse dirigée par

Armando DOMICIANO DE SOUZA, à l'UNS

et

Alex Cavaliéri CARCIOFI, à l'USP

soutenue le 11 septembre 2015

Jury:

Alex Cavaliéri CARCIOFI	USP (Brésil)	Président et directeur de thèse
Armando DOMICIANO DE SOUZA	UNS (France)	Directeur de thèse
Samer KANAAN	UV (Chili)	Rapporteur
Pièrre KERVELLA	LESIA (France)	Rapporteur
Jon BJORKMAN	UT (É.-U.A.)	Examinateur
Ronaldo Savarino LEVENHAGEN	UNIFESP (Brésil)	Examinateur

Daniel Moser Faes

Uma visão interferométrica de discos de estrelas quentes

Tese apresentada ao Departamento de Astronomia do Instituto de Astronomia, Geofísica e Ciências Atmosféricas da Universidade de São Paulo como requisito parcial à obtenção do título de **Doutor em Ciências**.

Sob orientação de:
Alex Cavaliéri Carciofi (USP)
&
Armando Domiciano de Souza (UNS)

Área de concentração: Astronomia

São Paulo
2015

To my ancestors, whom left Trento
in search of a new life in Terra Incognita Brasil

And to the king whose reign I found
going through the virage Fairmont *and the* virage du Portier...

Acknowledgements

First of all, I thank my advisors Alex C. Carciofi & Armando Domiciano de Souza. In addition to science, they shared with me moments of joy and pain in my developing process. I also acknowledge other great researchers I met and with whom I could learn or be inspired by: J. Bjorkman, Th. Rivinius and D. Baade. Also important, K. Bjorkman, A. Granada; in Nice, P. Bendjoya, P. Stee, F. Millour, F. Farrock and T. Lanz; in Brazil, R. Costa, W. Maciel and A. Damineli. A special thanks to G. Meynet, who kindly helped me in Switzerland after been stolen!

I acknowledge the support from FAPESP (grants 2010/19060-5 and 2012/04916-7). This research made use of SIMBAD and VIZIER databases (CDS, Strasbourg), as well as NASA Astrophysics Data System. Also, the Jean-Marie Mariotti Center (JMMC) Softwares. This work was possible by the use of the computing facilities of the Laboratory of Astroinformatics (IAG/USP, NAT/Unicsul), whose purchase was done by the Brazilian agency FAPESP (grant 2009/54006-4) and the INCT-A.

En français, je remercie tous mes amies que j'ai rencontrais pendant mon séjour en France: Felipe & Virginie; Marcia, Ana Paula, Jacques & Marília; Ricardo, Letícia & Ricardo. Tous les bénévoles du Fourneau Économique, en particulier la souer Anne-Marie et Galina. Aussi, l'atelier de chant choral de l'UNS. Les étudiants et post-docs du labo Lagrange et de l'OCA, en special Paul & Lina; Samir & Zeinab; Gustavo, André & Suelen. Comment me manque le beau temps à Nice, du pain, du vin et des fromages! Mais surtout les tours de vélo... Cyril & Laura, je ne vous ai pas oublié!

Em português, agradeço aos meus pais, Marlize e Severino. Ao meu pedaço, Thamirys. A todos os amigos do BeACoN: Rodrigo, Cyril, Despo; Leandro, Bruno, Mohammad, Daiane; Bednarski, André Luiz e Artur. E os agregados, Robert, Fellipy e Marcelo. Aos meus *homemates* Daniel e Arianna. Aos amigos brasileiros que visitei na Europa: Aiara (Heidelberg), Michael & Sonia (Heilbronn); Andressa (em Munique, e sem passaporte!) e Melina (Berlim e Leipzig); Thaíse (em Pádua) e Marcus (Paris). A todos que, de alguma forma, me ajudaram nesta conquista, os meus sinceros agradecimentos!

This thesis was written in LaTeX making use of the IAGTESE class developed by students of IAG/USP.

"*It is only by going through a volume of work that your work will be as good as your ambitions. And I took longer to figure out how to do this than anyone I've ever met.*"

Ira Grass

"*Soit dit en passant, c'est une chose assez hideuse que le succès.*
Sa fausse ressemblance avec le mérite trompe les hommes."

Victor Hugo

"*Foi vendo as coisas que eu vi, foi procurando entendê-las,*
foi contemplando as estrelas, que eu aprendi a rezar."

José Fernandes de Oliveira

Abstract

Optical long baseline interferometry was recently established as a technique capable of resolving stars and their circumstellar environments at the milliarcsecond (mas) resolution level. This high-resolution opens an entire new window to the study of astrophysical systems, providing information inaccessible by other techniques.

Astrophysical disks are observed in a wide variety of systems, from galaxies up to planetary rings, commonly sharing similar physical processes. Two particular disk like systems are studied in the thesis: (i) B He-rich stars that exhibits magnetic fields in order of kG and that trap their winds in structures called magnetospheres; and (ii) Be stars, fast rotating stars that create circumstellar viscous disks.

This study uses the interferometric technique to investigate both the photosphere proper and the circumstellar environment of these stars. The objective is to combine interferometry with other observational techniques (such as spectroscopy and polarimetry) to perform a complete and well-constrained physical description of these systems. This description is accompanied by radiative transfer models performed by the HDUST code.

The first firm detection of a hot star magnetosphere in continuum linear polarization is reported, as a result of the monitoring campaign of σ Ori E at the Pico dos Dias Observatory (OPD/LNA). The polarimetric data was modeled by a single-scattering "dumbbell+disk" model, that describes the magnetosphere as constituted of two blob-like structures (at the intersection to the rotation and magnetic equators) and a circumstellar disk at the magnetic equator. The polarimetric modeling predicts a lower blob to disk mass ratio than the expect from the RRM (Rigid Rotating Magnetosphere) model, that provides a good spectroscopic description of these magnetospheres.

In addition to σ Ori E, we report the first polarimetric detections of the magnetospheres of HR 7355 and HR 5907. Our analysis indicate that these structures share similar properties, such as polarimetric modulation amplitude and mass distribution. In the case of the HR 5907, we also report the first interferometric detection of a magnetosphere with differential phase amplitude of about 3 degrees with AMBER-VLTI/ESO.

A new interferometric phenomenon, called CQE-PS (Central Quasi-Emission Phase Signature), was described and identified as a useful tool for the study of Be circumstellar disks, in particular for shell stars. Departures from a S-shaped differential phases occur when the disk obscures part of the stellar photosphere. This disk absorption alters the phase signal mainly near the rest wavelengths and can introduce a central reversal in the phases profile. This phenomenon can be used to probe disk size, density and radial slope. It may even provide an estimate for the (maximum) stellar angular size.

The photosphere of the Be star Achernar was studied in detail using high-precision visibilities and closure phase information from PIONIER-VLTI/ESO. This is the first precise photospheric characterization of a Be star and is, up to date, the characterization of the star with the highest mass and rotation rate. The variable line profile of Achernar and high-precision photometric frequencies are analyzed in the light of these new parameters. These results have great significance for stellar models and for the Be stars, such as the determination of the gravitational darkening coefficient.

We present the BeAtlas project as part of BeACoN group from IAG-USP. It consists of a systematic grid of Be stars models generated by the HDUST code aiming at a comprehensive investigation of Be stars and their state-of-art modeling, the VDD (Viscous Decretion Disk). As first project application, we argue that Achernar is not a typical main-sequence star, displaying characteristics of a star leaving the main sequence: it exhibits an big size and a luminosity higher than the expected for its mass.

The recent outburst of Achernar was investigated and modeled. For the analysis of the activity, a large set of observational data was obtained, such as AMBER spectro-interferometry, FEROS spectroscopy (ESO) and optical polarimetry (OPD/LNA). These observations contain the first spectro-interferometric study of a Be star disk evolution, angularly resolving the growing disk.

The secular evolution of the newly formed disk is characterized and the VDD modeling prescription was employed. The AMBER interferometric analysis shows no evidence of

a polar wind in this active phase. The Hα spectroscopy exhibits a slow and gradual evolution, and reaches a near stationary regime just after $\sim$1.6 years. This feature will allow to estimate the disk viscous diffusion coefficient with dynamic VDD modeling.

Keywords: stars: individual (Achernar), stars: fundamental parameters, techniques: interferometric, circumstellar matter, stars: emission-line, Be, stars: magnetic field

Résumé

Interférométrie optique/IR à longue base a été récemment mis en place comme une technique capable de résoudre spatialement les étoiles et leurs environnements circumstellaires au niveau de la milliseconde d'angle (*mas*). Cette haute résolution ouvre toute une nouvelle fenêtre pour l'étude de les systèmes astrophysiques, fournissant des informations inaccessibles par d'autres techniques.

Disques astrophysiques sont observées dans une grande variété de systèmes, de galaxies jusqu'à anneaux planétaires, partageant communément processus physiques similaires. Deux disques particuliers sont étudiés dans la thèse: (i) les étoiles B He-riches qui présente des champs magnétiques de l'ordre de kG et que confine leurs vents dans des structures appelées magnétosphères; et (ii) les étoiles Be, rotateurs rapides qui présentent des disques circumstellaires épisodiques.

Cette étude utilise la technique interférométrique pour étudier à la fois la photosphère et l'environnement circumstellaire de ces étoiles. L'objectif est de combiner l'interférométrie avec d'autres techniques d'observation (telles que la spectroscopie et la polarimétrie) pour effectuer une description physique complète et bien contraindre ces systèmes. Cette description est acquise par l'interprétation des l'ensemble des observations par des modèles de transfer radiati effectués par le code de HDUST.

La première détection d'une magnétosphère d'une étoile chaude en polarisation linéaire du continuum est rapporté, à la suite de la campagne de surveillance de σ Ori E au Observatoire Pico dos Dias (OPD/LNA). Les données polarimétrique ont été interprétées par un modèle simple de diffusion composé d'un "haltère + disque", qui décrit la magnétosphère comme constitué de deux structures comme sphéroïdes (à l'intersection de les équateurs rotationnel et magnétiques) et un disque circumstellaire à l'équateur magnétique. La

modélisation polarimétrique prédit une masse pour le sphéroïde au rapport du disque inférieure à celle attendue par la modélisation RRM (*Rigid Rotating Magnetosphere*), qui fournit une bonne description spectroscopique de ces magnétosphères.

En plus de σ Ori E, nous présentons les premières détections polarimétriques pour les magnétosphères de HR 7355 et HR 5907. Notre analyses indique que ces structures partagent des propriétés similaires, comme l'amplitude de la modulation polarimétrique et la distribution de masse. Dans le cas de la HR 5907, nous présentons également la première détection interférométrique d'une magnétosphère avec une amplitude de phase différentiel d'environ 3 degrés avec AMBER-VLTI/ESO.

Une nouvelle signature interférométrique, appelé CQE-PS (*Central Quasi-Emission Phase Signature*), a été décrite et identifiée comme un outil efficace pour étudier des disques circumstellaires Be, en particulier pour les étoiles *shell* (étoiles avec disques vues par l'équateur). Départs de phases différentielles en forme de "S" se produisent lorsque le disque obstrue une partie de la photosphère stellaire. Cette absorption pour le disque modifie le signal de phase essentiellement à proximité des longueurs d'onde de repos et peut introduire une inversion de phase central dans le profil des phases. Ce phénomène peut être utilisé pour sonder la taille du disque, et son profil radial de densité. Il peut également fournir une estimation de la taille (diamètre) angulaire maximale de l'étoile.

La photosphère de l'étoile Be Achernar a été étudiée en détail en utilisant des visibilités de haute précision et de l'information de clôture de phase de PIONIER-VLTI/ESO. Ceci est la première caractérisation précise de la photosphère une étoile Be et est, à ce jour, la caractérisation de l'étoile avec le taux de masse et de rotation le plus élevé. Le profil de raie variable de Achernar et fréquences photométriques de haute précision sont analysés à la lumière de ces nouveaux paramètres. Ces résultats ont une grande importance pour les modèles stellaires et pour les étoiles Be, telles que la détermination du coefficient de assombrissement gravitationnel.

Nous présentons le projet BeAtlas dans le cadre du groupe Beacon de l'IAG-USP. Il se compose d'une grille systématique de modèles Be étoiles générés par le code HDUST visant à une recherche approfondie des étoiles Be et de leur modélisation "état de l'art", le VDD (disque de décrétion visqueux). Comme première application du projet, nous soutenons que Achernar est pas une étoile de la séquence principale typique, présentant des caractéristiques d'une étoile laissant la séquence principale: elle présente une grande

taille et une luminosité plus élevée que le prévu pour sa masse.

La récente activité de Achernar a été étudié et modélisé. Pour l'analyse de l'activité récente du disque, un grand ensemble de données d'observation a été obtenu, comme spectro-interférométrie AMBER, spectroscopie FEROS (ESO) et polarimétrie optique (OPD/LNA). Ces observations permettent la première étude spectro-interférométrique de l'évolution temporelle d'un disque de étoile Be (croissance du disque résolue angulairement).

L'évolution séculaire du disque juste formé est caractérisé. Visant à obtenir un modèle physique réaliste de l'environnement circumstellaire de Achernar, le code HDUST a été utilisé avec un modèle de prescription VDD. L'analyse interférométrique AMBER ne montre aucun signe d'un vent polaire dans cette phase active. Le spectroscopie Hα présente une évolution lente et progressive, et atteint un régime stationnaire après seulement $\sim 1,6$ années. Cette fonctionnalité permettra d'estimer le coefficient de diffusion visqueuse du disque avec la modélisation de la dynamique VDD.

Mots-clés: étoiles: matière circumstellaire - transfert radiatif - étoiles: paramètres fondamentales, Be, raie d'émission, Be, champ magnétique, individuelle (Achernar), - techniques: interférométrique

Resumo

Interferometria óptica de longa linha de base recentemente estabeleceu-se como uma técnica capaz de resolver estrelas e seus ambientes circunstelares no nível de mili segundos de arcos (*mas*). Esta alta resolução abre uma janela inteiramente nova para o estudo de sistemas astrofísicos, fornecendo informações inacessíveis por outras técnicas.

Discos astrofísicos são observados numa ampla variedade de sistemas, de galáxias à discos planetários, em geral compartilhando de processos físicos similares. Dois sistemas de discos foram estudados nesta tese: (i) o estrelas B ricas em He e que possuem campos magnéticos da ordem de kG e que confinam seus ventos em estruturas chamadas magnetosferas; e (ii) estrelas Be, estrelas de rotação rápida que criam um disco circumstelar viscoso.

Este estudo usa a técnica interferométrica para investigar ambas a própria fotosfera e o ambiente circunstelar destas estrelas. O objetivo é combinar a interferometria com outras técnicas observacionais (tal como espectroscopia e polarimetria) para realizar uma descrição física completa e precisa destes sistemas. Esta descrição é acompanhada por modelos de transferência radiativa executados pelo código HDUST.

A primeira deteção segura de uma magnestosfera de estrela quente em polarização no contínuo é relatada, como um resultado da campanha de monitoramento de σ Ori E no Observatório Pico dos Dias (OPD/LNA). Os dados polarimétricos foram modelados por um modelo "alteres+disco" de espalhamento simples, que descreve as magnetosferas como constituídas de duas estruturas esferoidais (na intersecção dos equadores de rotação e o magnético) e um disco circunstelar no equador magnético. A modelagem polarimétrica prevê uma menor razão entre a massa do blob e o disco que o previsto pelo modelo RRM (*Rigid Rotating Magnetosphere*), que provê uma boa descrição espectroscópica destas mag-

netosferas.

Além de σ Ori E, nós apresentamos as primeiras detecções polarimétricas das magnetosferas de HR 7355 e HR 5907. Nossa análise indica que estas estruturas compartilham propriedades similas, como amplitude da modulação polarimétrica e distribuição de massa. No caso de HR 5907, nós também apresentamos a primeira detecção interferométrica de uma magnetosfera com amplitude de fase diferencial de certa de 3 graus com o AMBER-VLTI/ESO.

Um novo fenômeno interferométrico, chamado de CQE-PS (*Central Quasi-Emission Phase Signature*), foi descrito e identificado como um ferramenta útil para o estudo de discos circunstelares de Be, em particular para estrela do tipo *shell*. Devido um formato de 'S' nas fases diferenciais ocorre quando o disco obscurece parte da fotosfera estelar. Esta absorção do disco altera o sinal da fase principalmente próximo aos comprimentos de onda do repouso e pode introduzir um reverso central no perfil das fases. Este fenômeno pode ser usado para sondar o tamanho do disco, densidade e inclinação radial. Ele pode até fornecer uma estimativa para o (máximo) tamanho angular estelar.

A fotosfera da estrela Be Achernar foi estudada em detalhes usando visibilidades de alta precisam e informação de fechamento de fase do PIONIER-VLTI/ESO. Esta é a primeira caracterização fotosférica de precisão de uma estrela Be e é, até o momento, a caracterização da estrela de maior massa de taxa de rotação. O perfil de linha variável de Achernar e frequências fotométricas de alta-precisão foram analizadas à luz destes novos parâmetros. Estes resultados tem grande significância para modelos estelares and para as estrelas Be, tal como a determinação do coeficiente de escurecimento gravitacional.

Nós apresentamos o projeto BeAtlas como parte do grupo BeACoN do IAG-USP. Ele consiste de uma grade sistemática de modelos de estrelas Be gerados pelo código HDUST com o objetivo de uma investigação abrangente de estrelas Be e seu "estado da arte" em modelagem, o VDD (*Viscous Decretion Disk*). Como primeira aplicação do projeto, nós argumentamos que Achernar não é uma estrela típica de sequência principal, mostrando características de uma estrela deixando a sequência principal: ela exibe um grande tamanho e uma luminosidade mais alta que o esperado para sua massa.

A recente ejeção por Achernar foi investigada e modelada. Para a análise da atividade, a amplo conjunto de dados observacionais foi obtido, tal com espectrointerferometria AMBER, espectroscopia FEROS (ESO) e polarimetria óptica (OPD/LNA). Estas observações

contém o primeiro estudo espectro-interferométrico da evolução de um disco Be, angularmente resolvendo o disco em crescimento.

A evolução secular do recém formado disco é caracterizada e a prescrição de modelagem VDD foi empregada. A análise interferométrica AMBER não mostra evidência de um vento polar nesta fase ativa. A espectrocopia Hα exibe uma lenta e gradual evolução, e alcança um regime quase estacionário somente após $\sim 1,6$ anos. Esta característica permitirá estimar o coeficiente de difusão viscosa através da modelagem dinâmica VDD.

Palavras-chave: : individual (Achernar), estrelas: parâmetros fundamentais, técnicas: interferométrica, material circunstelar, estrelas: linha de emissão, Be, estrelas: campo magnético

Contents

List of Figures

List of Tables

Foreword

[1]*As some of you may know, my main goal is to become a scientist. It's a challenge for a student to write a whole thesis. Scientists are trained to be brief. Everything I have learned in my entire academic life can be boiled down to a dozen bullet points, several of which I already forgot.*

You would feel kind of perturbed if you took a big thick thesis and all it had in it was a dozen bullet points, particularly if several of them seemed to be "filler". So, my "plan for excellence" is to repeat myself and cite previously published works to take up some page space. In marketing terms, this is called "adding value". In science, it is called "methodological rule". And for your reading pleasure I will include many colorful but unnecessary figures.

Bonne lecture!

[1] Adapted from the Scott Adams' book "The Dilbert Principle".

Chapter 1

Introduction

1.1 Massive stars

Stars are not equal. This statement is clear when looking at the night sky. Stars have different brightness and different colors. While the observed brightness is not an absolute quantity as it is influenced by distance, the visuals colors are directly related to the stellar temperatures.

The term *hot stars* refers to the stars with surface temperatures above 10,000 Kelvin (K), appearing as blue-white stars in the night sky with temperature much higher than our Sun. According to the usual spectral classification, these stars correspond to the O and B types. This classification was defined in Harvard, USA, in late nineteenth century when spectroscopy established as a regular observational technique.

The luminosity of the stars was then compared with their colors in the so-called Hertzsprung-Russell (HR) diagram, in reference to the pioneer works of Ejnar Hertzsprung and Henry Norris Russell (independently done in 1911 and 1913, respectively). It was found that these quantities are not randomly distributed as most stars appear to be ordered in a path, called "the main sequence", where the bluest stars were also the more luminous.

OB main sequence stars are only approximately 0.1% of the stars in the Solar neighborhood but are the most common type in the night sky (Ledrew, 2001). The reason is they are the brightest stars (i.e., they can be easily seen even distant) and they are rare in being formed. The empirical function that describes the distribution of initial masses for a population of stars is known in astronomy as Initial Mass Function (IMF). For example, Salpeter (1955) found that the number of stars decreases rapidly with increasing mass.

Defining $\Phi(m)dm$ as the fraction of stars with a mass between $m - dm/2$ and $m + dm/2$, Salpeter parametrized the IMF by a power-law on the form

$$\Phi(m)\, dm \propto m^{-\alpha}\, dm\,, \tag{1.1}$$

with the value of exponent $\alpha = 2.35$.

Studies of main sequence binary stars (e.g., Harmanec, 1988) that allowed the determination of their respective masses, established the relation between their temperatures and masses. The conclusion is temperature, luminosity and mass are mutually dependent quantities for these stars.

As examples of empirical mass-radius and mass-luminosity relations, we reproduce the expressions from Maciel (1999)

$$\log\left(\frac{L}{L_\odot}\right) \sim 3.8 \log\left(\frac{M}{M_\odot}\right) + 0.08\,; \tag{1.2}$$

$$\log\left(\frac{R}{R_\odot}\right) \sim 0.64 \log\left(\frac{M}{M_\odot}\right) + 0.011. \tag{1.3}$$

They are valid for $M > 0.2M_\odot$ and for $1.3 < M/M_\odot < 20$, respectively.

As the knowledge about the stellar evolution consolidated, it became clear that the main sequence is the longest period of evolution of a non-degenerated star and when its properties are more stable. The main feature of this evolutionary phase is hydrogen-burning as the stellar power source.

The Vogt-Russel theorem, named after the astronomers Heinrich Vogt and Henry Norris Russell, states that the structure and observed properties of a star, in equilibrium, is uniquely determined by its mass and chemical composition. This implies that the main parameter that distinguishes the majority of stars is their masses.

The term *massive stars* defines to stars with masses higher than 8 Solar masses ($M_\odot$). This mass limit constraint massive stars to the spectral O and B types, reinforcing that massive stars are so hot stars - and vice-versa.

O and B types overview

The standard spectral classification was based on relative strengths of absorption lines. All of the spectral types were subdivided with a numerical suffix from 0 to 9. A star with line strengths midway between A0 and B0 types is classified as A5 type star.

The stellar spectra is also classified into classes. These classes distinguished basically the luminosity of the objects. This is known as the Yerkes spectral classification, or Morgan-Keenan classification (lead by the astronomers William Wilson Morgan and Philip C. Keenan) done in middle of the tweentieth century as an extension to the Harvard classification. Denoted by Roman letters I to V, the brightness of stars falls along the sequence from I luminous supergiants, III normal Giants up to V main sequence stars (dwarfs), the main objects of this study.

An O-type main sequence star (O V) is a very hot, blue-white star of spectral type O. They have temperatures higher than 30,000 K and so appear on the left of the HR diagram. Their large luminosity exceeds the Solar one ($L_\odot$) more than 30,000 times and their masses are higher than 16 $M_\odot$. Due to their high photospheric temperature, O type stars can ionize Helium (He) atoms and their spectra show prominent He II absorption lines, as well as strong lines of other ions with high energy ionization potential. Hydrogen (H) and neutral He lines are weak since these elements are almost completely ionized.

Due to high temperature and luminosity, O-type stars end their lives rather quickly (few dozen million years) in violent supernova explosions, resulting in black holes or neutron stars. Most O-type stars are young, massive, main sequence stars, but the central stars of planetary nebulae, old low-mass stars near the end of their lives, may have O spectra as well as white dwarfs stars.

B V type stars have masses roughly from 3 to 16 $M_\odot$ and surface temperatures between 10,000 and 30,000 K. Their luminosity range between 200 and 30,000 $L_\odot$. Their spectra have neutral He, and moderate H lines, since a substantial part of the hydrogen is ionized.

Many B-type stars (and some O-type) exhibit peculiar features in their spectra. A characteristic that is considerably common in B-type stars is their high rotation rates.

1.1.1 Astrophysical context

Massive stars play a crucial role in astrophysics. Due to they large luminosity, they contribute in an important way to the integrated spectrum of galaxies. With their strong winds, they feed the interstellar medium with momentum and kinectic energy, impacting on the star formation rate. Massive stars are also the main producers of cosmic heavy elements, including those necessary for life, and drive galatic chemical evolution. At the end of their short lifetimes they originate very energic events as supernovae and probably

are the progenitors of gamma-ray bursts. See Leitherer et al. (1992) and Puls et al. (2008) for an overview.

ISM and star formation

Spiral arms are high density regions of galaxy disks that are rich in gas and dust. The densest regions, in the form of molecular clouds, lead to the formation of stars, some of which are O- and B-type stars and that are easily identifiable due to their high brightness. Also, as these stars have short lifetimes, they cannot move great distances before their death and so they stay in or relatively near the place where they originally formed.

Massive stars are then typically located in regions of active star formation, such as the spiral arms of spiral galaxies. These stars illuminate any surrounding material and are largely responsible for the distinct colors of galaxy's arms.

As massive star dies, it may explode as a supernova. As the core collapses, it releases vast amounts of particles and energy that blow the star apart as they blast through space. The massive explosion produces shock waves that compress the ISM material surrounding the dying star. This compression leads to a new round of star birth. These characteristic make massive stars tracers of ISM and star-formation in galaxies.

OB star associations

The chief distinguishing feature of the members of a stellar association is that the most stars have similar chemical composition and ages, since they are gravitationally connected since their formation. In young stellar associations, most of the light comes from O- and B-type stars, so such associations are called OB associations.

OB associations are sparsely populated groupings of stars, typically between a few tens and a few hundreds of light-years across. They consist mainly of very young stars that have formed in the relatively recent past (a few million or tens of millions of years ago) from the same large interstellar cloud. Their study allow evaluating the initial mass function of star formation and chemical enrichment in galaxies in time and space.

1.1.2 Peculiar hot stars

The spectral study of stars revealed that a significant part of the hot stars had peculiar features, even among the ones that appeared to share most of their features with main

sequence stars. This study focuses on the study of B-type peculiar stars with circumstellar disks. Here is made a short presentation of the peculiar characteristics and their occurrence in hot stars. The detailed presentation of the studied subtypes are done in their respective chapters.

Peculiar hot stars as sometimes called *active OB stars*. Spectroscopic peculiarities are very common in OB-type stars, many of them displaying emission from their circumstellar environments. An interesting fact that should deserve greater research in the future is the role of binarity in this peculiars stars, since at least 44% of hot stars are in binary or multiple systems (Mason et al., 2009; Sana and Evans, 2011). The binarity should also play an important role in the star rotation rate, since it allows angular momentum exchanges. The review by Rivinius et al. (2013) includes a good summary of peculiar hot stars:

- **SPB**: Slow Pulsating early-type B stars with periods of a few hours;
- **β Cep**: B type stars with photometric variability period of a few days;
- **Herbig Ae/Be**: pre main sequence stars with accretion disks;
- **OB Supergiant**: post main sequence stars including, **LBV** (Luminous Blue Variable), **WR** (Wolf-Rayet), **P Cyg**, and **VV Cep** subtypes stars.
- **Oe**: O-type stars with strong winds and that exhibit emission lines;
- **He-rich**: early B-type stars with unusual strong lines of non-ionized He. They are often associated with strong magnetic fields in their photospheres.
- **Bn**: B-type stars displaying broad line profiles but no emission signal, usually interpreted as very fast edge-on rotators.
- **Be**: B-type main sequence stars whose spectra have shown or show emission lines. At least 20% of B-type stars are Be stars in our Galaxy with higher proportion in lower metallicity environments.

Table 1.1 contains the main spectral properties that characterize the active OB stars.

It is noteworthy that the term *peculiar* is sometimes used to describe specifically the chemical composition of the stellar photospheres, with a proper phenomenology associated. One example is Sirius, with weak Ca II K-line and strong metallic lines, classified as an Am star.

Table 1.1 - Selected spectral properties of peculiar hot stars and their observed presence in different classes of (non-supergiant) B-type stars. Circumstellar line emission formed in: (1a) equatorial decretion disk, (1b) accretion disk, (1c) corotating clouds. Other properties include (2) low-order line profile variations, (3) radial and/or short-period pulsation, (4) rapid rotation, (5) large-scale magnetic field, (6) surface abundance anomalies. Adapted from Porter and Rivinius (2003), originally on Baade et al. (2003).

	Observed general property							
Star group	1a	1b	1c	2	3	4	5	6
Classical Be	√	-	-	√	-	√	-	-
Herbig Ae/Be	-	√	-	-	-	-	-	-
He-rich	-	-	√	-	-	√	√	√
SPB	-	-	-	√	-	-	-	-
β Cep	-	-	-	-	√	-	-	-
Bn	-	-	-	-	-	√	-	-
He-abnormal and Bp	-	-	-	-	-	-	√	√

Note: The presence (or not) of each property should not be regarded as *sine qua non*, but rather expresses a statistically expected property.

1.2 Radiative transfer

Radiative transfer is the branch of physics that describes the propagation of electromagnetic radiation (light) through a material medium. The interaction of the light with matter can be described in terms of absorption, emission, and scattering processes. Analytic solutions to the radiative transfer can be applied for simple cases but for more realistic media, with complex multiple effects, numerical methods are required.

Consider the case of traveling particles over a medium consisted of isolated particles. The numerical density of the particles is n and their section collision cross section σ. The quantity

$$l = \frac{1}{n\sigma}\,, \tag{1.4}$$

is defined as the *mean free path* of the traversing particles. This scenario can be applied to a incident light beam of intensity I_λ

$$dI_\lambda = -n\sigma_\lambda I_\lambda\, dz = -\rho\kappa_\lambda I_\lambda\, dz\,, \tag{1.5}$$

where dI_λ is the change in the intensity, dz is the distance traveled, ρ the density of the particles and κ_λ is called *absorption coefficient* or *opacity*. The opacity is thus the cross

section for absorbing particles (photons, in our case) per mass of the medium and usually is a function of wavelength, density and temperature.

A useful definition is the *optical depth*

$$\tau_\lambda = -\int_0^Z \kappa_\lambda \rho \, dz. \tag{1.6}$$

This allows describing the light absorption as

$$I_\lambda = I_{\lambda 0} \exp^{-\tau_\lambda}, \tag{1.7}$$

solution of Eq. 1.5. Beyond absorption, the (pure) emission is described as

$$dI_\lambda = j_\lambda \rho \, dz, \tag{1.8}$$

where j is the *emission coefficient* of the medium. Combining the absorption and the emission terms

$$\begin{aligned} dI_\lambda &= -\kappa_\lambda \rho I_\lambda \, dz + j_\lambda \rho \, dz \\ -\frac{1}{\kappa_\lambda \rho}\frac{dI_\lambda}{dz} &= I_\lambda - \frac{j_\lambda}{\kappa_\lambda}. \end{aligned} \tag{1.9}$$

The ratio of the emission coefficient to the absorption coefficient is called the *source function* $S_\lambda \equiv j_\lambda/\kappa_\lambda$. Applying this and the optical depth definitions on above equation yields the *radiative transfer equation* (RTE)

$$\frac{dI_\lambda}{d\tau_\lambda} = I_\lambda - S_\lambda. \tag{1.10}$$

The physical conditions of a material medium can be described by the thermodynamic quantities. The optical properties of the medium, necessary for the radiative transfer problem solution (as S_λ and τ_λ), depends on the states of the medium.

A common assumption made when solving the thermodynamic statistical equilibrium is the *local thermodynamic equilibrium* (LTE). The reason for adopting LTE is that it enormously simplifies the calculation of states which matter (electron, atoms, ions, molecules) can be configured. It assumes that locally all thermodynamical states (as velocity distribution, Saha-Boltzmann distribution over degrees of excitation and ionisation, etc.) are described by a single temperature value. This is particularly important for describing gaseous media, and allows the optical properties be easily calculated to the radiative transfer solution. If LTE is assumed, the mean intensity J_λ of the system is described by the

Planck function B_λ. The Planck function B_λ is defined as

$$B_\lambda = \frac{2\pi hc^2}{\lambda} \frac{1}{\exp \frac{hc}{\lambda kT} - 1}, \tag{1.11}$$

where λ is the electromagnetic wavelength, h is the Planck constant, c the speed of light, k the Boltzmann constant and T the temperature of the body.

In low-density environments, however, the particle collision rates are low and energy is not equally distributed. The states assume a complex configuration and can no longer be associated with a single temperature value (and $J_\lambda \neq B_\lambda$), condition which is defined as non-LTE equilibrium. There are many astrophysical environments where departure from LTE are important. For example, the escaping photons of a star destroy the LTE equilibrium at its atmosphere (Mihalas and Athay, 1973). The non-LTE effects are specially important when analyzing spectral lines, where the particle level populations determines its optical properties.

1.3 Concepts of stellar astrophysics

In this section we briefly present the concepts of stellar astrophysics that are particularly important to this study. A key component that profoundly changes the stellar structure and evolution is the stellar rotation. The effects originated by rotation include geometrical deformation and photospheric gravity darkening, which can be observed only by high angular resolution (HRA) techniques, as well as evolutionary effects such as rotational chemical composition mixing. The proper consideration of these and other photospheric characteristics are fundamental when comparing models and observations since the modern HRA techniques are very sensible to brightness distribution of the targets (i.e., optical interferometry).

Stellar atmospheres and limb darkening

Stellar atmospheres are the connecting links between the observations and stellar astrophysics. In particular, the emergent spectrum of the *photosphere* (the atmospheric layer from which light is radiated) provide the way to estimated the internal stellar parameters of interest.

Limb darkening (LD) is an optical effect that occurs in the photospheres of stars, including our Sun, where the center of the stellar surface appears brighter than the edges or

limb. LD is important in several areas of stellar physics, including the study of transiting extrasolar planets, eclipsing binary stars, interferometry and some gravitational microlenses.

The radiation reaching and observer from a star can be described as the emission along his line of sight up to that point where it becomes opaque. When looking the edge of a star, the emission reaching the observer do not come from the same physical depth as when considering the stellar center because the line of sight travels over an oblique angle through the stellar atmosphere. In other words, the stellar radius at which one see opaque (optical depth $\tau \approx 1$) increases as the line of sight moves towards the edges (an analogy can be made with the air mass of a star at the observer's zenith and another near the horizon).

The effective temperature of the stellar photospheric region decreases for an increasing distance from the star. And the radiation emitted from a high-density gas is a strong function of temperature. So when one look at a larger radius at the limb regions, one is actually seeing a cooler region when compared to the center of the stellar surface.

The optical depth along non-vertical ray (as along a stellar atmosphere) is given by

$$\tau_\lambda = \tau'_\lambda \sec\theta\,, \tag{1.12}$$

where θ is the angle to vertical. So, the RTE becomes

$$\mu \frac{dI_\lambda}{d\tau'_\lambda} = I_\lambda - S_\lambda\,, \tag{1.13}$$

where $\mu \equiv \cos\theta$. The solution of the RTE presumes that we know the source function. For the top of the stellar atmosphere, where $\tau' \sim 0$, we expand S_λ using Taylor series

$$S_\lambda(\tau') \approx S_\lambda(0) + \dot{S}_\lambda(0)\tau'_\lambda = a + b\tau'_\lambda. \tag{1.14}$$

Using it at the RTE yields

$$I_\lambda(\tau'_\lambda = 0, \mu) = S_\lambda(\tau'_\lambda = \mu)$$

$$I_\lambda(0, \mu) = S_\lambda(\tau_\lambda = 1). \tag{1.15}$$

Eq. 1.15 is known as *Eddington-Barbier relation*, stating that for a source function of $S_\lambda = a + b\tau'$, the emergent specific intensity along a given ray is just equal to the source function at optical depth unity ($\tau \approx 1$) along that ray. It offers an interesting insight to understand the limb darkening effect. LD expresses how the specific intensity I_λ varies

as a function of angle to the the normal direction μ. An example of a LD law is (Claret, 2000)

$$\frac{I_\lambda(\mu)}{I_\lambda(1)} = 1 - \sum_{k=1}^{n} a_k(1-\mu^{k/2})\,, \tag{1.16}$$

where the terms a_k are the *limb darkening coefficients*.

Stellar wind

Stellar wind is a branch of contemporary astrophysics with wide ramifications. It is a common stellar phenomenon, even in low mass stars, such as the Sun. In the case of the Sun, the mass loss is negligible, with a small impact in its evolution. Nevertheless its effects are easily seen as the wind influences our planetary magnetosphere and the heliosphere has a rich phenomenology when interacting with the local ISM (Frisch et al., 2011).

Stellar winds constitute a hydrodynamic phenomenon of circumstellar gas flow. In the case of hot or red giants stars, the observed mass loss rates are significant, affecting drastically the evolution of these stars. The main characteristic of hot stars winds is the dominant role that radiation plays in the energy and momentum balance of the circumstellar plasma. Thus, massive stars mass loss rates are determined from the calculation of the radiative acceleration in their winds.

The fundamental theoretical works on stellar winds are the ones by Lucy and Solomon (1970), who identified line scattering as the mechanism that could drive stellar winds. However these authors predicted mass loss rates that were too low compared to the observations, as they assumed that only a few optically thick lines were present. The situation improved due to the landmark paper by Castor et al. (1975) (hereafter CAK), who included an extensive line list that yielded a significant larger value for mass loss rate.

The mass loss rate $\dot{M}$ is related to the density (ρ) profile and velocity (v) profiles. From the mass conversation relation:

$$\dot{M} = 4\pi r^2 \rho(r) v(r)\,, \tag{1.17}$$

for a spherically symmetric wind in the steady-state regime. The velocity law usually assumed in the CAK theory, known as *beta law*:

$$v(r) \simeq v_0 + (v_\infty - v_0)\left(1 - \frac{R_*}{r}\right)^\beta\,, \tag{1.18}$$

where v_0 is the wind initial speed and v_∞ is called the terminal speed. See Lamers and Cassinelli, 1999 for an overview.

As example of mass loss rates, Kudritzki and Puls (2000) show the following relation to the mass loss of O-type stars of the solar neighborhood (III, V classes)

$$\log\left[\dot{M}v_\infty\left(\frac{R_*}{R_\odot}\right)^{1/2}\right] = 19.87 + 1.57\log\left(\frac{L_*}{L_\odot}\right), \tag{1.19}$$

with $\dot{M}$ is given in $M_\odot\,\mathrm{yr}^{-1}$ and v_∞ in km s^{-1}.

1.3.1 Stellar Rotation

Stars can rotate up to their critical rotational limit, i.e., a rotation that produces a centrifugal force that can completely cancel the gravitational force at the stellar surface. Thus, rotational effects should be much more pronounced closer to the equator then the poles.

The rotational effects can profoundly transform the internal stellar configuration (for example, a core rotating faster than the outer envelope), changing the equilibrium configuration and driving internal instabilities which transport both chemical elements and angular momentum. The book from Maeder (2009) is an excellent reference about this subject.

Rotational effects have usually been studied spectroscopically via the broadening of photospheric absorption lines. Recently, rotational effects were also detected interferometrically. van Belle et al. (2001) measured the oblateness of a star, Altair, for the first time. Domiciano de Souza et al. (2003) found the first indication of strong stellar oblateness for Achernar with VLTI-VINCI interferometer; and Monnier et al. (2007) did the first directly detection of the effect on a main sequence star via interferometric imaging of Altair using the CHARA interferometric array.

Up to now, seven rapid rotating stars have their rotational oblateness measured by interferometry (van Belle, 2012). A summary of these measurements is at Table 1.2.

Table 1.2 - List of rapid rotating stars observed stars interferometrically to date.

Proper name	Bayer designation	Spectral type	Rotation rate (W)	Ref.
Achernar	α Eri	B3Vpe	0.838(10)	1
Alderamin	α Cep	A7IV-V	0.730(39)	2
Altair	α Aql	A7IV-V	0.696(12)	3
Caph	β Cep	F2III-IV	0.688(66)	4
Rasalhague	α Oph	A5IV	0.634(17)	2
Regulus	α Leo	B8IVn	0.783(38)	4
Vega	α Lyr	A0V	0.701(28)	5

(1) Domiciano de Souza et al. (2014), (2) Zhao et al. (2009), (3) Monnier et al. (2007), (4) Che et al. (2011), (5) Peterson et al. (2006).

Rotation rate notation

Rotational velocities can be expressed in many ways, both in angular (Ω) and linear (v) velocities. Stellar rotational rates are usually defined as fractions of their critical values

$$v_{\rm crit} = \sqrt{\frac{2}{3}\frac{GM_*}{R_p}};\ \Omega_{\rm crit} = \sqrt{\frac{8}{27}\frac{GM_*}{R_p^3}}. \tag{1.20}$$

The factor 3/2 comes from the oblateness $R_{\rm eq} = 3/2R_p$ for critical solid body rotation, known as Roche approximation. The Roche model describe equipotential surfaces considering centrifugal forces due to rotation in addition to gravity. As pointed out by Rivinius et al. (2013), the description of the rotational rate in terms of this quantities are only meaningful in the Roche approximation. The authors suggest then the use the quantity W, defined in terms of the equatorial orbital speeds

$$v_{\rm orb} = \sqrt{\frac{GM_*}{R_{\rm eq}}};\ \Omega_{\rm orb} = \sqrt{\frac{GM_*}{R_{\rm eq}^3}}, \tag{1.21}$$

$$W = \frac{v_{\rm rot}}{v_{\rm orb}}. \tag{1.22}$$

Equatorial orbital quantities (and so W) are independent on the details of how the star rotates (e.g., rigid vs. differential rotation as scenarios usually explored in the literature) and W directly defines what velocity boost is required for a given star to launch material into the closest possible orbit. In this study we endorse the use of this quantity.

Useful relations between rotational rates and rigid rotators are

$$W = \sqrt{2\left(\frac{R_{\rm eq}}{R_p} - 1\right)}\,, \tag{1.23}$$

$$\frac{\Omega}{\Omega_{\rm crit}} = \sqrt{\frac{27}{8}\frac{W^2}{(1+0.5W^2)^3}}. \tag{1.24}$$

Geometrical oblateness

Here we present the structural geometrical effect of the stellar rotation under the assumption of a Roche's equipotential surface. In this approximation, rotating stars are assumed to be rigid rotators, i.e., the angular velocity Ω is a constant with respect to stellar latitude.

The stellar surface constant equipotential ϕ can be written as

$$\phi(\theta, r) = -\frac{GM}{r(\theta)} - \frac{1}{2}\Omega^2 r^2(\theta)\sin^2\theta\,, \tag{1.25}$$

and then compared to the one at polar direction ($\theta = 0$)

$$\frac{GM}{r(\theta)} + \frac{1}{2}\Omega^2 r^2(\theta)\sin^2\theta = \frac{GM}{R_{\rm p}}. \tag{1.26}$$

This can be related to the local effective gravity ($\vec{g}_{\rm eff}$)

$$\vec{g}_{\rm eff} = -\nabla\phi\,, \tag{1.27}$$

$$\vec{g}_{\rm eff} = \left[-\frac{GM}{r^2(\theta)} + \Omega^2 r(\theta)\sin^2\theta\right]\hat{r} + \left[\Omega^2 r(\theta)\sin\theta\cos\theta\right]\hat{\theta}\,, \tag{1.28}$$

The surface effective gravity modulus is then

$$g_{\rm eff}(\theta) = \left[\left(-\frac{GM}{r^2(\theta)} + \Omega^2 r(\theta)^2\sin^2\theta\right)^2 + \Omega^4 r^2(\theta)\sin^2\theta\cos^2\theta\right]^{1/2}. \tag{1.29}$$

Equation 1.26 can be rearranged trigonometrically to determine $r(\theta)/R_p$ for a given W (or Ω, from Collins and Harrington, 1966)

$$\frac{r(\theta)}{R_p} = \cos\left(\frac{\arccos(\Omega/\Omega_{\rm crit}\sin\theta) + 4\pi}{3}\right) \times \left(\frac{-3}{\Omega/\Omega_{\rm crit}\sin\theta}\right)\,, \tag{1.30}$$

with $0 < \theta \leq \pi/2$, i.e., from pole ($\theta = 0$) to the equator ($\theta = \pi/2$).

Polar radius and luminosity

Polar radii and luminosity values can only be determined by model of internal structure that considers rotation. In a first approximation, however, one may consider these quantities as independent of rotation.

Indeed, the polar radius has a weak dependence on the rotation rate, which implies small changes of internal structure brought by centrifugal force. While the equatorial radius strongly inflates with rotation, the polar radius decreases by a few percent in general ($\lesssim 2\%$ at critical rotation for typical B and late type O stars, between 3 and 20 $M_\odot$; Ekström et al., 2008).

The luminosity can also be considered as constant in the range of masses corresponding to B type stars. As shown for instance by Maeder (2009), a simple relation can be obtained,

$$\frac{L(\Omega/\Omega_{\rm crit})}{L(0)} = 1 - b\left(\frac{\Omega}{\Omega_{\rm crit}}\right)^2 , \tag{1.31}$$

with b=0.07, 0.065 and 0.06 for a 3, 9 and 20 $M_\odot$ respectively. The above ratios reaches at most 7% for critically rotating stars. For stars rotating below $\Omega/\Omega_{\rm crit} = 0.5$ ($W \sim 0.3$), the difference between luminosity of a rotating star and a non-rotating counterpart is less than 1%.

Gravity darkening

While rotation increases the total stellar surface area, it also decreases the average radiative flux (i.e., temperature) per unit area to keep the (near) constant luminosity. The decrease of the surface effective gravity implies in differences in the emergent flux and the effective temperature according to the latitude, $T_{\rm eff}(\theta)$. Thus, the emission of a rotating star is the integration of spectra of different gravities and temperatures, and is dependent on the viewing angle.

This decreasing flux as function of co-latitude in rotating stars is called *Gravity darkening* or *von Zeipel effect*, after the pioneer work by von Zeipel (1924). According to von Zeipel, the local emergent flux should be proportional to the local effective gravity. To a pure radiative envelope (i.e, a black body), this implies that $T_{\rm eff} \propto g_{\rm eff}^{1/4}$, where the equatorial regions of the star are fainter and cooler that the polar ones.

The von Zeipel relation can be generalized using a power law in the form of $T_{\rm eff} \propto g_{\rm eff}^{\beta}$. Even so, Lucy (1967) applied the von Zeipel principle not to a black body emission but to

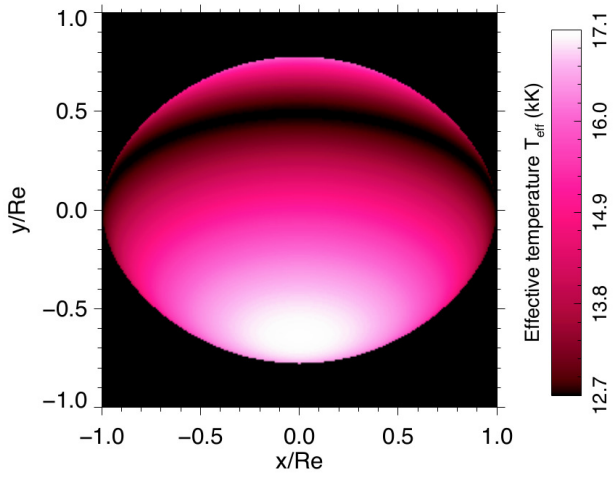

Figure 1.1: The temperature map of the fast-rotating star Achernar ($W \simeq 0.84$) seen at $i \simeq 60°$. The effects of the geometrical oblateness ($R_{\rm eq}/R_p = 1.352$) and the gravity darkening ($\beta = 0.166$) are easily identified (Domiciano de Souza et al., 2014).

a (pure) convective envelope. The author found the value of $\beta = 0.08$, indicating that the traditional von Zeipel exponent could overestimate the temperature differences between stellar pole and equator. Indeed, interferometric results showed $0.08 < \beta < 0.25$ for the photosphere of rotating stars (van Belle, 2012). This was interpreted as the existence of a thin convective layer at the surface of these stars, but alternative scenarios exist. The effects of the geometrical oblateness and the gravity darkening can be seen in Fig. 1.1 applied to the Be star Achernar. More details are in Chapter 5.

1.4 The Be stars

Be stars are main sequence B type stars that show, or has shown in the past, Balmer lines in emission (Jaschek et al., 1981), attributed to a circumstellar (CS) disk. Be stars are fast rotators (Rivinius et al., 2006) and this fact brings several consequences to its structure and evolution. These stars are the fastest rotating stars in the main sequence, making them key targets to study stellar evolution at high rotation rates.

In the Galaxy, about 15-20% of all field B-type stars are Be stars, but with the Be phenomenon as such extending from late O- to early A-type stars. The proportion of Be stars increases in the Large Magellanic Cloud (LMC) and especially in the Small Magellanic Cloud (SMC), and can be high as one-half in the B0-B4 subtypes range (Martayan et al., 2006, 2007). It is agreed that the relative frequency of Be stars are anti-correlated with metallicity. No evidence of magnetic field in Be stars exists, although recent magnetism

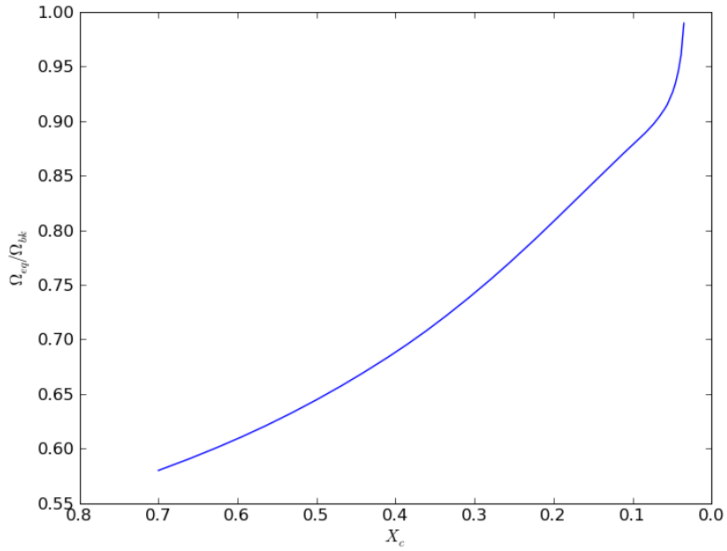

Figure 1.2: Equatorial angular velocity divided by the Keplerian angular velocity at equator as a function of the Hydrogen mass fraction of the star (X_c) for a constant total angular momentum ($M = 7M_\odot$ and $Z \sim 0.014$). The x-axis is inverted because the value of X_c decreases due to H fusion by the star along the main sequence. (Rieutord and Espinosa, 2013).

surveys point to a rate of ∼10% over all the B-type range (e.g., Wade et al., 2014).

Be stars are known to be rapid rotators and this property is believed to be fundamentally linked to the existence of the disk. Another mechanism(s) must act together with rotation to explain the phenomenon, where the material ejected by the star ought to reach Keplerian rotation in progressively higher energy orbits. Although great strides to assess the photosphere-disk interface has been made, the additional mechanism(s) has not yet been conclusively identified.

1.4.1 Be stars evolution and rotation rates

It is known that rotating stars transport angular momentum from their interior towards the surface during their evolution. The classical picture is that single B-type stars that have a sufficiently large rotational rate ($\Omega/\Omega_{\rm crit} > 0.8$, or $W > 0.53$) at the zero age main sequence (ZAMS) will approach their critical limit towards the end of the main sequence (e.g. Ekström et al., 2008 and Georgy et al., 2013). This effect can be seen in Fig. 1.2, there the expected rotation rate calculated with the ESTER code (Espinosa Lara and Rieutord, 2007) is related to the Hydrogen fraction present in the stellar core ($X_c \gtrsim 0.1$, the main sequence).

The increasing the rotation rate with evolution does not imply the absence of rapid

rotators early in the MS. It indicates that evolution will make stars that were moderately rotating stars to rotate faster towards the end of the MS, a phase at which fast rotators would likely to exist. Observations of stars in very young open clusters show that there exists a mass-dependent distribution of rotational velocities with age (Huang et al., 2010), and despite being rare, it is possible to have very fast rotators early in the MS.

Traditional stellar evolution models do not contradict this picture, and early evolutionary models (for example, the op. cit.) did not contain predictions of stars rotating close to the critical limit during the whole MS. For example, all the evolutionary tracks presented by Georgy et al. (2013) assume that the star rotates as a solid body at the ZAMS. Just after the ZAMS, because of meridional circulation, the internal rotational velocity distribution is readjusted, reducing the rotational velocity rate at the surface, in particular for the most rapid rotators.

This constraint was recently overcome by making a better treatment of pre-MS phases. A more realistic internal structure of the star at the ZAMS was obtained by Haemmerlé et al. (2013) and applied by Granada and Haemmerlé (2014), so their models can describe fast rotators all over the MS phase. The evolutionary phase where the Be phenomenon occurs is a topic that undoubtedly deserves a detailed examination.

1.5 Astrophysical disks

Astrophysical disks are the (near-)continuous media in orbit around a massive central body. They are observed in a wide variety of astrophysical systems, and they are created in both inflows and outflows whenever the rotation speed of the orbiting material greatly exceeds the radial flow speed. Examples of disk systems formed during infall include young stellar objects, mass transfer binaries, and active galactic nuclei (AGN). Similarly, outflowing disks also form around luminous stars, such as B[e] stars, and possibly luminous blue variable and asymptotic giant branch (AGB) stars.

The presence and structure of astrophysical disks are driven by angular momentum and mass transfer with the central body, where viscosity is often the key element (see Pringle, 1981 for a review). Disks are long-lived structures (i.e., are stable for many orbits), and may exhibit waves and perturbations. These instabilities are related to important but not yet fully understood processes of star and planet formation, as well as formation of

galactic structure and intracluster medium structure (from AGN feedbacks). For review on instabilities and waves in astrophysical disks, see Balbus (2003).

1.5.1 Thin disks

In a thin disk (i.e., $z \ll r$), the surface density profile $\Sigma(r)$ can be obtained from the Navier-Stokes equations in cylindrical symmetry, integrated over disk height. The mass conservation equation is

$$\frac{\partial \Sigma}{\partial t} + \frac{1}{r}\frac{\partial}{\partial r}\left(r \Sigma v_r\right) = 0\,, \tag{1.32}$$

and the angular momentum conservation is

$$\frac{\partial}{\partial t}\left(\Sigma r^2 \Omega\right) + \frac{1}{r}\frac{\partial}{\partial r}\left(r \cdot \Sigma r^2 \Omega \cdot v_r\right) = \frac{1}{r}\frac{\partial}{\partial r}\left(r \cdot \Sigma r \cdot \nu r \frac{\partial \Omega}{\partial r}\right)\,, \tag{1.33}$$

where v_r is the radial velocity, Ω is the angular velocity, $r\partial\Omega/\partial r$ the velocity shear, and ν is the kinematic viscosity.

The above equations can be combined to a diffusion equation for the surface density

$$\frac{\partial \Sigma}{\partial t} = \frac{3}{r}\frac{\partial}{\partial r}\left[r^{1/2}\frac{\partial}{\partial r}\left(\nu \Sigma r^{1/2}\right)\right]\,, \tag{1.34}$$

for a point-mass potential $\Omega = \left(GM/R^3\right)^{1/2}$. The vertical thickness H follows from hydrostatic equilibrium

$$\frac{1}{\rho}\frac{\partial P}{\partial z} = \frac{\partial}{\partial z}\left[\frac{GM}{\left(r^2+z^2\right)^{1/2}}\right] \approx -\frac{GMz}{r^3}\,, \tag{1.35}$$

and the scale height $H(r)$ can be determined as

$$-\frac{1}{\rho}\frac{c_s^2 \rho}{H} \simeq -\frac{GMH}{r^3}\,, \tag{1.36}$$

with $c_s = \sqrt{k_{\rm B}T/\mu m_H}$ the disk sound speed. Therefore

$$H \simeq c_s \left(\frac{GM}{r^3}\right)^{-1/2} \simeq \frac{c_s}{\Omega} \simeq \frac{c_s}{v_\phi} r. \tag{1.37}$$

Viscosity

The timescale for viscous disk evolution is

$$\tau \sim \frac{r^2}{\nu}\,, \tag{1.38}$$

estimated from Eq. 1.34 by taking $\frac{\partial^2}{\partial r^2} \rightarrow \frac{1}{r^2}$ and $\tau^{-1} = \frac{1}{\Sigma}\frac{\partial \Sigma}{\partial t}$. The kinematic viscosity ν is sometimes described as "molecular viscosity"

$$\nu \simeq v_T \lambda \,, \tag{1.39}$$

where v_T is the thermal velocity and λ is the mean free path. More often, specially in the Be stars context, the kinematic viscosity is described in terms of "α-disk" parametrization (Shakura and Sunyaev, 1973)

$$\nu = \alpha c_s H \,, \tag{1.40}$$

where α is a dimensionless constant. α can be interpreted as the efficiency on which viscosity arising from collisions in a turbulent medium moving in eddies of length-scale $\sim H$ at velocity $v \sim c_s$. It is an often *ad-hoc* assumption α constant with time or with radius.

The main physical explanation of the viscosity mechanism in astrophysical disks is the magneto-rotational instability (MRI; e.g., Balbus and Hawley, 2002). Roughly speaking, MRI is originated by magneto-hydrodynamical instabilities in a differentially rotating and magnetized disk. This would drive turbulence, producing viscosity at tapping the rotational energy.

1.5.2 Circumstellar disks

The disks around hot stars are the result of the hydrodynamical transport of the material and its radiative heating. From the point of view of their opacity, the disks of hot stars are relatively simple when compared to their cool stars counterparts. In the case of the last, the dominant opacity sources and dust and molecular gas, which depend on the rather complicated chemistry within the protostellar disk. In the case of the former, however, the disk is comprised mostly of ionized atoms and free electrons. This makes hot star disks ideal laboratories for studying the physics of outflowing disks.

As discussed by Bjorkman and Carciofi (2005), the mechanism by which the stellar outflow is produced have important consequences on the disk structure. The azimuthal velocity v_ϕ of the main circumstellar environments are

$$v_\phi = \begin{cases} v_{\rm rot}(r/R_*) & \text{(magnetically dominated; } r < R_{\rm A}) \,, \\ v_{\rm rot}(r/R_*)^{-1} & \text{(radiatively driven),} \\ v_{\rm rot}(r/R_*)^{-1/2} & \text{(viscously driven),} \end{cases} \tag{1.41}$$

where $v_{\rm rot}$ is the disk azimuthal velocity at the stellar equator, and $R_{\rm A}$ is the Alfvén radius, the maximum extent of closed magnetic loops (see e.g., Ud-Doula et al., 2008). The velocities reflect different interactions of the circumstellar material with their central star. For example, a azimuthal velocity proportional to the radius set a centrifugal driven envelope, as one trapped by a magnetic field. If the envelope has a Keplerian rotation profile this is equivalent to angular momentum exchanges to balance the gravitational force at different distances. And, if the azimuthal velocity decreased linearly with radius, the envelope angular momentum is conserved, setting a radiatively driven wind. Specifically for this work are evaluated disks dominated by magnetism (B-type He-rich stars; Chap. 3) and by viscosity (Be stars).

1.5.3 Be star disks

The investigation of the photosphere of Be stars, and of their circumstellar (CS) disks, has entered a new era during last years, both observationally and theoretically. Optical and infrared interferometry played a key role in the recent development of the Be field. It is a technique capable of bringing qualitatively new information by resolving the stars and their disks at the milliarcsecond (mas) level. Due to the relatively strict magnitude limits of current interferometers, bright nearby Be stars are among the most popular and most frequently observed targets.

From both observational and theoretical studies it is known that a considerable part of circumstellar disks, notably those of Be stars, are geometrically thin and rotate in a Keplerian fashion. Although spectroscopic evidences already suggested that Be stars disk rotated in a Keplerian way (e.g., the CQE line profiles in shell stars; Hanuschik, 1995), interferometric observations provided a more precise and reliable evidence of this rotational configuration (Meilland et al., 2007 observed the first interferometric evidence of Keplerian profile in a Be star, followed by Kraus et al., 2012; Wheelwright et al., 2012). This allowed identifying kinematic viscosity as the mechanism that makes these disks grow: viscous torques in the Keplerian disk transfer angular momentum from the base of the disk outwards, thus allowing the gas particles to reach progressively wider orbits.

The viscous decretion disk (VDD) model (Lee et al., 1991; Bjorkman, 1997; Okazaki, 2001) is now regarded by many as the paradigm that offers the needed conceptual framework to explain the observed properties of the disks. Be star disks are highly-ionized

environments, radially driven by viscosity and where non-LTE effects are also important. The vertical direction is pressure-supported, confirming that the complete solution of their structure is also determined by the radiative equilibrium - and then dependent of the radiative transfer solution. The VDD model, solved by radiative transfer, have proved to be fully consistent with multiple disk observations. See Rivinius et al. (2013) for a dedicated review.

The emergence of the VDD model to explain the Be star circumstellar disks ensures their similarity with (viscous) accretion disks that are present in various astrophysical scales, from galactic discs, AGNs, to X-ray binary stars. In most of these systems - including Be stars - little is known about mechanisms that originate the viscosity, that drives angular momentum and mass transfer and that fine-tune their structures.

The CS disk surface density, $\Sigma(r,t)$, as function of time is given by a simplified form of the Navier-Stokes equations (Okazaki, 2007)

$$\frac{\partial\Sigma(r,t)}{\partial t} = \frac{1}{\tau_{\rm vis}}\left(\frac{3}{r}\frac{\partial}{\partial r}\left[r^{1/2}\frac{\partial}{\partial r}(r^2\Sigma(r))\right] + \Sigma_{\rm in}(t)\frac{r_{\rm in}^2}{r_{\rm in}^{1/2}-1}\frac{1}{r}\delta(r-r_{\rm in})\right), \tag{1.42}$$

where $r_{\rm in}$ is the disk injection radius, $\Sigma_{\rm in}$ the injected surface density, and

$$\tau_{\rm vis} = \frac{(GMR_{\rm eq})^{\frac{1}{2}}}{\alpha c_s^2}, \tag{1.43}$$

controls the radial flow (α is the Shakura-Sunyaev's viscous parameter and c_s the disk sound speed).

The steady-state solution of Eq. 1.42 (i.e., $\partial\Sigma/\partial t = 0$ with $\Sigma_{\rm in} \neq 0$) yields

$$\Sigma(r) = \frac{\dot{M}v_{\rm orb}R_{\rm eq}^{1/2}}{3\pi\alpha c_s^2 r^{3/2}}\left[\left(\frac{R_0}{R_{\rm eq}}\right)^{1/2} - 1\right], \tag{1.44}$$

where $\dot{M}$ is the disk mass injection, and R_0 is a constant from the torque momentum equation integration, sometimes called as *disk truncation*.

The disk material is often parametrized in the literature as the density ρ (mass per volume), related to the surface density by

$$\Sigma(r) = \int_{-\infty}^{\infty}\rho(r,z)dz, \tag{1.45}$$

where the density can be written in the parametric form

$$\rho(r,z) = \rho_0\left(\frac{R_{\rm eq}}{r}\right)^m \exp\left[-\frac{1}{2}\left(\frac{z}{H}\right)^2\right], \tag{1.46}$$

with H as the disk scale height. The steady-state solution of the surface density leads to $m = 3.5$. This and further details of the VDD models are presented in Appendix A. Second order effects, as non-isothermal disk scale height, can be investigated in steady-state disks (Carciofi and Bjorkman, 2008).

Haubois et al. (2012) studied the viscous dynamical evolution of Be stars, solved by radiative transfer. Their study included the temporal evolution of the disk density for different scenarios, including disk build-up and dissipation processes. They showed that the main parameters that controls the Be stars light curves at different wavelengths are mass disk injection history, inclination angle i and the α viscosity parameter.

The temporal variation of some fundamental quantities in Be stars are related to their disk surface density profiles. In particular, we highlight that the density power-law index $m > 3.5$ mimics a dynamical disk at growing process and $m < 3.5$ the opposite, namely a disk in dissipation. Other important results are that long wavelength light curves (as mm) are useful for disk size determination. Physical parameters from these systems can be inferred from their light curves, however a degenerescence exists in the parameters and the sets of decretion scenarios for a given (short-term) observed light curve. This degenerescence can be avoided with more observables and a longer time coverage of the observations.

1.6 The optical long baseline interferometry (OLBI) technique

The investigation of the photospheric and the circumstellar emission of hot stars entered a new phase in the first decade of the twentieth first century. Optical and infrared interferometry were established as a novel technique capable of bringing qualitatively new information by resolving stars and their surroundings at the milliarcsecond (mas) level. Due to the relatively bright magnitude limits of interferometers, nearby hot stars (notably Be stars) are among the most popular and most frequently observed targets.

Principles of interference

In common cases, light can be treated as composed of particles (photons). We can think about photometry as a photons count process and a small telescope image as a photon count with spatial information. However, interesting phenomena are associated with light

when we consider its wave properties. One example is the light polarization. Other one is the interference: waves can combine themselves in a constructive and destructive way depending on their frequencies and phases (position).

The motivation behind the interference is to be able to increase of spatial resolution when looking at a celestial object and it is discussed below. Radio astronomy took to advantage of this principle since at least the 1960's. Optical interferometry needed to wait until the twentieth first century to systematically make use of it. This time difference is explained by the technological boundaries needed by the two different wavelength domains. While in radio frequencies we can easily record the actual wave format information (and perform the interference when appropriated at a later time), in optics this is impossible since the involved frequencies are too high to be processed by any electronic device. In optical frequencies the interference must be done in real time in the optical system. Further more, the optical length in which the interference occurs is crucial to result. The required precision is of the order of the wavelength to be combined. This means that only optical paths determined in fractions of μm are capable to perform the desired interference. And this was an insuperable technological barrier until a decade ago.

The double-slit experiment

In 1801 Thomas Young demonstrated the light has wave properties trough the double-slit experiment (also referred as Young's experiment)[1].

Consider the light as and electromagnetic wave $\vec{E}$, linearly polarized in $\hat{x}$ and propagating along $\hat{z}$

$$\vec{E} = \mathrm{Re}\left\{a \exp\left[2\pi i \left(vt - \frac{z}{\lambda}\right)\right]\right\} \hat{x} = \mathrm{Re}\{a \exp(-i\phi) \exp(2\pi i v t)\}\hat{x}. \tag{1.47}$$

With z fixed and $\phi = 2\pi z/\lambda$, we can write

$$\vec{E} = \tilde{E} \exp(2\pi i v t)\hat{x}\,, \tag{1.48}$$

where $\tilde{E} = a \exp(-i\phi)$.

In the double slit experiment, a light source (as the Sun) illuminates a plate pierced by two parallel slits, and the light passing through the slits is observed on a screen behind

[1] We recommend watching the video "The Original Double Slit Experiment" by Veritassium (https://www.youtube.com/watch?v=Iuv6hY6zsd0) about their research on Young's original work.

the plate. At any given point on the image plane, the observed intensity I will be given by the modulus squared of the summation of the electric field $\vec{E}$ arriving from the two slits. If we call these $\vec{E_1}$ and $\vec{E_2}$, we can write the detected intensity as

$$\begin{aligned} I &= \left\langle (\tilde{E_1} + \tilde{E_2})^* \times (\tilde{E_1} + \tilde{E_2}) \right\rangle \\ &= \left\langle \tilde{E_1}^2 \right\rangle + \left\langle \tilde{E_2}^2 \right\rangle + \left\langle \tilde{E_1} \tilde{E_2}^* \right\rangle + \left\langle \tilde{E_1}^* \tilde{E_2} \right\rangle \\ &= \left\langle \tilde{E_1}^2 \right\rangle + \left\langle \tilde{E_2}^2 \right\rangle + \left\langle 2\|\tilde{E_1}\|\|\tilde{E_1}\| \cos(\phi) \right\rangle , \end{aligned} \tag{1.49}$$

where ϕ is the phase difference between the electric field components $\vec{E_1}$ and $\vec{E_2}$ and the angle brackets refer to the time average. Here, as above, ϕ is phase or spatial positioning of the wave. The first two terms of this equations refer to the mean intensity seen in the double-slit fringe pattern, while the third term, which is associated with the modulation of the fringes from light to dark, clearly encodes the values of the complex products $\left\langle \tilde{E_1} \tilde{E_1}^* \right\rangle$ and $\left\langle \tilde{E_1}^* \tilde{E_1} \right\rangle$, i.e., the visibility function and its complex conjugate. If we assume $\|\tilde{E_1}\| = \|\tilde{E_2}\| = E$, the modulation is $0 < I < 4E^2$.

Angular resolution

Diffraction refers to the phenomena which occur when a wave encounters an obstacle. The spatial resolution of a lens (like a telescope) is set by diffraction limit of the incident light. The diffraction pattern is the Fourier transform[2] of the aperture intensity distribution. The pattern resulting from a uniformly-illuminated circular aperture has a bright region in the center and is known as Airy disk (named after George Biddell Airy).

The angle at which the first Airy lobe goes to zero, measured from the direction of incoming light, is given by the approximate formula:

$$\sin\theta \approx \theta \approx 1.22 \frac{\lambda}{D} , \tag{1.50}$$

where θ is in radians, λ is the wavelength of the light and D is the diameter of the aperture. In case of telescope, D is the telescope diameter and θ is the angular size of a emitter that the telescope can isolate (or *resolve*).

In the double slit experiment - and in the two telescopes configuration - it is possible to demonstrate that the first Airy disk minimum, used as criterion for the optical system

[2] A brief definition of Fourier transform is done at Appendix B.

resolution and defined as *diffraction limit*, will be

$$\theta \approx 1.22 \frac{\lambda}{B}\,, \tag{1.51}$$

where B is the separation of the incoming light wave (in the case of celestial observations, it is the separation of the telescopes projected in the direction of the target, referred as $\vec{B}_{\rm proj}$; see below).

Atmospheric seeing sets the maximum effective resolution of an image at optical wavelengths to $\approx$ 0.5 arcsec or worse, depending on the meteorological conditions. The diffraction limit of a large telescope is much smaller, being $\approx$ 20 miliarcsec for a 4 m telescope, and can be pursued by modern active-optics techniques. However, if we combine the light from two far apart telescopes ($B = 300$ meters), the angular resolution is $\approx$ 0.3 miliarcsec. Of course, this is a challenging value since the influence of the atmosphere and instrument must be taken into account.

1.6.1 Visibilites and phases

The quantity registered in interferometry is the normalized complex visibility $\tilde{V}$. The visibility amplitude $\|\tilde{V}\|$, in terms of the registered fringes intensities I, is

$$\|\tilde{V}\| = \frac{I_{\rm max} - I_{\rm min}}{I_{\rm max} + I_{\rm min}}\,, \tag{1.52}$$

ranging from 0 to 1. When $\|\tilde{V}\| \approx 0$, the source is considered as an extended object, which is called *fully resolved* target. When $\|\tilde{V}\| \approx 1$, a source is considered as a point-like source and is called *unresolved* target. Since visibility $\tilde{V}$ is a complex quantity, its amplitude is often expressed as V^2.

The complex visibility $\tilde{V}(\vec{u})$ is function of the vector $\vec{u}$, the spatial frequency of the projected baseline $\vec{B}_{\rm proj}$, $\vec{u} = \vec{B}_{\rm proj}/\lambda$. $\vec{B}_{\rm proj}$ is not just the separation of the telescopes (B), but this separation projected in the object direction. Typically, $\|\vec{B}_{\rm proj}\| \propto B\cos\zeta$, where ζ is the zenithal angle of the object.

The van Cittert-Zernike theorem (van Cittert, 1934; Zernike, 1938) relates the complex visibility $\tilde{V}(\vec{u})$ to the Fourier transform of the brightness distribution $\mathscr{I}(\vec{r},\lambda)$ of an extended source on the plane of sky

$$\tilde{V}(\vec{u}) = \frac{\iint \mathscr{I}(\vec{r},\lambda)\exp\left(-2\pi i\,\vec{u}\cdot\vec{r}\right) d^2\vec{r}}{\iint \mathscr{I}(\vec{r},\lambda)\, d^2\vec{r}} = \|\tilde{V}\|\exp\left(i\phi\right), \tag{1.53}$$

where $\vec{r}$ is the on-sky plane angular position and ϕ is the visibility *phase*. A common quantity used in high spectral resolution interferometry are the differential phases $\phi_{\rm diff}$ defined as

$$\phi_{\rm diff}(\lambda, \lambda_{\rm r}) = \phi(\lambda) - \phi(\lambda_{\rm r})\,, \tag{1.54}$$

where $\lambda_{\rm r}$ is a wavelength of reference simultaneously observed.

The atmospheric influence and closure phases

So far, we have neglected the influence of the atmosphere over the aperture of the telescope. Indeed, the amplitude of the visibilites can obtained with relative high accuracy and the vast majority of optical interferometry results before the 2000's are from the visibility amplitudes alone. Unfortunately, turbulent atmosphere causes a big displacement (or decomposition) of the incoming wavefront, destroying the fringe phase information. This effect is sometimes called *piston effect*.

One condition that is crucial to successfully perform the full interference is to cancel the optical path difference (OPD) between the beams for the different telescopes. Even though adaptive optics makes possible to trace the fringe pattern and correct wavefront delays arriving each telescope, the absolute phase information is lost (e.g., Mariotti, 1994). However, with the advent of telescope arrays (three or more telescopes), the *closure phase* can be used to overcome this difficulty.

In a three-telescope system, each one receives the wavefront with phase ψ_n and delay e_n. Summing the phase information of telescopes combined two by two, the piston effect can be canceled to reveal fundamentally new information about the sources under study, not contained in the visibility amplitudes. Indexing the phases according to the telescopes combined

$$\begin{aligned} \psi_{12} &= \phi_{12} + e_2 - e_1\,, \\ \psi_{23} &= \phi_{23} + e_3 - e_2\,, \\ \psi_{31} &= \phi_{31} + e_1 - e_3\,, \end{aligned} \tag{1.55}$$

the closure phase O_{123} for the three antennas can then be obtained as

$$\begin{aligned} O_{123} &= \psi_{12} + \psi_{23} + \psi_{31} \\ &= \phi_{12} + \cancel{e_2} - \cancel{e_1} + \phi_{23} + \cancel{e_3} - \cancel{e_2} + \phi_{31} + \cancel{e_1} - \cancel{e_3} \\ &= \phi_{12} + \phi_{23} + \phi_{31}. \end{aligned} \tag{1.56}$$

Or, in equivalent way, by the *bispectrum* $\tilde{B}_{123} = \tilde{V}_{12}\tilde{V}_{23}\tilde{V}_{31}$, the complex product of the visibilities from the array ($\tilde{B}_{123} = \|\tilde{B}_{123}\| \exp iO_{123}$). Similarly, multiple telescopes beams can be rearranged three by three to provide closures phases independently in a multiple array (for example, a four telescopes system provide 6 simultaneous closure phase measurements).

Closure phases are often interpreted as the amount of asymmetry in the target's brightness distribution. It has a crucial role in different interferometric analysis, specially for the image reconstruction techniques. For an overview on the role of closure phases and the information it contains, see Monnier (2003). The main point is that if the Fourier space of the image (called *uv* plan) is properly sampled with closure phases, we can apply an inverse Fourier transform on the data and rebuild an image that may have as much information as a regular image, depending on the extension of *uv* coverage. See Thiébaut (2013) for a recent review on interferometric image reconstruction techniques and the mathematical problems they contain.

1.6.2 The VLTI AMBER and PIONIER interferometeric beam-combiners

This study contains an extensive amount of data from the Very Large Telescope Interferometer (VLTI) facility of ESO (European Southern Observatory) in Paranal, Chile (Haguenauer et al., 2012). VLTI interferometri telecopes array can be set with utility telescopes (UTs, 8.2 m), or with the auxiliary telescopes (ATs, 1.8 m). The baseline lengths ATs can vary between 8 to 200 meters, depending on the observational period availability. With UTs, the baselines ranges between 46 to 130 m.

AMBER is an near-infrared spectro-interferometer that operates in the J, H, and K bands (i.e., from 1.0 to 2.4 μm), described by Petrov et al. (2007). The instrument was designed to be used with two or three beams, allowing to measure both differential and closure phases. AMBER can be used with an external fringe tracker, the FINITO. On the UTs it is possible to reach $H = 7$ and on the ATs the limiting magnitude is $H = 5$. There are three possible spectral resolution ($R = \Delta\lambda/\lambda$) modes: (i) high resolution (HR) $R = 12000$; (ii) medium resolution (MR) $R = 1500$; and (iii) low resolution (LR) $R = 35$.

PIONIER is a H-band four-telescope combiner with high precision visibilities measurements and multiple (four) closure phase information and is described by Le Bouquin et al. (2011). PIONIER tracks its own fringes. The magnitude limit is $H = 8$. This value is

independent of whether ATs or UTs are used, and UTs should only be used when other issues (such as availability of guide stars or need for small interferometric field of view) prohibit the use of ATs. It has only two spectral capabilities: $R = 5$ or $R = 30$ across the H band.

1.6.3 Remarks on interferometry

We described hitherto the main concepts of optical interferometry that are used for this study. The only missing topic is the *spectro-interferometry*, or the interferometry with high spectral resolution. In spectro-interferometry it is sometimes useful to describe the interferometric quantities in terms of differential quantities (notably the differential phases). The idea behind this is that within a small wavelength range, all the atmospheric effects are roughly the same. So, instead of losing all, for example, phase information, we can measure its difference with respect to a reference wavelength measurement observed simultaneously. This is particularly suitable for line profiles, where the kinematics of the target can be addressed and the continuum region is the natural choice as reference.

We emphasize that the end product of an interferometric observation is not a regular image but the Fourier transform of the brightness distribution on the field-of-view of all the telescopes. This introduces new features when analyzing interferometric data. For example, in Sect. 4.2 we discuss how emissions can be measured with higher resolution than the nominal resolution of the interferometer (Eq. 1.51) using phase information.

Another important feature is that the interpretation of the data in physical terms can be very dependent on the model used (i.e., the assumptions made), which makes it crucial to have a realistic brightness distribution of the target - something only achieved by proper solution of radiative transfer. The discussion of the inference of physical parameters from interferometric data will permeate this study.

1.7 Other observational techniques

Important techniques used to investigate the properties of hot stars include asteroseismology, spectroscopy, polarimetry (their combination, spectropolarimetry) and interferometry. The combination of these multiple techniques, which mostly are probes different physical processes, offers new and fundamental investigation tools for these stars. Behind

this idea was organized the IAU Symposium 307 "New Windows on Massive Stars" (Geneva, Switzerland, on June 2014) and is the context where this study is inserted.

1.7.1 Spectroscopy

Spectroscopy in astrophysical context is the technique that investigates the intensity of a light beam as a function of wavelength or frequency. This technique is present in the study of hot stars since at least the observations of Pietro Angelo Secchi of the Be star γ Cas in 1866, whose Hβ line featured an intense emission characteristic[3].

Spectrographic instruments that analyze the light along visible range are usually single or cross-dispersed grating spectrographs. (Single) Diffraction gratings are the most useful optical dispersing element due to its high luminous efficiency when compared this other elements, as prisms. The linear dispersion can be easily adjusted and the plane grating can be used over a wide range of angles of incidence, simply rotating the grating.

This simplicity makes spectrographs very popular instruments among amateur astronomers. Amateur astronomers can provide great contribution, either in databases with professional astronomers (e.g., BeSS database[4]), or in the form of individual observations. In particular, we mention here the discovery of the active phase of Achernar in 2013 by the amateur astronomers Tasso Napoleão and Marcon (Brazil), and their contribution with subsequent observations (as other obtained from BeSS).

The resolution of the spectrographs can be substantially increased by the use of cross-dispersed diffraction gratings, which become common after the 1980's. This instruments are known as *echelle* spectrographs. In this study we employed observations from different echelle spectrographs. The spectroscopic observations used are described in Sect. 6.3.

1.7.2 Polarimetry

As mentioned previously, the polarization of light results from its (vectorial) wave properties. From Eqs. 1.47 and 1.48, the more general case of any light wave propagating

[3] About this discovery, we reproduce here the comments from Rivinius et al. (2013): *"In the heyday of nationalism, this [observation] was communicated in French language to a German Journal by an Italian astronomer, working at the international organization of the time, the Vatican"*.

[4] http://basebe.obspm.fr/basebe/

in the direction $\hat{z}$

$$\vec{E} = (\tilde{E}_1\hat{x} + \tilde{E}_2\hat{y})\exp(2\pi ivt)\,, \tag{1.57}$$

$$\begin{aligned}\tilde{E}_1 &= a_0\exp(-i\phi)\,,\\ \tilde{E}_2 &= a_0\exp(-i\phi + i\gamma).\end{aligned} \tag{1.58}$$

Equations 1.57 and 1.58 represents the electromagnetic wave position over time. They describe an ellipse, or an elliptically polarized light.

There are two particular cases of the elliptical polarization:

- $\boldsymbol{\gamma = \pm\pi/4}$, where the electromagnetic vectors describe a circle (or *circular polarization*);
- $\boldsymbol{\gamma = 0}$ or $\boldsymbol{\pm\pi/2}$, where the electromagnetic vectors describe a single line (or *linear polarization.*

The Stokes parameters

Using an equation equivalent to the 1.57, George Gabriel Stokes defined in 1852 a set of parameters as follows and that are known as *Stokes parameters*

$$I \equiv \|\tilde{E}_1\|^2 + \|\tilde{E}_2\|^2, \tag{1.59a}$$

$$Q \equiv \|\tilde{E}_1\|^2 - \|\tilde{E}_2\|^2, \tag{1.59b}$$

$$U \equiv 2\mathrm{Re}(\tilde{E}_1\tilde{E}_2{}^*), \tag{1.59c}$$

$$V \equiv -2\mathrm{Im}(\tilde{E}_1\tilde{E}_2{}^*). \tag{1.59d}$$

The parameter I represents the light total intensity, the parameters Q and U the linear polarization and V the circular polarization. Stokes parameters allow to relate the light polarization characteristics on a convenient way

$$Q^2 + U^2 + V^2 \leq I^2. \tag{1.60}$$

In particular, the degree of polarization P and its orientation θ are defined as

$$P = \frac{\sqrt{Q^2 + U^2 + V^2}}{I}\,, \tag{1.61}$$

$$\theta = \frac{1}{2}\arctan\frac{U}{Q}\,, \tag{1.62}$$

where P is the polarized light fraction, $0 \leq P \leq 1$, 100% polarized. For a given observational error on the linear polarization measurement ($\sigma_P \equiv \sigma_Q \equiv \sigma_U$), it is possible to show that the orientation angle error θ is

$$\sigma_\theta = 28.6\sigma_P \,, \tag{1.63}$$

with θ in degrees, neglecting the standard stars orientation determination errors used to put the observation in the celestial frame.

1.8 Polarization in selected contexts

1.8.1 Linear polarization of circumstellar disks

Hot star disks are usually composed of highly ionized and low density gas. This condition favors the Thomson's scattering by free electrons whose scattering opacity is independent of the wavelength (λ). In this process, the electrons oscillate in the same frequency of the incident light beam, which leads to the reemission in the same frequency of incidence. Protons, that are much heavier than electrons, are little affected by the incoming light. As the polarization of the re-emitted beam depend on its angle of incidence, the light is linearly polarized in this process.

The degree of polarization by scattering depends upon the density of the medium and its geometry with respect to the incoming light. Given its simple geometry, the polarization of a circumstellar disk indicates precisely its orientation on the sky plane. But more complex configurations can be probed by linear polarization without angularly resolving it (e.g., Brown and McLean, 1977).

Linear polarization still offers additional diagnosis of the circumstellar medium. The region of the disk where the scattering occurs depends on the geometric shape of the disk. Defining

$$\zeta = \frac{d}{dr}\left(\frac{H(r)}{r}\right) \,, \tag{1.64}$$

ζ can used to classify disks in there main shapes: (i) $\zeta > 1$ for *flaring* disks; (ii) $\zeta < 1$ for *self-shadowed* disks; and the special case (iii) $\zeta = 0$ for *flat* disks ("flat" here means that $H(r) \propto r$). From the observational point of view, ζ should not be determined as function of the scale height itself, but as function of the height above the midplane where

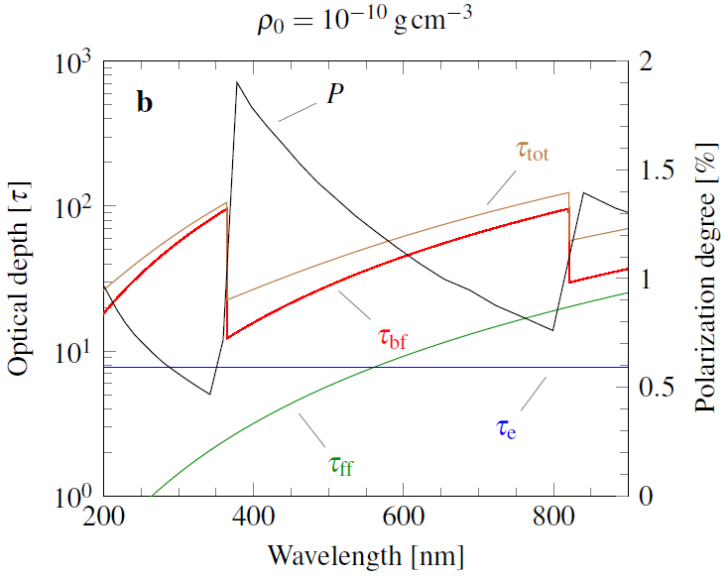

Figure 1.3: Polarized spectrum P and radial optical depth contributions along the midplane of a typical Be disk. The total optical depth $\tau_{\rm tot}$ is the sum of the optical depth for each continuum opacity source (free-free $\tau_{\rm ff}$, bound-free $\tau_{\rm bf}$, and Thomson scattering τ_e). (Rivinius et al., 2013).

the disk becomes transparent, sometimes called *surface height*. In Eq. 1.64 we assumed their equality, what would be just an approximation.

Early interferometric measurements constrained the Be stars disk thickness within the 3° to 20° range (Wood et al., 1997), indicating these disks might be flared. As the stellar flux reaching the disk is much more intense in its inner regions and the flaring can block direct irradiation of their outermost regions, light polarization come from the closest region to the star. This is in agreement with the theoretical predictions of a thin disk ($H \ll R_*$), pressure-supported scale height (Eq. 1.37). Thus, the polarization level is not set by disk radius, but almost exclusively by the gas density (except for very small disks, i.e., $R_d \sim R_*$).

The polarized spectra of Be stars often displays a sawtooth shape (Fig. 1.3, black line), with abrupt changes very close at Hydrogen photoionization thresholds. The sawtooth polarization can be understood as roughly the combination of electronic scattering (τ_e) in addition to the pre-scattering H I absorption ($\tau_{\rm bf} + \tau_{\rm ff}$). The opacity dependence of the gas with λ roughly results in $\kappa_{\rm HI}\rho \propto \lambda^3$ (e.g., Bjorkman and Bjorkman, 1994, Eq. 30) within the thresholds.

Even if spectropolarimetric information is not available, broadband polarimetric imaging can be useful in determining the density of these environments. Haubois et al. (2014) show examples of how broad-band polarization can be employed to probe Be star disks

growth and destruction.

1.8.2 Interstellar polarization

The interstellar medium (ISM) is the matter that fills the space between stars in a galaxy. This matter is not homogeneous and is composed by energetic particles (cosmic rays), gas and dust. This material interacts with the background emitted light on their way towards Earth. In the context of this study, this interaction mainly bring two results: (i) a selective absorption, stronger in smaller wavelengths (extinction), and (ii) changes in the linear polarization.

The mechanism by which ISM changes the light polarization was originally proposed by Hall (1949) and Hiltner (1949), and consists of the alignment of non-spherical dust grains over the light path generating a selective polarized absorption. The first explanation of this phenomenon was done by Davis and Greenstein (1951), accounting that in the presence of an external magnetic field, paramagnetic dust grains have an induced magnetic moment and tend to align to the field. This was further developed by Dolginov and Mitrofanov (1976) who established the current view of the alignment process where the radiative torque has an important contribution to dust grains alignment.

Given the wave nature of light, where the electromagnetic fields oscillate perpendicular to the propagation direction, the ISM light polarization due to the magnetic grains alignment only reveals the $\vec{B}$ perpendicular to the line-of-sight, i.e., $B_\perp$. The $B_\parallel$ is hard to be measured and cannot be traced by linear polarization.

The photospheric emission of main sequence stars is (mostly) unpolarized. If a given star has a substantial amount of circumstellar material (e.g., a Be star with its disk), its emergent spectrum will become linearly polarized. So, when observing such a star, the observed polarization $P_{\rm obs}$ will be the result of the ISM and the intrinsic ($_*$) circumstellar components

$$\begin{aligned} P_{\rm obs}^2 &= \frac{(Q_{\rm obs})^2 + (U_{\rm obs})^2}{I^2}\,, \\ P_{\rm obs} &= \frac{\sqrt{(Q_{\rm ISM}+Q_*)^2 + (U_{\rm ISM}+U_*)^2}}{I}. \end{aligned} \tag{1.65}$$

As light absorption, the ISM polarization depends on the wavelength. The detailed spectral characteristics depend on the ISM conditions, primarily the grains shape and composition.

Serkowski et al. (1975) establish an empirical relation $P_{\rm ISM}(\lambda)/P_{\rm max}$, where $P_{\rm max}$ is loosely related to the extinction coefficient $E(B-V)$

$$3.0 \leq \frac{P_{\rm max}}{E(B-V)} \leq 9.0, \tag{1.66}$$

with units % and mag, respectively. The value 9.0 represents the maximum ISM efficiency to polarize the light with the increasing $E(B-V)$. The wavelength dependence of polarization ($P_{\rm ISM}$) is described by

$$P_{\rm ISM}(\lambda) = P_{\rm max} \exp\left[-K \ln^2\left(\frac{\lambda_{\rm max}}{\lambda}\right)\right], \tag{1.67}$$

where K variable was introduced by Wilking et al. (1980). $K = 1.15$ corresponds to the original Serkowski et al. formulation.

Methods for determining the ISM polarization

In the context of circumstellar disks, there are four methods that can be applied to determine the ISM polarization components (Quirrenbach et al., 1997): (i) Pure photospheric emission, if the CS disk is dissipated; (ii) Q/U components and $\lambda_{\rm max}$ are the same for field stars; (iii) Hydrogen line profile depolarization; (iv) QU diagram analysis;

Method (i) is suitable to the case of variable stars. If at a given time there is no evidence of circumstellar emission (for example, pure photospheric line profiles), the observed polarization will be a direct measure on the ISM one. See Chap. 5 for an example to the Be star Achernar.

Field stars are stars angularly close to the target star (typically, within one degree). They may be selected by having a very low or zero intrinsic polarization. If nearby stars show a regular pattern in the Q/U ratio and $\lambda_{\rm max}$, their light should be traveling over the same ISM component(s) and then the field stars polarization can be used to infer the ISM polarization of the target (method ii). It is usually not enough that the probed stars are angularly nearby the target: they should also be in a similar distance to the target, when this information is available.

The third method (iii) is the line profile depolarization (McLean and Clarke, 1979). The principle of the method is that Hydrogen recombination transitions are, in the absence of magnetic fields, unpolarized. But it has some drawbacks. For this method, high spectral resolution observations are required and H line profiles wavelengths do not contain exclusively the (unpolarized) line emission. An underlying polarized emission may be

also present. The ratio of line ($P_*(\lambda)$) to continuum polarization ($P_*(\lambda_C)$) is given by the empirical relation

$$\frac{P_*(\lambda)}{P_*(\lambda_C)} = \frac{1}{1+\chi(\lambda)}\,, \tag{1.68}$$

where $\chi(\lambda)$ is the ratio of the intensity of the unpolarized emission to the polarized one in the underlying λ. Thus, $\chi \to 0$ means that there is no significant unpolarized line-emission [$P_*(\lambda) = P_*(\lambda_C)$]; and $\chi \to \infty$ means that to no significant polarized continuum emission exists [$P_*(\lambda) \to 0$]. An adequate estimate of $\chi(\lambda)$ is necessary for the precise application of this method.

1.8.3 Circular polarization and the Zeeman effect

In 1896, Pieter Zeeman discovered that, when light was in the presence of magnetic fields, single spectral lines were splitted into two or more lines. This phenomenon is due to the interaction between the magnetic field and the inherent magnetic moment of the microscopic particle (neutral atom, ion, or molecule). As an example, a transition that have total spin of zero between its states has the magnetic moment determined by the orbital motion of the electrons. The line transition have energy E and in the presence of a magnetic field its energy can be change by the among of $\pm\Delta E$

$$\Delta E = \mu_B \|\vec{B}\|\,, \tag{1.69}$$

where $\mu_B = \dfrac{eh}{4\pi m_e} \simeq 9.274 \times 10^{-21}$ erg G^{-1} is the Bohr magneton, with e the electron charge, h the the Planck constant and m_e the electron mass. The energy difference changes the line wavelength λ according to the relation

$$\Delta\lambda = \frac{hc}{\Delta E}\,, \tag{1.70}$$

where c is the light speed. A more detailed description of the Zeeman effect can be found in quantum physics textbooks.

The Zeeman components of a spectral line, radiated along the magnetic field direction, are circulary polarized. So, when observing a stellar atmosphere with the presence of a large-scale magnetic field with a non-zero component perpendicularly to the observers line-of-sight ($\|B_\perp\| > 0$), the circular polarization within the spectral lines will be circularly polarized (i.e., Stokes $V \neq 0$).

Polarization studies inside spectral lines can be performed with spectropolarimetry, that is the combination of the polarimetry and spectroscopy observational techniques. In the weak field approximation ($\|\vec{B}\| \lesssim 30$ kG), valid for most of stars, the circular polarization will be proportional to the strength of the (dipolar) magnetic field and the intensity variation (dI) over the wavelength step ($d\lambda$; Landi Degl'Innocenti and Landi Degl'Innocenti, 1973)

$$V(\lambda) \propto \frac{dI}{d\lambda}\|B_{\perp}\|. \tag{1.71}$$

Zeeman signatures in stellar spectra are generally extremely small, typical polarization amplitudes of 0.1%. Thus, detecting them requires measurements of polarization with signal-to-noise level of about 10^4. A multi-line approach for increasing the signal-to-noise of the measured polarization was proposed by Semel (1989). This approach, known as the LSD method (Least Squares Deconvolution), was successfully used for detecting stellar circular polarization as an indication of magnetism by Donati et al. (1997).

Chapter 2

Methods and tools

In this chapter we contextualize the work from its host institution, the Institute of Astronomy, Geophysics and Atmospheric Sciences at the University of São Paulo (IAG-USP). It made use of several computing resources and scientific softwares. We present here the main employed tools, including some developments made during the PhD.

2.1 The BeACoN group

In 2009, Prof. Alex C. Carciofi started at IAG-USP the BeACoN group, the *Be Aficionados Collaborative Network*. The group has a number of important collaborators, including Dr. Armando Domiciano de Souza and other astronomers of the interferometric group of the Observatoire de la Côte d'Azur, which made this study possible. The aim of the group is to investigate the Be phenomenon and to obtain a realistic physical model of the circumstellar environment of the Be in interaction with the photosphere.

The main modeling tool of the group is the radiative transfer code HDUST, described below. This is the first PhD thesis of the group, as part of the continuous application of HDUST models to reproduce different observational quantities since 2006. It is also, to our knowledge, the first thesis in a Brazilian institution based on optical/IR long baseline interferometry (OLBI).

2.1.1 The IRAF reduction package BEACON

The BeACoN group is conducting a spectroscopic and polarimeter survey of Be stars, hot magnetic and other peculiar stars the OPD (Observatório Pico dos Dias, LNA-MCT)[1].

[1] More info available at http://www.lna.br/opd/opd.html

The survey already contains more than 3000 individual observations since 2006 of about 50 stars. A complementary survey is also in execution to determine the interstellar polarization of these stars through field observations of stars. The data reduction is done via the BEACON package[2] based on IRAF (Image Reduction and Analysis Facility; Tody, 1993).

Polarimetry

The polarimetric data shown in this thesis are results of the survey. The survey uses a CCD camera with a polarimetric module described by Magalhães et al. (1996), consisting of a rotating half-wave plate and a calcite prism placed in the telescope beam. A typical observation consists of 8 or 16 consecutive wave plate positions separated by 22.5°. In each observing run at least one polarized standard star is observed in order to calibrate the observed position angle. The polarimetric reduction algorithm is described by Magalhães et al. (1984). It is an adaptation of the PCCDPACK package (Pereyra, 2000) for the particular observing mode we use in the survey. Basically, since many targets have quite small polarization values (as is the case of Achernar, see Chapters 5 and 6), a high S/N ratio is required to reach the typical target polarization accuracy aimed in the survey (0.01%, for which a S/R $\sim 10^5$ is required). This high S/N is reached by taking a large number of frames for each waveplate position.

Spectroscopy

The spectroscopic component of the survey are based on two main instruments: (i) the ECass, a long slit Cassegrain spectrograph and (ii) the MUSICOS (Multi-SIte Continuous Spectroscopy). The reduction of long slit spectra was incorporated to the BEACON package using the algorithm from Faes (2011). After a French donation to the Brazil, the MUSICOS spectrograph become available at the OPD in 2012. The donation was reported by Franco (2010), and its availability by Prates Campos and Domicini (2010).

MUSICOS is a bench spectrograph fed by a fiber optic at the telescope focus (Baudrand and Bohm, 1992). It covers a wide spectral range in two non-simultaneous modes: "blue" (3800-5400 Å), and "red" (∼5400-8800 Å). It has a resolving power of $R \approx 30000$. Given its simultaneous high resolution and wide spectral coverage, MUSICOS replaced the Ecass in the survey.

[2] Available at https://github.com/danmoser/beacon.

Unfortunately, no support concerning the reduction of the data was supplied. So I developed a reduction algorithm for the instrument in the BEACON package, adapted to the OPD detectors. A reduction manual is under development, and will be available in the BeACoN website for the community.

2.1.2 *Radiative transfer code* HDUST

HDUST is one of the most performing Monte Carlo radiative transfer codes to date (Carciofi and Bjorkman, 2006, 2008). It is a fully three-dimensional (3D), non-local thermodynamic equilibrium (NLTE) code designed to solve the coupled problems of radiative transfer, radiative equilibrium and statistical equilibrium for arbitrary gas density and velocity distributions.

The HDUST code has already been successfully applied to the analysis of a number of Be and B[e] stars and is used to analyze and interpret the observational dataset present in this study. Since its first publication in 2004, HDUST has contributed to 22 refereed publications. One example is shown in Fig. 2.1, where multiple observables of the star ζ Tau are reproduced.

Spectral lines synthesis of rotating stars

Until early 2013, HDUST could provide accurate line profiles only for non-rotating stars. This is because in its default mode, the code used photospheric models of low resolution from Kurucz (1979) for greater computational efficiency. In order to compute the photospheric line profile, a file with the (non-rotating) photospheric model needed to be provided by the user. As a result, the photospheric line profile did not include the effects of gravity darkening.

Prof. Carciofi and I upgraded the HDUST code to read accurate photospheric line profiles for different effective temperatures and effective surface gravity. The profiles were computed by SYNSPEC, a general spectrum synthesis program. SYNSPEC is an auxiliary routine, based on IDL, of the stellar atmosphere models TLUSTY (Hubeny, 1988). The line grid is encoded in the External Data Representation (XDR) binary format.

The new version of the code upgrade was validated by comparisons with the CHARRON code (Code for High Angular Resolution of Rotating Objects in Nature; Domiciano de Souza et al., 2002, 2012).

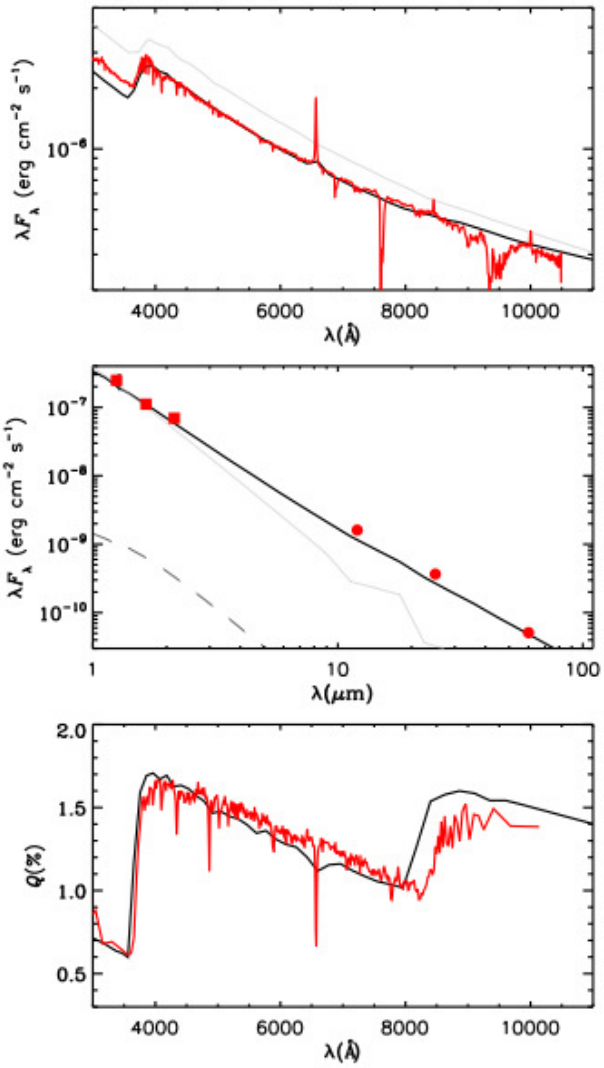

Figure 2.1: HDUST fit of the emergent spectrum (visible *top*; IR *middle*) and polarization (bottom) of ζ Tau (Carciofi et al., 2009). The observations are in red and model in black.

2.1.3 BeAtlas *project*

Aiming at a comprehensive investigation of Be stars and VDD scenario, the project BeAtlas came about. The project consists of a systematic grid of models generated by the hdust code. The grid was designed to cover the whole known range of parameters of these stars and has the broad goals of (i) testing the universality of the VDD by applying it to large samples of Be stars; (ii) serving as a tool for planning interferometric observations of Be stars, and (iii) serving as a starting point for fitting data of individual stars.

The Be emission strongly depends on the stellar photospheric configuration, which changes along the stellar evolution. The stellar evolution models used to derive the photospheric parameters of the central stars are from the group at the University of Geneva (Georgy et al., 2013; Granada et al., 2013). The first phase of the project, we selected twelve stellar masses from 3.4 up to 14.6 $M_\odot$ (corresponding to the spectral types B9 and B0.5, respectively) and five stellar rotation rates to keep the central star parameters spacing representative. The stars are assumed to be rigid rotators in the Roche approximation, so that there is a well know relation between W and the stellar oblateness ($R_{\rm eq}/R_{\rm pole} = 1.1$ to 1.45, corresponding to $W \sim 0.45$ to 0.95; Eq. 1.23). The gravity darkening β exponent was assumed to be a function of W, according to the relation of Espinosa Lara and Rieutord (2011, more details on this subject are given in Chapter 5).

In addition to mass and W, we also modeled stars with different ages in the main sequence. Following the natural parameterization of stellar evolution models, we chose X_c, the fraction of H in the core, as an age indicator. The values simulated are listed in Table 2.1. Note that in the first phase of the grid, all purely photospheric models were computed. However, disk models were computed inicially for $X_c = 0.3$ only.

The disk were parameterized according to the VDD model. We chose seven different base surface density ($\Sigma_0 = 0.05$ to 2.0 g cm^{-2}) corresponding to different stellar mass-loss rates and four exponents for the volume density (Eq. 1.46): $m = 3.5$, that corresponds to a steady-state isothermal disk, a smaller value $m = 3.0$ that can be associated to either a dissipating disk (Haubois et al., 2012) or a disk truncated by a secondary star (Okazaki et al., 2002), and two larger values ($m = 4.0$ and 4.5) which can be associated to young disks (Haubois et al., 2012). In addition, we computed models for which the radial density structure were given by the non-isothermal solution of the radial viscous diffusion problem

Table 2.1 - List of parameters of Be stars of the BeAtlas project.

Parameter	List of values
Spec. Type	B0.5, B1, B1.5, B2, B2.5, B3, B4, B5, B6, B7, B8, B9
Mass ($M_\odot$)	14.6, 12.5, 10.8, 9.6, 8.6, 7.7, 6.4, 5.5, 4.8, 4.2, 3.8, 3.4
X_c (Fraction of H in the core)[a]	0.08, 0.30, 0.42, 0.54, 0.64, 0.77
Metalicity Z	0.014
Oblateness (R_{eq}/Rp)	1.1, 1.2, 1.3, 1.4, 1.45
Rotation rate W	0.447, 0.633, 0.775, 0.894, 0.949
Σ_0 ($g\,cm^{-2}$)	0.02, 0.05, 0.12, 0.28, 0.68, 1.65, 4.00
Mass density radial exponent (m)[b]	3.0, 3.5, 4.0, 4.5 + non-isothermal steady-state
Disk radius (R_{eq})	50
Inclination angle (i; deg.)	0.0, 27.3, 38.9, 48.2, 56.3, 63.6, 70.5, 77.2, 83.6, 90.0

[a] The list corresponds to the photospheric models. X_c=0.30 is the only value for models with disk currently available.
[b] Based on the parametric prescription of $\rho_0(R_{eq}/r)^m$.

(Carciofi and Bjorkman, 2008). The simulation disk radius is $50R_{eq}$ for each star. One can define *pseudo-photosphere* as the region of the disk that is radially opaque to continuum or line radiation and therefore dominates the disk emission. The radius of this pseudo-photosphere[3] depends on the wavelength considered. For instance, Haubois et al. (2012) points that, for a steady-state disk, the pseudo-photosphere extends to $\sim 2R_{eq}$ at the V band. For line transitions, such as Hα, this region can be as large as $10 - 20R_{eq}$. This means that models with disks larger than the pseudo-photosphere are essentially identical. Thus, BeAtlas models are suitable for isolated Be stars, or those with long period binary companions, until the *mm* wavelengths. The effects of truncated disks, resulted from short-period binary interactions, are not covered in the first phase of the project, but are planned for the subsequent phase. Finally, the observables are generated to ten different observer's line-of-sight equally spaced in the cosine range ($\cos i = 0$ to 1). Table 2.1 contains the list of the main simulated parameters of the project.

This grid corresponds to approximately 25,000 models, for which high resolution spectroscopy, polarimetry and imaging (mainly targeting the interferometric quantities) were

[3] The term pseudo-photosphere can have other definitions. For example, in Harmanec (1994) it denotes the region within which the disk viewed face-on is optically thick and so looks like an extension of the stellar photosphere.

computed. The calculations required an extensive use of computational resources executed at the AstroInformatics Laboratory at IAG-USP (Brazil)[4]. The time estimated for computing were nine months at the regular queue schedule.

I was involved in all steps of the BeAtlas project so far. I participated in the project design discussions (i.e., the quantities to be simulated and the relevant parameters needed) and I also developed the tools to handle the project data, since code execution, validation tests and analysis. These tools are part of the pyhdust library, described below. The project also has the participation of the post-doc Rodrigo Vieira, the PhD students Leandro R. Rímulo and Bruno C. Mota and the undergraduated student André L. Figueiredo, from IAG-USP.

The first phase of BeAtlas models was finished in middle of this year (2015), and a few applications are currently being developed: (i) Bruno Mota, PhD student of Prof. Alex Carciofi at USP (Brazil), is leading the application of the models to constrain the stellar parameters of rotating stars by comparison with ultra-violet data from IUE (International Ultraviolet Explorer) satellite; (ii) Tiago Souza, MSc student of Prof. Marcelo Borges at ON (Observatório Nacional, Brazil), is fitting the H band features of Be stars seen by APOGEE survey; and (iii) André Figueiredo, undergrate student of Prof. A. Carciofi, is assessing how the slope of the polarization spectrum can be used to constrain the central star rotational rate after the discovery by Klement et al. (2015). Many other applications are expected in the near future.

2.1.4 pyhdust *library*

pyhdust is an open-source Python language-based library to manipulate observations and models of astrophysical objects and was entirely developed during this thesis work. It is available at https://github.com/danmoser/pyhdust. Its main modules are:

- **pyhdust**: functions to manipulate hdust output files;
- **input**: functions to generate hdust input files;
- **beatlas**: functions related to the beatlas project;
- **phc**: *physical constants* and general use functions module;

[4] More information at http://lai.iag.usp.br.

- **interftools**: functions to manipulate and plot interferometric data;
- **poltools**: the same as above, for polarimetric data;
- **fieldstars**: functions to analyze and plot polarization data of field stars;
- **spectools**: functions to manipulate and plot spectroscopic data;
- **singscat**: single scaterring modeling tools, presented in Chapter 3.

Most of the analysis and graphs presented in this work were performed using PYHDUST, as well all the BEATLAS project management so far. It interfaces other Python libraries, such as PYFITS, used for reading *fits* format files, and the EMCEE minimization library, among others. A more detailed documentation is available at http://astroweb.iag.usp.br/~moser/doc/.

2.2 *Monte Carlo Markov chain code* EMCEE

The Monte Carlo Markov Chain method (MCMC) is a class of algorithms that can be used for fitting arbitrary multi-parametric functions to data. This work makes use of the EMCEE code, a Python language implementation of the MCMC method whose algorithm is described by Foreman-Mackey et al. (2013). The code has been used in a growing number of astrophysics papers[5] and it is applied in different minimization process in this work.

Briefly, from a set of parameters and a given likelihood function, MCMC method computes the probability density function (PDF) by sampling each of the model parameters, with resolution set by the number of *walkers*. The likelihood function do not need to be normalized. The convergence of the sample around the maximum likelihood distribution will be satisfied if a sufficient number of *iterations* are performed. The best-fitting parameters values must be chosen from the PDFs by the user, depending on the nature of the minimization.

In our analyzes, we established the likelihood function as inversely proportional to the $\chi^2_{\rm red}$ value, commonly defined to measure a goodness of data fit

$$\chi^2_{\rm red} = \frac{\chi^2}{\nu} = \frac{1}{\nu}\sum \frac{(\text{model} - \text{data})^2}{\sigma^2}\,, \tag{2.1}$$

[5] A list of EMCEE application in astrophysical literature is available at http://dan.iel.fm/emcee/current/testimonials

where ν is the number of degrees of freedom and σ the error associated to the data. The elected criterion to determine the best-fitting values was to choose the median value of the sampled PDFs. The errors were estimated from their (non-symmetric) PDF histograms area, containing approximately 34.1% of the occurrences from the median (i.e., equivalent to one σ if the PDF approach a normal distribution). The PDF can also be jointed in frequency maps, in order to verify the correlation between the multiple parameters.

Chapter 3

Magnetospheres of hot stars

Magnetism is a fundamental property of the stars and play an important role in stellar evolution. For low-mass stars, the magnetic field is believed to be generated through dynamo processes within their convective envelopes as it occurs in our Sun. Indeed, most cool stars exhibit a large number of solar-like activity phenomena, i.e., a considerable magnetic variability. Unlike their low-mass counterparts, magnetic fields of massive stars are very stable on timescales of months and even years. This stability, the simple topographical features, and their no scalability with rotation, are evidences that magnetic fields of hot stars were generated in early stages of stellar evolution. This scenario is known as *fossil field*, although the role of binarity is not well determined. See Donati and Landstreet, 2009 for a review.

Recent surveys using Zeeman diagnostics (e.g., MiMeS, Magnetism in Massive Stars, Wade et al., 2011) show that approximately 10% of hot stars possess strong (dipolar) magnetic fields (∼1-10 kG). The magnetic field presence, however, differ for different subtypes of hot stars. Important in the context of this study is that not a single magnetic Be star was detected. And among the Bp stars, the incidence fraction of magnetic fields is high, especially in the ones with chemical peculiarities. See Shultz et al. (2014) and references therein.

The term *magnetosphere* refers to the channeled stellar wind into a circumstellar structure that results from the dynamical interaction of the stellar magnetic field with stellar rotation and mass loss. Petit et al. (2013) analyzed a comprehensive number of magnetic hot stars and proposed a classification of the magnetospheres based on the radial structure of the circumstellar environment. The magnetospheres can be described in terms of the Alfvén radius $R_{\rm A}$ and (Keplerian) co-rotation radius $R_{\rm K}$.

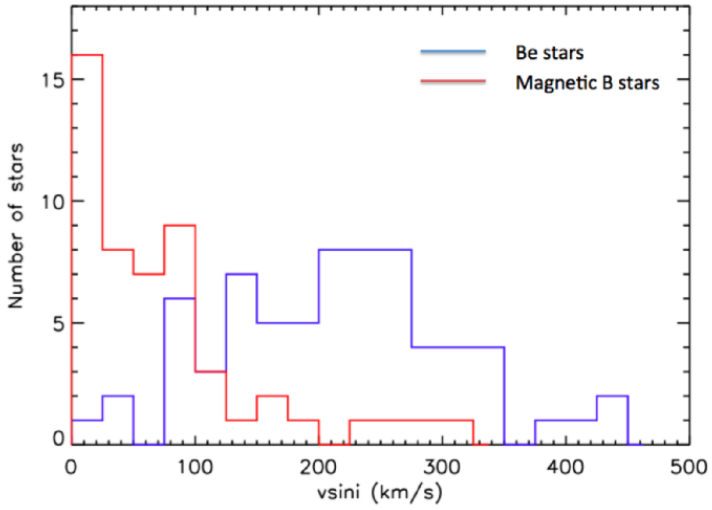

Figure 3.1: The projected rotational velocities of the MiMeS Be stars sample compared to those of the known magnetic B stars (Wade et al., 2014).

$R_{\rm A}$ can be estimated as (Ud-Doula et al., 2008)

$$R_{\rm A} = R_{\rm eq}[0.3 + (\eta_* + 0.25)^{1/4}]\,, \tag{3.1}$$

where η_* is the *wind magnetic confinement parameter*, and $R_{\rm K}$ is

$$R_{\rm K} = \frac{3}{2} R_p \left(\frac{\Omega}{\Omega_{\rm crit}}\right)^{-2/3} = R_{\rm eq} W^{-2/3}. \tag{3.2}$$

If $R_{\rm A} < R_{\rm K}$, the star is classified as having a *dynamical magnetosphere*. Otherwise, $R_{\rm A} > R_{\rm K}$, the star possess a *centrifugal magnetosphere*. Thus, magnetic stars with high rotational rates tend to generate centrifugal magnetospheres.

Unlike the Be phenomenon, the magnetism in fast rotating stars appears to be rare. This is illustrated in Fig. 3.1, where the frequent low $v \sin i$ values of B-type magnetic stars contrasts with the broad distribution of Be stars in the MiMeS survey. Indeed, until the discoveries of HR 7355 (Rivinius et al., 2010 and Oksala et al., 2010, $P = 0.52\,$d, $v \sin i = 310\,$km s^{-1}) and HR 5907 (Grunhut et al., 2012, $P = 0.508\,$d, $v \sin i = 280\,$km s^{-1}), no star with magnetosphere had been found with a rotation rate that exceeds the moderate equatorial velocity of the archetype magnetic star σ Ori E with $v \sin i = 160\,$km s^{-1}.

The centrifugal magnetospheres

The centrifugal magnetospheres are a characteristic of He-rich stars, which have the strongest magnetic fields detected in non-degenerate stars since the 1970's observations

(Landstreet and Borra, 1978; Borra and Landstreet, 1979). The strong magnetic fields have a number of consequences for photospheric and circumstellar structures, with rich phenomenology synchronized to the stellar rotational period. For example, a $\sim 10\,\mathrm{kG}$ dipole magnectic field detected in this kind of stars lead to not yet fully understood chemical stratification processes. At the magnetic poles, there are Helium-rich spots, which, as the star rotates, lead to a periodic modulation of the Helium (and other) lines (Townsend and Owocki, 2005).

These magnetospheres are observed via Balmer emission line variations and gyrosynchrotron emission in the radio waveband, as well as ultraviolet resonant lines. State-of-the-art models go a long way in quantitatively explaining the rich series of high-resolution spectra of the magnetospheres (e.g., Grunhut et al., 2012; Rivinius et al., 2013). However, only interferometry and polarimetry observations can directly assess the geometrical configuration of the circumstellar plasma (the latter without actually resolving it).

The magnetospheres can be modeled via the Rigidly Rotating Magnetosphere model (RRM; Townsend and Owocki, 2005), a time-independent, semi-analytic formalism which is able to treat arbitrary magnetic topologies. RRM solves the density along the surface defined by the intersection of the magnetic field with the minima of the stellar rotating gravitational potential. Hydrostatic equilibrium is assumed along the magnetic field lines, with the wind material settling on this disk-like structure. The typical configuration is the stellar rotation not aligned to the magnetic field, configuring a oblique rotator. In this case, where the dipolar magnetic field direction does not coincide with the rotational axis, RRM predicts a warped disk with the densest regions corresponding to the intersections of the magnetic and rotational equators (here called "blobs"). Fig. 3.2 shows the predicted column density of the magnetospheres for three different configurations of the inclination angle i and the angle β between the magnetic axis and the rotational axis. When first applied to $\sigma\,\mathrm{Ori\,E}$ (Townsend et al., 2005) the RRM model was able to reproduce the shape of emission lines as well as the photometric depths of eclipses by the plasma clouds of magnetospheres.

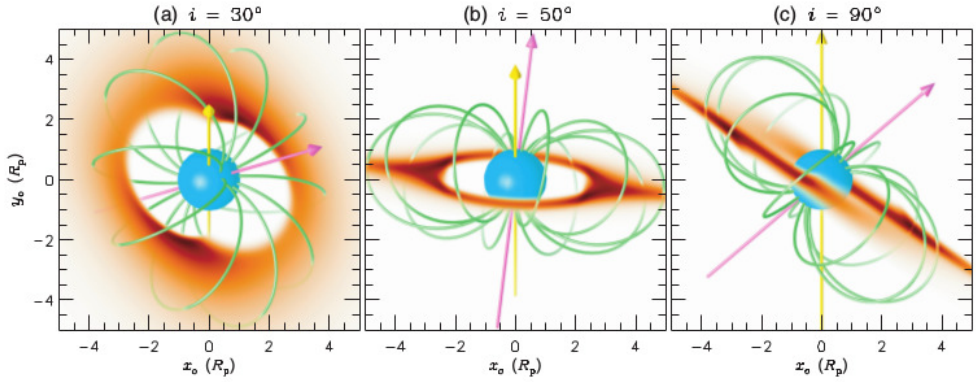

Figure 3.2: Maps of the column density to observers for three RRM configurations: (a) $\{i, \beta\} = 30°, 50°$ at a rotational phase $\phi = 81°$; (b) $\{i, \beta\} = 50°, 50°$ at $\phi = 171°$; (c) $\{i, \beta\} = 90°, 50°$ at $\phi = 81°$. In all three cases, $W \approx 0.3$. Black/opaque corresponds to the highest column density, and white/transparent to the lowest, with intermediate levels shown in orange. The axes are drawn as arrows: yellow/upright for the rotation axis and magenta/oblique for the magnetic axis. Magnetic field lines with a summit radius of 5 polar radius (i.e., stellar radius at the rotational poles) are indicated in green (Townsend, 2008).

3.1 Polarimetry of magnetospheres and σ Ori E

The σ Ori system is a multiple system containing five stars. σ Ori A is an O-type star, while the B, D and E are B-type stars and C is an A-type, all of them dwarfs. The closest stars are A and B, separated by $\sim$ 250 mas, while σ Ori E is the more distant, apart $\sim$ 42.5 arcseconds from AB (Hoffleit and Warren, 1995). The first linear polarimetric observations of the σ Ori system was carried out by Kemp and Herman (1977), who marginally detected a periodic modularization of σ Ori E. The measured modulation amplitude was of the order of 0.1%, with accuracy of $\sim$ 0.05%.

Polarization is a very useful technique that allows one to probe the geometry of the circumstellar scattering material. One consequence of the material accumulation in hot star magnetospheres is its high temperature and high ionization. The stellar light is scattered by the circumstellar free electrons and produces a linearly polarized signal. So, the magnetospheres are excellent targets for the BeACoN group tools, namely our high-precision polarimetry and the radiative transfer modeling - complemented by optical interferometry. Our first application to σ Ori E resulted in the paper by Carciofi et al. (2013), who reported the first firm detection of a hot star magnetosphere in continuum linear polarization.

In Fig. 3.3, we present the results of the observational campaign of σ Ori E until 2013. We started studying the polarization signal by a model-independent analysis. Here we summarize the steps:

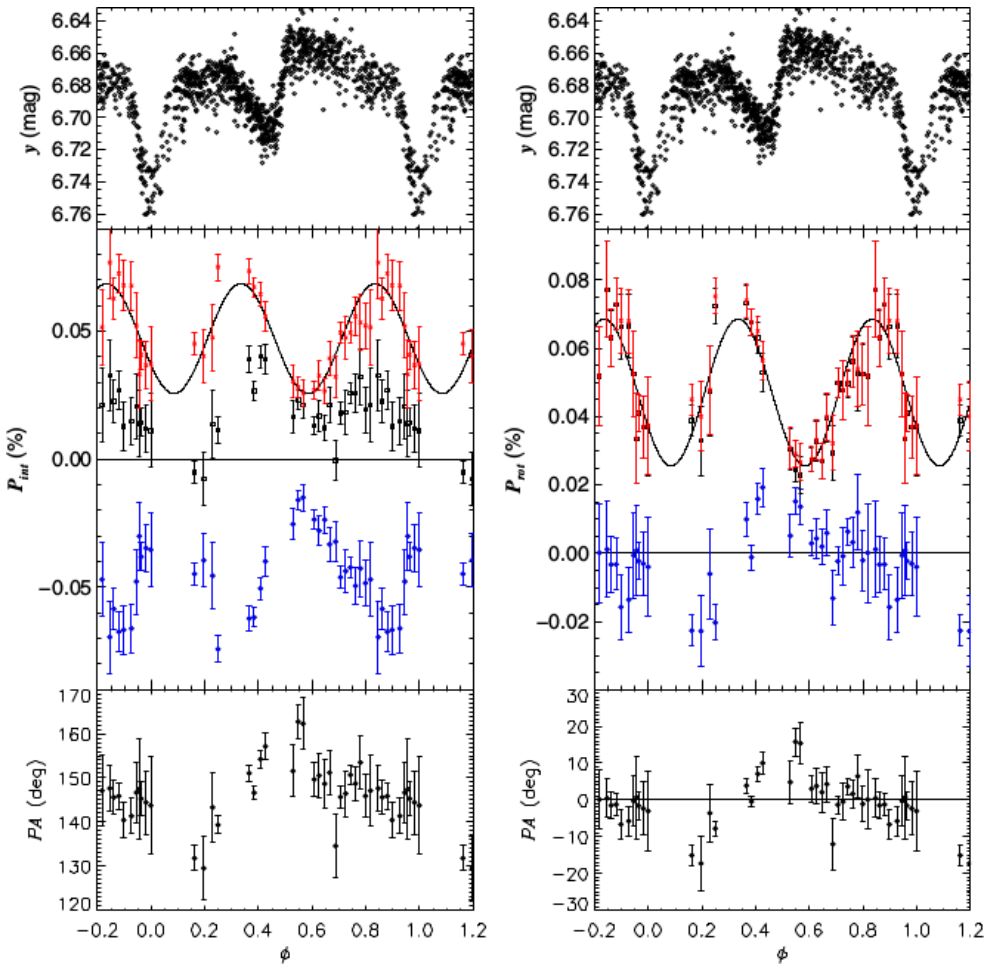

Figure 3.3: Variation of the intrinsic polarization of σ Ori E compared with photometric variations (y filter). *Top panels*: y filter photometric data from Hesser et al. (1977), folded in phase. *Middle*: intrinsic P (red), Q (black), and U (blue). *Bottom*: intrinsic position angle. *Left*: the polarization data are displayed in the equatorial reference frame. The polarization of σ Ori AB was used as a measure of the IS polarization. *Right*: same as the left plot, rotated such that $\langle U_{\rm int} \rangle = 0$. The solid lines are the result of a cosine function fitting (Eq. 3.3). (Carciofi et al., 2013).

- The raw data, determined in the instrumental frame, is rotated to the equatorial reference frame using calibration data from standard polarized stars. The calibrated data is shown in Fig. 3.3, left panel.

- The ISM polarization components $Q_{\rm ISM}$ and $U_{\rm ISM}$ are removed from the data. The ISM polarization towards σ Ori E was estimated using the measured polarization of σ Ori AB.

- The data is again rotated, in this step to align the system to the celestial North. This was done by forcing the average value of the U parameter across the rotation period to be zero. The intrinsic polarization is shown in Fig. 3.3, right panel.

- The intrinsic polarization maximum and minimum can then be evaluated and, given the double polarimetric oscillation within one photometric period, the following equation was fitted to the data

$$P(\phi) = P_0 + A\cos[4\pi(\phi - \delta)]\,, \tag{3.3}$$

  making use of the Levenberg-Marquardt algorithm (Marquardt, 1963).

- This polarization curve, model-independent, can used to determine the intrinsic polarization characteristics, such as symmetry and delay relative to photometric curve, δ (measured as phase).

The results of this analysis are summarized in Table 3.1. The considered ISM polarization values are in Table 3.2. We highlight the nearly symmetric modulation ($\chi^2_{\rm red} = 0.97$) at twice the frequency of the photometric cycle with amplitude $A \sim 0.02\%$, and the presence of a constant polarization component $P_0 \sim 0.047\%$, i.e., the polarization degree is never zero. This means that the magnetosphere is always asymmetric, irrespective of viewing angle.

Eq. 3.3 is a cosine function, defined in terms of the photometric curve. The minimum of polarization and photometry coincide when $\delta = \pm 0.25$ (the value of $\delta = 0$ would be equivalent to the polarization maximum at the photometric minimum). The derived value of $\delta \sim -0.17$ indicates that the maximum of photospheric absorption does not occur when the main component generating the polarization is aligned with the photosphere. This is the result of an asymmetric circumstellar cloud, and is discussed in more detail below.

Table 3.1 - Polarimetry best-fitting parameters of a cosine function with double the rotational frequency (Eq. 3.3) for σ Ori E, HR 5907 and HR 7355. The considered ISM components are in Table 3.2.

	$\langle P_{\rm raw}\rangle$ %	P_0 %	A %	δ phase	$\Delta\theta{\rightarrow}\langle U\rangle{=}0$ deg.	$\chi^2_{\rm red}$ -
σ Ori E[a]	-	0.0471(9)	0.021(1)	-0.17(1)	150.0(-)	0.67
σ Ori E	0.328(3)	0.0484(11)	0.0205(17)	-0.167(7)	148.1(1)	0.97
HR 5907	0.619(5)	0.0410(60)	0.0184(87)	-0.180(37)	77.4(2)	2.80
HR 7355	0.029(8)	0.1457(31)	0.0199(42)	0.005(16)	86.4(2)	0.67

[a] From Carciofi et al. (2013).

Table 3.2 - Interstellar polarimetric components at V-band of σ Ori E, HR 5907 and HR 7355, obtained by the methods indicated.

Star	Method	$P_{\rm IS}$ (%)	$Q_{\rm IS}$ (%)	$U_{\rm IS}$ (%)	$\theta_{\rm IS}$ (deg)
σ Ori E[a]	Field stars	0.350(15)	-0.348(15)	0.040(15)	86.7(0.4)
σ Ori E[a]	Grid minimization	0.351(10)	-0.350(10)	0.025(10)	88.0(0.3)
σ Ori E	MCMC minimization	0.314(11)	-0.314(12)	0.015(9)	88.6(0.3)
HR 5907	Field stars	0.602(45)	-0.275(36)	0.535(61)	58.6(3.0)
HR 5907	MCMC minimization	0.606(27)	-0.318(27)	0.516(23)	60.8(0.8)
HR 7355	Field stars	0.142(37)	0.141(37)	-0.017(37)	176.6(1.1)
HR 7355	MCMC minimization	0.011(24)	0.006(16)	0.009(24)	28.2(0.7)

[a] From Carciofi et al. (2013).

The derived fitting of Eq. 3.3 can be used as reference for a more precise model fitting, physically based, and where the ISM components and the on-sky orientation are simultaneously determined.

The radiative transfer solution of the RRM model

In an attempt to reproduce the observed polarization modulation of σ Ori E, we fed the predicted density distribution of the RRM model of Townsend et al. (2005) to HDUST. All stellar and geometrical parameters were kept fixed to the values determined by Townsend et al. (2005), and the only free parameter in the model was the density scale of the magnetosphere.

The results of this modeling are shown in Fig. 3.4. We could not find a model that simultaneously matched both the photometry and the polarimetry. A higher density model

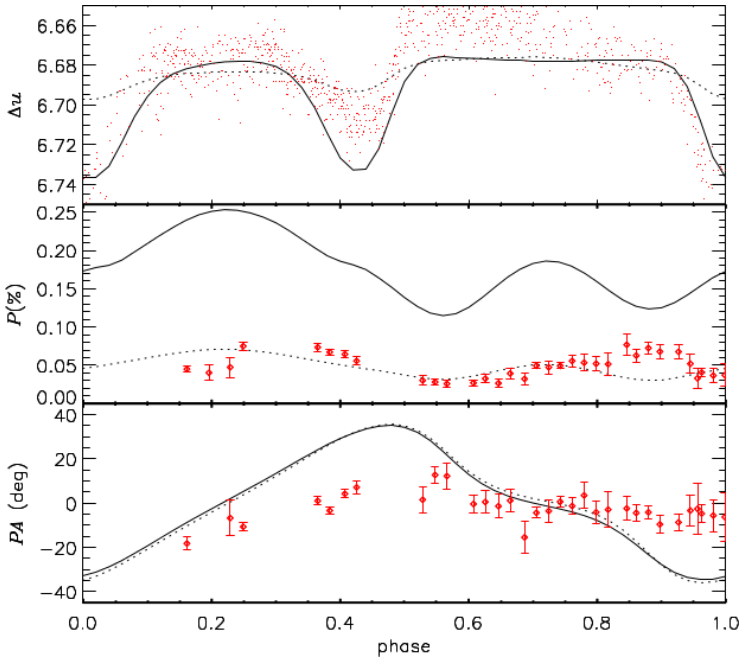

Figure 3.4: Modeling of the intrinsic polarization of σ Ori E using the RRM model (observations are in red). The only free parameter is the maximum number density in the magnetosphere, which was set to 10^{12} cm^{-3} (solid lines) to reproduce the depth of the eclipses and 2.5×10^{11} cm^{-3} (dotted lines) to reproduce the amplitude of the linear polarization (Carciofi et al., 2013).

(solid line) that matches the depth of the photometric eclipses predicts a polarization amplitude that is three times larger than what is observed. Conversely, a lower density model that reproduces the amplitude of the polarization fails to reproduce the photometric amplitude.

Importantly, the detailed shape of the polarization curve was not well matched, in particular the position angle variation. Since the polarization position angle is sensitive to the geometry of the scattering material, this discrepancy indicated that the primary difficulty with the basic RMM model is the shape of its density distribution predicted by the model. Based on these results, we decided to build an ad-hoc, albeit physically motivated, model for the magnetosphere.

3.1.1 Single scattering model

The RRM predicts the existence of diametrically opposed plasma clouds confined in the rotational equator (and a diffuse plasma disk close to the magnetic equator). Based on this idea, and after the suggestion from S. Owocki (priv. comm.), we developed a simple ad-hoc magnetosphere model that consists of two spherical blobs situated in the equatorial

plane at the intersection between this plane and the magnetic equator, where most of the circumstellar material is located. This configuration mimics a *dumbbell* a shape. The plane where the "dumbbdell" rotates is tilted by an angle β from the rotational equator, equivalent to its magnetic equatorial plane.

The Q and U Stokes parameters can be described as a function of orbital phase for a given inclination angle i following a simple single-scattering approach (valid only in the optically thin limit, or $\tau \ll 1$). The scattered flux is first determined in the frame of the star using the formalism described in Bjorkman and Bjorkman (1994, Eq. 6) and then rotated to the frame of the observer (Bjorkman and Bjorkman, 1994, Eq. 20).

For the geometrical configuration of the magnetosphere, we adopted a few fixed parameters whose values were based on the model of Townsend et al. (2005). We set the blobs as spheres, with radius $R_{\rm blob}$. We emphasize that the value of $R_{\rm blob}$ is somewhat arbitrary, since in the limit of $R_{\rm blob} \ll R_*$ and in the single-scattering approximation, a large, tenuous blob is roughly equivalent to a dense, small blob. In other words, what really controls the polarization level of each component is their total scattering mass. For the inclination angle we adopt two possible values: i = 70°, corresponding to a projected counterclockwise rotation of the blobs on the sky and $180° - 70° = 110°$, corresponding to a clockwise rotation.

We started the scattering modeling of σ Ori E neglecting the disk component of the magnetosphere, as predicted by the RRM model (Fig. 3.2). However, our initial results showed that only two blobs could not explain the observed polarization incursions in the QU plan. As shown in Fig. 3.5, right panel, the result of two blobs rotation over the QU plane is an double coincident ellipse. If only a tilted disk is present, a similar result is found: a double "banana"-shaped track in the QU plane. Only the combination of these two structures can reproduce the measured QU track, which led to inclusion of the disk component in the model.

As discussed for the blob size, the disk geometrical thickness is also somewhat arbitrary: if the single-scattering approximation holds, a thinner, denser disk is equivalent to a thicker, less dense disk. Below, we summarize the criteria used to define the geometrical configuration of the "dumbbell+disk" model:

- The stellar radius adopted is the equatorial one ($R_* = R_{\rm eq}$). The current version of the code does not take into account the star oblateness neither the gravity darkening

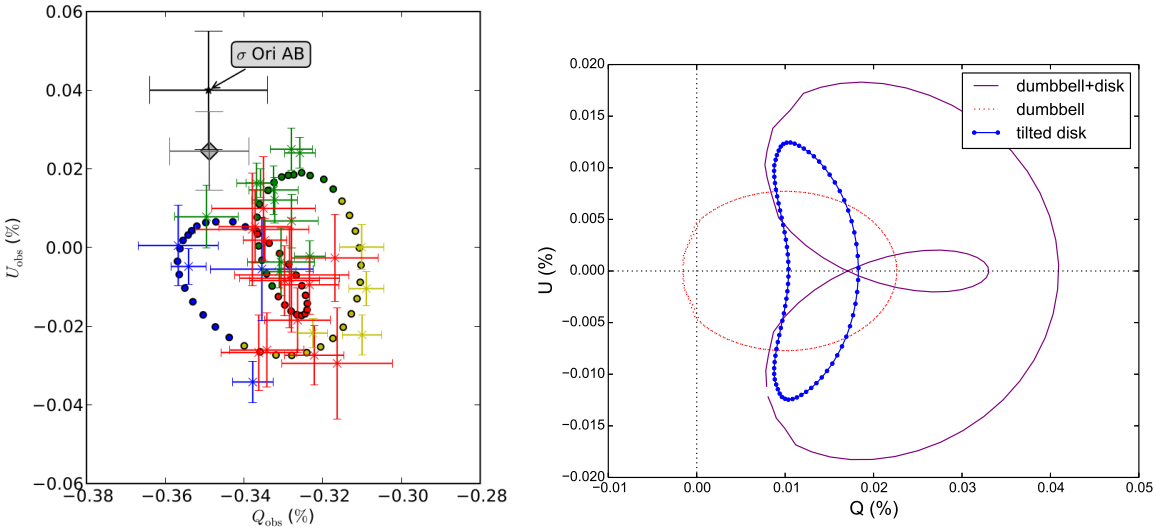

Figure 3.5: Left: QU plot of the observed data of σ Ori E (points with error bars). The orbital phase correspondence of the points is as follows: blue, δ-(δ+0.25), orange, (δ +0.25)-(δ+0.50), green, (δ+0.50)-(δ+0.75), and red, (δ+0.75)-δ. The filled circles show the best-fitting model, including the IS component as gray diamond. The IS polarization of σ Ori AB is indicated (Carciofi et al., 2013). *Right:* The intrinsic polarization of the "dumbbell+disk" model with the typical double-loop heart shape (purple line). The curves of the isolated components are also shown: the dumbbell component (red dashed-line) and the tilted disk (blue line with dots). Due to their symmetry, the property $\langle U \rangle = 0$ is always valid (considering a integer number of cycles). Also, the disk component makes that always $U > 0$.

effect. These effects are important for near-critical rotating stars, and are planned for the near future.

- The center of the blob is at $R_{\rm K}$, the co-rotation (or "Keplerian") radius (Eq. 3.2). For slow and moderate rotators (e.g., σ Ori E), the blob position is $\gtrsim 2.5 R_{\rm eq}$. For fast rotators, the blob may be very close to the stellar photosphere due to small value of the co-rotating radius.

- The blob diameter is fixed as $2/3 R_*$.

- The polarimetric period is the same from photometry (and spectroscopy), but an arbitrary phase shift can be applied.

- The disk component (rather, a ring) has the same radial position and size of the blob, with fixed scale height of $H = 0.01 R_*$.

This configuration is illustrated in Fig. 3.6 for different orbital phases and at the viewing angle $i = 70°$. The resulted modeling with dumbbell+disk components is shown in Fig. 3.7. The here described scattering code is available at the PYHDUST library.

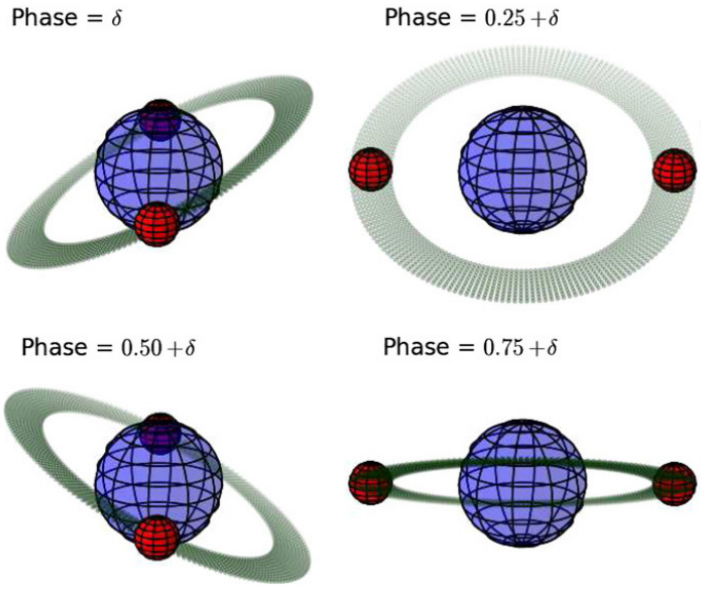

Figure 3.6: Geometric conception of the "dumbbell + disk" model to scale ($i = 70°$). The corresponding phase is indicated, where δ is the phase shift between photometric and polarimetric minima (Carciofi et al., 2013).

The main results of this study are: (i) it confirms the RRM prediction of two main circumstellar structures for the magnetosphere, namely a thin disk and two over-density regions at the intersection of the rotation and magnetic planes; (ii) the RRM model prediction for the total scattering mass of each of these components do not agree with the polarization data. In particular, the derived mass for the "disk" component is much larger than the expected. This challenges RRM description for this star, as pointed out by (Townsend et al., 2013).

3.1.2 New minimization process of σ Ori E polarization light-curve

The polarization survey of sigma Ori E continued after the publication of the first results. Fig. 3.8 shows the fit for all intrinsic data (top panel), as well the observed QU points. We also present the data binned in phase (bottom panel). The procedure adopted is to divide the $[0, 1]$ phase interval in 20 bins of $\Delta\text{phase} = 0.05$. The polarization value for each bin in then the weighed average of all points belonging to that bin.

The previous and new best-fitting values of Eq. 3.3 for σ Ori E are presented in Table 3.1. The addition of a few more observational points did not changes the derived values of polarization bias level, amplitude of modulation and phase shift in respect to the photometric curve.

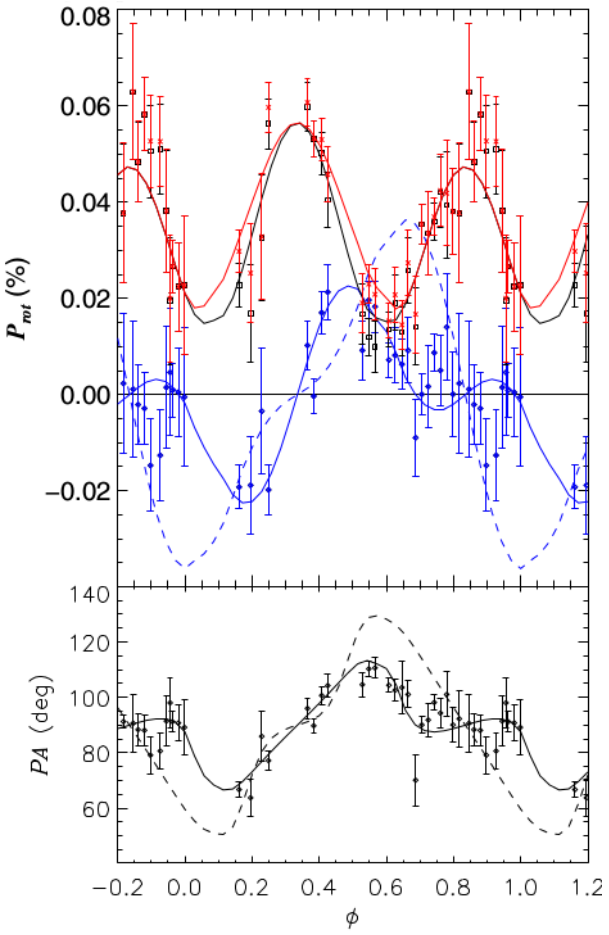

Figure 3.7: Polarization of σ Ori E compared to the single-scattering model. The solid line is for our best-fitting model with $i = 70°$ and the dashed line is for $i = 110°$ (Carciofi et al., 2013).

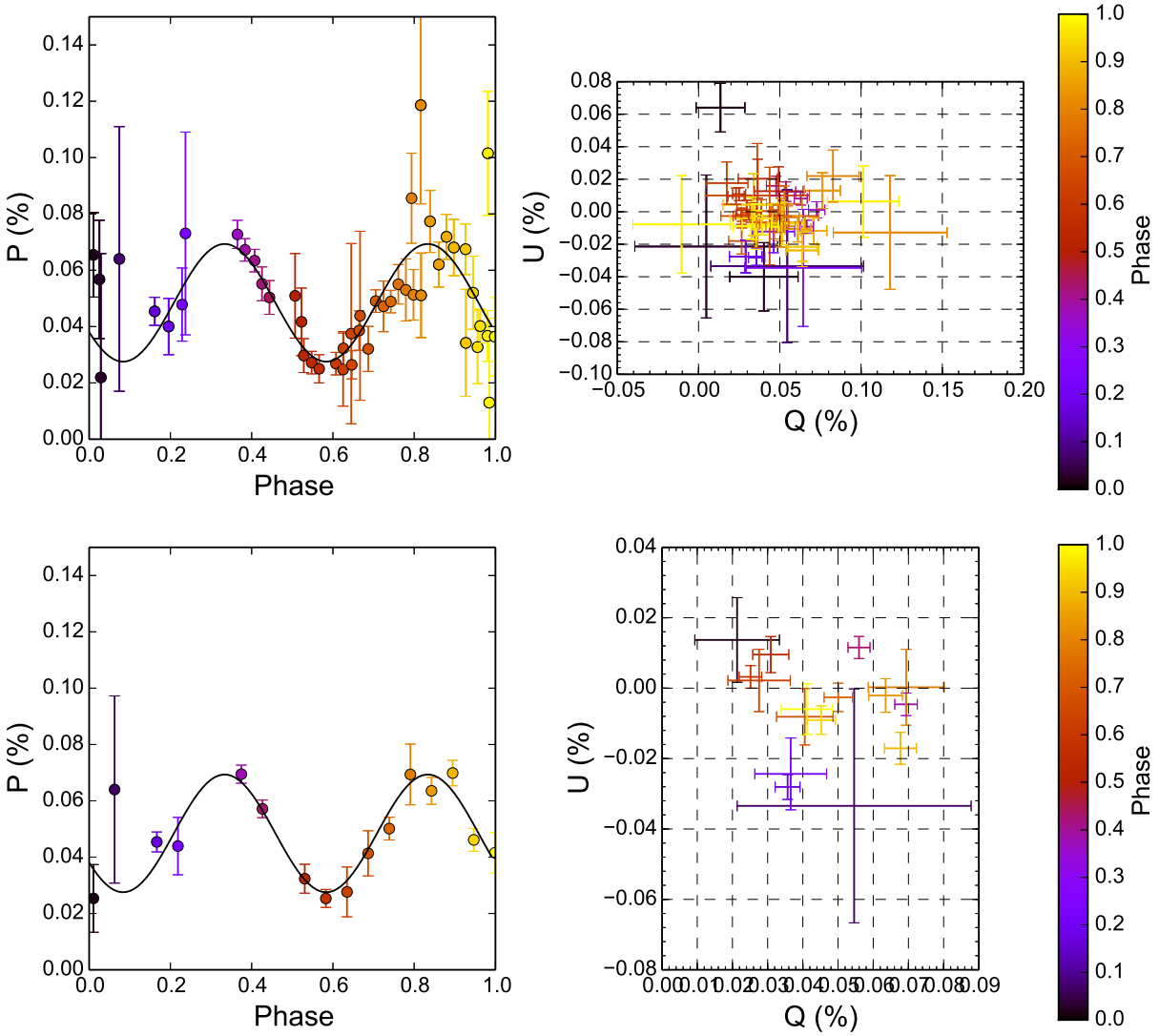

Figure 3.8: V-band linear polarization measurements of σ Ori E. *Left:* subtracted interstellar components (Table 3.1). The line corresponds to the best fit of Eq. 3.3. *Right: QU* diagram of the observed polarization on the celestial frame. *Top*, all observational points. *Bottom*, the data points binned in phase. Their values in the celestial frame are in Table C.1.

The fit of the "dumbell+disk" model shown in Carciofi et al. (2013) was performed manually, by changing the parameters around a χ^2 minimum that was found by computing a model grid. Here we present new results for σ Ori E, applying the Monte Carlo Markov chain (MCMC) method for our most recent data set. The minimization simultaneously determines all the selected physical parameters involved in the modeling. This method allows to evaluate the correlation between the parameters and the uncertainty in their determination, in a self-consistent analysis.

To standardize the σ Ori E analysis with the other smaller stars, which have lower signal-to-noise (S/R) ratio, the first step is to group the polarization data into regular phase intervals, i.e., the Q and U Stokes components. In this way, the data points have a higher signal and also a uniform phase sampling. Then, for each *model* (or set of parameters randomly generated in the MCMC simulation), the following steps are performed:

1. The intrinsic polarization model is generated in the stellar reference system (i.e., for which North is aligned to the stellar spin axis) for all rotational phases.

2. The model is rotated to the equatorial system. Here, it is important to distinguish between counter- and clockwise rotation. This is done by allowing i to vary.

3. Interstellar polarization components $Q_{\rm ISM}$ and $U_{\rm ISM}$ are randomly sampled within a pre-determined interval (by default, determined by field stars analysis).

4. The χ^2 value is computed to determine the likelihood associated with model parameters, which is higher the lower the χ^2 value, defined as

$$\chi^2 = \sum_i^N \left[\frac{Q_{\rm obs}(\phi_i) - Q_{\rm mod}(\phi_i)}{\sigma_{Q(\phi_i)}}\right]^2 + \sum_i^N \left[\frac{U_{\rm obs}(\phi_i) - U_{\rm mod}(\phi_i)}{\sigma_{U(\phi_i)}}\right]^2 , \qquad (3.4)$$

   where N is number of phase bins and ϕ_i their values.

5. Based on the likelihood of the current parameters, a new set is generated until reaching the number of iterations defined by the user.

Fig. 3.9 and 3.10 show the MCMC PDFs and their correlations, minimizing simultaneously seven model parameters (the five parameters fitted in Table 3.3, in addition to i and β). They confirm the rotational direction of the star as counter-clockwise, since $i \sim 70°$ (median $\chi^2_{\rm red} = 4.74$, in contrast to the median $\chi^2_{\rm red} = 9.65$ at $i \sim 110°$). They

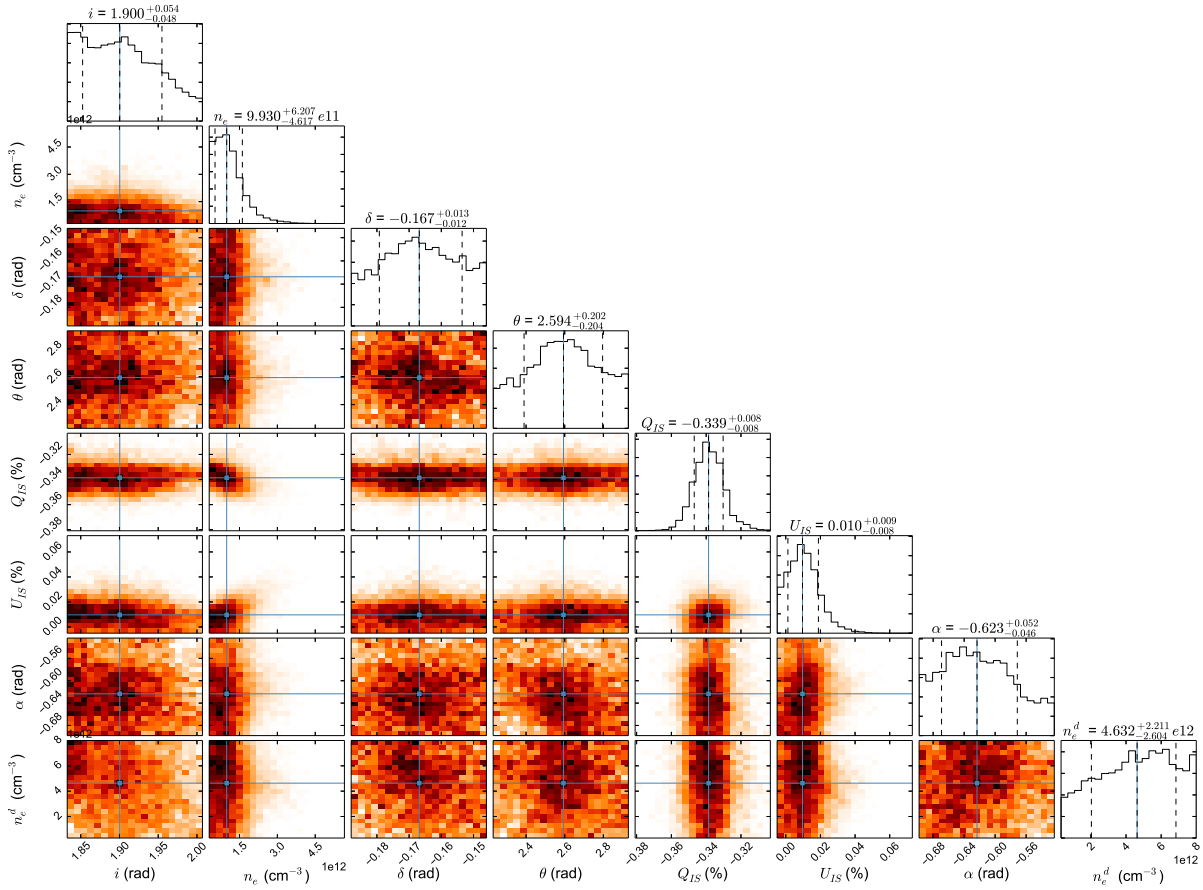

Figure 3.9: The MCMC probability density distributions for the "dumbbell+disk" polarization modeling to σ Ori E at $i \sim 70°$, and the corresponding correlation maps. Here the inclination angle i and the obliquity $\alpha = 90° - \beta$ are left free, but the results show that they are degenerate within the selected intervals. The heat-like color map indicate the highest probabilities (black) to the lowest (white). *From left to right (or top-bottom):* inclination angle (rad), blob electronic density (cm^{-3}), phase shift, on-sky orientation angle (θ), the interstellar Q component (%), interstellar U component (%), the complementary angle between the rotation and magnetic axes (rad) and disk electronic density (cm^{-3}). The dashed vertical lines in the histograms indicate the percentile of 16% (-1σ), the median and the percentile of 84% (1σ) of each distribution.

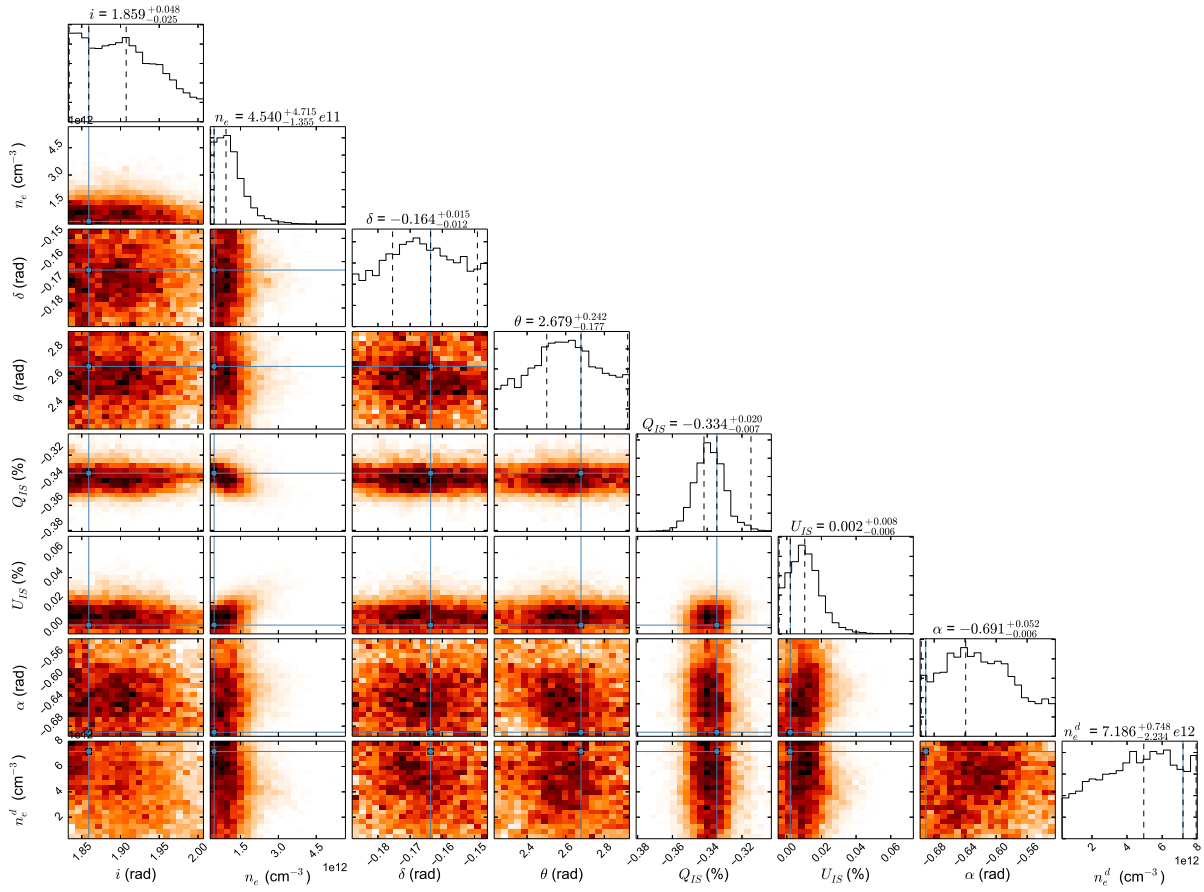

Figure 3.10: Same as previous figure, but for $i \sim 110°$.

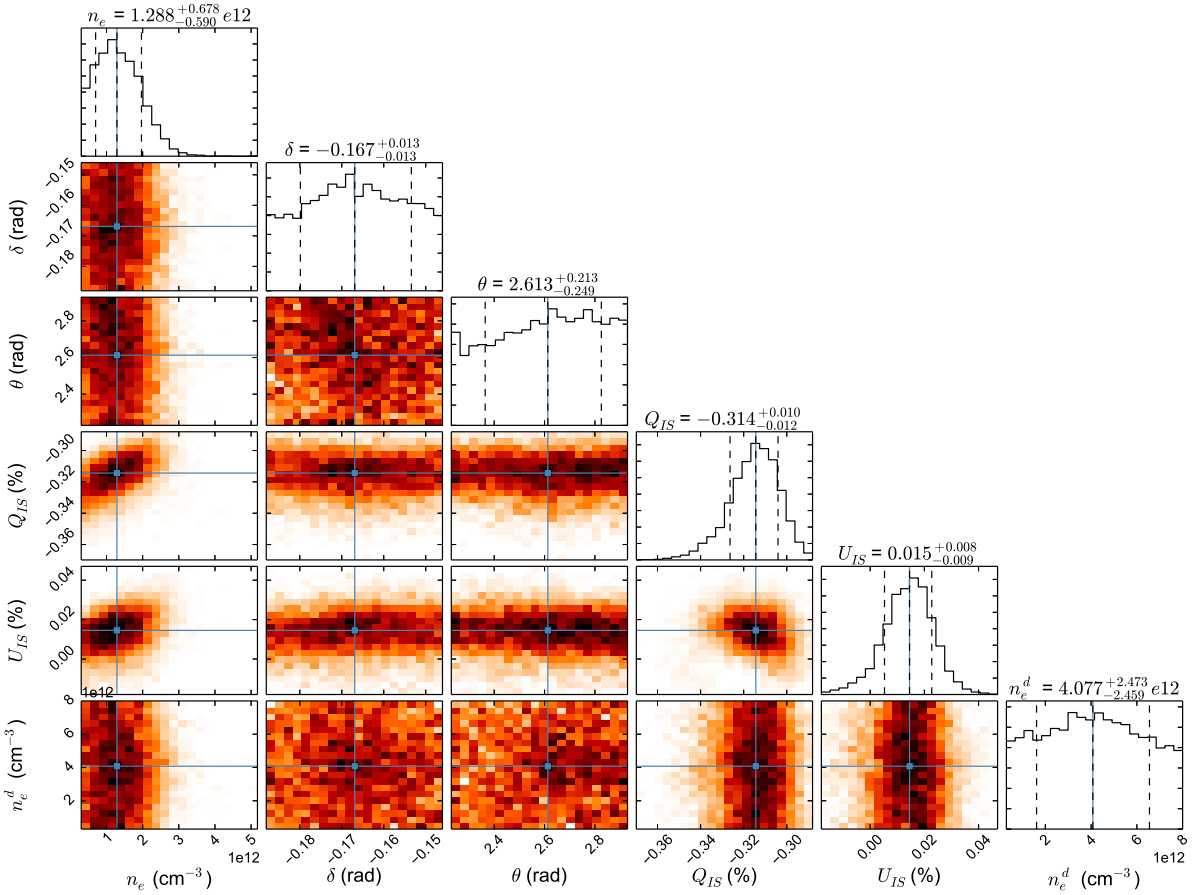

Figure 3.11: Same as previous figure, but for $i = 70°$ and $\alpha = 90° - \beta$ ($\beta = 55°$), kept fixed.

also show that the inclination angle i and the magnetic obliquity β can not be constrained within the selected intervals. In our code, the obliquity is set by the complementary angle $\alpha = 90° - \beta$ shown in the figures. We fixed parameters i and β to the values adopted by Townsend et al. (2013) to determine the other main polarimetric physical parameters (Fig. 3.11). The previous and newly derived parameters are listed in Table 3.3.

When comparing the results of MCMC minimization with results from Carciofi et al. (2013), it is important to be aware that better stellar parameters (from Townsend et al., 2013) were used. The stellar equatorial radius decreased from 4.28 to 3.77 $R_\odot$, modifying the parameterized volume of the magnetosphere, and the rotational rate changed from $W = 0.29$ to 0.26, modifying the co-rotational radius. Thus, the new findings indicate: (i) 30% denser blob, but with a smaller total mass; (ii) a density 50% higher to the disk, and that led to a slightly higher mass. In the end, the ratio $2M_{\rm blob}/M_{\rm d} \simeq 1.0$, a value $\sim 20\%$ lower than previously determined.

Table 3.3 - Best-fitting parameters of single scattering "dumbbell+disk" model for σ Ori E, HR 5907 and HR 7355 magnetospheres with MCMC minimization. The fitted and fixed parameters are indicated. The parameters marked as "ref." would not change the polarization curve in the current version of the modeling.

Star	σ Ori E[a]	σ Ori E[b]	HR 5907[c]	HR 7355[d]	Params.
Hipparcos parallax (mas)	-	-	7.64(0.37)	3.66(0.38)	ref.
B_p (kG; dipole)	9.6	9.6	10	11	ref.
$\Omega/\Omega_{\rm crit}$	0.5	0.454	0.80	0.89	ref.
W	0.29	0.26	0.53	0.63	ref.
Zero phase (MJD)	42778.329	42778.329	47913.19	54940.33	fixed
Rotational period P (days)	1.1908229	1.1908229	0.508276	0.5214404	fixed
i (deg)	70/~~110~~	70	70/110[e]	60/~~120~~	fixed
β (deg)	62	55	7	75	fixed
α (deg)	28	35	83	15	fixed
$R_{\rm eq}$ ($R_\odot$)	4.28	3.77	3.1	3.69	fixed
R_p ($R_\odot$)	4.11	3.65	2.72	3.06	ref.
Spec. CS emission ($R_{\rm eq}$)	$\gtrsim 2$	$\gtrsim 2$	1.2-4.4	2-4	ref.
$R_{\rm K}$ ($R_{\rm eq}$)	2.38	2.54	1.74	1.63	ref.
Blob mean dist. ($R_{\rm eq}$)	2.38	2.54	1.90[f]	2.54[f]	fixed
min. blob dist. ($R_{\rm eq}$)	2.05	2.21	1.57	2.21	fixed
max. blob dist. ($R_{\rm eq}$)	2.71	2.87	2.23	2.87	fixed
n_e (10^{12} cm^{-3})	$1.0^{+0.6}_{-0.9}$	$1.29^{+0.68}_{-0.59}$	$0.72^{+0.55}_{-0.32}$	$1.53^{+1.17}_{-0.86}$	fitted
δ (phase)	$-0.17^{+0.02}_{-0.02}$	$-0.167^{+0.013}_{-0.013}$	$0.08^{+0.16}_{-0.17}$	$-0.02^{+0.18}_{-0.16}$	fitted
θ (deg)	$150.0^{+7.0}_{-7.0}$	$149.7^{+12.2}_{-14.3}$	78^{+12}_{-13}	88^{+12}_{-14}	fitted
n_e^d (10^{12} cm^{-3})	$2.7^{+1.0}_{-1.0}$	$4.1^{+2.5}_{-2.5}$	$3.8^{+2.5}_{-2.4}$	$4.4^{+2.3}_{-2.6}$	fitted
$M_{\rm blob}$ (10^{-12} $M_\odot$)	4.00	3.47	1.08	3.86	ref.
$M_{\rm disk}$ (10^{-12} $M_\odot$)	6.50	7.07	2.66	7.11	ref.
$2M_{\rm blob}/M_{disk}$	1.23	0.98	0.81	1.09	ref.

[a] From Carciofi et al. (2013). Their analysis exclude the inclination angle of $i \sim 110°$.

[b] Reference values from Townsend et al. (2013).

[c] Reference values from Grunhut et al. (2012).

[d] Reference values from Rivinius et al. (2013).

[e] The accuracy of the data is unable to clearly define the direction of rotation. The indicated values are the most likely.

[f] Based on velocity measurements of spectroscopic lines (op. cit.).

3.2 Polarimetry of magnetospheres and HR 7355

HR 7355 is a hot magnetic star with very similar properties to σ Ori E (Rivinius et al., 2013). The main difference is that HR 7355 possesses the highest rotational rate known among stars harboring centrifugal magnetospheres ($W = 0.63$), closely accompanied by HR 5907. This has important implications to the RRM model: the rotation near break-up of fast rotating stars poses a puzzle since magnetic fields should brake the stellar rotation.

Unlike σ Ori E, HR 7355 does not belong to a multiple stellar system and exhibits a low raw polarization level, what makes it hard to determine the interstellar polarization. The IS component of the polarization was estimated by the selected field stars listed in Table 3.4. The selection criteria was (i) stars angularly close to target, (ii) stars with compatible Hipparcos distance, and (iii) stars with no known peculiarity, preferably at main sequence.

Our results for the intrinsic polarization of HR 7355 show a much higher average polarization than σ Ori E (0.146% vs. 0.047%). However, the fit of the polarization with Eq. 3.3 reveals a similar polarimetric amplitude, i.e., $\sim$ 0.02% (Fig. 3.12). The derived position angle PA is $\sim 86.4°$. Before applying the "dumbbell+disk" for this star, we investigate the effects that the high rotation rate could cause in the polarimetric signal of this star.

3.2.1 Effects of high rotation in the polarization

We know that high rotational rates profoundly changes the characteristics of the stellar surface. This, in turn, must be reflected in the circumstellar disk polarization signal once the light flux and its incidence angle on the disk are modified. Bjorkman and Bjorkman (1994) studied this problem in the context of polarization of Be stars disks.

In disk-like circumstellar environments, such as the magnetospheres, the scattered radiation is dominated by light from the stellar equator. On the one hand, these equatorial regions have a lower effective temperature - and lower flux - than the higher latitudes of the star due to gravity darkening. With less flux been polarized by the disk and more unpolarized stellar light reaching the observer, the net result should be a smaller observed polarization level. This depolarization would be larger the faster the stellar rotation rate. On the other hand, the bigger equatorial radius yields a bigger stellar surface area and a disk material reconfiguration due to a different potential. The consequence of these

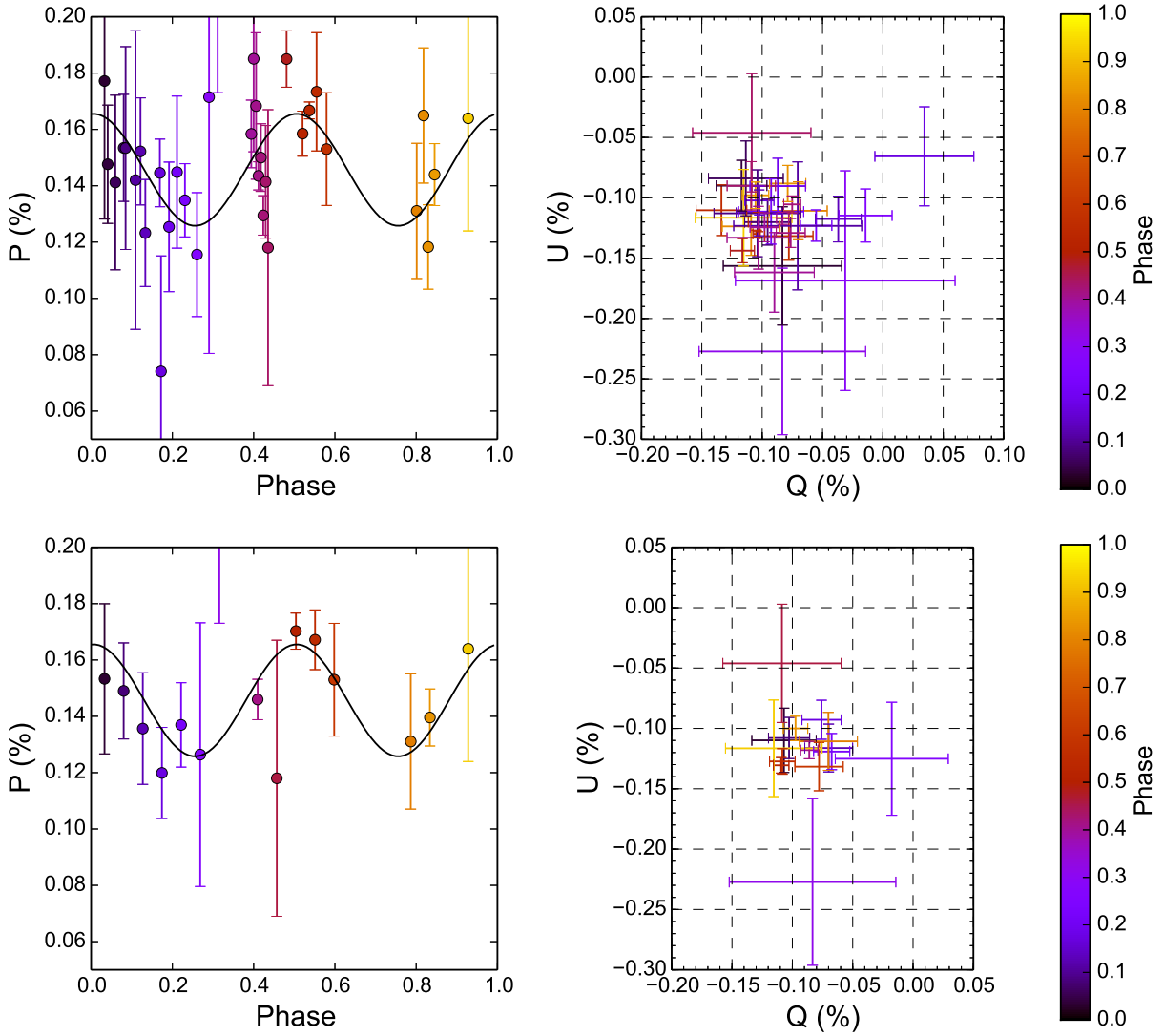

Figure 3.12: V-band linear polarization measurements of HR 5907. *Left:* subtracted interstellar components (Table 3.1). The line corresponds to the best fit of Eq. 3.3. *Right:* QU diagram of the observed polarization on the celestial frame. *Top*, all observational points. *Bottom*, the data points binned in phase. Their values in the celestial frame are in Table C.3.

Table 3.4 - V-band polarization measurements of HR 7355 field stars.

Star	Date	Q (%)	U (%)	P (%)	σ (%)	θ (deg)	σ_θ (deg)
HIP95027	14mai20	0.1742	-0.2521	0.3064	0.0082	152.3	0.8
HIP95604	14jul31	0.0950	-0.0902	0.1310	0.0132	158.3	2.9
	14mai20	0.0517	-0.0152	0.0539	0.0073	171.8	3.9
	11set29	0.0639	-0.0162	0.0659	0.0112	172.9	4.9
HIP95386	11jun13	0.2612	0.0783	0.2727	0.0147	8.3	1.5
	11jun13	0.2337	0.0679	0.2434	0.0118	8.1	1.4
HIP95412	11jun15	0.2429	-0.0321	0.2450	0.0111	176.2	1.3
	11jun16	0.2350	-0.0712	0.2456	0.0189	171.6	2.2
HIP95782	14set24	-0.0867	0.1814	0.2010	0.0240	57.8	3.4

changes in polarization are difficult to anticipate.

In Fig. 3.13 we show the V-band polarization of a Be star with a mass and disk density compatible with the ones expected to centrifugal magnetospheres (i.e., B2V star with $n \sim 10^{12}$ particles per cm^3) as function of the stellar rotation rate and seen at different inclination angles. The Be models employed are from the BeAtlas project, presented in Chapter 2. It is known that the polarization of ionized circumstellar disks increases with the inclination angle i due to increased projected asymmetry (a face-on disk has a null polarization). The maximum level occurs at $i \sim 70°$, angle at which effects of photospheric and disk self absorption become important. In the figure, we see that up to angles $i \sim 60°$ the polarization level decreases with rotation angle, but for angles near edge-on viewing, the reverse is observed.

The effect of high stellar rotational rate could be important for the analysis of HR 7355, and other fast rotating magnetosphere stars, such as HR 5907 (next section). Indeed, the polarization level can decrease up to $\sim$ 50% with rotation, for small inclination angles ($i \lesssim 30°$). However, for the inclination angle derived by spectroscopic modeling of HR 7355 ($i \sim 60°$) and its rotation rate ($W = 0.63$), the expected effect is of the order of $\Delta P = \|P(W = 0.63)/P(0)\| \lesssim 6\%$, and was neglected in this work.

The absence of material near the stellar equator in the centrifugal magnetospheres could lead to different conclusions than those of Be disks. To verify this, we executed radiative transfer simulations for which the Be disk was truncated to a disk between 2 to 3 $R_{\rm eq}$ and with uniform density as function of the radius. A very similar result was found

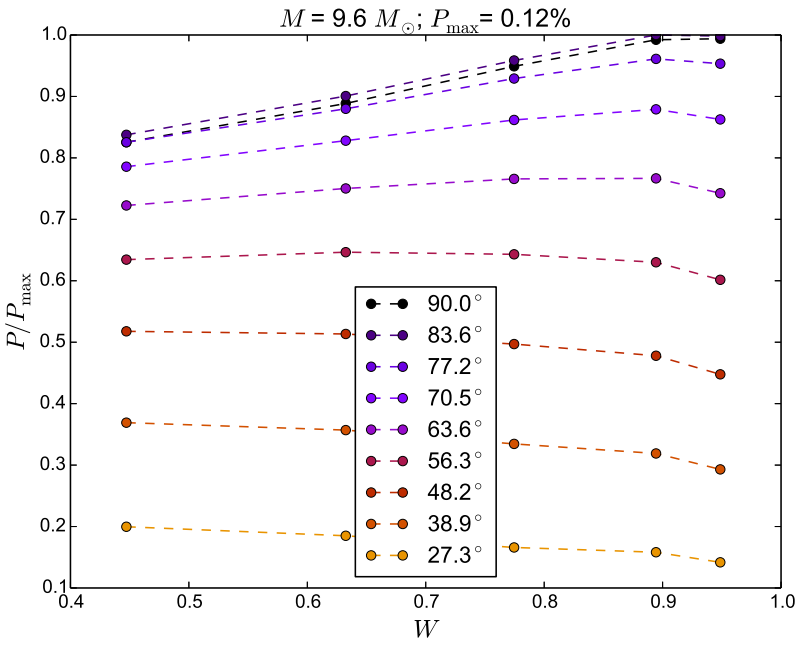

Figure 3.13: Relative V-band polarization level of a Be star as function of the stellar rotation rate seen at different inclination angles. The considered star has mass $M = 9.6 M_\odot$ with a steady-state viscous decretion disk with base superficial density of $\Sigma_0 = 0.02$ g cm^{-3}.

than the one shown in Fig. 3.13. The inclusion of a fast rotating star is planned for the "dumbbell+disk" modeling tool in the near-future, providing a better physical description of the system, particularly for those seen at a small inclination angles.

3.2.2 *The minimization of the HR 7355 polarization curve*

The higher rotational rate of HR 7355 situates the circumstellar co-rotational radius $R_{\rm K}$ closer to the star. The expected value for HR 7355 is $R_{\rm K} = 1.63\ R_{\rm eq}$. According to the "dumbbell+disk" polarization modeling, the blobs are centered at this distance, with radius of $1/3\ R_{\rm eq}$. This means that to the the circumstellar material almost touches the stellar surface.

To explore the effect of the different distances of the blobs to the star, we considered two distinct mean distances: (i) $R_{\rm blob} = R_{\rm K} = 1.63\ R_{\rm eq}$ and (ii) $R_{\rm blob} = 2.54\ R_{\rm eq}$, the same value as σ Ori E. This second value is supported by the emitting spectroscopic lobes characteristics of $R = 2$-$4\ R_{\rm eq}$ from Rivinius et al. (2013). A smaller CS distance in the "dumbbell+disk" model reflects in a smaller density needed to reach the same polarization level, but it also changes the detailed shape of the polarimetric light-curve components Q

and U.

As first result, we found that assuming the blobs at the the co-rotational radius yields a much worse overall fit (median $\chi^2_{\rm red} = 4.75$ for $R_{\rm blob} = 1.63 R_{\rm eq}$) than assuming the blob is located at large distances ($\chi^2_{\rm red} = 2.75$ for $R_{\rm blob} = 2.54 R_{\rm eq}$). Secondly, as occurred to σ Ori E, the minimization was unable to constraint the inclination angle (i) and the obliqueness of the magnetic field with the rotation (β). Also, we found a sightly better result for a inclination angle of $i \sim 60°$ than for $i \sim 120°$, but the differences in fit quality are small ($\chi^2_{\rm red} = 2.53$ vs. 3.07). The MCMC minimizations for $i \sim 60°$ and $i \sim 120°$ are shown in Fig. 3.14 and Fig. 3.15, respectively. The best-fitting values are listed in Table 3.3. The derived densities (and masses) for the blob and disk components are very similar to the ones determined to σ Ori E. Only the blobs appear do to $\sim 10\%$ denser, leading to $2M_{\rm blob}/M_{\rm d} \simeq 1.1$.

A higher accuracy in the parameters is expected as we gather new data from our running survey. The spectropolarimetric analyzes of field stars with the Wilking-Serkowski fitting might help solve the discrepancy between the IS value derived from them ($P \sim 0.142\%$) in comparison the one fitted by the MCMC method, compatible with null value ($P \sim 0.006\%$). In addition, we will carry on a more in-depth investigation of an interesting feature: these results, both from the model-independent and from the MCMC minimization ($\delta = 0.005(16)$ and $0.08(17)$, respectively), indicate that the minimum of the photometry is anti-correlated with polarization (i.e., the maximum of polarization occurs at photometry minimum, defined as the phase $\phi = 0$, as seen in Fig. 3.12). This would imply in a complex configuration for the circumstellar environment, with the blobs not being responsible for the region simultaneously dominating the polarization and photosphere absorption in the light-curve. In this case, the presence of photosphere spots may be important.

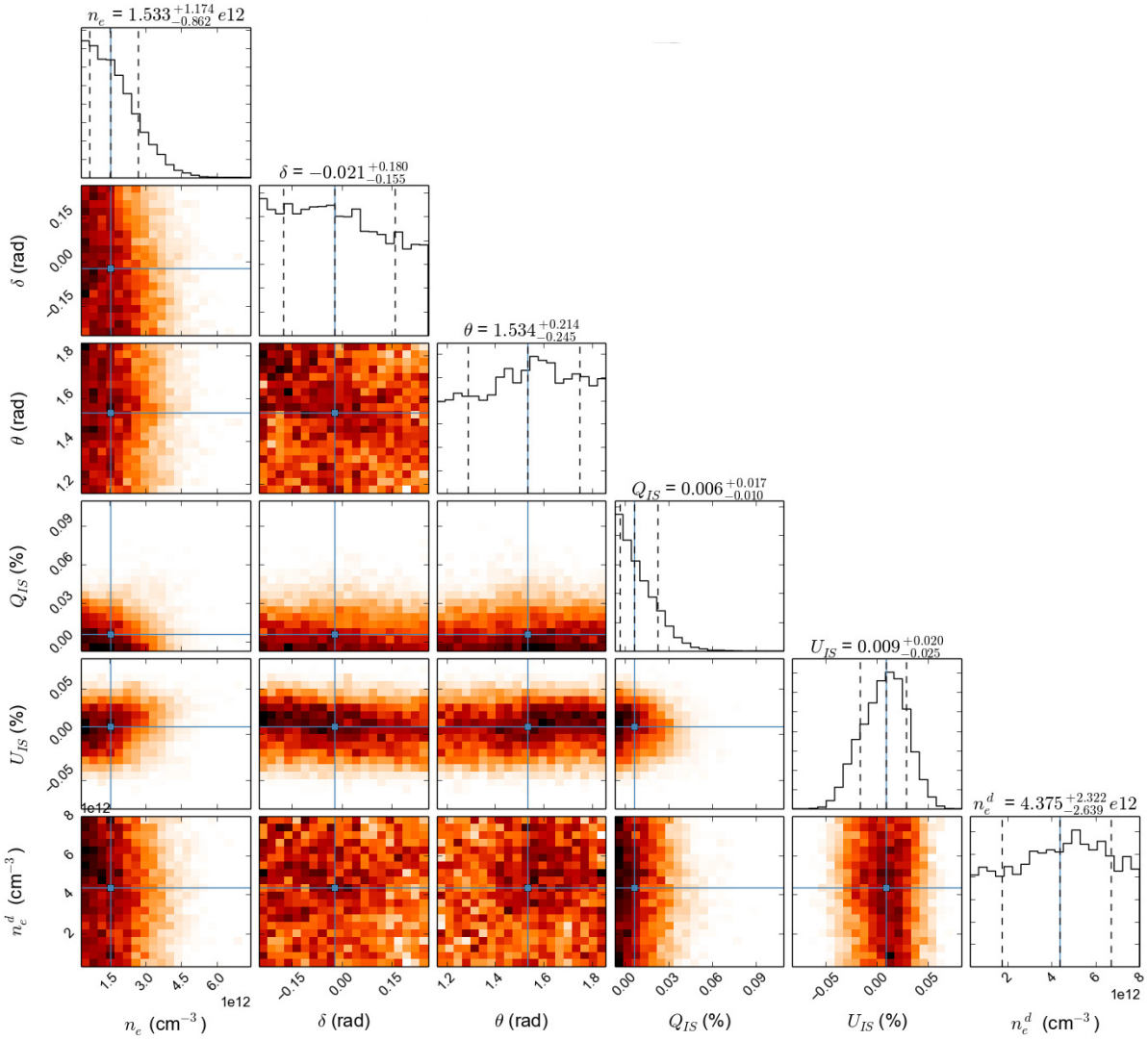

Figure 3.14: The MCMC probability density distributions for the "dumbbell+disk" polarization modeling to HR 7355 at $i = 60°$, and the corresponding correlation maps. The heat-like color map indicate the highest probabilities (black) to the lowest (white). *From left to right (or top-bottom):* inclination angle (rad), blob electronic density (cm^{-3}), phase shift, on-sky orientation angle (θ), the interstellar Q component (%), interstellar U component (%), the complementary angle between the rotation and magnetic axes (rad) and disk electronic density (cm^{-3}). The dashed vertical lines in the histograms indicate the percentile of 16% (-1σ), the median and the percentile of 84% (1σ) of each distribution.

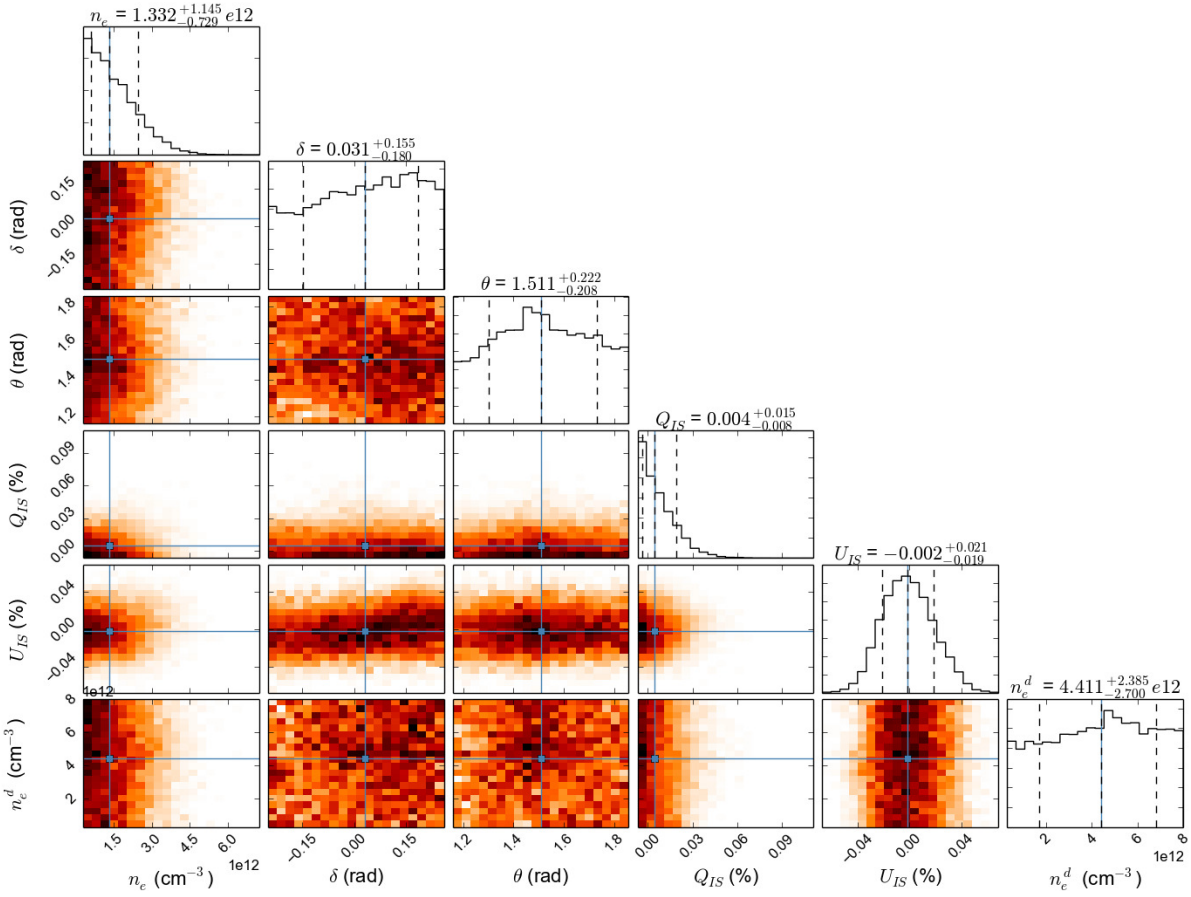

Figure 3.15: The same as previous figure, but for $i = 120°$.

3.3 Magnetospheres seen by interferometry and HR 5907

The bright B2V star HR 5907 ($V_{\rm mag} = 5.4$) hosts a confirmed dense, magnetically bound circumstellar material, displaying a high rotation rate for a magnetic star ($W = 0.53$; Grunhut et al., 2012). Among the three magnetic stars analyzed in this work, HR 5907 is the one with the worst S/N in the polarimetric data. The raw polarization data of HR 5907 shows a marginal signal of modularization as compared to σ Ori E (Fig. 3.16). Also differently from that star, HR 5907 do not belong to a multiple stellar system what make much harder estimate the ISM polarization contribution. The field stars used to estimate the interstellar components of HR 5907 are in Table 3.5. The criteria employed in their selection were the same as used to HR 7355. The resulting values for the interstellar polarization components are in Table 3.1.

The intrinsic polarization HR 5907 is shown in Fig. 3.16. Despite the fewer polarimetric observations among the magnestospheres analyzed here, and the corresponding low signal-to-noise ratio the model-independent fitting (Eq 3.3; $\chi^2_{\rm red} = 2.80$) resulted in very close values of σ Ori E magnetosphere, with a oscillation amplitude $A \sim 0.02\%$ and a base level of $P_0 \sim 0.04\%$. The derived position angle was 77.4°, value which is useful when interpreting the available interferometry observations of the star.

3.3.1 The spectrointerferometry of HR 5907

The proximity of HR 5907 (parallax of 7.64(37) mas) and its short rotation period ($P = 0.508$ d) sets a good opportunity to characterize its magnetosphere using interferometry. Thus, AMBER observations were proposed aiming at determining the detailed spacial configuration of the co-rotating magnetosphere. Spectrointerferometry offers a unique way

Table 3.5 - V-band polarization measurements of HR 5907 field stars.

Star	Date	Q (%)	U (%)	P (%)	σ (%)	θ (deg)	σ_θ (deg)
	11mai11	-0.1763	0.4408	0.4747	0.0097	55.9	0.6
hip78099	11mai11	-0.2392	0.4100	0.4747	0.0097	60.1	0.6
	11set29	-0.2438	0.4246	0.4896	0.0141	59.9	0.8
hip77858	11jun29	-0.5358	0.3780	0.6557	0.0123	72.4	0.5
hip77960	11set28	-0.1772	1.0196	1.0349	0.0117	49.9	0.3

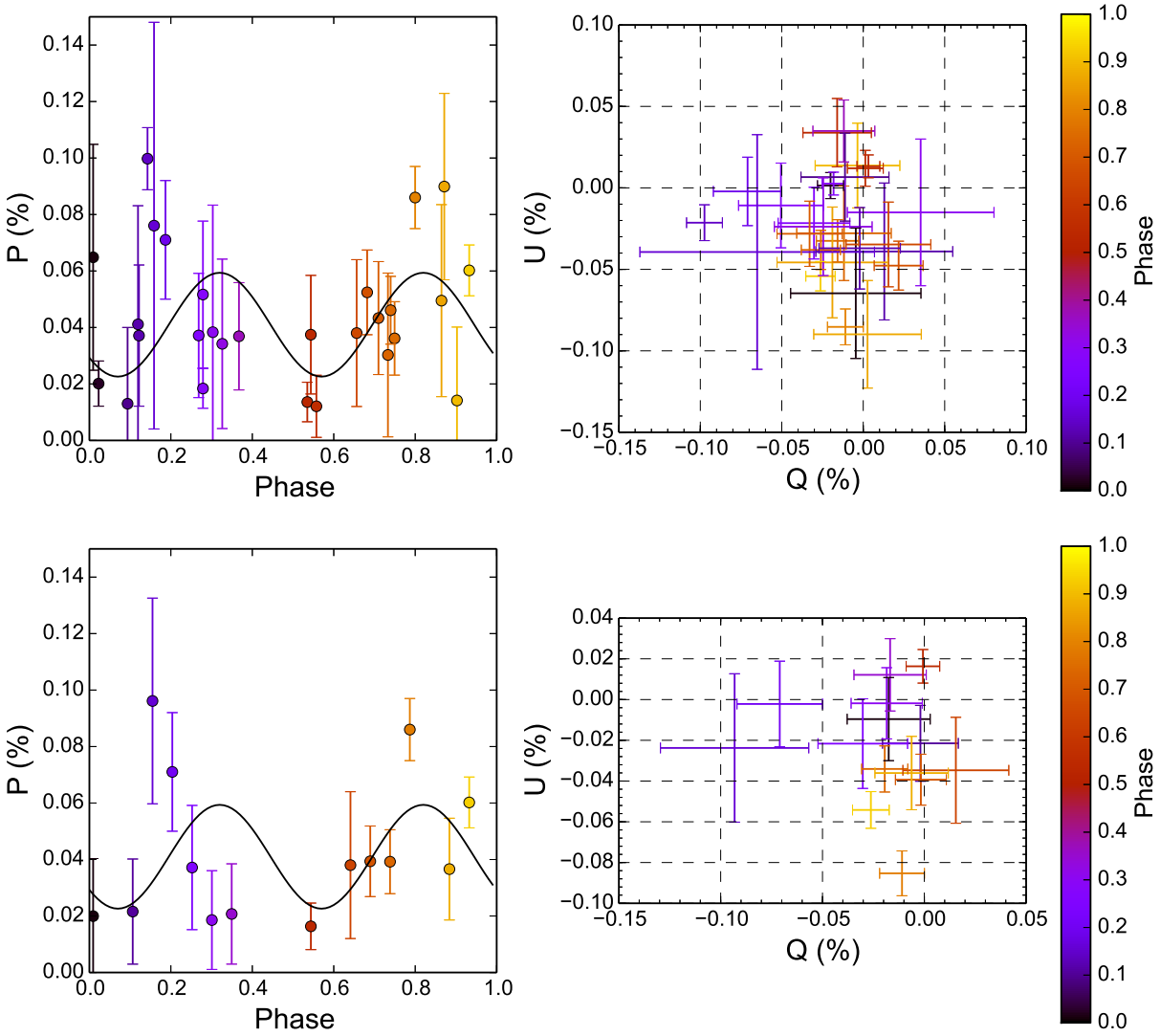

Figure 3.16: V-band linear polarization measurements of HR 5907. *Left:* subtracted interstellar components (Table 3.1). The line corresponds to the best fit of Eq. 3.3. *Right:* QU diagram of the observed polarization on the celestial frame. *Top*, all observational points. *Bottom*, the data points binned in phase. Their values in the celestial frame are in Table C.2.

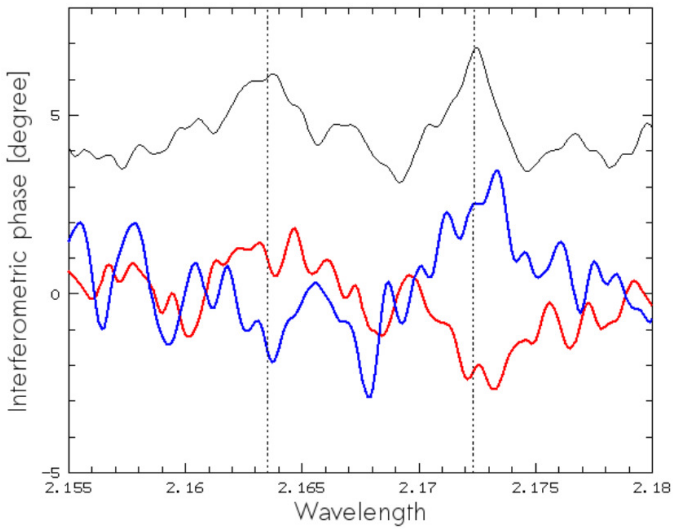

Figure 3.17: Upper profile: flux observed by AMBER across the Brγ line (scaled and filtered with a 5 pixel Gaussian for display). The emission peaks correspond to those seen in Hα at that rotational phase. *Lower profiles*: Filtered interferometric phases for baselines K0→A1 and A1→I1. An interferometric phase signal of the order of about 3° is seen at the position of the red emission peak, one of about 1.5° going into the other direction for the blue peak (Rivinius et al., 2012).

to investigate the stellar brightness distribution at multiple spectral channels, proving both spatial and kinematical information.

Visual spectroscopic and circular polarimetric data was analyzed by Grunhut et al. (2012) and predicted a magnetosphere detectable by interferometry across the Brγ line. This scenario was tested by observations, aiming at deriving data for a quantitative analysis of the magnetosphere. The data resulted in the first interferometric detection of magnetosphere, but in a somewhat smaller signature of ∼3° phase difference (Fig. 3.17). The details of observations and the results obtained are given in the proceedings paper Rivinius et al. (2012), attached to the end of this chapter. Even though we can surely say that the magnetosphere was detected in phase, the data quality, due to the really bad observational conditions, prevents the use of the data for a more qualitative characterization of the magnetosphere.

About the interferometric observations, if the star is aligned at PA = 77.4° as the of linear polarization indicates, the disk is oriented at 167.4°. For the interferometer configuration described in Table 3.6 (telescopes K0, A1 and I1), the 100 m of effective distance can be applied: A1→I1, $B_{\rm proj}$ = 105.1 m, $\Delta\theta_{\rm disk}$ = 11° and K0→A1, $B_{\rm proj}$ = 127.4 m, $\Delta\theta_{\rm disk}$ = 34.6°. The third baseline, besides having a smaller size ($B_{\rm proj}$ = 46.6 m), was almost aligned to the stellar pole, where no phase shift is expected ($\Delta\theta_{\rm pole}$ = 3.8°).

Table 3.6 - Projected baselines for AMBER observations of HR 5907 (Rivinius et al., 2012).

Stations	$\|\vec{B}_{\rm proj}\|$ (m)	PA (deg)
K0→A1	127.4	-158.0
A1→I1	105.1	1.6
I1→K0	46.6	106.4

The observed phase shift can be estimated from the angular displacement of photocenter (Eq. 4.1, discussed in Chapter 4). Grunhut et al. (2012) show that the circumstellar emission of HR 5907 can be up to 15% brighter than the star at the Hα line profile. Assuming this brightness to Bracket γ Hydrogen line (Brγ, $\lambda_{\rm vac}$ = 21661.178 Å) and that the emission is concentrated in the co-rotation radius ($R \sim 2R_{\rm eq}$), this results in a photocenter shift of $\Delta p = 0.26$ stellar radius $\left(\Delta p = \frac{1\times0+0.15\times2}{1+0.15}R_*\right)$. This shift, applied to the values of HR 5907 (Table 3.3), results in a angular shift of 0.03 mas. This phase shift, seen by an interferometer of 100 m of projected baseline, yield a phase of ∼2.5°, what is roughly the observed value.

3.3.2 The minimization of the HR 5907 polarization curve

The MCMC minimization PDFs for HR 5907 polarimetric curve using the "dumbbell+disk" model are in Fig. 3.18 for $i \sim 60°$ and Fig. 3.19 for $i \sim 120°$. The mean $\chi^2_{\rm red}$ are 7.95 and 6.42, respectively. The best-fitting parameters are listed in Table 3.3. As discussed for HR 7355, we neglected the effects of stellar rotation on the modeling of HR 5907 due to its inclination angle ($i \sim 70°$).

Further polarimetric HR 5907 observations are been carried out at OPD/LNA in order to complete phase coverage and increase precision of the polarimetric signal. The derived polarimetric phase shift obtained $\delta = 0.08$ is very similar to the value found for σ Ori E, indicating an asymmetric magnetosphere. The low values found for circumstellar environment ($n_e \sim 1 - 3 \times 10^{12} M_\odot$) are likely the result of the irregular modulation seen in the data. Still, with the data available the MCMC constrain of the ISM polarization was compatible with field stars observations. The current minimization points at a lower density of magnetosphere by a factor of 1/2.5. The region of intersection of the magnetic field and rotational planes (the blobs) has a smaller factor, yielding a $2M_{\rm blob}/M_{\rm disk} \sim 0.8$, i.e., ∼ 20% lower than for σ Ori E.

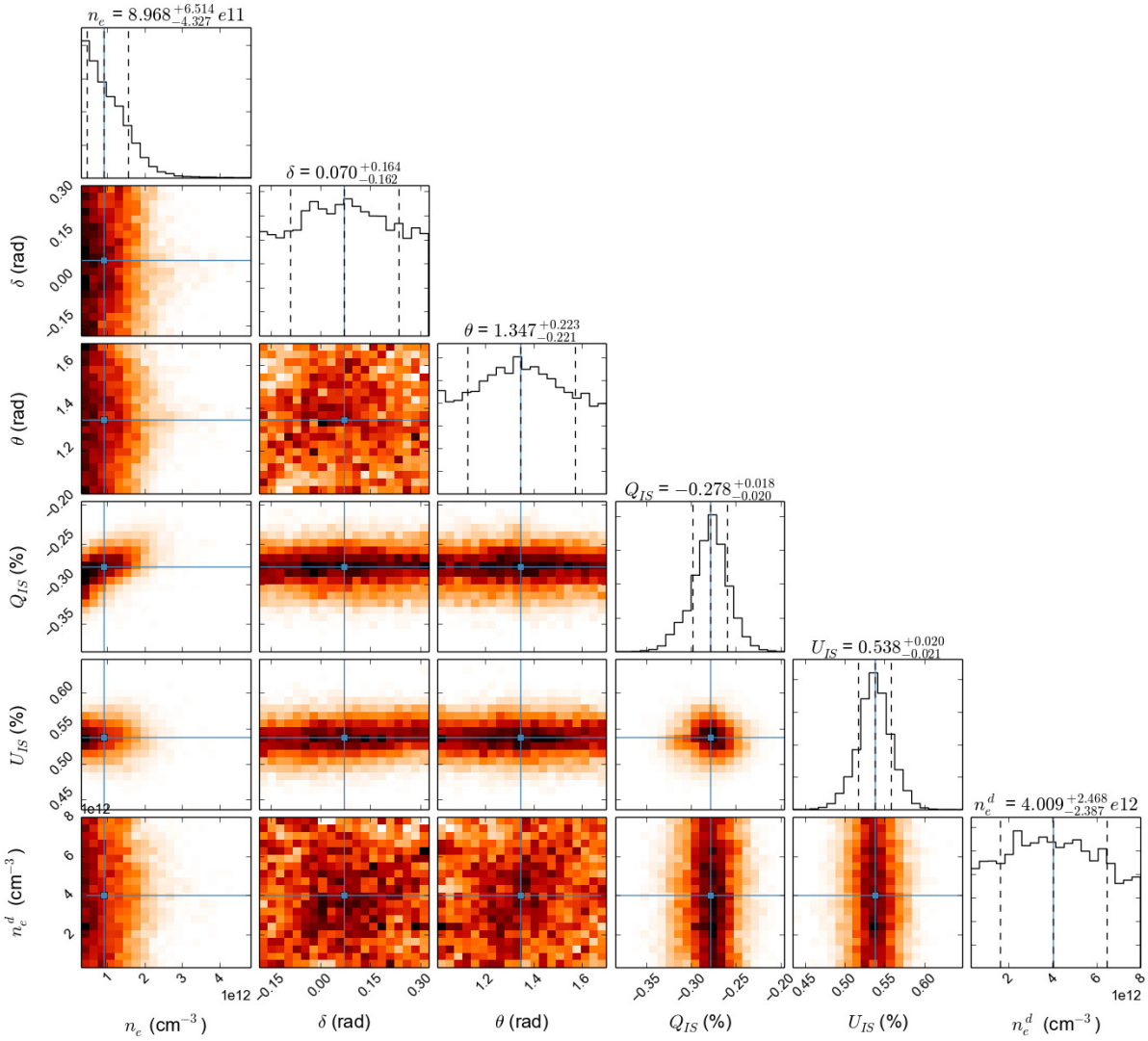

Figure 3.18: The MCMC probability density distributions for the "dumbbell+disk" polarization modeling to HR 5907 at $i = 70°$, and the corresponding correlation maps. The heat-like color map indicate the highest probabilities (black) to the lowest (white). *From left to right (or top-bottom):* inclination angle (rad), blob electronic density (cm^{-3}), phase shift, on-sky orientation angle (θ), the interstellar Q component (%), interstellar U component (%), the complementary angle between the rotation and magnetic axes (rad) and disk electronic density (cm^{-3}). The dashed vertical lines in the histograms indicate the percentile of 16% (-1σ), the median and the percentile of 84% (1σ) of each distribution.

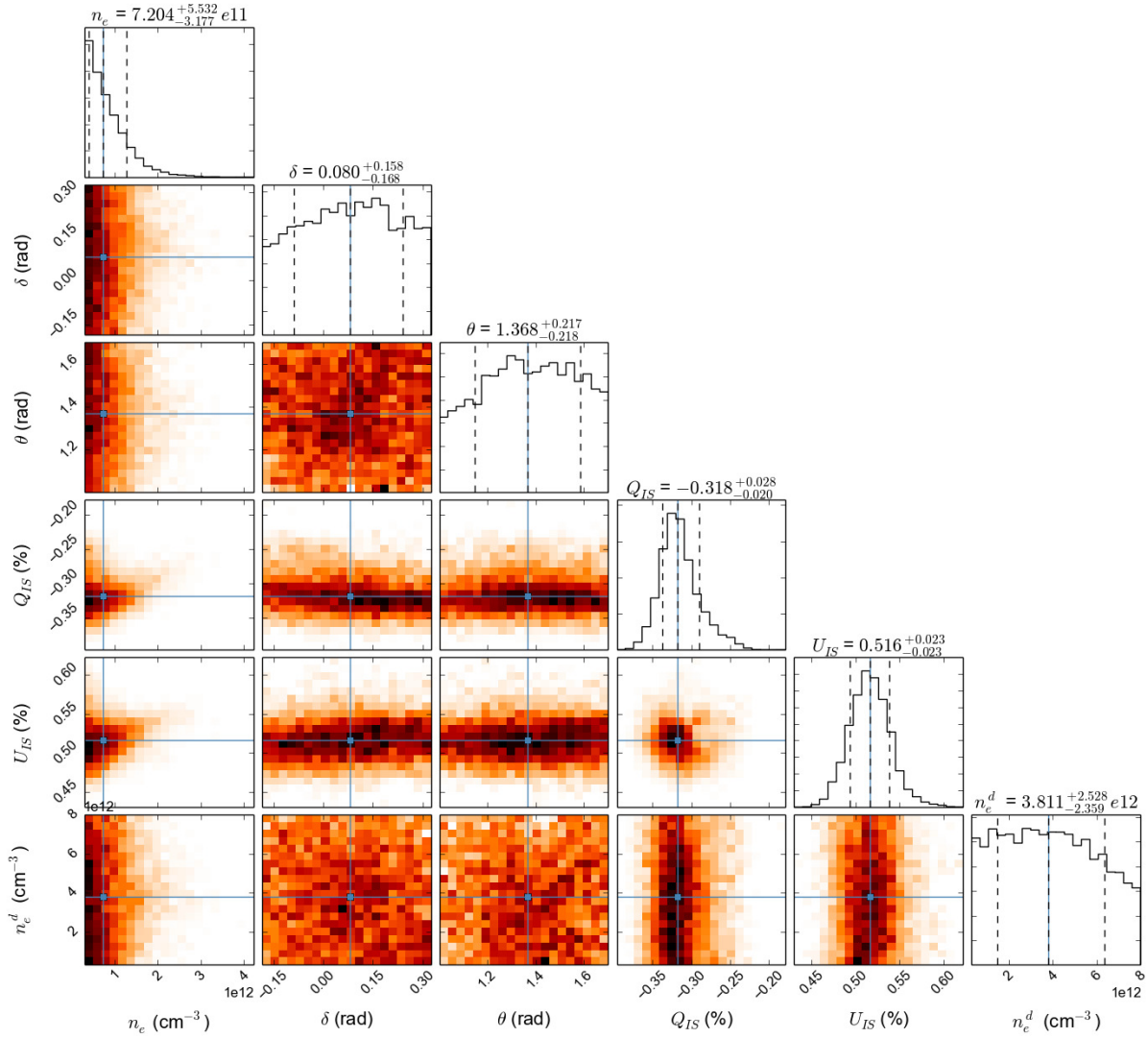

Figure 3.19: Same as previous figure, but for $i = 110°$.

3.4 Chapter summary

High-precision linear polarization measurements were carried out at the OPD/LNA (Brazil) for three hot magnetic stars that exhibit centrifugal magnetospheres: σ Ori E, HR 7355 and HR 5907. To σ Ori E, this resulted in the first firm detection of a magnetosphere in polarimetry, reported by Carciofi et al. (2013). Subsequently, this structure was also detected for the other two stars, a yet unpublished result and that we expect to publish soon.

Although RRM model is able to reproduce the shape of emission lines as well as the photometric depths of eclipses by the plasma clouds of magnetospheres, it fails at describing the detected polarization curves. For this reason, and the fact the densities of magnetospheres are low, we made a single scattering ad-hoc model based on the two main geometrical components predicted: two diametrically opposed blobs connected by a tilted disk.

Our dubbed "dumbbell+disk" model appeared as a useful tool to interpreted the polarization signal of the magnetospheres and determine their intrinsic physical parameters. In particular, we could determine the orientation of the σ Ori E system and the mass ratio of the blob vs. disk components $2M_{\rm blob}/M_{disk} \sim 1.0$, a value slight lower than previously determined by Carciofi et al. (2013) but that keeps the model interpretation, i.e., the inability of the RRM modeling simultaneously fit the photometric and the polarimetric light curves.

We show that two other magnetospheres, namely HR 5907 and HR 7355, have a polarimetric oscillation amplitude very similar to σ Ori E, although having a lower signal-to-noise lightcurve (Table 3.1). The absence of fast-rotating stellar effects in the polarization modeling appears to do not alter considerably simulations for $i \sim 70°$, the case of the analyzed stars. The low polarimetric signal prevented a precise determination of the magnetosphere parameters with MCMC minimization, such as the direction of rotation. Even so, an interesting result was obtained: HR 7355 displays $2M_{\rm blob}/M_{disk} \sim 1.1$, similar to σ Ori E, while HR 5907 has an lower $2M_{\rm blob}/M_{disk} \sim 0.8$ and overall scattering mass. This can be the result of the low S/N light curve or due to the obliqueness of the magnetic field with rotation, β: while σ Ori E and HR 7355 have $\beta \gtrsim 55°$, the rotation and magnetic axis of HR 5907 are almost coincident, with $\beta \sim 7°$.

Table 3.7 - List of hot magnetic stars observed in linear polarization in the survey at OPD/LNA.

Star	$V_{\rm mag}$	Star	$V_{\rm mag}$	Star	$V_{\rm mag}$
δ Ori C	6.85	HD 64740	4.61	τ Sco	2.81
θ^1 Ori C	5.13	HD 96446	6.68	HR 7355	6.02
σ Ori E	6.66	σ Lupi	4.42	HD 191612	7.84
HD 37776	6.98	HR 5907	5.40		
HD 57682	6.40	HD 148937	6.77		

The future perspectives are: (i) extend our polarimetric observation dataset of magnetic stars observable in the southern hemisphere (Table 3.7), having a comprehensive phase coverage for them; (ii) improve the scattering modeling to include stellar rotational effects, and improve HR 5907 and HR 7355 polarimetric model fitting; (iii) create an interface to feed the "dumbdell+disk" structure into HDUST, which does not employ the single scattering approximation and treats continuum opacity in addition to electron scattering. This allows to investigate the photometric light curve shape and its relation to the polarimetry.

The spatial information of the resolved magnestopheres provides constraints to analysis of magnetic field and the resulted trapped material around the rotating star. The magnestosphere geometry is directly related to fundamental stellar parameters, as field strength and configuration; angles between rotation and magnetic dipole axis; the role of the rotation velocity to shape the magnetosphere and to govern the mass flow through it; among many others. The relevance of here presented studies is to help constraining some of the parameters that drive this interaction between wind, field and rotation.

3.5 Publication: Polarimetric Observations of σ Ori E

The Astrophysical Journal Letters, 766:L9 (5pp), 2013 March 20 doi:10.1088/2041-8205/766/1/L9

POLARIMETRIC OBSERVATIONS OF σ ORIONIS E

A. C. Carciofi[1], D. M. Faes[1], R. H. D. Townsend[2], and J. E. Bjorkman[3]
[1] Instituto de Astronomia, Geofísica e Ciências Atmosféricas, Universidade de São Paulo, Rua do Matão 1226, Cidade Universitária, 05508-900 São Paulo, SP, Brazil; carciofi@usp.br
[2] Department of Astronomy, University of Wisconsin-Madison, Sterling Hall, 475 N. Charter Street, Madison, WI 53706, USA
[3] Ritter Observatory, Department of Physics & Astronomy, University of Toledo, Toledo, OH 43606, USA
Received 2013 February 5; accepted 2013 February 19; published 2013 March 5

ABSTRACT

Some massive stars possess strong magnetic fields that confine plasma in the circumstellar environment. These *magnetospheres* have been studied spectroscopically, photometrically, and, more recently, interferometrically. Here we report on the first firm detection of a magnetosphere in continuum linear polarization, as a result of monitoring σ Ori E at the Pico dos Dias Observatory. The non-zero intrinsic polarization indicates an asymmetric structure whose minor elongation axis is oriented 150.°0 east of the celestial north. A modulation of the polarization was observed with a period of half of the rotation period, which supports the theoretical prediction of the presence of two diametrally opposed, corotating blobs of gas. A phase lag of -0.085 was detected between the polarization minimum and the primary minimum of the light curve, suggestive of a complex shape of the plasma clouds. We present a preliminary analysis of the data with the Rigidly Rotating Magnetosphere model, which could not reproduce simultaneously the photometric and polarimetric data. A toy model comprising two spherical corotating blobs joined by a thin disk proved more successful in reproducing the polarization modulation. With this model we were able to determine that the total scattering mass of the thin disk is similar to the mass of the blobs ($2M_{\rm b}/M_{\rm d} = 1.2$) and that the blobs are rotating counterclockwise on the plane of the sky. This result shows that polarimetry can provide a diagnostic of the geometry of clouds, which will serve as an important constraint for improving the Rigidly Rotating Magnetosphere model.

Key words: circumstellar matter – polarization – stars: individual (σ Ori E) – stars: magnetic field

Online-only material: color figures

1. INTRODUCTION

The helium-strong star σ Orionis E (HD 37479; B2 Vpe; $m_V = 6.66$) has long been known to possess a circumstellar magnetosphere that is formed by wind plasma that is trapped by a strong dipolar magnetic field ($\approx$10 kG; Landstreet & Borra 1978). The presence of this magnetosphere can be inferred by the eclipse-like dimmings on its light curve, which is thought to occur when plasma clouds go in front of the star twice every rotation cycle (Townsend et al. 2005; Hesser et al. 1977; Groote & Hunger 1982). This star has been the testbed for important advancements in our theoretical understanding of these magnetospheres. The Rigidly Rotating Magnetosphere (RRM) models of this star were successful in reproducing the observed variability in emission line profiles and photometry (Townsend et al. 2005).

Polarization is a very useful technique that allows one to probe the geometry of the circumstellar scattering material without angularly resolving it (e.g., Brown & McLean 1977). Kemp & Herman (1977) carried out the first polarimetric observations of the σ Ori system, but their results where largely inconclusive because of the small values of the intrinsic polarization. In this Letter we present the results of high-precision ($\sigma \sim 0.01\%$) polarization monitoring of σ Ori E, which has resulted in the first firm detection of the polarization modulation produced by a corotating magnetosphere.

2. OBSERVATIONS

Broadband linear polarization data were obtained from 2010 August to 2011 September, using the IAGPOL image polarimeter attached to the 0.6 m Boller and Chivens telescope at Pico dos Dias Observatory (OPD/LNA). We used a CCD camera with a polarimetric module described in Magalhães et al. (1996), consisting of a rotating half-wave plate and a calcite prism placed in the telescope beam. In each observing run at least one polarized standard star was observed in order to calibrate the observed position angle. HD 23512 and HD 187929 were used as polarized standards.

Although typical polarimetric observations consists of eight consecutive wave plate positions (hereafter WPP) separated by 22.°5 (Carciofi et al. 2007), in this work we chose to use 16 consecutive WPPs in order to increase the signal-to-noise ratio. Also, to reach the high accuracy needed to monitor the modulation of the polarization, a large number of frames (typically from 20 to 100) were obtained at each WPP. Since the exposure times ranged from 0.3 to 1 s per frame, the temporal resolution of our observations varies from 7 to 34 minutes, including telescope and instrument overheads. These values are short enough to temporally resolve the polarimetric variation over the 1.19-day period of the star. Details of the data reduction can be found in Magalhães et al. (1984).

3. INTERSTELLAR POLARIZATION

Kemp & Herman (1977) report similar values of the polarization for σ Ori AB, σ Ori C, and σ Ori D, which suggests that all these stars belong to the same physical system, and that the measured polarization is of interstellar (IS) origin.

We measured the *BVRI* polarization of σ Ori AB and C and our results are largely consistent with the ones of Kemp & Herman (1977). We used our measured V-band polarization of σ Ori AB ($P = 0.351(15)\%$; 86.°7; $Q = -0.348(15)\%$; $U = 0.040(15)\%$) as an estimate of the IS polarization toward σ Ori E.

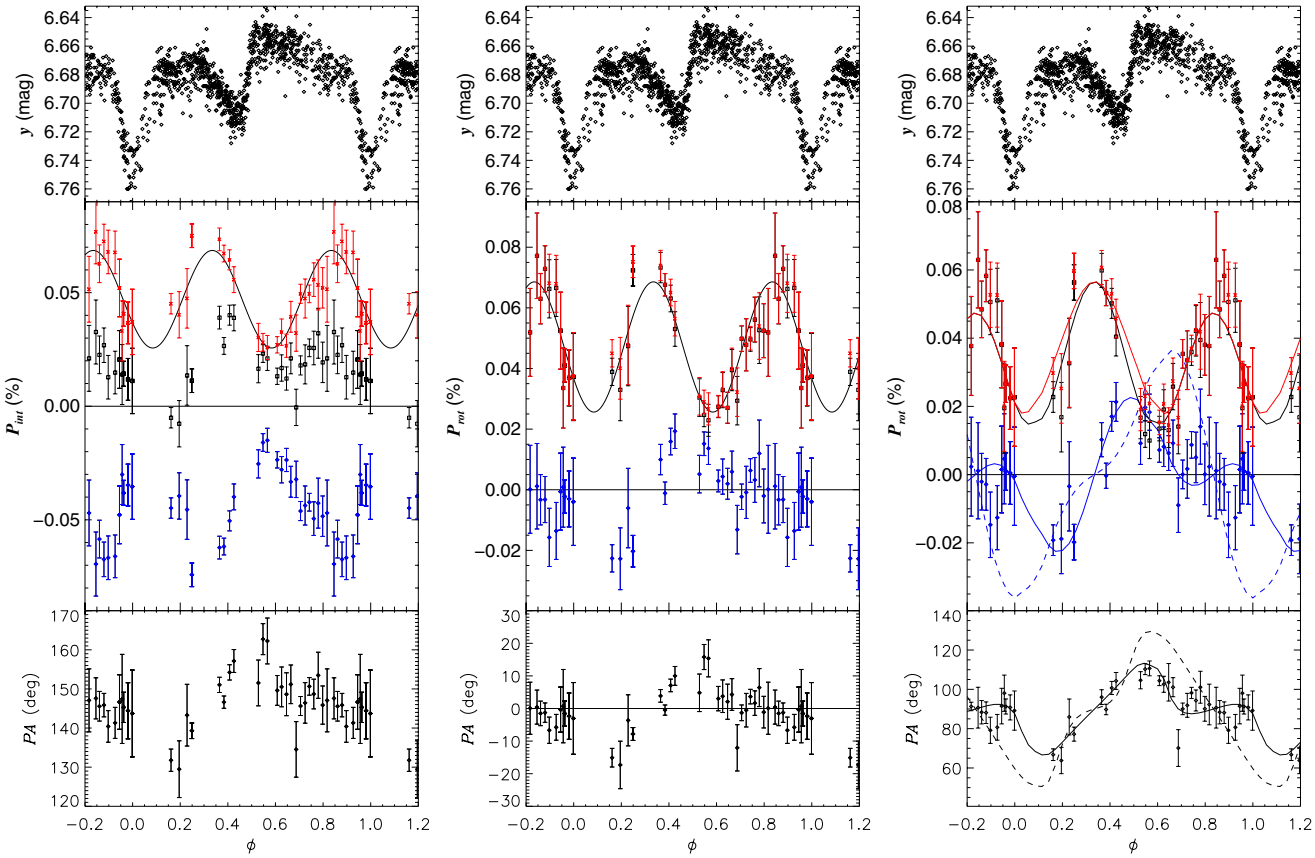

Figure 1. Variation of the intrinsic polarization of σ Ori E compared with photometric variations in the y filter. Top panels: y filter photometric data from Hesser et al. (1977), folded in phase. Middle panels: intrinsic P (red), Q (black), and U (blue). Bottom panels: intrinsic position angle. Left plot: the polarization data are displayed in the equatorial reference frame. The polarization of σ Ori AB was used as a measure of the IS polarization. Middle plot: same as the left plot, rotated such that $\langle U_{\rm int}\rangle = 0$. Right plot: polarization compared to the single-scattering model. The solid line is for our best-fitting model with $i = 70^\circ$ and the dashed line is for $i = 110^\circ$. For this plot we used the estimate for the IS polarization and θ made in Section 6.

(A color version of this figure is available in the online journal.)

4. RESULTS

The V-band σ Ori E observations are shown in the left plot of Figure 1. The data were folded in phase (ϕ) using the ephemerides of Townsend et al. (2010). Shown is the intrinsic polarization, calculated by subtracting the IS polarization, estimated using σ Ori AB, from the observed Q and U Stokes parameters. The polarization has a double-peaked structure, with maxima of about 0.07% occurring at phases around 0.3 and 0.8 and minima occurring around phases 0.1 and 0.6. We note that the values reported here are in broad agreement with the data of Kemp & Herman (1977), but a more quantitative comparison is hampered by the insufficient accuracy of the latter data.

There is a clear anti-correlation between the photometric and polarimetric variations, with the polarization minima roughly coinciding with the photometric maxima and vice versa, but there are important differences between the two curves. One such difference lies in their symmetry: the photometry is clearly asymmetric, with the secondary minimum occurring at about phase 0.4 (the primary minimum occurs at $\phi = 0$ by definition), and the behavior of the two inter-minima being very different from each other. The polarization curve, however, seems to be roughly symmetric with respect to $\phi \approx 0.6$. That the asymmetry is seen in the photometry but not in the polarization is further supporting evidence that—as hypothesized in Townsend et al. (2005)—the asymmetric light curve arises due to contamination of the circumstellar signal by a photospheric signal. That is, the photometric variations come from a combination of magnetospheric eclipses and photospheric abundance inhomogeneities, and therefore lack rotational symmetry; but conversely, because the polarization variations come solely from magnetospheric electron scattering, we do see rotational symmetry in their case.

In order to determine the location of the polarization minimum, we fitted the data between $\phi = 0.45$ and 0.75 with a parabola, using the Levenberg–Marquardt algorithm (Marquardt 1963). We find that the minimum of the intrinsic polarization occurs at $\phi_{\rm min} = 0.61 \pm 0.03$. To determine the location of the maximum, the same procedure was applied to the data between $\phi = 0.7$ and 1. According to this fit the maximum of the polarization occurs at $\phi_{\rm max} = 0.84 \pm 0.04$.

To further assess the symmetry of the data, we fitted the polarization data with the following function:

$$P(\phi) = P_0 + A\cos[4\pi(\phi - \delta)], \quad (1)$$

which implicitly assumes a period of half of the orbital period for the polarimetric data. The result of the fit gives $P_0 = 0.0471\% \pm 0.0009\%$, $A = 0.021\% \pm 0.001\%$, and $\delta = -0.17 \pm 0.01$, with a reduced $\chi^2 = 0.67$. The fitted function is displayed as the black line in the middle plot of Figure 1.

The data seem to be well represented by Equation (1), which indicates that, contrary to the photometry, the polarization curve

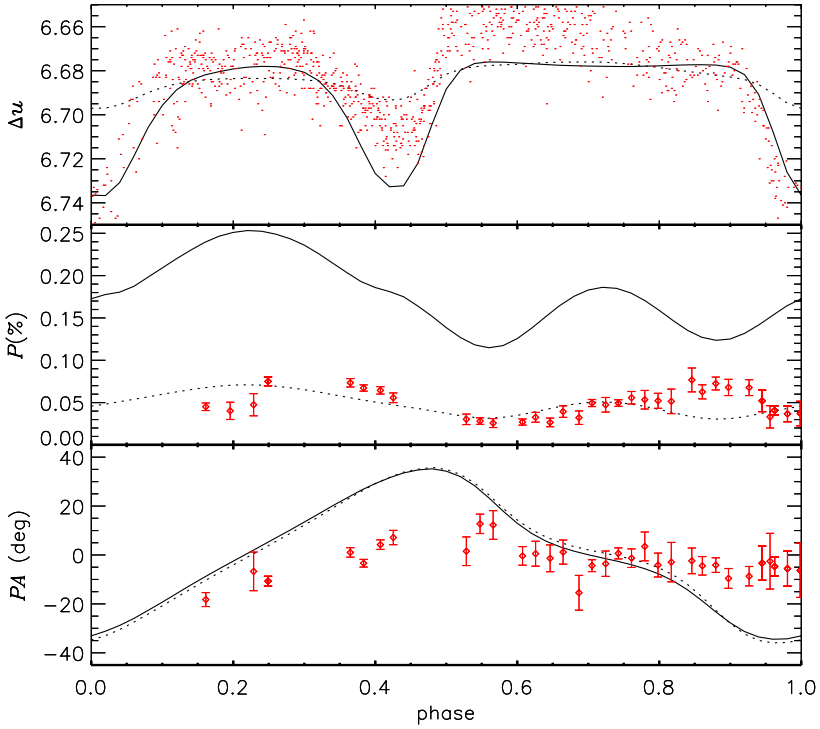

Figure 2. Modeling of the intrinsic polarization of σ Ori E using the RRM model (observations are in red). The only free parameter is the maximum number density in the magnetosphere, which was set to 10^{12} cm^{-3} (solid lines) to reproduce the depth of the eclipses and 2.5×10^{11} cm^{-3} (dotted lines) to reproduce the amplitude of the linear polarization.

(A color version of this figure is available in the online journal.)

is roughly symmetric. From Equation (1), the positions of the minima are $\phi = 0.08$ and 0.58, and the maxima are at $\phi = 0.33$ and 0.83. Those values are in good agreement with the phases derived above via a parabola fitting. The minimum and maximum values of the polarization are, respectively, $P_0 - A = 0.026\% \pm 0.001\%$ and $P_0 + A = 0.068\% \pm 0.001\%$.

An important feature of the intrinsic polarization of σ Ori E is that it is never zero. This indicates that there is some degree of asymmetry of the scattering material (as seen projected onto the plane of the sky) throughout the entire rotation period.

The data shown in the left plot of Figure 1 are in the equatorial frame. The weighted average of all the data gives a value of $\langle Q_{\rm int} \rangle = 0.023\%$ and $\langle U_{\rm int} \rangle = -0.040\%$, which, in turn, results in an average position angle of $\langle \theta_{\rm int} \rangle = 150\overset{\circ}{.}0$. This value tells us the (average) direction of the minor axis of the asymmetric structure. Furthermore, the small variation of the position angle (Figure 1, left) tells us that the direction of the minimum elongation axis changes little ($\approx 10^\circ$–15°, at most) as the star rotates.

This last point is better understood if we rotate the intrinsic polarization by $\langle \theta_{\rm int} \rangle$ so that the average value of U is zero (Figure 1, right plot). In this new frame, we see that the amplitude of the rotational modulation of U is small. If we assume that the symmetry axis is parallel to the rotation axis, we conclude that the projected axis of symmetry of the magnetosphere varies little as the star rotates. As discussed below, this has quite important consequences for the RRM model.

Another noteworthy feature of the polarization curve is that there is a phase shift of -0.085 between the primary minimum of the light curve and the polarization minimum. The RRM model of Townsend et al. (2005) predicts the existence of two plasma clouds corotating with the star. If the clouds were symmetrical and the photospheric fluxes were homogeneous, there should be no phase difference between the polarization and photometric curves; the observed phase shift, therefore, is likely a result of cloud asymmetries and photospheric abundance inhomogeneities.

5. RRM MODEL

Townsend et al. (2005) applied the RRM model to σ Ori E with good success. This model predicts the accumulation of circumstellar plasma in two corotating clouds, situated in magnetohydrostatic equilibrium at the intersections between the magnetic and rotational equators. Comparison with the available data (photometry and Hα line profiles) showed that the model provided a good quantitative description of the circumstellar environment.

In an attempt to reproduce the observed polarization modulation of σ Ori E, we fed the predicted density distribution of the RRM model of Townsend et al. (2005) to the HDUST radiative transfer code (Carciofi & Bjorkman 2006). Since all stellar and geometrical parameters were taken from Townsend et al. (2005), the only free parameter in the model is the density scale of the magnetosphere.

The results of this modeling are shown in Figure 2. We could not find a model that simultaneously matched both the photometry and the polarimetry. A higher density model (solid line) that matches the depth of the photometric eclipses predicts a polarization amplitude that is three times larger than what is observed. Conversely, a lower density model that reproduces the amplitude of the polarization fails to reproduce the photometric amplitude.

Furthermore, the detailed shape of the polarization curve, in particular the position angle variation, is not well matched. Since the polarization position angle is sensitive to the geometry of the scattering material, this discrepancy indicates that the primary

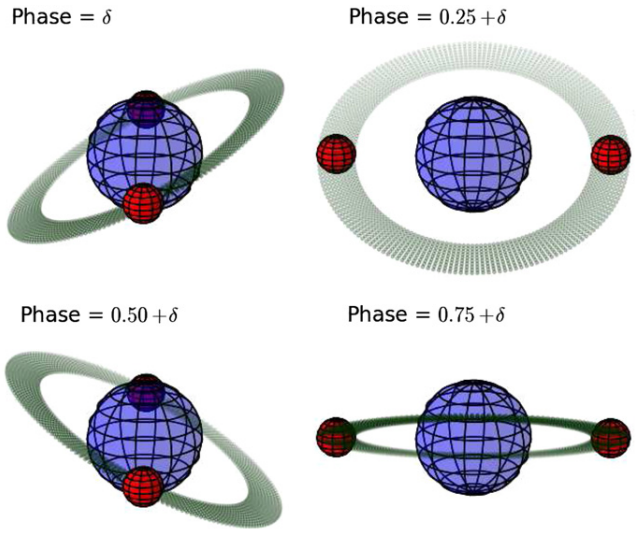

Figure 3. Geometric conception of the "dumbbell + disk" model to scale.
(A color version of this figure is available in the online journal.)

difficulty with the basic RMM model is the shape of its density distribution.

6. SINGLE-SCATTERING MODEL

We now explore what changes must be made to the basic RRM model to better reproduce the shape of the polarimetric variability. The RRM predicts the existence of diametrally opposed plasma clouds confined in the rotational equator and a diffuse plasma disk close to the magnetic equator. Based on this idea, we developed a simple toy model for σ Ori E that consists of two elements: (1) a thin uniform disk tilted by an angle ψ from the rotational equator and (2) a pair of spherical blobs situated in the equatorial plane at the intersection between this plane and the magnetic equator, thus forming a "dumbbell-like" structure. This configuration is illustrated in Figure 3, for several orbital phases and for a viewing angle of 70°.

Since the polarization is small, we may perform the calculation of the Q and U Stokes parameters as a function of orbital phase for a given inclination angle i following a simple single-scattering approach (valid only in the optically thin limit). The scattered flux is first determined in the frame of the star using the formalism described in Bjorkman & Bjorkman (1994, Equation (6)) and then rotated to the frame of the observer (Bjorkman & Bjorkman 1994, Equation (20)).

For this initial study, we adopted five fixed parameters, listed in Table 1, whose values were based on the models of Townsend et al. (2005). They are the stellar radius, $R_\star$, the distance of the blobs from the star, d_b, the size of the blobs, R_b, the geometrical thickness of the disk, H_d, and the inclination angle, i. The adopted value for R_blob is somewhat arbitrary, since in the limit of $R_\mathrm{blob} \ll R_\star$ and in the single-scattering approximation, a large, tenuous blob is roughly equivalent to a dense, small blob. For the same reason, the disk geometrical thickness is also somewhat arbitrary: if the single-scattering approximation holds, a thinner, denser disk is equivalent to a thicker, less dense disk. In other words, what really controls the polarization level of each component is their total scattering mass. For the inclination angle we adopt two possible values: $i = 70°$, corresponding to a projected counterclockwise rotation of the blobs on the sky and $180°–70° = 110°$, corresponding to a clockwise rotation.

Table 1
Parameters of the Single-scattering Model

Parameter	Value	Type
i (deg)	70 or 110	Fixed
$R_\star$ ($R_\odot$)	4.3	Fixed
d_b ($R_\star$)	2.4	Fixed
R_b ($R_\star$)	1/3	Fixed
H_d ($R_\star$)	0.01	Fixed
n_e^b (e^- cm^{-3})	$1.0^{+0.6}_{-0.9} \times 10^{12}$	Fitted
n_e^d (e^- cm^{-3})	$2.7 \pm 1 \times 10^{12}$	Fitted
ψ (deg)	28	Fitted
Q_IS(%)	-0.35 ± 0.01	Fitted
U_IS (%)	0.025 ± 0.010	Fitted
θ (deg)	150 ± 7	Fitted
δ	-0.17 ± 0.02	Fitted

In this analysis we made *no previous assumptions about the IS polarization*, i.e., we fitted directly the observed Q and U Stokes parameters. The adopted modeling procedure is as follows.

1. Choose values for electron number density in the blob and disk (n_e^b and n_e^d), the phase lag, δ, between the photometric primary minimum ($\phi = 0$) and the orbital phase where the blobs are aligned with the line of sight, the tilt angle of the disk, ψ, and the position angle of the equatorial plane in the plane of the sky, θ. These five parameters define a unique model for the intrinsic Q and U in the equatorial frame.
2. Choose values for Q_IS and U_IS and use them to calculate synthetic observed Q and U parameters.
3. Calculate the reduced χ^2 of the model.
4. Repeat steps 1 and 3 for several hundred of values for the seven free parameters and choose the model with minimum χ^2.

The parameters of our best-fitting model (reduced $\chi^2 = 2.8$) are listed in Table 1. The estimated errors are for a 95% confidence interval. A notable result is that the IS polarization, independently obtained by this analysis, is consistent (within the errors) with the estimate made using σ Ori AB as a measure of the IS. Both the orientation of the equatorial plane in the sky (θ) and the phase lag (δ) are consistent with the estimate made in Section 4. The resulting blob density corresponds to an electron optical depth of $\tau = 0.13$, which does not violate the optically thin assumption. It is worth mentioning that our estimate for the electron density in the blobs, $10^{12}\ e^-$ cm^{-3}, is in good agreement with the values derived by Groote & Hunger (1982) and Smith & Bohlender (2007) using the Inglis–Teller formula. From the best-fitting parameters one can calculate the mass of each model component. Assuming a molecular weight of 0.6, which corresponds to a fully ionized gas with solar chemical composition, the mass of each blob is $M_\mathrm{b} = 6.0 \times 10^{-12}\ M_\odot$ and the mass of the disk is $M_\mathrm{d} = 1.0 \times 10^{-11}\ M_\odot$. Therefore, we obtain that both components have similar masses ($2M_\mathrm{b}/M_\mathrm{d} = 1.2$).

In Figure 1 (right plot), we show the observations corrected by the IS polarization of Table 1. The solid curves correspond to the best-fitting single-scattering model. The two minima of the model polarization occur at the phases for which the two blobs are aligned with the line of sight. At these phases, the model Q parameter is the minimum and the U parameter is the maximum (negative for $\phi \approx \delta$ and positive for $\phi \approx 0.5 + \delta$), because the disk dominates the polarized flux at these phases. Conversely, the polarized flux is dominated by the blobs at the phases at

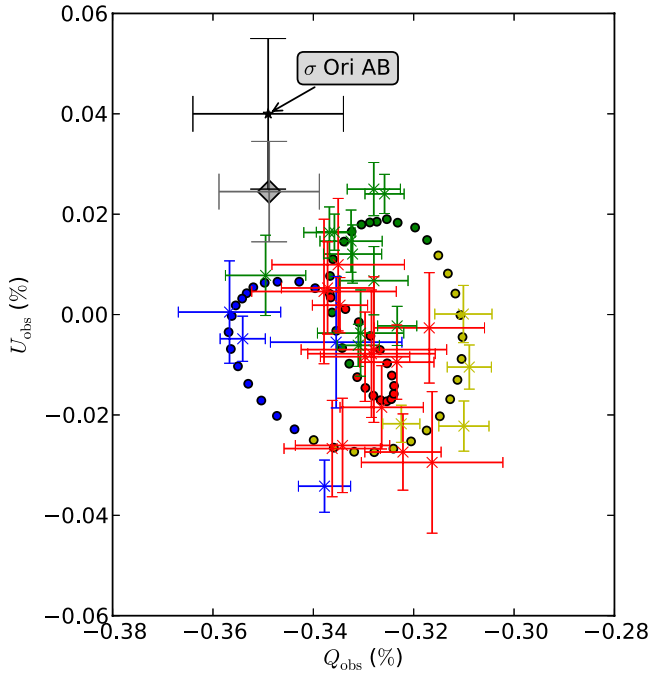

Figure 4. QU plot of the observed data (points with error bars). The orbital phase correspondence of the points is as follows: blue, δ–($\delta + 0.25$), orange, ($\delta+0.25$)–($\delta+0.50$), green, ($\delta+0.50$)–($\delta+0.75$), and red, ($\delta+0.75$)–δ. The filled circles show the best-fitting model of Table 1. The IS polarization of σ Ori AB is indicated. The gray diamond shows the IS of Table 1.

which the blobs are on the side of the star ($\phi \approx 0.25 + \delta$ and positive for $\phi \approx 0.75 + \delta$).

An interesting result is that the data allowed us to firmly establish that the blobs are rotating counterclockwise on the plane of the sky. In the right plot of Figure 1, the solid curves show the best-fitting model for $i = 70^\circ$ (reduced $\chi^2 = 2.8$) while the dotted curves correspond to the best-fitting model with $i = 110^\circ$ (reduced $\chi^2 = 5.1$). The former is clearly a much better fit to the data.

An alternative comparison between the data and the single-scattering model is made in Figure 4, where we plot the observed (i.e., uncorrected for IS polarization) U versus Q parameters. The blue points correspond to the phase range δ–($\delta + 0.25$), the orange ones from ($\delta + 0.25$)–($\delta + 0.50$), the green ones from ($\delta + 0.50$)–($\delta + 0.75$), and the red ones from ($\delta + 0.75$)–δ. In the QU plane the behavior of the data is quite different from the first half-cycle to the second: while in the first half (blue and orange points) the data forms a nearly circular outer loop, in the second half (green and red points) there is an inward incursion. The model reproduces this behavior.

It is important to point out that the two-component model (blob+disk) adopted by us is required to produce such a behavior in the QU plane. For instance, a model with only the blobs would form a symmetric double ellipse in the QU plane, while a model with only the tilted disk would result in a shape resembling a crescent moon. The observed curve, composed of an outer loop and an inner incursion, can only be obtained by a combination of these two components.

7. CONCLUSIONS

The polarimetric data presented here for σ Ori E have an accuracy of at least one order magnitude better than those shown in the work of Kemp & Herman (1977) and thus represent the first firm detection of the polarization modulation of a corotating magnetosphere. The intrinsic polarization, calculated using σ Ori AB as a measure of the IS polarization, displays a roughly symmetric sinusoidal curve ranging from 0.02% to 0.08%, with a period of half of the orbital period and a phase lag of -0.085 between the polarization minimum and the primary minimum of the light curve. The polarization position angle is also variable. Its mean value of 150.°0 indicates that the minor elongation axis of the asymmetric structure around σ Ori E is oriented 150.°0 east of the celestial north.

A preliminary analysis made with the RRM model (Townsend et al. 2005) suggests that it is difficult to fit both the photometry and the polarization simultaneously. This seems to imply that the geometry of the plasma clouds, as predicted by the current version of the model, is incorrect.

However, the data were well reproduced by a two-component model, consisting of two spherical, diametrally opposed blobs and a disk tilted with respect to the rotational equator. This model was physically motivated by the RRM model, which predicts accumulation of centrifugally supported wind plasma in a disk-like structure with the highest densities (corresponding to the blobs) at the points where the magnetic equator intersects the rotational equator. This model provided useful constraints on the total scattering mass of each component. Also, it provided an independent estimate for the IS polarization, as well as for the orientation of the equatorial direction in the plane of the sky. Our best-fitting model suggests that the mass of each blob is $M_{\rm b} = 0.6 \times 10^{-12}\, M_\odot$ and the mass of the disk is $M_{\rm d} = 1.0 \times 10^{-11}\, M_\odot$, which indicates that both components have similar masses ($2M_{\rm b}/M_{\rm d} = 1.2$). Also, the tilt angle of the disk with respect to the plane of the sky is 28°, similar to the angle between the rotational and magnetic axes (Townsend et al. 2005). Finally, the model allowed us to determine that the blobs are rotating counterclockwise on the plane of the sky.

A.C.C. acknowledges support from CNPq (grant 308985/2009-5) and Fapesp (grant 2010/19029-0). D.M.F. acknowledges support from FAPESP (grant 2010/19060-5). R.H.D.T. acknowledges support from NSF grants AST-0908688 and AST-0904607, and NASA grant NNX12AC72G. This work has made use of the computing facilities of the Laboratory of Astroinformatics (IAG/USP, NAT/Unicsul), whose purchase was made possible by the Brazilian agency FAPESP (grant 2009/54006-4) and the INCT-A.

REFERENCES

Bjorkman, J. E., & Bjorkman, K. S. 1994, ApJ, 436, 818
Brown, J. C., & McLean, I. S. 1977, A&A, 57, 141
Carciofi, A. C., & Bjorkman, J. E. 2006, ApJ, 639, 1081
Carciofi, A. C., Magalhães, A. M., Leister, N. V., Bjorkman, J. E., & Levenhagen, R. S. 2007, ApJL, 671, L49
Groote, D., & Hunger, K. 1982, A&A, 116, 64
Hesser, J. E., Ugarte, P. P., & Moreno, H. 1977, ApJL, 216, L31
Hesser, J. E., Ugarte, P. P., & Moreno, H. 1977, ApJL, 216, L31
Kemp, J. C., & Herman, L. C. 1977, ApJ, 218, 770
Landstreet, J. D., & Borra, E. F. 1978, ApJL, 224, L5
Magalhães, A. M., Benedetti, E., & Roland, E. H. 1984, PASP, 96, 383
Magalhães, A. M., Rodrigues, C. V., Margoniner, V. E., Pereyra, A., & Heathcote, S. 1996, in ASP Conf. Ser. 97, Polarimetry of the Interstellar Medium, ed. W. G. Roberge & D. C. B. Whittet (San Francisco, CA: ASP), 118
Marquardt, D. 1963, SJAM, 11, 431
Smith, M. A., & Bohlender, D. A. 2007, A&A, 475, 1027
Townsend, R. H. D., Oksala, M. E., Cohen, D. H., Owocki, S. P., & ud-Doula, A. 2010, ApJL, 714, L318
Townsend, R. H. D., Owocki, S. P., & Groote, D. 2005, ApJL, 630, L81

3.6 Publication: The interferometric signature of the rapidly corotating magnetosphere of HR 5907

The Interferometric Signature of the Rapidly Corotating Magnetosphere of HR 5907[1]

Th. Rivinius*, A. C. Carciofi†, J. Grunhut**, G. Wade**, D. Baade*, S. Štefl* and D. M. Faes†

*ESO - European Organisation for Astronomical Research in the Southern Hemisphere, Chile & Germany
†Instituto de Astronomia, Geofísica e Ciências Atmosféricas, Universidade de São Paulo, Brazil
**Royal Military College, Kingston, Canada

Abstract. We report on interferometric AMBER/VLTI observations of the magnetic B2Vn star HR 5907 to detect the signature of the co-rotating magnetically-bound plasma. We obtained the first ever successful interferometric observation of magnetically bound material.

Keywords: Stars: mass loss; Stars: magnetic fields, Stars: individual: HR5907
PACS: 97.10.Fy; 97.10.Ld

INTRODUCTION

HR 5907 is a very rapidly rotating B2V star ($P = 0.508\,\mathrm{d}$, $v \sin i = 280\mathrm{km\,s^{-1}}$) that was recently detected to host a several kilogauss magnetic field [1]. Spectroscopic and polarimetric data show that the star has corotating circumstellar material, meaning the magnetic field dominates the circumstellar environment.

Judging from the Balmer and Paschen line emission of HR 5907, the outer extent of the magnetosphere is about three to four stellar radii (since for rigid corotation $v_{\max} = R_{\max} \times v \sin i$). Taking preliminary stellar parameters derived from the spectroscopic data ([2], in particular: $R_\star \approx 3$ to $4 R_\odot$) and the Hipparcos parallax of 8 mas, this translates to a photosperic diameter of about 0.15 mas and a dimension of the magnetosphere of 0.5 to 0.7 mas. As we expect magnetospheric emission to be of the order of 10% of the photospheric emission for Brγ (from the Balmer emission and decrement), this introduces a maximum shift of the observed photocenter in the emission lobes vs. the adjacent continuum of the order of 40 to 90 as red and bluewards of this line at quadrature, respectively. At baselines of about 100 meters in the K-band, this corresponds to about 5 to 10° interferometric phase shift, which is at the detection limit for the AMBER instrument [3] at the VLTI for a 5th magnitude star. A signature in visibility is not expected, since the circumstellar structure is too small to be resolved considering the observational errors.

[1] Based on observations collected at the European Organisation for Astronomical Research in the Southern Hemisphere, Chile, under program-ID 087.D-0133.

Stellar Polarimetry: From Birth to Death
AIP Conf. Proc. 1429, 102-105 (2012); doi: 10.1063/1.3701910

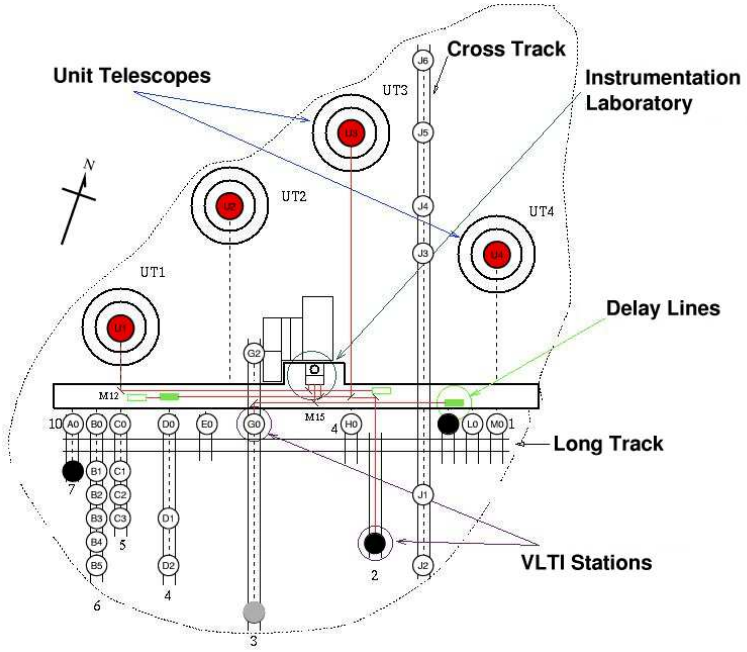

FIGURE 1. Site layout of the VLTI stations. Plannend were AT stations A1–G1–K0, actually used were stations A1–I1–K0 (filled black, G1 filled light grey). From `www.eso.org`.

OBSERVATIONS

Interferometric observations were carried out with AMBER, fed by the VLTI Auxiliary Telescopes (1.8m), scheduled for the nights of 2011 April 6/7 and April 22/23, with three hours in each of the two nights. The strategy was to detect the photocenter shift in the line vs. the continuum for two rotational phases seperated by 0.5 cycles, to have the emissive structure in different positions with respect to the star. The requested baseline triangle was A1–G1–K0.

The first epoch was entirely lost to bad weather, with all telescopes of the observatory closed. The second epoch was more fortunate: the fringe tracker FINITO [4] delivered a perfect stabilization for about 1h, but then degraded due to degrading seeing/coherence time. We note, however, that the object is at the brightness limit of the instrument, requiring exceptionally good conditions for stabilization. Due to technical problems on station G1, we had to use station I1, effectively rendering the baseline K0–I1 useless due to its insufficient length for our purpose. In turn, the other two baselines K0→A1 and A1→I1 were now similar enough to confirm each other's result (with inverse sign, due to the way baselines are associated to stations in the reduction process, see Fig. 1 for the station layout on Paranal).

In addition, we obtained linear broad-band polarization data, using the IAGPOL image polarimeter attached to the 0.6-m Boller & Chivens telescope at OPD/LNA in Brazil. In each observing run at least one polarized standard star was observed to calibrate the observed position angle. The interstellar contribution was estimated with the nearby field stars HR 5906 and HD 142705.

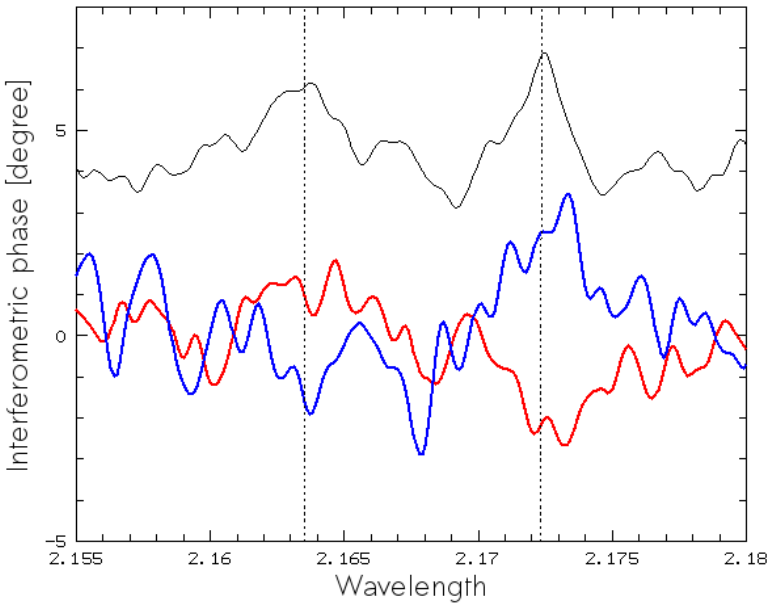

FIGURE 2. Upper profile: flux observed by AMBER across the Brγ line (scaled and filtered with a 5 pixel Gaussian for display). The emission peaks correspond to those seen in Hα at that rotational phase. Lower profiles: Filtered interferometric phase for baselines K0→A1 and A1→I1. An interferometric phase signal of the order of about 3° is seen at the position of the red emission peak, one of about 1.5° going into the other direction for the blue peak.

RESULTS

Due to the unfavourable conditions, we collected only about 1/4 of the data expected, in East-West baseline orientations. The signal in these baselines is weaker than expected, but clearly detected as different from the noise in the surrounding continuum (see Fig. 2). Since both baselines are largely parallel and of similar length, they are of limited use in constraining the actual orientation and shift of the photocenter on sky.

The polarimetric data can be used to circumvent this to some extent: The polarization angle, which is essentially E–W as well (Fig. 3), points to an elongated structure largely N–S oriented. This means that the observed baselines were approximately perpendicular to the structure, and the observed projected photocenter shifts are much smaller than the real ones on sky. The rotational phase, $\phi = 0.47$, indicates we observed the system around maximum elongation, so that the smaller signal than expected, only about half, is due to geometric projection only, and the real signal on sky might even be larger than originally estimated.

CONCLUSIONS

We have detected a photocenter shift of about 25 as and -12 as for the red and blue Brγ peak emission, respectively, in E–W direction at rotational phase $\phi = 0.47$. Unfortunately, the position angle of the elongated structure could not be constrained inter-

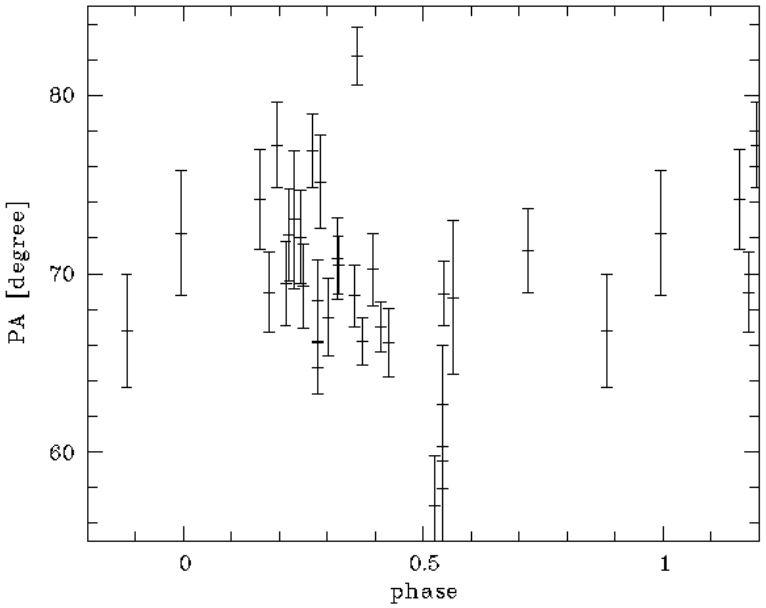

FIGURE 3. Phased polarization position angle of HR 5907.

TABLE 1. Projected baselines used for observations.

Stations	projected length	projected PA (N→E)
K0→A1	127.4 m	−158°
A1→I1	105.1 m	1.6°
I1→K0	46.6 m	−106.4°

(I1→K0 too short to show expected signal)

ferometrically (data quality not high enough, third baseline missing), but polarimetry suggests observed baselines were quite off from a structure that is elongated more in the N–S direction (perpendicular to the polarization PA).

Notwithstanding these challenges, these observations resulted in the first interferometric detection of a magnetically bound and centrifugally supported magnetosphere. To constrain a model for this structure interferometrically, further observations with more favourable baselines and probably bigger telescopes will be needed, as the observations were clearly magnitude limited.

REFERENCES

1. J. Grunhut, et al., "Discovery of the shortest rotational period, non-degenerate, magnetic massive star by the MiMeS Collaboration" in *Active OB Stars*, edited by C. Neiner, G. Wade, G. Meynet, and G. Peters, *IAU Symposium* **272**, Cambridge Journals, 2011, pp. 186–187.
2. J. Grunhut, et al., *MNRAS* in press, (2011).
3. R.G. Petrov, et al., *A&A* **464**, pp. 1-12 (2007).
4. M. Gai, et al., "The VLTI Fringe Sensors: FINITO and PRIMA FSU" in New Frontiers in Stellar Interferometry, edited by W.A. Traub, *SPIE Proc.* **5491**, Glasgow, 2004, pp. 528-539.

Chapter 4

Spectrointerferometry applied to the Be star disks

Spectrointerferometry is sensitive to the brightness distribution in narrow spectral channels of a given target. This can be used to relate the velocity with the angular position of the emission, and may map the velocity profile of a rotation system. Indeed, the detailed measurements that have demonstrated that Be disks rotate in a Keplerian fashion made use of this technique (Meilland et al., 2007; Kraus et al., 2012; Wheelwright et al., 2012).

An important feature of spectrointerferometry that needed to be investigated was departures from the expected differential phases (DP) of Be stars, which are discussed below. As and example, Kraus et al. (2012) reported that a phase reversal was registered at the DP signal of the Be star β CMi only for the longest baseline available, indicating that this could be an over-resolution effect. Meilland et al. (2012) and Štefl et al. (2014) also report these complex shape phases.

In Faes et al. (2013) we presented a systematic study of how the DPs are affected by how resolved is the target by the interferometer. In addition to differentiate the resolved vs. non-resolved effects, we discovered a new phenomenon, which we dubbed CQE-PS, that can profoundly affect the phase profile, and provide useful new quantitative information about the disk and the star. This paper is as appendix, and our main findings and conclusions are summarized in this chapter.

The Central-Quasi Emission (CQE)

Before the spectro-interferometric era, one of the first strong indications that Be disks are Keplerian came from high-resolution spectroscopy ($R > 30000$) of shell stars, which are stars with strongly rotationally-broadened photospheric lines and additional narrow absorption lines. They are understood as ordinary Be stars seen edge-on, so that the line-

of-sight towards the star probes the CS equatorial disk. Hanuschik (1995) and Rivinius et al. (1999) studied the so-called *Central Quasi-Emission* (hereafter, CQE) peaks, where the disk, under certain circumstances, causes a cusp in the deepest region of the line profile of shell stars. The existence of the CQE implies slow radial motions of the gas (much smaller than the sound speed), which means the disk is supported by rotation.

The same mechanism that produces the CQE observed in shell star line profiles can cause important changes in the monochromatic intensity maps of the Be star plus disk system, with observable effects on the interferometric quantities. This effect was dubbed *CQE Phase Signature* (Faes et al., 2012). Similar to the spectroscopic CQEs, the CQE Phase Signature (hereafter, CQE-PS) can only be studied by high spectral resolution observations ($R > 2500$), such as can be obtained by the new generation of interferometers (AMBER/VLTI at near infrared, or VEGA/CHARA, Mourard et al., 2009, at visible range).

The initial studies made on the CQE profiles (Hanuschik, 1995; Rivinius et al., 1999) demonstrated its strong dependence on the distribution and velocity field of the CS material. Likewise, the CQE-PS has a high sensitivity to structural components of the CS disk - and even to the stellar size.

4.1 A Be star reference model

To study the DPs of Be stars at different angular resolutions and to characterize the CQE-PS with our modeling tool, HDUST, a realistic model for the Be + disk system needed to be defined. For the central star we adopt a rotationally deformed and gravity darkened star whose parameters are typical of a B1 Ve star. The stellar geometry is described by an oblate spheroid with stellar flux determined by traditional von Zeipel effect, where the local effective temperature is proportional to the local surface gravity as $T_{\rm eff} \propto {g_{\rm eff}}^{0.25}$ (at that time, the variations in von Zeipel coefficient β with the rotation rate of the star were not yet well established, see next chapter). For the CS disk description, we adopted the VDD model. For the case of isothermal viscous diffusion in the steady-state regime, the disk volume density has the particularly simple form $\rho(r) = \rho_0 (R_{\rm eq}/r)^{-m}$, where $m = 3.5$.

The interferometric quantities depend on the spatial resolution with which the object is seen. To explore different configurations we define the quantity $\nu_{\rm obs}$, the ratio between

Table 4.1 - Reference Be model parameters (Faes et al., 2013).

Parameter	Symbol	Ref. Case
Spectral type	-	B1 V
Mass	M	11.0 $M_\odot$
Polar radius	$R_{\rm pole}$	4.9 $R_\odot$
Pole temperature	$T_{\rm pole}$	27440 K
Luminosity	$L_\star$	10160 $L_\odot$
Critical velocity	$v_{\rm crit}$	534.4 km/s
Rotation rate	W; $\Omega/\Omega_{\rm crit}$	0.53; 0.80
Oblateness	$R_{\rm eq}/R_{\rm pole}$	1.14
Gravity darkening	$T_{\rm pole}/T_{\rm eq}$	1.16
Disk radius	$R_{\rm disk}$	10 $R_\star$
Disk density scale	n_0	10^{13} cm^{-3}
Density exponent	m	3.5
Inclination angle	i	45°
Spectral resolving power	R	12 000
Baseline/distance	$\nu_{\rm obs}$	1 m pc^{-1}

the baseline length of the interferometer and the distance to the star. The unit used is m pc^{-1}. The fundamental quantities for the model are listed in Table 4.1.

Rivinius et al. (2013) considered this a very representative model for a Be star and chose it to perform many of the analyzes on their review paper, with simulations conducted by me.

4.2 *Differencial phases in the resolved and unresolved regimes*

One important characteristic of interferometric differential phases arises when the target is *marginally-resolved*, i.e., $\vec{u}\cdot\vec{r} \ll 1$. In this case, interferometric differential phases (hereafter DP or just phases) can directly map the target's photocenter (e.g., Domiciano de Souza et al., 2004, Eq. 4):

$$\phi_{\rm diff}(\lambda,\lambda_r) = -2\pi\vec{u}\cdot[\vec{\epsilon}(\lambda)-\vec{\epsilon}(\lambda_r)]\,, \tag{4.1}$$

where $\vec{\epsilon}(\lambda)$ and $\vec{\epsilon}(\lambda_r)$ vectors are respectively the *photocenters* for λ and λ_r, a reference wavelength. The usual procedure is to take λ_r on the adjacent continuum of the spectral line, where $\vec{\epsilon}(\lambda_r)=0$. These photocenter measurements can be made at very high angu-

lar resolution without resolving the target, with astrometric determinations with higher precision than the nominal interferometer resolution. One example is reported by Carciofi et al. (2009), where the photocenter displacements were measured with precision smaller than 0.1 miliarcsecond on the Be star ζ Tauri.

The monochromatic on-sky brightness distribution of a Be star with a circumstellar disk can be highly asymmetric for wavelengths across the emission line profile. This is illustrated in Fig. 4.1. At continuum wavelengths (velocity a) the images show the star surrounded by a centro-symmetric continuum emission. We defined the DP to be zero at those wavelengths. As we move from the continuum toward line center (a to d), the line flux at a given wavelength range initially increases as a result of progressively larger emission lobes and then decreases as the emission area decreases toward line center (d). This creates the familiar W-shaped pattern in the visibilities and the S-shape pattern in the DPs.

Another important characteristic of differential phases arises when the target is *resolved*, i.e., $\vec{u}\cdot\vec{r} \gtrsim 1$. The photocenter position is no longer proportional to the phase shift, but the phase value is still a function of the photocenter position. This corresponds to the so-called *non-astrometric regime* and means that the phase still bears a relation to the photocenter position, but this relation is no longer simple. The astrometric and non-astrometric regimes are illustrated in Fig. 4.2.

For a typical Be star, the threshold limiting the two regimes is the ratio $\nu_{\rm obs} = \frac{\|\vec{B}_{\rm proj}\|}{d} \sim 1.5\ {\rm m\,pc^{-1}}$, where $\vec{B}_{\rm proj}$ is the projected baseline of the interferometer and d the target distance in parsecs. For $\nu_{\rm obs} < 1.5\ {\rm m\,pc^{-1}}$ one has the astrometric regime; otherwise, the non-astrometric. This corresponds roughly to $\vec{u}\cdot\vec{r} \sim 0.37$. The transition of between the phases regimes can be clearly seen in Fig. 4.3.

Kraus et al. (2012) proposed an explanation to the phase reversal that is not valid for β CMi. According to them, the visibility function of the line emitting region would pass through a visibility null, transiting from the first to the second visibility lobe. This effect could reverse the direction of the photocenter vector, but is not expected observationally for Be stars. As an example, in the bottom panels of Fig. 4.3 a phase signal is reversed at $\nu_{\rm obs} \sim 2\ {\rm m\,pc^{-1}}$ with a visibility value of $V^2 \sim 0.4$. To reach the visibility minimum, $\nu_{\rm obs} \gg 3\ {\rm m\,pc^{-1}}$, while β CMi was observed with $\nu_{\rm obs} \sim 2\ {\rm m\,pc^{-1}}$. Note that the recent modeling by Klement et al. (2015) points to an inclination angle $i \sim 45°$, very close to our

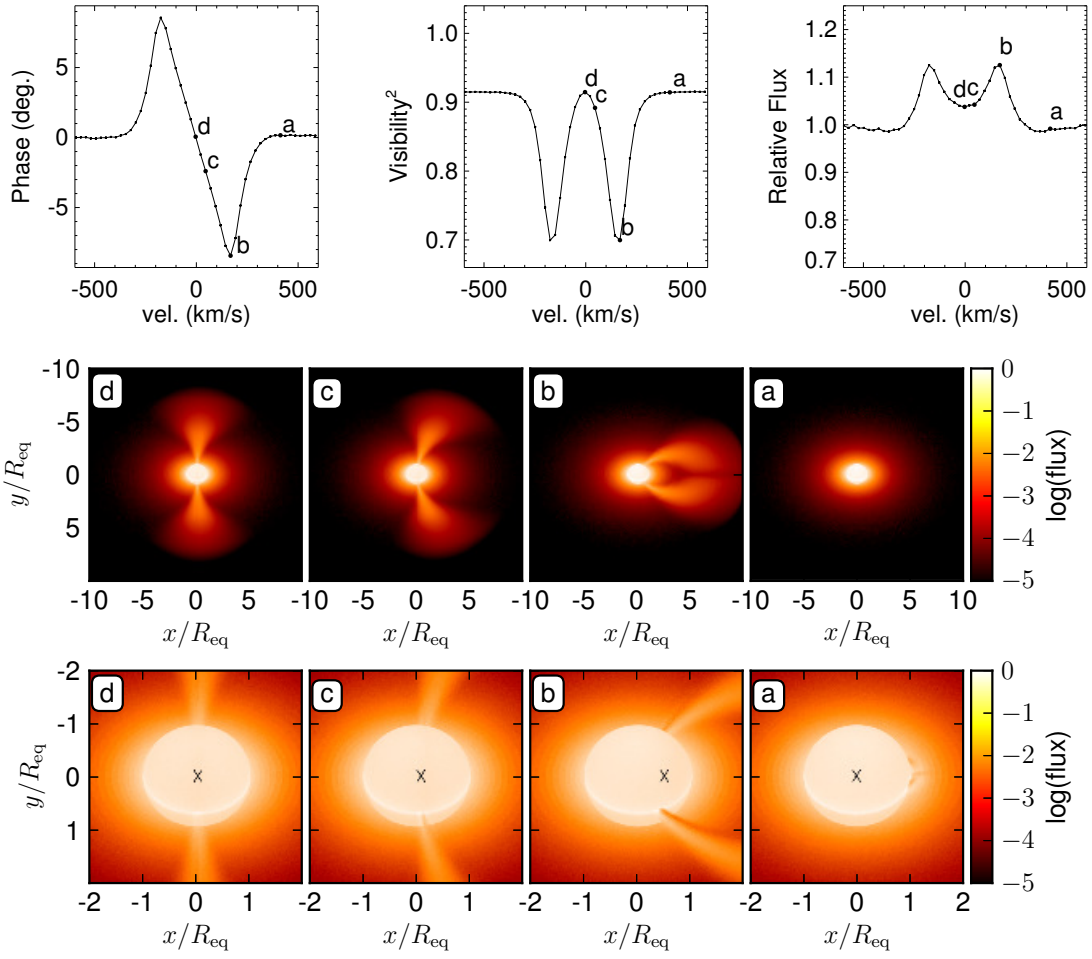

Figure 4.1: Top 3 panels: Interferometric Brγ differential phases, visibilities, and line profile for the reference model. Calculations were made for $\nu_{obs} = 1\,\mathrm{m\,pc^{-1}}$ (target marginally resolved), and baseline orientation parallel to the disk equator. *Bottom panels:* Model images for different spectral channels (as indicated in the upper panels), at different spatial scales. The photocenter position is indicated by a black cross. The disk inclination angle is $i = 45°$. Absorption bands can be identified at velocities (b) and (c) but they little alter the stellar flux in the line-of-sight. (Faes et al., 2013).

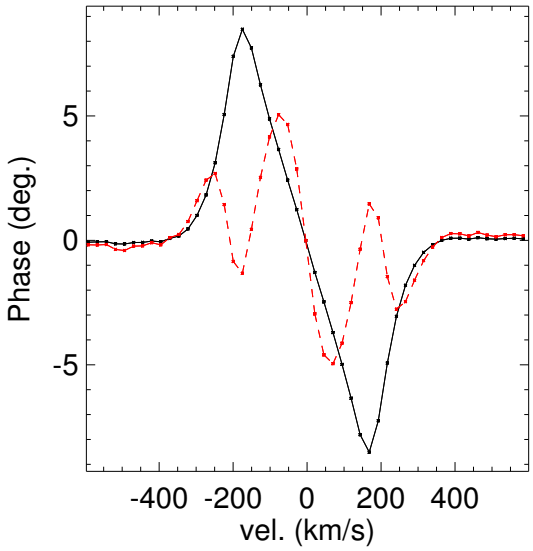

Figure 4.2: Differential phase signal for the Be reference model. The black (full) line corresponds to $\nu_{\rm obs} = 1\,{\rm m\,pc^{-1}}$ (astrometric regime) and the red (dashed) line to $\nu_{\rm obs} = 2.5\,{\rm m\,pc^{-1}}$ (non-astrometric regime). (Faes et al., 2013).

reference model.

4.3 The CQE-Phase Signature (CQE-PS)

Line emission from the rotating disk is the most important factor controlling the detailed shape of the DP for our reference model. However, in some circumstances the line absorption of photospheric light by the disk can have a strong impact on these observables. The absorption that generates the CQE-PS effect changes the S-shaped phases by introducing an inflection in the central part of the line or, if it is strong compared to disk emission, the absorption even transforming the phases to a double S-shape as a result of a central phase reversal.

This process is better understood with the aid of Fig. 4.4, where we plot the results for the reference case seen at an inclination angle $i = 90°$ (edge-on). At continuum wavelengths, the dark lane across the star is caused by continuum (free-free and bound-free) absorption in the CS disk (Fig. 4.4, velocity *a*). For the short wavelength range corresponding to the emission line profile, the continuum opacity may be regarded as constant, so we do not expect to see changes in continuum absorption in the narrow frequency range covered. In spectral channels across the Brγ line, additional line (bound-bound) absorp-

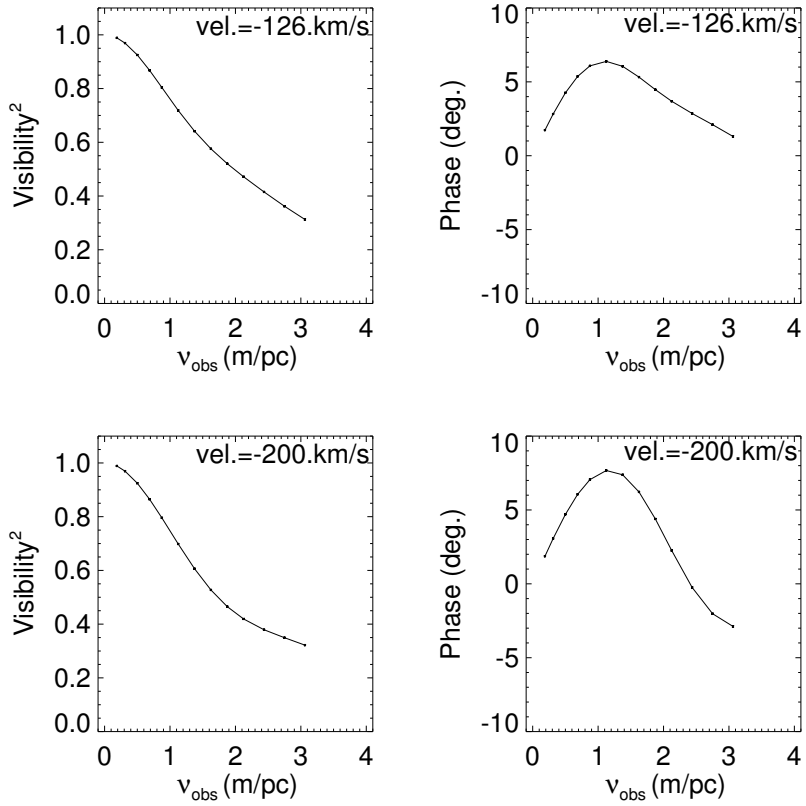

Figure 4.3: The squared visibility V^2 and differential phases for the Be star reference model at radial velocities of vel.$= -126\,\mathrm{km\,s^{-1}}$ and vel.$= -200\,\mathrm{km\,s^{-1}}$ as function of $\nu_{\rm obs}$, the ratio between the length of the baseline and the distance of the target ($\|\vec{B}_{\rm proj}\|/d$). The linear correspondence of the phase with the increasing spatial resolution ($\nu_{\rm obs} \lesssim 1.5\,\mathrm{m\,pc^{-1}}$) characterizes the astrometric regime. (Faes et al., 2013).

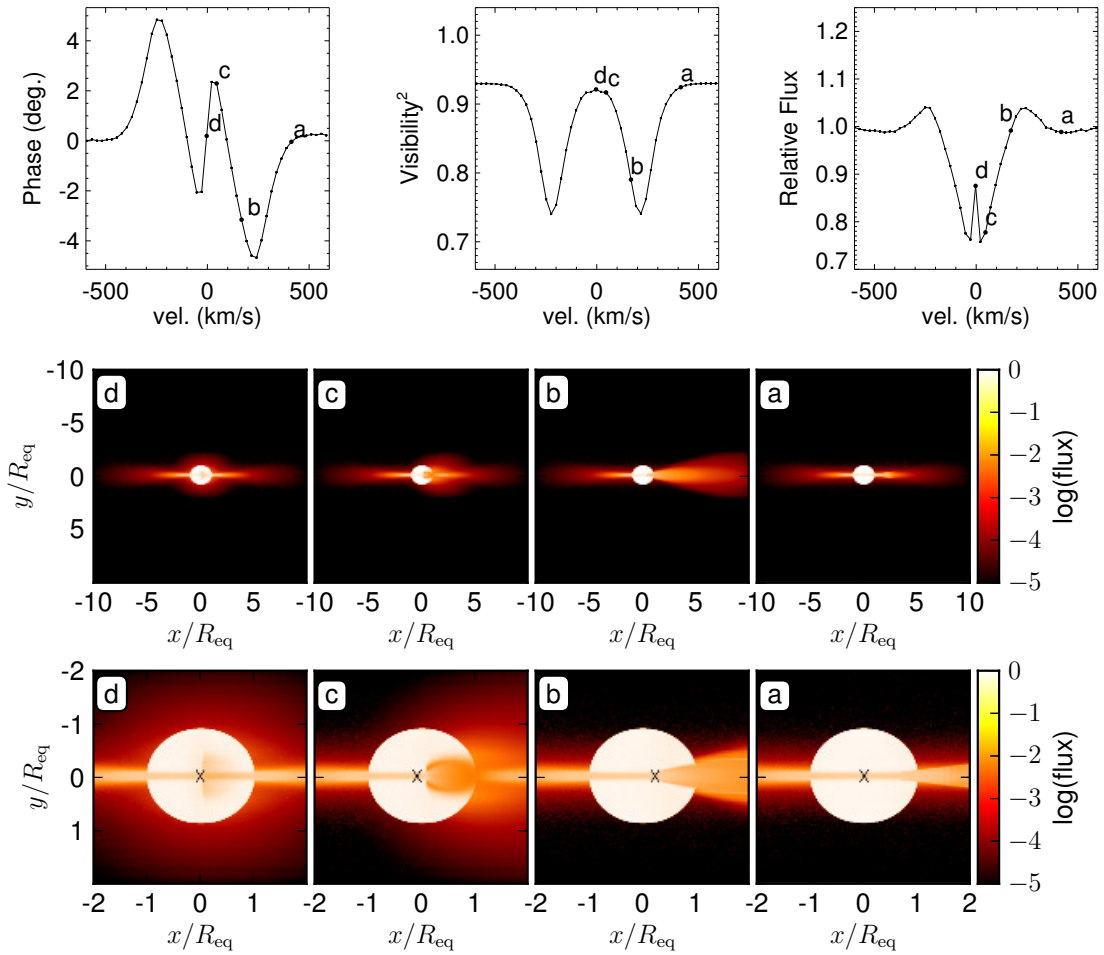

Figure 4.4: Same as Fig 4.1, but for $i = 90\,\mathrm{deg}$. (Faes et al., 2013).

tion of photospheric light by HI atoms is seen (velocities b to d). This line absorption has a differential aspect because it depends on the line-of-sight velocity of the absorbing material. For high line-of-sight velocities, v_{proj}, only a minor part of the star is affected by line absorption (velocity b). Going towards lower velocities, i.e., towards the line center, this fraction increases, until it reaches a maximum at about $50\,\mathrm{km\,s^{-1}}$ (velocity c). The precise value depends on the outer disk size and density. Closer to the line center, the lowest line-of-sight velocities are no longer absorbed (velocity d), giving rise to the spectroscopic CQE effect. Spectroscopic CQEs are thus, in spite of their name, not related to any emission process but are an absorption phenomenon.

As shown in Fig. 4.5, the projected Keplerian iso-velocities over the stellar surface cover bigger disk areas as smaller velocities are considered and also the bigger the disk is. This indicates that the highest opacities occur under these conditions, i.e., large disks for

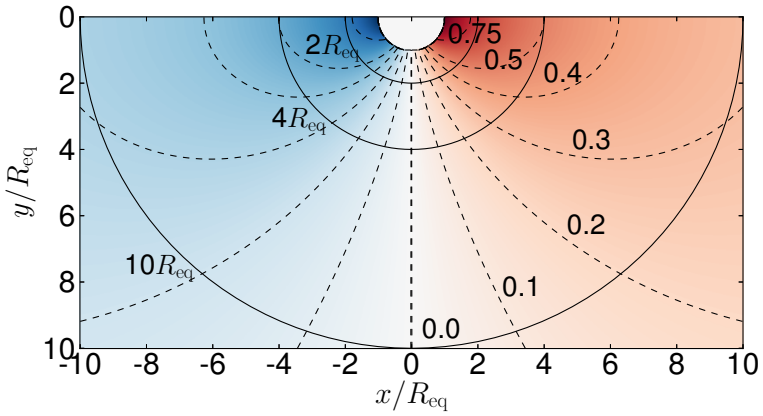

Figure 4.5: Isovelocity contours (dashed lines) for a Keplerian disk. Each curve corresponds to a fraction of the projected orbital speed at the base of the disk ($v_{\rm orb}\sin i$), as indicated. The solid lines indicate different disk outer radii.

small projected speeds, stating the importance of the disk size for the occurrence of the CQE-related phenomena.

The line absorption across parts of the stellar disk generates a considerable decrease in the stellar flux, which in turn will affect the photocenter position of the system, with a corresponding signal in the DP. This is clearly seen in Fig. 4.4 as the "wiggle" in the center of the DP profile; the highest distortion is seen where the CS absorption is strongest, i.e., at about $50\,{\rm km\,s^{-1}}$. We observe the competition between spectral line emission from the disk at line-of-sight distances from the meridian higher than $1R_{\rm eq}$, which tends to shift the monochromatic photocenter towards one side, and disk spectral line absorption at line-of-sight distance from the meridian lower than $1R_{\rm eq}$, which shifts the photocenter toward the opposite side. So, at wavelengths close to the line emission peak (Fig. 4.4, velocity b), the disk emission dominates over disk absorption and the photocenter position is shifted toward the emission lobe. For wavelengths closer to the line center (Fig. 4.4, velocity c), however, even though there is some disk emission, the absorption is more important and the photocenter position is shifted to the opposite direction of disk emission, with a corresponding change of sign of the DP. We conclude that the spectroscopic phenomenon of the CQE has an interferometrical counterpart (dubbed CQE-PS) that presents itself as a central reversal in the DP profile. We note that this central reversal is an intrinsic phenomenon and is independent of the reversals of resolved signals discussed above.

The CQE-PS occurence depends on the inclination angle on which the system is seen, since the disk must block the photospheric emission. This means that the effect will to be

maximum for stars viewed equator-on, a characteristic of the so called shell stars. A list of nearby Be shell stars can be found in Catanzaro (2013) and are good candidates to the look for this phenomenon observationally.

4.4 The CQE-PS diagnostic potential

One example of angular displacements of photocenter within a line profile used as diagnostic of the CS envelope was done by Stee (1996), where he studied the response of the photocenter as function of the envelope rotational law. So far we described the CQE-PS as dependent of the projected disk speeds, opacity and size. Thus, the actual differential phases shape defined by the CQE-PS depend on the disk properties, having a comprehensive diagnostic potential. Faes et al. (2013) demonstrated that the signal is sensitive to the CS disk density, disk size, and the radial density distribution of the CS material. Varying each of these parameters generated a characteristic shape in the differential phase diagram. This can be seen in Fig. 4.6, where the DP profiles of different disk base densities and sizes are compared.

Importantly, when Be stars change their brightness, this can originate in the star, the disk, or both. Although most of the observed variations are attributed to disk changes (e.g., Haubois et al., 2012), the CQE-PS can be used to assess this question because it is very sensitive to the disk part whence most of the excess flux in the visible range comes from.

The CQE-PS may even provide an estimate for the (maximum) stellar angular size. The reason is that the effect should take place over the stellar surface, since it is related to absorption of photospheric light by the disk (Fig. 4.4). As interferometric phases are sensitive to angular displacements, this shift is proportional to the size of the stellar photosphere. More specifically, Faes et al. (2013) discuss that $0 < \Delta\epsilon < \frac{2}{5}\frac{R_{\rm eq}}{d}$, where is $\Delta\epsilon$ the angular displacement with the presence of photospheric absorption.

4.5 Chapter summary

The interferometric DPs can directly map the target's photocenter if its marginally-resolved. For the rotating disks of Be stars, the expected DP profile is a smooth S-shape. Departures of S-shaped in (symmetric) Be disks can occur in two independent ways: (i)

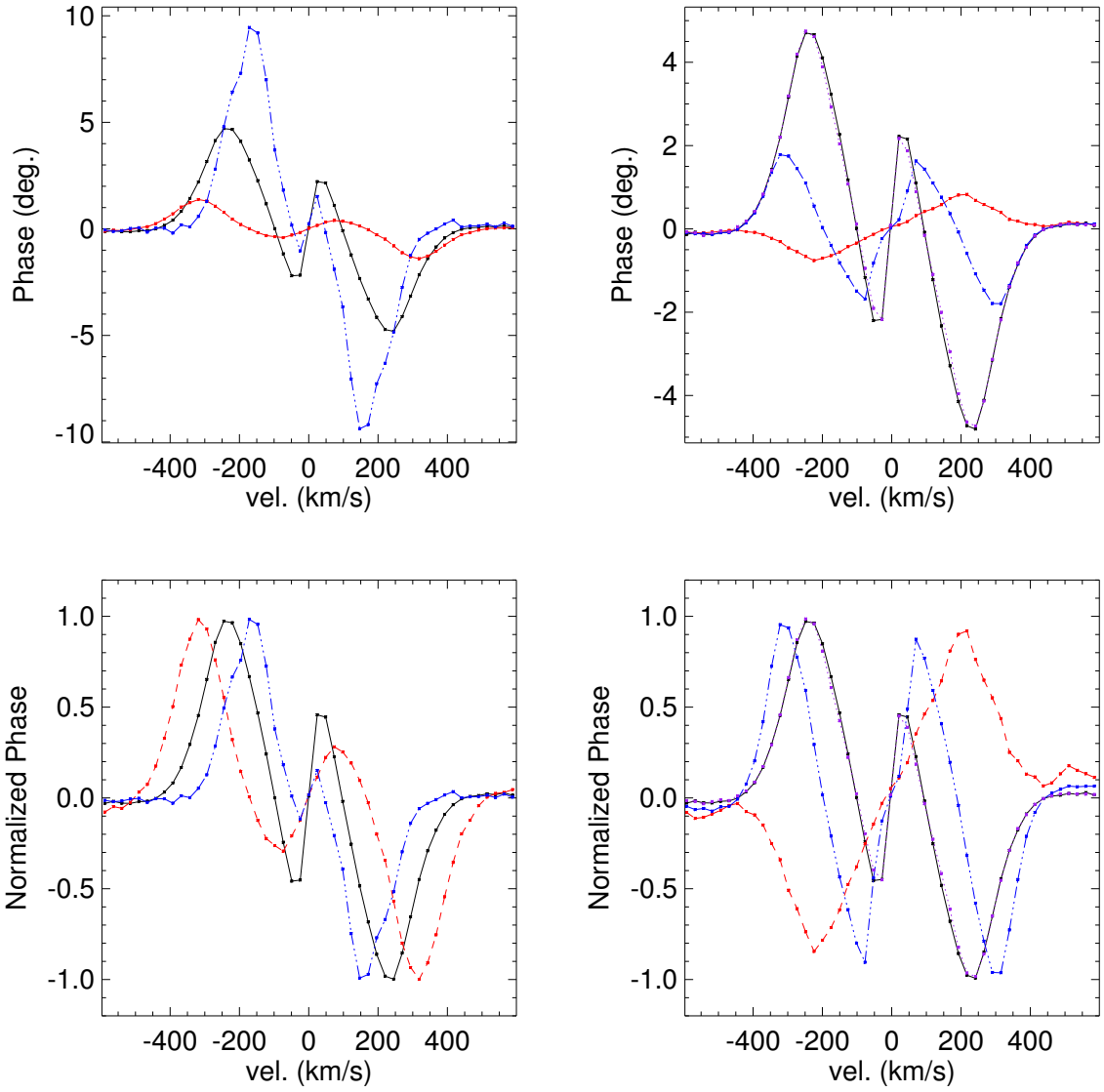

Figure 4.6: Left: Differential phase signal for the Be reference model at $i = 90°$ for low ($10^{12}\,\mathrm{cm}^{-3}$, red dashed line) and high density ($10^{14}\,\mathrm{cm}^{-3}$, blue dot-dashed line) models. The reference model is the intermediate value (black full line). *Right:* The reference model at $i = 90°$ for different disk sizes: $R_{\mathrm{disk}} = 2$ (red dashed line), 4 (blue dot-dashed line), 10 (black full line) and 20 $R_\star$ (purple pointed line). The signal for $R_{\mathrm{disk}} = 10$ and 20 $R_\star$ are almost coincident, indicating that they have the same pseudo-photospheric size (as seen in Chap. 2). (Faes et al., 2013).

the target is actually resolved, and complex phase behavior is expected; (ii) additional physical processes are occurring in addition to the (pure) line emission.

We call *CQE-PS* the phase signature of the phenomenon equivalent to the spectral CQE (Central Quasi Emission) in shell stars. Its origin relies on the disk absorption of the photospheric light so that it can considerably change the photocenter position close to the line rest wavelength. The shape and amplitude of the CQE-PS depends on a number of parameters, both intrinsic to the system and related to the observational setup (baseline length and orientation, and spectral resolution).

Using a realistic model consisting of a rotating B1 V star with a viscous decretion disk, we made an initial study to assess to diagnostic potential of CQE-PS. Certain conditions and parameters make the effect more pronounced. Observationally, the effect is strongest for edge-on viewing (shell stars) and for baselines oriented parallel to the disk equator.

Among the several model parameters explored, we found that the signal is sensitive to the CS disk density, disk size, and the radial density distribution of the CS material. Varying each of these parameters generated a characteristic shape in the differential phase diagram, which demonstrates the diagnostic potential of the CQE-PS. Keplerian rotation deviations could also be observed.

A remarkable result of the CQE-PS is its ability to make a (lower) estimate of the stellar angular size even when the observed squared visibilities are close to unity. This result may extend the distance range at which such an estimate can be made with interferometry. The full power of this diagnostic tool will be realized when applied to observations over a rotational of structural variability, as V/R cycles of disk growing/dissipation process.

In Chapter 6 we make the first report of the observation of the CQE-PS for the Be star Achernar.

4.6 Publication: Diff. phases as a sensitive physical diagnostic of circumstellar disks

Astronomy & Astrophysics manuscript no. cqe_astroph
June 6, 2013

Differential interferometric phases at high spectral resolution as a sensitive physical diagnostic of circumstellar disks

D. M. Faes[1,5], A. C. Carciofi[1], Th. Rivinius[2], S. Štefl[3], D. Baade[4], and A. Domiciano de Souza[5]

[1] Instituto de Astronomia, Geofísica e Ciências Atmosféricas, Universidade de São Paulo, Rua do Matão 1226, Cidade Universitária, 05508-900, São Paulo, SP, Brazil, moser@usp.br, carciofi@usp.br
[2] European Organisation for Astronomical Research in the Southern Hemisphere, Casilla 19001, Santiago 19, Chile
[3] European Organisation for Astronomical Research in the Southern Hemisphere / ALMA, Alonso de Córdova 3107, Santiago, Chile
[4] European Organisation for Astronomical Research in the Southern Hemisphere, Karl-Schwarzschild-Str. 2, 85748 Garching bei München, Germany
[5] Lab. J.-L. Lagrange, UMR 7293 - Observatoire de la Côte d'Azur (OCA), Univ. de Nice-Sophia Antipolis (UNS), CNRS, Valrose, 06108 Nice, France

Received 18 February 2013 / Accepted DD MMMMM YYYY

ABSTRACT

Context. The circumstellar disks ejected by many rapidly rotating B stars (so-called Be stars) offer the rare opportunity of studying the structure and dynamics of gaseous disks at high spectral as well as angular resolution.
Aims. This paper explores a newly identified effect in spectro-interferometric phase that can be used for probing the inner regions of gaseous edge-on disks on a scale of a few stellar radii.
Methods. The origin of this effect (dubbed central quasi-emission phase signature, CQE-PS) lies in the velocity-dependent line absorption of photospheric radiation by the circumstellar disk. At high spectral and marginal interferometric resolution, photocenter displacements between star and isovelocity regions in the Keplerian disk reveal themselves through small interferometric phase shifts. To investigate the diagnostic potential of this effect, a series of models are presented, based on detailed radiative transfer calculations in a viscous decretion disk.
Results. Amplitude and detailed shape of the CQE-PS depend sensitively on disk density and size and on the radial distribution of the material with characteristic shapes in differential phase diagrams. In addition, useful lower limits to the angular size of the central stars can be derived even when the system is almost unresolved.
Conclusions. The full power of this diagnostic tool can be expected if it can be applied to observations over a full life-cycle of a disk from first ejection through final dispersal, over a full cycle of disk oscillations, or over a full orbital period in a binary system.

Key words. techniques: interferometric – circumstellar matter – stars: emission-line, Be

1. Introduction

Circumstellar (CS) disks can assume importance at various phases of the life cycles of single and binary stars. They are the place of fundamental physical processes related to properties and evolution of their central objects. Be stars are a unique class of objects that allow studying the creation, evolution and destruction of CS disks. In these main-sequence objects, the disks are fed from mass lost from their rapidly rotating central stars (Porter & Rivinius 2003). Questions such as how the CS material can be supported against the stellar gravity and how angular momentum can be transferred from inner to external regions remained open for a long time. In the past two decades, optical and infrared interferometry played a key role in developing our understanding of these astrophysical systems. For instance, the pioneering measurements of Quirrenbach et al. (1997) provided strong evidence that the CS matter around Be stars is distributed in a geometrically thin structure (i.e., a disk). More recently, detailed measurements have demonstrated that Be disks rotate in a Keplerian fashion (Meilland et al. 2007; Kraus et al. 2012; Wheelwright et al. 2012).

The strong developments in the observations were accompanied by significant progress in our theoretical understanding of these systems. Recently, a consensus is emerging that the viscous decretion disk (VDD) model, first suggested by Lee et al. (1991) and subsequently developed by Bjorkman (1997), and Okazaki (2001), among others, is the best candidate to explain the observed properties of Be disks (Carciofi 2011; McGill et al. 2011). Detailed hydrodynamical calculations (e.g., Okazaki 2001; Jones et al. 2008) have demonstrated that VDDs rotate in a nearly Keplerian fashion, in agreement with the results from spectro-interferometry (Meilland et al. 2007; Kraus et al. 2012).

Before the spectro-interferometric era, one of the first strong indications that Be disks are Keplerian came from high-resolution spectroscopy ($R > 30000$) of shell stars, which are stars with strongly rotationally broadened photospheric lines and additional narrow absorption lines. They are understood to be ordinary Be stars seen edge-on, so that the line-of-sight toward the star probes the CS equatorial disk. Hanuschik (1995) and Rivinius et al. (1999) studied the so-called *central quasi-emission* (hereafter, CQE) peaks, where the disk, under certain circumstances, causes a cusp in the deepest region of the line profile of shell stars. The existence of the CQE implies slow radial motions of the gas (much slower than the sound speed), which means that the disk is supported by rotation.

The same mechanism that produces the CQE observed in shell-star line profiles can cause important changes in the

monochromatic intensity maps of the Be star plus disk system, with observable effects on the interferometric quantities. This effect is dubbed *CQE phase signature* (Faes et al. 2012), and here its diagnostic potential is investigated.

Similar to the spectroscopic CQEs, the CQE Phase Signature (hereafter, CQE-PS) can only be studied by high spectral resolution observations ($R > 2500$), such as can be obtained by the new generation of interferometers (AMBER/VLTI at near-infrared, Petrov et al. 2007, and VEGA/CHARA at visible range, Mourard et al. 2009).

Part of the variability observed in Be stars is associated with structural changes in their CS disks. The temporal evolution of the observables can only be put in some sort of conceptual frame with the understanding of the physical processes that control the CS dynamics. Carciofi et al. (2012) studied the V-band magnitude evolution of 28 CMa during a phase of disk dissipation using the VDD model. This allowed the determination of the viscosity parameter governing the disk dynamics, as well its corresponding mass decretion rate. Haubois et al. (2012) provided another example of how CS disk and stellar parameters are intrinsically connected and how they can be inferred through a follow-up of various observables. In particular, the temporal evolution of the disk density (and corresponding continuum emission) is related to the mass-loss rate and episodes of mass injection and quiescence.

The initial studies made on the CQE profile (Hanuschik 1995; Rivinius et al. 1999) demonstrated its strong dependence on the distribution and velocity field of the CS material. Likewise, we show here that CQE-PS has a high sensitivity to structural components of the CS disk - and even to the stellar size. These parameters can then be related to the time evolution of the observables and other fundamental parameters of the system as in the cases mentioned above.

2. Model description

The mechanism behind the CQE-PS is the differential absorption of photospheric radiation by the CS disk (Sect. 3). This mechanism can be directly traced by the interferometric differential phase, and must be separated from other mechanisms that affect this quantity.

To study, characterize, and illustrate the CQE-PS, we adopted a realistic model for the Be + disk system. For the central star we adopted a rotationally deformed and gravity-darkened star whose parameters are typical of a B1 Ve star (Table 1). The stellar geometry is described by an oblate spheroid with stellar flux determined by the traditional von Zeipel effect (von Zeipel 1924), where the local effective temperature is proportional to the local surface gravity, $T_{\rm eff} \propto {g_{\rm eff}}^{0.25}$. For the CS disk description, we adopted the VDD model. For isothermal viscous diffusion in the steady-state regime, a state reached after a sufficiently long and stable decretion period (Haubois et al. 2012), the disk volume density has a particularly simple form $n(r) = n_0(R_{\rm eq}/r)^{-m}$, where $m = 3.5$ (Bjorkman & Carciofi 2005).

The interferometric quantities depend on the spatial resolution with which the object is seen. To explore different configurations we defined the quantity $\nu_{\rm obs}$, the ratio between the baseline length of the interferometer, and the distance to the star. The unit used is m pc^{-1}.

The calculations presented in this paper were made with the three-dimensional, non-local radiative equilibrium code HDUST (Carciofi & Bjorkman 2006, 2008).

Table 1. Reference Be model parameters.

Parameter	Symbol	Ref. Case
Spectral type	-	B1 V
Mass	M	11.0 $M_\odot$
Polar radius	$R_{\rm pole}$	4.9 $R_\odot$
Pole temperature	$T_{\rm pole}$	27440 K
Luminosity	$L_\star$	10160 $L_\odot$
Critical velocity	$v_{\rm crit}$	534.4 km/s
Rotation rate	$\Omega/\Omega_{\rm crit}$	0.8
Oblateness	$R_{\rm eq}/R_{\rm pole}$	1.14
Gravity darkening	$T_{\rm pole}/T_{\rm eq}$	1.16
Disk radius	$R_{\rm disk}$	10 $R_\star$
Disk-density scale	n_0	10^{13} cm^{-3}
Density exponent	m	3.5
Inclination angle	i	45°
Spectral resolving power	R	12 000
Baseline/distance	$\nu_{\rm obs}$	1 m pc^{-1}

2.1. Interferometric phases in the marginally resolved case

The quantity registered in interferometry is the normalized complex visibility $V(\mathbf{u})$. It is related to the Fourier transform of the brightness distribution $I(\mathbf{r}, \lambda)$ of a non-coherent and extended source on the plane of sky through the Van Cittert-Zernike theorem (Born & Wolf 1980):

$$V(\mathbf{u}) = \frac{\iint I(\mathbf{r},\lambda)\exp\left(-2\pi i \mathbf{u}\cdot\mathbf{r}\right) d^2\mathbf{r}}{\iint I(\mathbf{r},\lambda)\, d^2\mathbf{r}} = |V|\exp\left(i\phi\right), \quad (1)$$

where λ is the monochromatic wavelength and $\mathbf{u}$ the spatial frequency of the projected baseline $\mathbf{B}_{\rm proj}/\lambda$. $|V|$ ranges from 1 to 0 from a fully unresolved to a fully resolved object.

A common quantity used in high spectral resolution interferometry are the differential phases $\phi_{\rm diff}$,

$$\phi_{\rm diff}(\lambda, \lambda_{\rm r}) = \phi(\lambda) - \phi(\lambda_{\rm r}), \quad (2)$$

where $\lambda_{\rm r}$ is a wavelength of reference simultaneously observed. One important characteristic of differential phases arises when the target is *marginally resolved*, i.e., $\mathbf{u}\cdot\mathbf{r} \ll 1$. In this case, interferometric differential phases (hereafter DP or just phases) can directly map the target's photocenter (Domiciano de Souza et al. 2004, Eq. 4):

$$\phi_{\rm diff}(\lambda, \lambda_r) = -2\pi\mathbf{u}\cdot[\boldsymbol{\epsilon}(\lambda) - \boldsymbol{\epsilon}(\lambda_r)]\,; \quad (3)$$

the $\boldsymbol{\epsilon}(\lambda)$ and $\boldsymbol{\epsilon}(\lambda_r)$ vectors are the *photocenters* for λ and λ_r. The usual procedure is to take λ_r on the adjacent continuum of the spectral line, with $\boldsymbol{\epsilon}(\lambda_r) = 0$.

Photocenter measurements can be made at very high angular resolution using DP. One example is provided by Štefl et al. (2009), who achieved <0.1-mas relative photocenter astrometry in the Be star ζ Tauri.

We see below that the CQE-PS in DP occurs under quite specific circumstances, and its diagnostic potential is more relevant for some parameters than for others. To quantify this, we first studied a reference model for which the CQE-PS is not present, i.e., a model for which the canonical disk interferometric signatures apply. The adopted model parameters for the reference case are listed in the third column of Table 1.

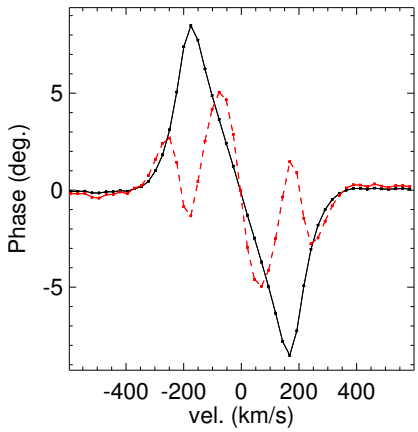

Fig. 2. Differential phase signal for the Be reference model (Sec. 2). The black (full) line corresponds to $\nu_{\rm obs} = 1\,{\rm m\,pc^{-1}}$ (astrometric regime) and the red (dashed) line to $\nu_{\rm obs} = 2.5\,{\rm m\,pc^{-1}}$ (non-astrometric regime).

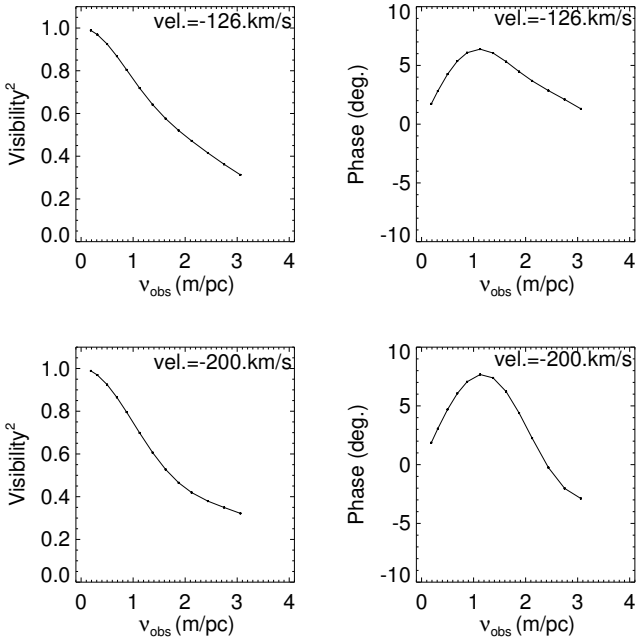

Fig. 3. Squared visibility and differential phases for the Be star reference model (Sec. 2) at radial velocities of vel.$= -126\,{\rm km\,s^{-1}}$ and vel.$= -200\,{\rm km\,s^{-1}}$ as a function of $\nu_{\rm obs}$, the ratio between the length of the baseline, and the distance of the target. The linear correspondence of the phase with the increasing spatial resolution ($\nu_{\rm obs} \lesssim 1.5\,{\rm m\,pc^{-1}}$) characterizes the astrometric regime.

For rotating Be disks, it is generally expected that DP have a simple S-shaped profile (Stee 1996). This can be easily understood from Fig. 1, which shows the Brγ line profile, the corresponding interferometric quantities and model images at different wavelengths for the reference model. Shown are results for $i = 45°$. At continuum wavelengths (velocity a, in Fig. 1) the images show the star surrounded by a centro-symmetric continuum emission. We defined the DP to be zero at those wavelengths. As we move from the continuum toward line center (a to d), the line flux at a given wavelength range initially increases as a result of progressively larger emission lobes and then decreases as the emission area decreases toward line center (d). This creates the familiar W-shaped pattern in the visibilities and the S-shape pattern in the DPs.

2.2. Interferometric phases in the resolved case

The association between the phase signal and the image's photocenter position is only possible if the marginally resolved condition is satisfied, since it permits the truncation of the Fourier expansion (Jankov et al. 2001). This is particularly important for Be stars because their on-sky size is wavelength dependent, mainly across emission lines whose monochromatic emission has a strong spatial dependence.

Outside the astrometric regime (i.e., $\mathbf{u}\cdot\mathbf{r} \approx 1$), Eq. (3) is no longer valid. A complex phase behavior is then expected since higher-order terms of the Fourier transform of the image are relevant and a direct correspondence between the DP and the photocenter position does not hold any longer. Fig. 2 compares the DP signal of our reference model in the astrometric regime and outside it. The reason the curves are so different is explained in Fig. 3 that plots the interferometric quantities for two wavelengths across Brγ as a function of $\nu_{\rm obs}$, the ratio between $|{\rm B_{proj}}|$ and the target's distance ($\nu_{\rm obs} \propto \mathbf{u}\cdot\mathbf{r}$). The astrometric regime corresponds to the linear growth of the phase shift with $\nu_{\rm obs}$ in Fig. 3 . When the target becomes marginally resolved ($\nu_{\rm obs} \gtrsim 1.5$), linear correspondence no longer holds, and in the fully resolved regime the phase shift may even decrease with increasing $\nu_{\rm obs}$.

The interferometric signature of a Be star comprises the stellar and the disk contributions; the visibility is equally affected by both, depending on the relative flux contributions, but the phase signal is dominated by the disk emission since it comes from a large angular distance. In general, the complex phase behavior seen in Fig 2, including change of sign, occurs always well before the disk is fully resolved. In Be stars, the presence of a small angular size star contributing a significant amount of flux moves the threshold for complex phase behavior further toward a visibility squared of unity, as seen in Fig. 3.

Based on our simulations, the astrometric regime is approximately valid up to squared visibilities of ≈ 0.8, which corresponds to $\nu_{\rm obs} \lesssim 1.5\,{\rm m\,pc^{-1}}$ for a typical Be star (we note the correspondence of $\mathbf{u}\cdot\mathbf{r}$ with $\nu_{\rm obs}$; the higher $\nu_{\rm obs}$ the higher $\mathbf{u}$). The exact value of these quantities depends on the target brightness distribution and relative flux contributions. One example of the complex behavior outside the astrometric regime is reported by Kraus et al. (2012), who modeled AMBER/VLTI data for the Be star β CMi. In this case, a phase reversal was registered at the DP signal of the longest baseline available for this nearby target (squared visibility of ≈ 0.7, $\nu_{\rm obs} \approx 2.2$).

Outside the astrometric regime a phase reversal is an example of the phenomenology that emerges entirely from long-baseline interferometry, where the phase signal no longer corresponds to displacements of the photocenter. In the text that follows all interferometric computations are provided in the marginally resolved regime (i.e., when Eq. 3 is valid) to adequately separate the CQE-PS phenomenon from the just described effects. However, the CQE-PS signal can be identified and isolated even outside the astrometric regime. The validity and characteristics of the CQE-PS under these conditions are discussed in section 3.3.

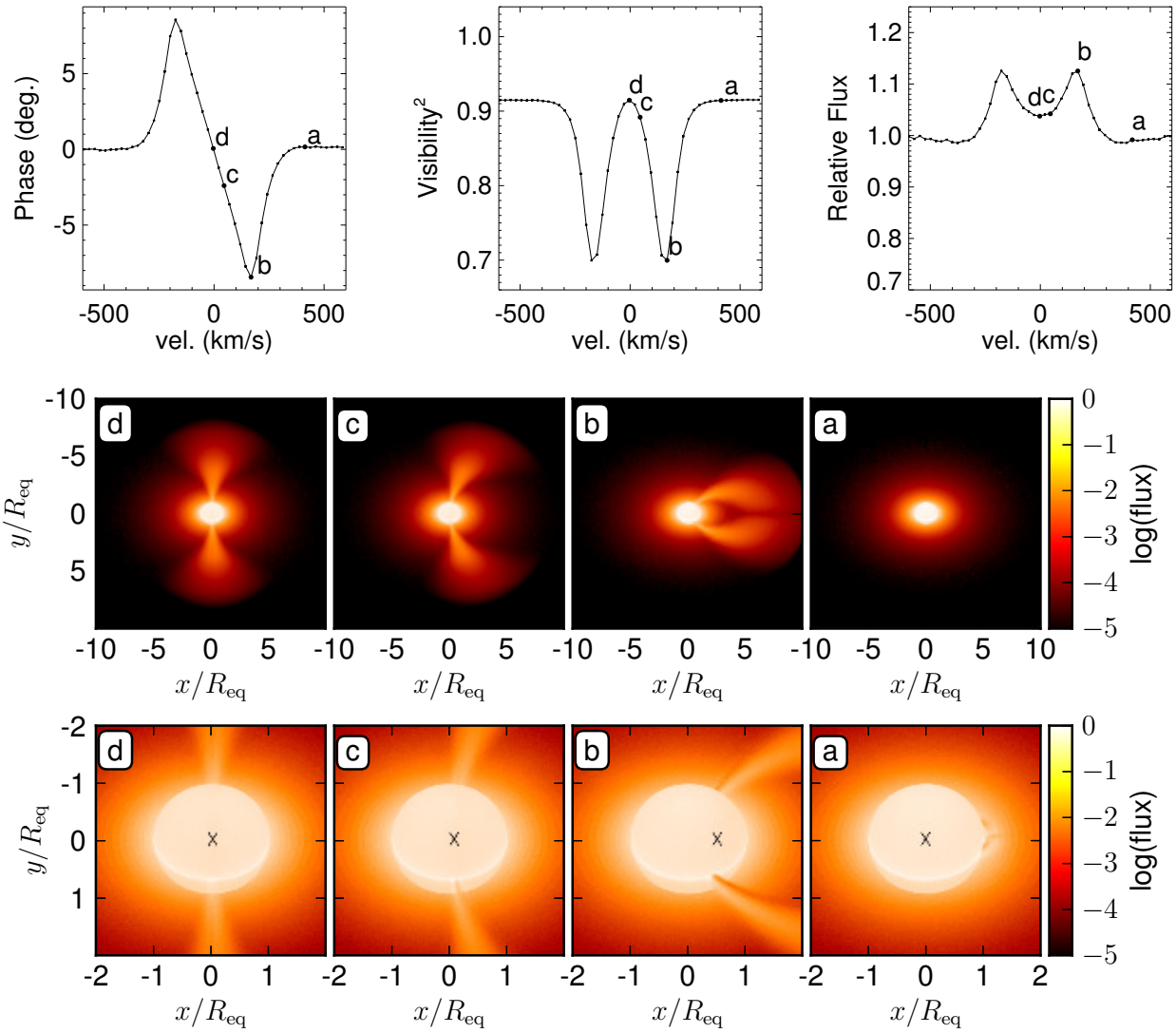

Fig. 1. Top 3 panels: Interferometric Brγ differential phases, visibilities, and line profile for the reference model. Calculations were made for $\nu_{\rm obs} = 1\,{\rm m\,pc^{-1}}$ (target marginally resolved), and baseline orientation parallel to the disk equator. Bottom panels: Model images for different spectral channels (as indicated in the upper panels) at different spatial scales. The photocenter position is indicated by a black cross. The disk inclination angle is $i = 45°$. Absorption bands can be identified at velocities (b) and (c) but they little alter the stellar flux in the line-of-sight.

3. The CQE phase signature

For the reference model described in Sect. 2.1, line emission from the rotating disk is the most important factor controlling the detailed shape of the DP. However, in some circumstances line absorption of photospheric light by the disk can also have a strong impact on these observables.

The spectroscopic phenomenon of the CQE was first predicted by Hanuschik (1995) for the so-called shell-absorption lines in nearly edge-on Be shell stars. The CQEs consist of narrow absorption lines well below the stellar continuum that show a central weak cusp, known as CQE peaks. Hanuschik pointed out that these peculiar profiles result from the minimum at zero radial velocity in the absorption of the photospheric flux by the rotating CS gas. However, Hanuschik expected them mainly in Fe II lines, which turned out to be formed at too large distances from the central star, where turbulence vs. orbital motion becomes strong enough to disturb the CQE signature. Later, Rivinius et al. (1999) identified these predicted CQE with previously unexplained observational features often seen in He I lines, and sometimes metallic shell lines.

This is better understood with the aid of Figs. 4 and 5, where we plot results for the reference case seen at an inclination angle $i = 90°$ (edge-on). At continuum wavelengths, the dark lane across the star is caused by continuum (free-free and bound-free) absorption in the CS disk (Fig. 4, velocity a). For the short-wavelength range corresponding to the emission line profile, the continuum opacity may be regarded as constant, so we do not expect to see changes in continuum absorption in the narrow-frequency range covered by Fig. 4. In spectral channels across the Brγ line, additional line (bound-bound) absorption of photospheric light by H I atoms is seen (Figs. 4, velocities b to d). This line absorption has a differential aspect because it depends on the line-of-sight velocity of the absorbing material (see below). For high line-of-sight velocities, $v_{\rm proj}$, only a minor part of the star is affected by line absorption (Fig. 4, velocity b). Going towards lower velocities, i.e., toward the line center, this fraction

increases, until it reaches a maximum at about 50 km s^{-1} (Fig. 4, velocity c). The precise value depends on the outer disk size and density. Closer to the line center, the lowest line-of-sight velocities are no longer absorbed (Fig. 4, velocity d), giving rise to the spectroscopic CQE effect. Spectroscopic CQEs are thus, in spite of their name, not related to any emission process, but are an absorption phenomenon.

Figure 4 can be understood with the aid of Fig. 5. We plot the projected velocity ($v_{\rm proj}$) in the line-of-sight vs. distance from meridian. $v_{\rm proj}$ is expressed in terms of $v_{\rm orb}\sin i$, the projected Keplerian orbital speed at the base of the disk ($v_{\rm orb} = (GM/R_{\rm eq})^{1/2}$). For a given $v_{\rm proj}$, the figure shows the range of distances from the meridian for which a given $v_{\rm proj}$ occurs along the line-of-sight. The fraction steeply increases from nearly zero at the meridian, where the line-of-sight velocity is zero, to a maximum close to $0.03\,v_{\rm orb}\sin(i)$ for the reference case (lower panel of Fig. 5, vertically hatched lines). From this point on, the fraction decreases linearly with $v_{\rm proj}$, so that at high projected velocities only light that originated close to the edge of the star can be absorbed by the disk. The dearth of absorbers with zero velocity reduces the line depth, leading to the (false) impression of line emission. Fig. 6 shows the isovelocity contours of a Keplerian disk. The figure explains why the portion of the star covered by low-velocity particles is much larger for larger disks than for smaller ones. For $R_{\rm disk} = 10\,R_{\rm eq}$, for instance, the largest surface coverage occurs for $v_{\rm proj} = 0.03\,v_{\rm orb}\sin(i)$ (lower panel of Fig. 5). The projected velocity for which this occurs increases with decreasing disk radius as $(R_{\rm eq}/R_{\rm disk})^{3/2}v_{\rm orb}\sin(i)$. So, for $R_{\rm disk} = 2\,R_{\rm eq}$ the largest surface coverage will occur for $v_{\rm proj} = 0.34\,v_{\rm orb}\sin(i)$. This shows the importance of the disk size for the spectroscopic CQE.

This line absorption across parts of the stellar disk generates a considerable decrease in the stellar flux, which in turn will affect the photocenter position of the system, with a corresponding signal in the DP. This is clearly seen in Fig. 4 as the "wiggle" in the center of the DP profile; the highest distortion is seen where the CS absorption is strongest, i.e., at about 50 km s^{-1}. We observe the competition between spectral line emission from the disk at line-of-sight distances from the meridian higher than $1\,R_{\rm eq}$, which tends to shift the monochromatic photocenter towards one side, and disk spectral line absorption at line-of-sight distance from the meridian lower than $1\,R_{\rm eq}$, which shifts the photocenter toward the opposite side. So, at wavelengths close to the line emission peak (Fig. 4, velocity b), the disk emission dominates over disk absorption and the photocenter position is shifted toward the emission lobe. For wavelengths closer to the line center (Fig. 4, velocity c), however, even though there is some disk emission, the absorption is more important and the photocenter position is shifted to the opposite direction of disk emission, with a corresponding change of sign of the DP. We conclude that the spectroscopic phenomenon of the CQE has an interferometrical counterpart (dubbed CQE-PS) that presents itself as a central reversal in the DP profile. We note that this central reversal is an intrinsic phenomenon and is independent of the reversals described in Sect. 2.2.

We expect that the interferometric CQE is more ubiquitous than its plain spectral counterpart. Fig. 5 indicates that any radial motion above about $0.03\,v_{\rm orb}\sin(i)$ would destroy the spectroscopic CQE signature in a $10\,R_{\rm eq}$ disk. This is true regardless of the nature of this velocity, i.e., whether it is bulk motion (e.g., out or in-flow) or generated by turbulence. We emphasize, however, that the interferometric CQE signature is not affected, this effect relies on obscuration that travels from one side of the star ($-1 > v_{\rm orb}\sin(i) > -0.03$) to the other ($0.03 > v_{\rm orb}\sin(i) > 1$), while the spectroscopic CQE requires the lowest obscuration to occur at $v_{\rm proj} = 0$.

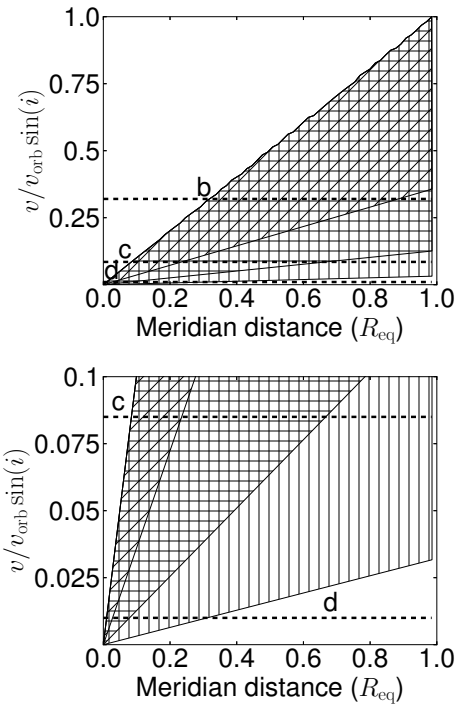

Fig. 5. Projected velocity of a Keplerian disk along the line-of-sight in units of the projected orbital speed at the base of the disk ($v_{\rm orb}\sin i$) vs. the normalized meridian distance (the distance to the stellar rotational axis in stellar radii). The intersection of a horizontal line with the hatched area indicates the range of meridian distances for which the projected velocity occurs. Results for different disk sizes are plotted: $R_{\rm disk} = 10\,R_{\rm eq}$, vertically hatched area; $4\,R_{\rm eq}$, horizontally hatched area; and, $2\,R_{\rm eq}$, diagonally hatched area. The velocities b to d from Figs. 1 and 4 are indicated as horizontal dashed lines. Top: full velocity range; bottom: zoom of the low-velocity components.

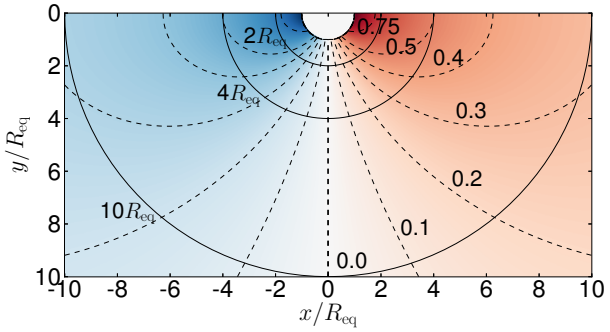

Fig. 6. Isovelocity contours (dashed lines) for a Keplerian disk. Each curve corresponds to a fraction of the projected orbital speed at the base of the disk ($v_{\rm orb}\sin i$), as indicated. The solid lines indicate different disk outer radii.

We conclude that the spectroscopic phenomenon of the CQE has an interferometrical counterpart (dubbed CQE-PS) that presents itself as a central reversal in the DP profile. We note that this central reversal is an intrinsic phenomenon and is independent of the reversals described in Sect. 2.2.

The effects of photocenter displacement can also be traced by the interferometric closure phases. In this work we only analyze the CQE effects on DP because they strongly rely on high spectral resolution data, providing a direct measure of the target's photocenter over the projected baseline. Accordingly, all discussions here are based on the photocenter of each spectral channel which is a quantity obtained by both techniques (closure phases and DP) in an equivalent way.

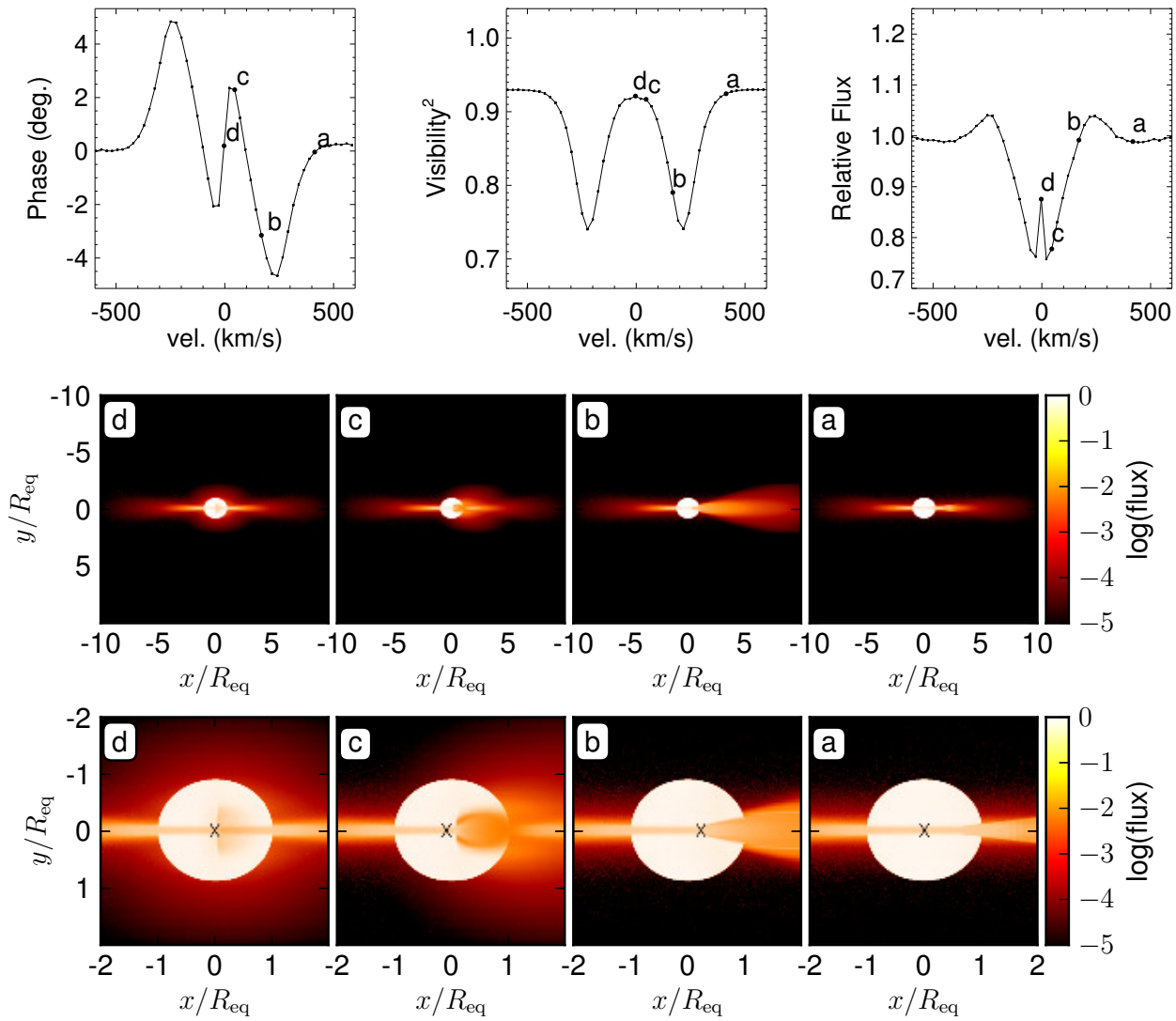

Fig. 4. Same as Fig 1 for $i = 90$ deg.

After understanding how disk absorption affects the DP, we now investigate under which circumstances the CQE-PS should be observable and what its diagnostic potential is for constraining the physical properties of the Be + disk system.

3.1. Spectral resolution

The CQE-PS critically depends on the spectral resolution of the interferometer, because the differential absorption that causes the CQE is only strong in a narrow wavelength range.

In Fig. 7, we see simulations of observations with different spectral resolutions for our reference model seen at $i = 90°$. The figure shows that the phase reversal would be unobservable at $R \approx 1500$, which is the medium resolution of the AMBER interferometer. Broader spectral channels also change the values of the DP since different emitting regions are sampled in each channel.

3.2. Geometrical considerations

Even if the physical conditions are ideal for CQE-PS, its occurrence strongly depends on the angle i and less intensely on the baseline on-sky orientation.

As an absorption effect, the CQE-PS will be stronger when the system is viewed edge-on, since the densest regions of the disks are those closest to the stellar equatorial region. Clearly, when the disk is viewed face-on, this phenomenon will not occur, since there is no absorbing material in front of the star. The effects of i on the CQE-PS are shown in Fig. 8, which demonstrates that the photocenter displacement due to the differential absorption is gradually weaker because less photospheric flux is absorbed for lower i.

Another factor that contributes to the amplitude of the CQE-PS is the baseline position angle. Because the photocenter displacements are expected to be parallel to the disk orientation, the CQE-PS will be highest when the baseline orientation is parallel to the disk major axis, as illustrated in Fig. 9.

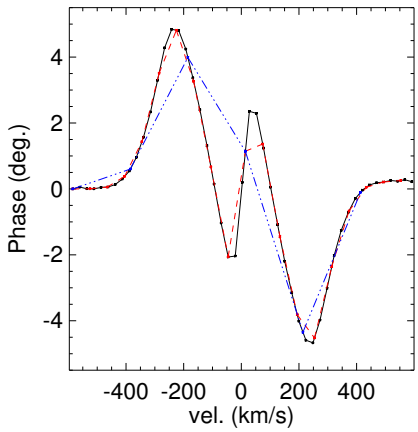

Fig. 7. Differential phase signal for the Be reference model with different spectral resolutions; R = 12000 black (full), R = 5000 red (dashed), and R = 1500 blue (dot-dashed) lines. Disk inclination angle is $i = 90°$.

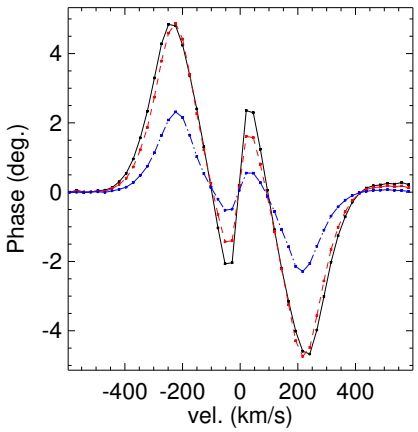

Fig. 9. Differential phase signal for the Be reference model for different angles between the projected baseline and the on-sky disk orientation: $\theta = 0°$ black (solid), $\theta = 45°$ red (dashed), and $\theta = 75°$ blue (dot-dashed) lines. Disk inclination angle is $i = 90°$.

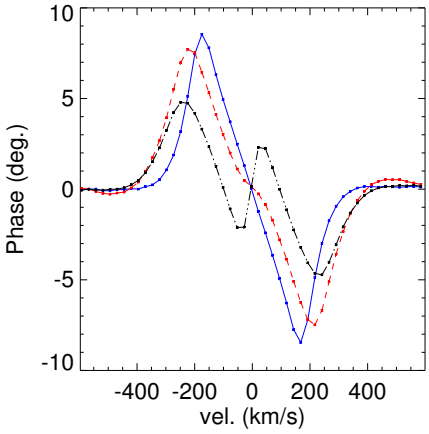

Fig. 8. Differential phase signal for the Be reference model for different disk inclinations: $i = 90°$ black (full), $i = 75°$ red (dashed), and $i = 45°$ blue (dot-dashed) lines.

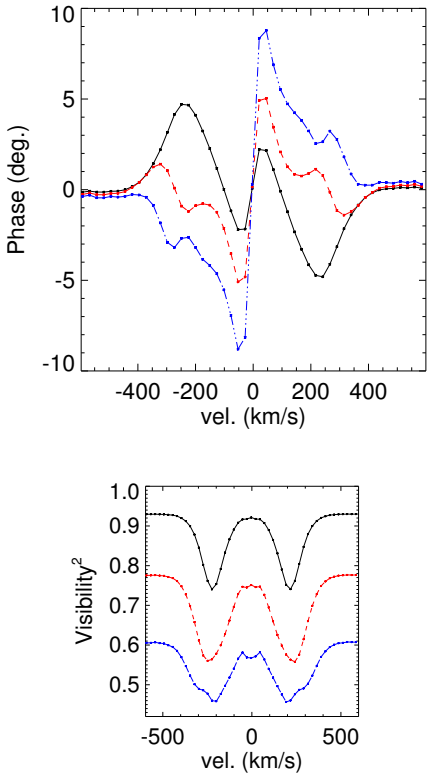

Fig. 10. Top: The differential phase signals for the Be reference model at $i = 90°$. The reference model is the black (full) line, observed with $\nu_{\rm obs}$ = 1 m pc^{-1} (astrometric regime); red (dashed) line $\nu_{\rm obs}$ = 2 m pc^{-1} and blue (dot-dashed) line $\nu_{\rm obs}$ = 3 m pc^{-1} (complex phase behavior). Bottom: The corresponding visibility signal.

3.3. CQE-PS outside the astrometric regime

The CQE-PS so far has been analyzed in the astrometric regime for which there is a direct correspondence between the target's photocenter and the DP. However, the CQE-PS is also present outside this regime, and the combination of the CQE-PS with high-resolution phase effects can result in very complex phase profiles. For instance, Fig. 10 shows how the DP signal is affected by higher spatial resolution: while the high-speed components display a complex behavior due to its more extended associated on-sky size, the CQE-PS part of the profile (low-velocity components) is still in the linear regime. Therefore, at high angular resolution the CQE-PS may even come to dominate the phase signal, which documents a phase reversal.

4. Diagnostic potential

In this section we investigate the effects of several physical parameters on the amplitude and shape of the CQE-PS. Hereafter, we assume that the interferometric baseline runs parallel to the stellar equator and $i = 90°$, since this choice maximizes the CQE-PS amplitude. All results shown were calculated for the reference model for $\nu = 1\,m\,pc^{-1}$, which corresponds to a typical Be star of spectral type B1 V seen at a distance of 100 pc and observed with baselines of 100 m.

In addition to the disk size, density slope, and density scale, we also explored the effects of stellar rotation rate and spectral type, disk scale height, and turbulent speed on the CQE-PS. We

found that the shape of CQE-PS is only little affected by these last parameters.

4.1. Disk density

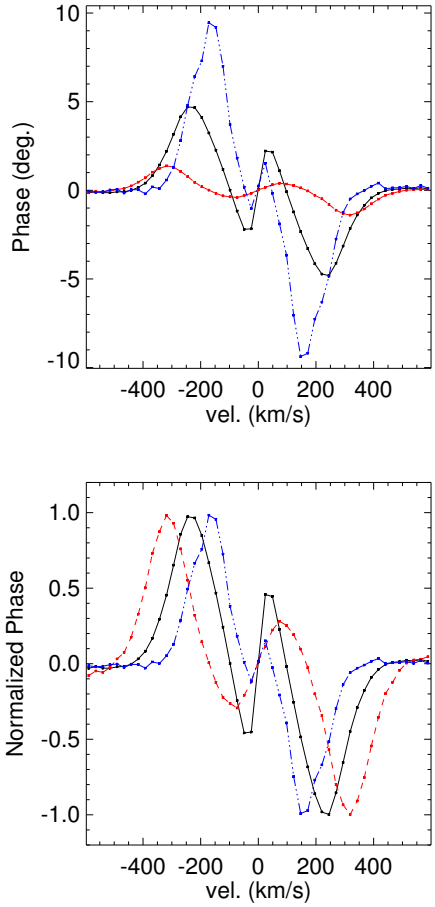

Fig. 11. Differential phase signal for the Be reference model for low- (10^{12} cm^{-3}, red dashed line) and high-density (10^{14} cm^{-3}, blue dot-dashed line) models. The reference model is the intermediate value (black full line).

The CQE-PS is a disk absorption effect, observable in the DP of Be stars together with the emission signal from the disk. The CS disk density is an important quantity for characterizing the stellar mass-loss rate and drives both the absorption and emission processes by the disk.

One can conceive two limits to the CQE-PS occurrence in terms of the disk density. Assuming a tenuous disk, absorption (both continuum and line) probably does not block the stellar photospheric flux very much, and we expect the phase profile to be little affected by it. At the other extreme,the opacity becomes so intense for very large disk densities that absorption is high, even at continuum wavelengths. However, emission is also quite high at high densities, therefore the occurrence of the CQE-PS in the high-density regime will depend on the process (absorption vs. emission) that controls the photocenter position at the wavelengths close to the line center.

In the top panel of Fig. 11 the effects of disk density on the CQE-PS are shown in a quantitative way. We considered three values for the number density at the base of the disk n_0: 10^{12} cm^{-3}, 10^{13} cm^{-3} (the reference model), and 10^{14} cm^{-3}. Since the DP amplitudes of these models are very different, the DPs were rescaled in the bottom panel to better illustrate the relative effect of the differential absorption versus differential emission on the shape of the DP. The relative weight of absorption vs. emission for different densities causes considerable changes in the detailed shape of the DP, which indicates that the CQE-PS can be a good quantitative diagnostic of disk density. For instance, in the high-density model (blue curve in Fig. 11) the emission almost completely outweighs the absorption, and as a result, the DP profile has just a slight hint of the CQE-PS. In our modeling we found that for a typical Be star, the density value that results in the highest contrast between the emission and absorption (i.e., the most pronounced CQE-PS) is $n_0 \sim 10^{13}$ cm^{-3}.

4.2. Disk size

In this subsection, we evaluate the effect of the disk outer radius on the CQE-PS. Very little is known about the actual size of Be star disks. For known Be binaries, such as ζ Tauri (Štefl et al. 2009), the disk is expected to be truncated at some radius (see, e.g., Carciofi et al. 2009), but for isolated stars there is in principle no limit for the disk size (Okazaki 2001).

Alternatively, one can define a region of the disk that is radially opaque to continuum or line radiation and therefore dominates the disk emission. The radius of this pseudo-photosphere[1] (R_p) depends on the wavelength considered; for instance, as discussed in Haubois et al. (2012), for a fully developed disk, the pseudo-photosphere extends to about $R_p = 2\,R_\star$ at the V band and $R_p = 4\,R_\star$ at the K band. For line transitions such as H I Brγ, this region can be as large as $R_p = 10$–$20\,R_\star$. If the physical size of the disk is larger than the radius of the pseudo-photosphere at a given band, observations in this band constrain only the latter, and not the former. This point is illustrated in Fig. 12, where we present simulations of the reference model with different truncation radii ($R_{disk} = 2$, 4, 10 and $20\,R_\star$). The models with the largest disk radii are essentially identical, which means that the size of the pseudo-photosphere for the reference model is $R_p \lesssim 10\,R_\star$.

The situation for small disk models is quite the opposite; as shown in Fig. 12, the CQE-PS provides an unequivocal constraint to the size of the disk. Insofar as we consider smaller disks, the size of the emitting lobes decreases; as a result, the central reversal of the DP profile, which is a measure of disk absorption, becomes increasingly more marked (see the red curve in Fig. 12, which shows results for $R_{disk} = 4\,R_\star$). The net effect is that the DP peak shifts away from the line center, because the low-velocity components of the disk were removed, and the amplitude of the central reversal increases. Interestingly, for very small disks the central reversal may even dominate the entire phase profile, providing what looks like an inverted phase profile. Observations of such a disk might be misinterpreted as a disk rotating in the opposite direction! Note, however, that disk emission for such a small disk still appears as small "wings" in the DP profile where no significant absorption is present and the disk emission can be clearly seen.

[1] Note that other works (e.g., Harmanec 1994, 2000) have used the term pseudo-photosphere to denote the region within which the disk viewed face-on is optically thick and so looks like an extension of the stellar phtosphere.

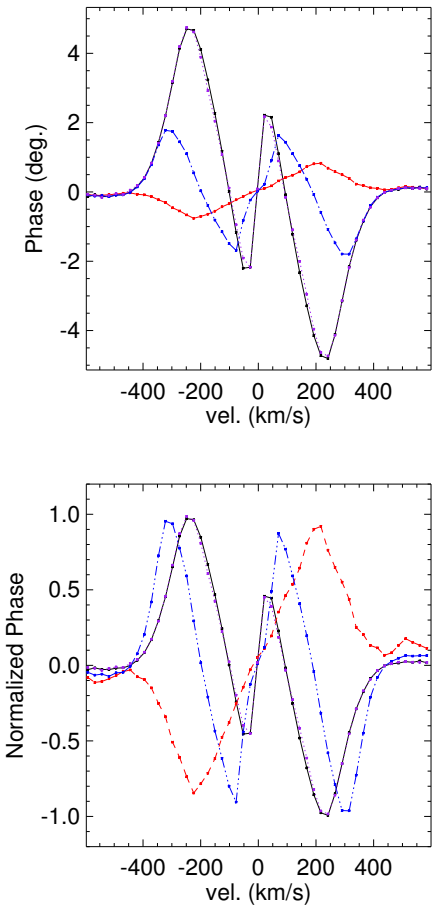

Fig. 12. Differential phase signal for the Be reference model for different disk sizes: $R_{\rm disk}$ = 2 (red dashed line), 4 (blue dot-dashed line), 10 (black full line) and 20 $R_\star$ (purple pointed line). The signals for $R_{\rm disk}$ = 10 and 20 $R_\star$ are almost coincident.

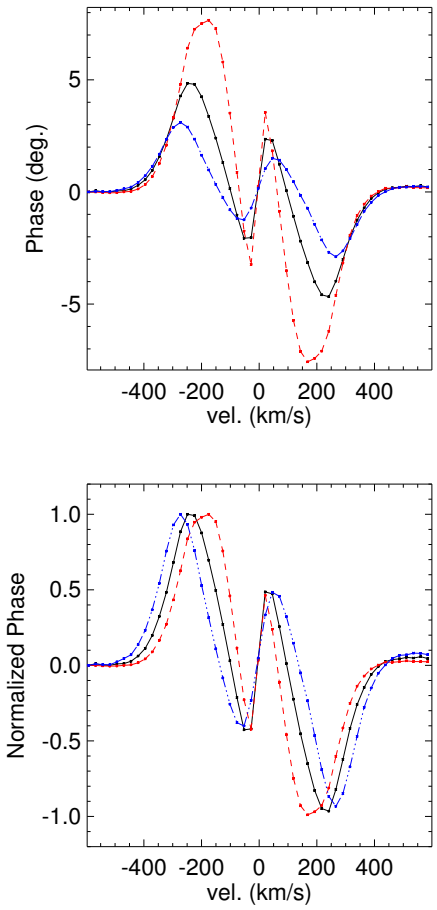

Fig. 13. Differential phase signal for the Be reference model with different radial density exponents: m = 3.0 (red dashed line), 3.5 (black full line) and 4.0 (blue dot-dashed line).

4.3. Radial density distribution

Haubois et al. (2012) studied the temporal evolution of viscous disks around Be stars and how different mass-loss rate histories affect the disk structure. It was found that the disk density profile is highly variable in time and that is is not possible to assign one single density slope m ($n \propto r^{-m}$) to the entire disk. However, constraining the disk slope from observations can be quite useful, since an actively forming disk will have quite different density slopes than dissipating disks. For the former case, m is typically larger than 3.5, while for the latter it is $m \lesssim 3$.

Here again the pseudo-photosphere concept can be useful. Flat disk-density distributions ($m < 3.5$) correspond to larger pseudo-photospheric radii, which lead to higher contributions of lower projected velocities in the phase profile, while the converse is true for sharp disk-density profiles ($m > 3.5$). Fig. 13 shows the Be reference model run for different radial density exponents. As the disk density slope decreases, the density becomes concentrated in the inner regions and the CQE-PS reversal feature broadens and increases in importance relative to the emission part of the phase profile.

Both a flat disk density distribution (low index m) and a high base density (n_0) enhance the disk emission in a similar way, thus creating large PS amplitudes (Figs. 11 and 13). However, the CQE-PS may allow distinguishing the two cases by comparing the detailed shape of the central reversal: whereas a higher density decreases the amplitude of the phase reversal, a lower index m increases it. This arises from the fact that for lower-density exponents the opacity decreases more slowly with radius. Therefore, a flat density slope is associated with more absorbing material in front of the star, which results in stronger contrasts between the flux from one side of the star vs. the other. This is illustrated in Fig. 5, which shows that the larger the size of the disk (or, equivalently, of the pseudo-photosphere), the larger the amount of material with the appropriate projected radial velocity.

4.4. Asymmetric configurations and time-dependence

The CQE-PS can be also employed to trace short-time CS variations thanks to its sensitivity to the disk inner regions. This information, linked to disk rotation, enables a disk azimuthal characterization. Similarly, it can map the evolution of the disk properties as a function of time.

The characterization of disk properties at different rotational phases would be useful for studying complex phenomena, such as the so-far unexplained triple-peaked Hα emission profiles (e.g., ζ Tauri, as in Štefl et al. 2009). This particular feature may be restricted to binary Be systems, but it is not well understood. Determining the disk configuration in such a system could offer some constraints for the influence of the companion.

Moreover, when Be stars change their brightness, this can originate in the star, the disk, or both. Although most of the observed variations are attributed to disk changes (Haubois et al. 2012), the CQE-PS can be used to settle this question because it is very sensitive to the disk part whence most of the excess flux in the visible range comes from.

4.5. Stellar angular size

Because CQE-PS absorption is generated across the stellar photosphere, it can be used to estimate the stellar angular size from the CQE-PS signal.

In a rotating disk, the positive (or negative) radial velocity components are projected at half of the stellar photosphere, which means that differential absorption can block at most half of the photospheric flux at a given wavelength. It can be easily demonstrated in this scenario of maximum absorption that the displacement of the photocenter due to absorption is a fraction $p \approx 2/5$ of the stellar radius, where p is the barycenter of a unitary and uniform vertical semi-circle:

$$p = \frac{2}{\pi} \int_0^1 \int_{-\sqrt{1-x^2}}^{\sqrt{1-x^2}} x \, dy \, dx \, . \tag{4}$$

The photocenter shift (Eq. 3) driven by absorption can be measured as $\Delta\boldsymbol{\epsilon} = p \cdot (R_{\rm eq}/d)$, where $R_{\rm eq}$ is the stellar radius, and d its distance with $0 < p < 2/5$. This quantity is particularly interesting because we have an estimate of the ratio of $R_{\rm eq}/d$ in a visibility-independent measurement.

In our reference model, which can be considered representative for the stars that exhibit the phase-reversal profile, the factor p is about 1/8. This value, lower than 2/5, is due to a smaller obscured area of the star and to the contribution of line emission by the disk. In any event, this analysis allows one to obtain a lower limit of the stellar radius.

5. Conclusions

With the advent of modern spectro-interferometers it became possible to measure the variation of the interferometric phase across an emission line. It was generally expected that these phase diagrams would display a simple S-shaped profile consisting of a single reversal, resulting from line emission from a rotating disk. This picture was largely confirmed by measurements made with moderate spectral resolution. However, at high spectral resolution, such as can be obtained by AMBER/VLTI, observations have shown a more complex phase profile. Conceptually, deviations from the canonical S-shaped profile can be expected in two circumstances: (i) by purely interferometric properties of observations outside the marginally resolved regime, where the differential phases no longer correspond to the photocenter of the system (i.e., end of the astrometric regime), and (ii) by physical processes accessible at high spectral resolution that affect the interferometric signal. We found for a typical Be system that the astrometric regime occurs when the visibilities are higher than 0.8. This corresponds to observations when $\nu_{\rm obs}$ is lower than $1.5\,{\rm m\,pc^{-1}}$. The exact value of this quantity depends on the target's brightness distribution.

We discussed the role of radiative transfer effects (ii, above), in particular, line transfer in a rotating disk, on determining the detailed shape of the high-resolution phase signal. We demonstrated that differential line absorption by the rotating disk can cause a well-defined photocenter displacement, which in turn affects the detailed shape of the interferometric phases. We dubbed this effect CQE-PS (central quasi-emission phase signature), in reference to the fact that the same mechanism produces the CQE phase profile of shell stars (Hanuschik 1995; Rivinius et al. 1999). A detailed explanation of the CQE-PS was presented in Sect. 3.

The shape and amplitude of the CQE-PS depends on a number of parameters, both intrinsic to the system and related to the observational setup (baseline length and orientation). Using a realistic model consisting of a rotating B1 V star with a viscous decretion disk, we made an initial study to assess to diagnostic potential of CQE-PS.

Among the several model parameters explored, we found that the signal is sensitive to the CS disk density, disk size, and the radial density distribution of the CS material. Varying each of these parameters generated a characteristic shape in the differential phase diagram, which demonstrates the diagnostic potential of the CQE-PS. The amplitude of the predicted signals in phase is higher than the error for the current interferometers with high spectral resolving power (typically $\lesssim 1^\circ$ for AMBER/VLTI and $\lesssim 3^\circ$ for VEGA/CHARA).

Certain conditions and parameters make the effect more pronounced. Observationally, the effect is strongest for edge-on viewing (shell stars) and for baselines oriented parallel to the disk equator. Physically, the effect is strongest for base disk densities of $n_0 \sim 10^{13}\,{\rm cm^{-3}}$ and disks larger than about $10\,R_\star$.

A remarkable result of the CQE-PS is its ability to make a (lower) estimate of the stellar angular size even when the observed squared visibilities are close to unity. This result may extend the distance range at which such an estimate can be made with interferometry.

The full power of this diagnostic tool will be realized when it is applied to observations over a full disk life-cycle, from first ejection through final dispersal, over a full V/R cycle of disk oscillation, or over a full orbital period in a binary system. The determination of the temporal dependence of the CS parameters will enable exploring fundamental physical processes operating in the disk, which are responsible for the disk evolution timescales, the stellar mass-loss rate, and mass ejection episodes.

Acknowledgements. DMF, ACC and ADS thank the CNRS-PICS program for supporting our Brazilian-French collaboration and the present work. DMF acknowledges support from FAPESP (grant 2012/04916-7). ACC acknowledges support from CNPq (grant 307076/2012-1) and FAPESP (grant 2010/19029-0). This work has made use of the computing facilities of the Laboratory of Astroinformatics (IAG/USP, NAT/Unicsul), whose purchase was made possible by the Brazilian agency FAPESP (grant 2009/54006-4) and the INCT-A.

References

Bjorkman, J. E. 1997, in Lecture Notes in Physics, Berlin Springer Verlag, Vol. 497, Stellar Atmospheres: Theory and Observations, ed. J. P. De Greve, R. Blomme, & H. Hensberge, 239
Bjorkman, J. E. & Carciofi, A. C. 2005, in Astronomical Society of the Pacific Conference Series, Vol. 337, The Nature and Evolution of Disks Around Hot Stars, ed. R. Ignace & K. G. Gayley, 75
Born, M. & Wolf, E. 1980, Principles of Optics Electromagnetic Theory of Propagation, Interference and Diffraction of Light
Carciofi, A. C. 2011, in Active OB Stars, Vol. 272, IAU Symposium, ed. C. Neiner, G. Wade, G. Meynet, & G. Peters, 325–336
Carciofi, A. C. & Bjorkman, J. E. 2006, ApJ, 639, 1081
Carciofi, A. C. & Bjorkman, J. E. 2008, ApJ, 684, 1374
Carciofi, A. C., Bjorkman, J. E., Otero, S. A., et al. 2012, ApJ, 744, L15
Carciofi, A. C., Okazaki, A. T., Le Bouquin, J.-B., et al. 2009, A&A, 504, 915
Domiciano de Souza, A., Zorec, J., Jankov, S., et al. 2004, A&A, 418, 781
Faes, D. M., Carciofi, A. C., Rivinius, T., et al. 2012, in Circumstellar Dynamics at High Resolution, Vol. 464, PASPC, ed. A. C. Carciofi & T. Rivinius, 141
Hanuschik, R. W. 1995, A&A, 295, 423

Harmanec, P. 1994, in NATO ASIC Proc. 436: The Impact of Long-Term Monitoring on Variable Star Research: Astrophysics, ed. C. Sterken & M. de Groot, 55
Harmanec, P. 2000, in Astronomical Society of the Pacific Conference Series, Vol. 214, IAU Colloq. 175: The Be Phenomenon in Early-Type Stars, ed. M. A. Smith, H. F. Henrichs, & J. Fabregat, 13
Haubois, X., Carciofi, A. C., Rivinius, T., Okazaki, A. T., & Bjorkman, J. E. 2012, ApJ, 756, 156
Jankov, S., Vakili, F., Domiciano de Souza, Jr., A., & Janot-Pacheco, E. 2001, A&A, 377, 721
Jones, C. E., Sigut, T. A. A., & Porter, J. M. 2008, MNRAS, 386, 1922
Kraus, S., Monnier, J. D., Che, X., et al. 2012, ApJ, 744, 19
Lee, U., Osaki, Y., & Saio, H. 1991, MNRAS, 250, 432
McGill, M. A., Sigut, T. A. A., & Jones, C. E. 2011, ApJ, 743, 111
Meilland, A., Stee, P., Vannier, M., et al. 2007, A&A, 464, 59
Mourard, D., Clausse, J. M., Marcotto, A., et al. 2009, A&A, 508, 1073
Okazaki, A. T. 2001, PASJ, 53, 119
Petrov, R. G., Malbet, F., Weigelt, G., et al. 2007, A&A, 464, 1
Porter, J. M. & Rivinius, T. 2003, PASP, 115, 1153
Quirrenbach, A., Bjorkman, K. S., Bjorkman, J. E., et al. 1997, ApJ, 479, 477
Rivinius, T., Štefl, S., & Baade, D. 1999, A&A, 348, 831
Stee, P. 1996, A&A, 311, 945
Štefl, S., Rivinius, T., Carciofi, A. C., et al. 2009, A&A, 504, 929
von Zeipel, H. 1924, MNRAS, 84, 665
Wheelwright, H. E., Bjorkman, J. E., Oudmaijer, R. D., et al. 2012, MNRAS, 423, L11

Chapter 5

Resolving the photospheres of fast rotating stars

The possibility of resolving stellar photospheres, specially for main sequence stars, has been a dream of astronomers for centuries. To know in detail the photospheric emission of other stars is critical for verifying our understanding of the process involved in stellar astrophysics. Rotation is an ingredient that causes great impact on the stars: it prolongs stellar lifetime, modify chemical yields, and is possibly reflected to the stellar remnant at the end of their lifetime.

Interferometric observations are sensitive to rotational effects, namely geometrical oblateness and gravity darkening. In order to understand these effects and verify a number of contemporary stellar rotational models being developed, a detailed investigation of the photosphere of rotating stars is needed.

Bn and Be stars are main sequence B-type stars with high rotation rates. On the one hand, Be stars can be easily recognized by their episodic emission lines. On the other hand, Bn stars are characterized by their broad absorption lines with the complete absence of circumstellar emission. Therefore, they are viewed roughly equator-on. A Bn star can resemble exactly as a Be star in its quiescent phase (i.e., a phase where the circumstellar disk is absent) if it is seen edge-on. The opposite, namely that a Bn star suddenly develops strong emission line could, in principle, occur. However, there is no such observational record. So, due to their similarity, Bn and Be stars in quiescent phases can share the same techniques for investigation and reconstruction of their photospheres. An-type stars possess the similar properties of Bn stars, while having smaller masses (and correspondingly, smaller surface temperatures).

Comments on fast B-type star evolution

Since Bn and Be stars display common properties, the question that arises is if the Be phenomenon belongs to a separate branch or a common phase in the evolution of rapidly rotating B star.

The numbers of Be and Bn stars contained in the Bright Star Catalogue (Hoffleit and Warren, 1995) are about equal. But global occurrence of the phenomenon is not easy to estimate: while the Be phenomenon is easily seen from any inclination angle, the Bn star are only recorded as such when seen close to equator-on viewing. Another issue is, while Bn fast rotators should remain as such throughout the main sequence due to the lack of braking mechanism for the angular momentum, the variability of the Be phenomenon makes it difficult to estimate how long the phenomenon is present during the main sequence phase.

In any case, occurrence of Be/Bn transitions appears to be absent. There are three main characteristics that differentiate Be and Bn stellar types and point to independent evolutionary paths: (i) no record in decades of Bn stars observations displaying any circumstellar emission; (ii) the complete absence of magnetic fields in Be stars, in contrast with a high incidence them among Bn stars; and (iii) the absence of non-radial pulsation in Bn stars, in contrast with the relatively high incidence among Be stars.

This chapter presents newly developed techniques for the photospheric characterization of fast rotating stars applied to the Be star Achernar. Before detailing these new techniques, we reproduce part of the interferometric review of this star presented in Faes et al. (2015).

5.1 The photosphere of Achernar probed by interferometry

Achernar (α Eridani, HD 10144) is the closest and brightest Be star in the sky. The successive generations of beam combiners of ESO-VLTI have being used to study Achernar. This section summarize these early interferometric studies. All parameters derived from interferometry strongly depend on modeling (i.e., accurate brightness distribution), which is wavelength dependent. This is particularly important for stars with (potential) circumstellar emissions in addition to the photospheric one. Nevertheless, fundamental physical properties from both photosphere and CS environment could be constrained based on the

high-angular resolution information available.

First oblateness determination with VLTI-VINCI

Domiciano de Souza et al. (2003) determined for the first time the oblateness of Achernar (and of a Be star) with K-band visibility data from VINCI interferometer. It was also the first estimation of the on-sky orientation of the star. The diameter ratio between the equator and the pole $R_{\rm eq}/R_p = 1.56$ was found adjusting V^2 to each projected position angle (PA) of the observations the size of the equivalent uniform disk, and then fitting and ellipse. This was a minimum value to the radius ratio since it was a projected ratio where Achernar is seen at a viewing angle $i \neq 90°$.

Although undoubtedly indicating a high rotation rate for the star, that was not necessarily implying a rotation above the Roche limit (i.e., $W > 1$): the radii ratio depends on the underlying stellar model (which the fit of multiple uniform disks is just a first approximation of the stellar brightness distribution). Knowing that the star had a little activity at the time of the observations (e.g., Vinicius et al. 2006), the authors have also explicitly ignored the contribution of the CS component in the data since it was a much weaker emission than the stellar one ($< 5\%$).

On a polar emission in the interferometric signal

Kervella and Domiciano de Souza (2006) analyzed Achernar's VINCI data from both K and H bands together. They have done a single fit on them adopting a uniform ellipse brightness distribution for the star. The diameter ratio between the equator and the pole was then $R_{\rm eq}/R_p = 1.41$ ($W = 0.906$; again a minimum value due to viewing-angle $i \neq 90°$).

In this scenario, the addition of a elongated CS envelope in the polar direction with Gaussian brightness distribution superimposed to the stellar model significantly improved the quality of the fitting. This CS component had $\approx 4.5\%$ of the total flux and removed the trend that appeared in the residuals of the uniform ellipse in PAs around the polar direction. This study was made using only the VINCI data as constraint, and did not relate the polar CS emission with other observables.

The first multi-technique analyzes

Carciofi et al. (2008) and Kanaan et al. (2008) have independently done a multi-

technique fitting of Achernar at the time of VINCI observations. They have used SED and Hα line profiles as constraints, and linked them with polarimetric estimates. Although taking into account the brightness distribution by the von Zeipel effect and the Roche geometry due to the high rotation of the star, they found distinct results: while Carciofi et al. argue that the presence of a residual CS disk in Achernar is sufficient to explain the observed quantities with a near-critical rotating star, Kanaan et al. conclude that at the time of the VINCI observations Achernar had either a small or no CS disk, but it did have a polar, stellar wind.

5.2 *Photospheres seen by Differential Phases*

We have seen at that the quantity recorded in interferometry is the normalized complex visibility $\tilde{V} = \|V\| \exp(i\phi)$, where a common quantity used in high spectral resolution interferometry are the differential phases $\phi_{\rm diff}$ (Sect. 1.6). Also, the interferometric DPs can be associate to photocenter positions, as discussed in Chap. 4. The relation of the phase signal and the photocenter position is useful when interpreting the differential phases signal of fast rotating stars. When looking at a rotating star in spectrointerferometry at a given spectral line, we are actually seeing the sum fo all positions on the stellar photosphere where the line center appears in the rest wavelength. An example is Fig. 5.1, where the photocenter displacements are show for a differential rotating star. For a rigid rotating star seen equator-on, as we go from $-v_{\rm rot}$ to $v_{\rm rot}$ spectral channels, we see a moving strip in all latitudes from one edge to another, passing over the rotation axis when $v_{\rm proj} = 0$ (line rest wavelength). The width of the line is proportional to the spectral channel range, i.e., the higher the spectral resolution on which the stellar surface is seen, the narrower the strip will appear (limited by atmospheric thermal or turbulent velocities).

When measuring the photosphere in continuum wavelengths, the interferometric phase signal points to the center of the projected disk (or ellipsoid, in case of fast-spinning stars). The presence of the strip within the line profile spectral channels will alter this. Since it is an absorption line, the photocenter is shifted towards the position opposite to the strip appearance. The interferometric phase signal for this scenario is a smooth S-shaped curve, centered at rest wavelength and with signal reaching the continuum at $\pm v \sin i$ wavelengths. This make An/Bn stars, with high $v \sin i$ values, excellent targets for

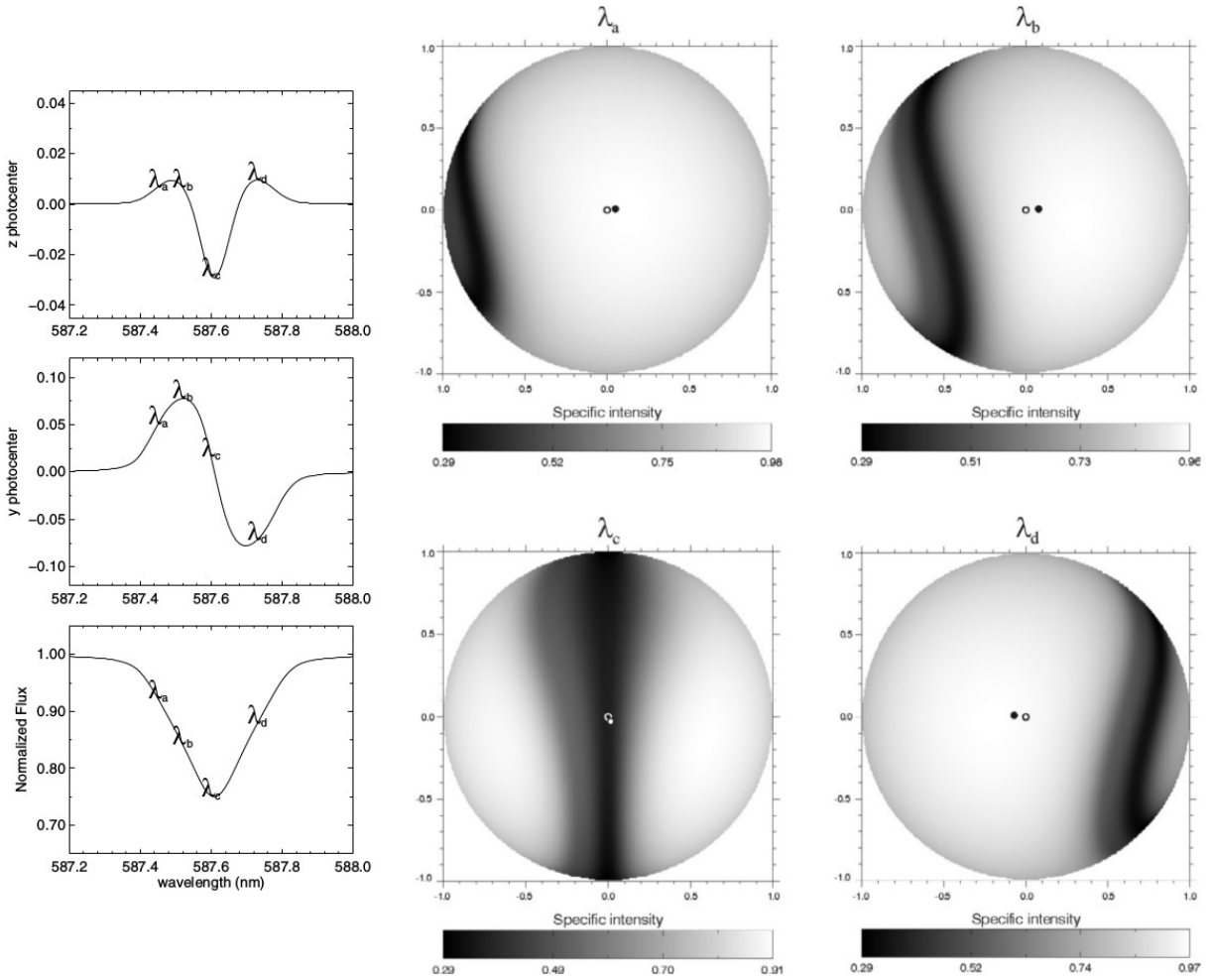

Figure 5.1: A differential rotating star and photocenter displacements within a spectral line (He I 5876 Å). *Left*: photocenter components, vertical (z; top) and horizontal (y; middle), and the normalized spectral flux (bottom) across the (asymmetric) line. Photocenter components are given in units of angular stellar radius. The letters indicate selected wavelengths corresponding to a region in the blue line wing (λ_a), the highest y value (λ_b), the central wavelength (λ_c), and the most positive value of z (λ_d). *Right*: intensity maps associated to the spectrointerferometric observables on the left side at the four selected wavelengths. The curved dark patterns correspond to Doppler shifts of the local line profile caused by differential rotation. These non-symmetrical intensity maps result in a displacement of the stellar photometric barycenter, i.e., the photocenter (filled circles), relative to the geometrical center (opened circles). (Domiciano de Souza et al., 2004).

applying spectrointerferometry.

The amplitude of the phase signal is proportional to the distance of the strip relatively to the stellar center, to the line depth in relation to continuous emission and to the length of the strip. The interferometric observations do not need to be in the marginally-resolved regime to apply this technique. What happens is that the phase signal loses the correspondence with the photocenter position but still depends on it. It is still possible to obtain information about the photocenter position, but this requires assumptions about the brightness distribution of the target (this was already discussed in Chap. 4).

The detailed DPs values, in any regime, will depend on the stellar parameters and can be used to recover the brightness distribution seen by the interferometer. Domiciano de Souza et al. (2012) show the expected DPs signal and its dependence with different stellar parameters.

I participated on the first determination of stellar parameters based on spectrointerferometry done by Domiciano de Souza et al. (2012) for the Be star Achernar based on VLTI-AMBER data and the CHARRON code. Since it is a Be star, it was important to the parameters assertion that at the time of interferometric observations no circumstellar emission was present. My main contribution to this study focused on this problem, determining if spectroscopic or polarimetric data indicated any circumstellar activity at the times of the AMBER observations. During all the considered period, the linear polarization levels were $P \lesssim 0.01(1)\%$ and the difference spectra, compared from the pure photospheric reference, were $\Delta\text{flux} \lesssim 0.01(1)\%$.

The derived equatorial angular diameter to Achernar was compatible with previous values from visibilities, and the diameter ratio was below the Roche limit ($R_{\rm eq}/R_p = 1.45; W = 0.949$). The list of best-fitted and respectely derived parameters is in Table 5.1. This first photospheric study with DPs was followed by Hadjara et al. (2014), who applied the technique to the An/Bn stars Altair, δ Aquilæ and Fomalhaut using the SCIROCCO code (Hadjara et al., 2013).

The DPs allows assessing information that goes beyond the diffraction limit of the optical interferometers since it is sensitive to photocenter position (sometimes referred as "super-resolution"). However, this analysis is based on strong assumptions about the photospheric absorption component: (i) the continuum emission is symmetric and determined only by the photosphere; (ii) the star must have a known pattern of rotation (e.g., rigid

Table 5.1 - Physical parameters of Achernar derived from AMBER differential phases at Brγ line with the CHARRON code (Domiciano de Souza et al., 2012).

Model free parameters fitted	Values and uncertainties
Equatorial radius ($R_\odot$)	11.6(0.3)
Equatorial rotation velocity ($\mathrm{km\,s^{-1}}$)	298(9)
Rotation-axis inclination angle (°)	78.5(5.2)
Position angle of the visible pole (°)	214.8(1.6)
Fixed and Derived params.	**Values**
Gravity darkening coefficient β	0.20
Rotation rate: W ($v_{\rm rot}/v_{\rm orb}$)	0.96
Radii ratio: $R_{\rm eq}/R_p$	1.45

rotation) and its shape is well set (e.g. projected Roche surface); (iii) the effect of gravitational darkening is properly considered; and (iv) the absorption profile depends only of the local temperature and gravity (i.e., no asymmetries along the absorption in different surface positions). Deviation from these assumptions will degrade the precision of the derived photospheric parameters. Although the method reproduce the spectrointerferometric data, the results obtained by Hadjara et al. (2014) indicate that a better error determination for the derived parameters is needed (see Sect. 5.4).

5.3 *Photospheres seen by Visibilities amplitudes and Closure Phases*

In Sect. 1.6 we said that closure phases add quantitative new information to the interferometric measurements. It also enables the the photospheric images techniques to operate, where Fourier analysis allows to rebuild arbitrary brightness distributions. However, these tools may require fine-tunning of numerical parameters to data fitting and sometimes strong hypotheses about the brightness distribution properties of the target need to be made.

One way of avoid using these tools is, instead of analyzing the signal to rebuild the image, is to create the expected images from the much fewer unknown parameters (i.e., the stellar photosphere parameters) and verify how they reproduce the observational data. With this methodology the Be star Achernar was revised applying the high precision visibilities measurements with closure phases information from the VLTI-PIONIER inter-

Table 5.2 - Physical parameters of Achernar derived from the RVZ model fitting (CHARRON code) to VLTI-PIONIER H band data using the MCMC method (Domiciano de Souza et al., 2014).

Model free parameters fitted	Values and uncertainties
Equatorial radius ($R_\odot$)	$9.16^{+0.23}_{-0.23}$
Equatorial rotation velocity ($\mathrm{km\,s^{-1}}$)	$298.8^{+6.9}_{-5.5}$
Rotation-axis inclination angle (°)	$60.6^{+7.1}_{-3.9}$
Gravity-darkening coefficient (β)	$0.166^{+0.012}_{-0.010}$
Position angle of the visible pole (°)	$216.9^{+0.4}_{-0.4}$
Derived parameters	**Values**
Rotation rate: W ($v_{\rm rot}/v_{\rm orb}$)	0.838
Radii ratio: $R_{\rm eq}/R_p$	1.352

ferometer by Domiciano de Souza et al. (2014).

The parametrization of the photosphere contained in the op. cit. work is based on the Roche surface for a rigid rotating star and a generalized von Zeipel description of the gravity darkening effect making use of the CHARRON code. This is here called RVZ (Roche-von Zeipel) model. For that work, I implemented a interface between CHARRON and the MCMC ensemble sampler EMCEE. This enabled the determination of the photospheric parameters that best-fitted the PIONIER data, their uncertainties, and possible correlations between the parameters determined.

The assumptions for the (parametric) modeling of the photospheric emission are: (i) the star must have a known shape due to its rotation (e.g. projected Roche surface); (ii) the effect of gravitational darkening is properly handle; and (iii) the photosphere emission depends only of the local temperature and gravity.

The list of RVZ model free parameters fitted for the synthetic photosphere is in Table 5.2. Fig. 5.2 shows the minimized paramaters PDFs and their correlations. The inclination angle i is clearly correlated with the equatorial velocity $V_{\rm eq}$, so that the derived pair $\{V_{\rm eq}, i\}$ is indicated along the $V_{\rm eq}\sin i$ constant value.

Residual disk characterization

The method described so far can only be applied to the photosphere of the star alone. The presence of any circumstellar emission should be taken into account in determining the photospheric parameters. In the op. cit. work I actively contributed to the investigation

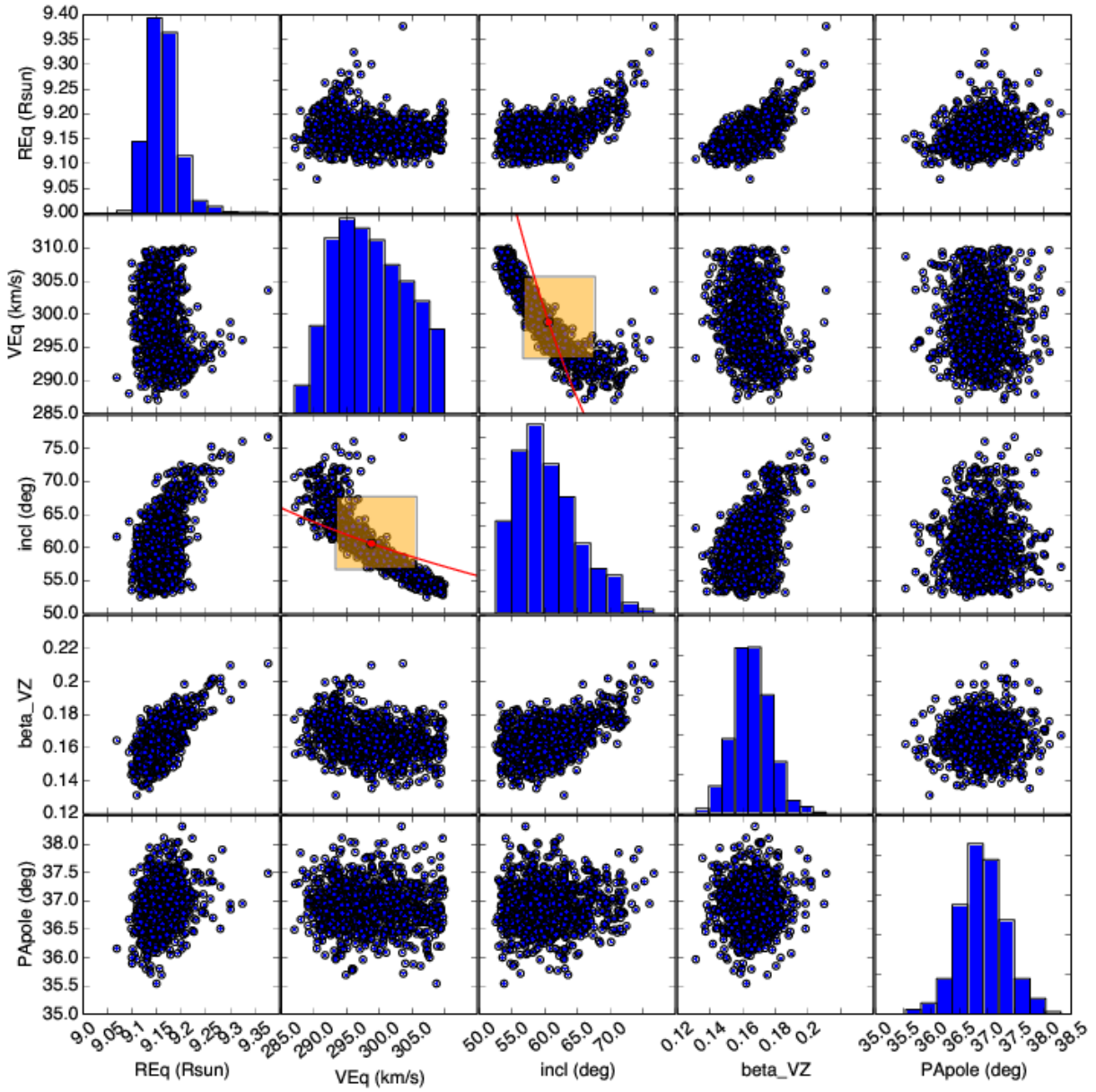

Figure 5.2: Probability density functions (PDFs) of the derived stellar parameters for Achernar and their correlation maps, corresponding to the PIONIER visibilites and closure phases minimization with CHARRON code. *From left to right (or top-bottom):* equatorial radius (Solar unit), equatorial velocity ($\mathrm{km\,s^{-1}}$), inclination angle (degrees), von Zeipel coefficient, and on-sky position angle of the rotation axis (degrees). The derived values to $\{V_{\rm eq}, i\}$ are indicated as a dot along the $V_{\rm eq}\sin i$ constant value line (in red).

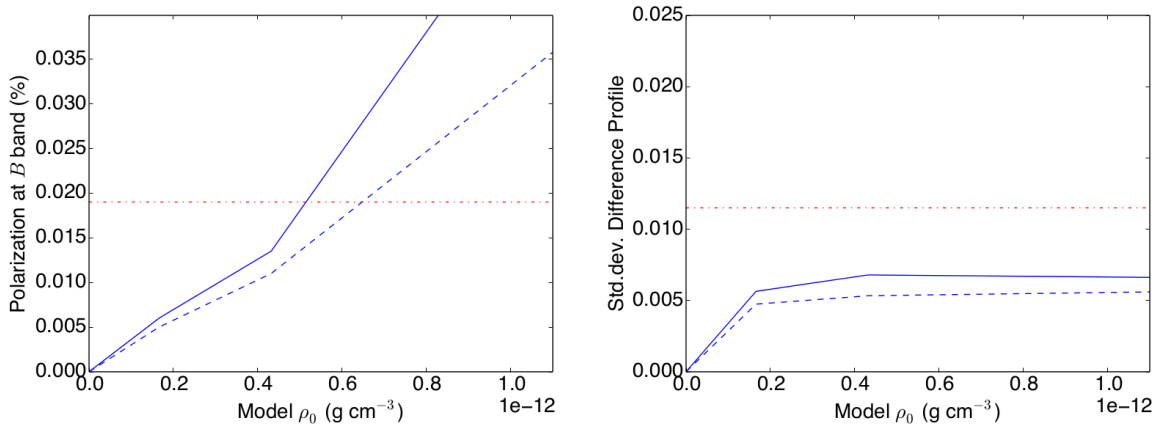

Figure 5.3: (*Left*) B-band polarization and (*right*) standard deviation of difference Hα profile as function of disk base density ρ_0 for the residual disk models based on Carciofi et al. (2008). The standard deviation is the root mean square of the disk model spectrum minus the pure photospheric profile. The horizontal dot-dashed lines represent the observational limits of average polarization and difference profile determined from observations performed at the epoch of interferometric observations. While the measured Hα difference profile level does not impose a limit to ρ_0, the measured average polarization sets a strict upper limit to this quantity: $\rho_0 \lesssim 0.52 \times 10^{-12}$ g cm^{-3} (Domiciano de Souza et al., 2014).

of spectroscopic and polarimetric data at the times of PIONIER observations of Achernar. Within the observational uncertainties, no positive activity was detected (in polarization, $P \lesssim 0.01(1)\%$ and the difference spectra to the photospheric profile, $\Delta\text{flux} \lesssim 0.01(1)\%$). The negative detection in these techniques do not exclude the possibility of a tenuous residual disk. Although not detectable in one or more techniques, a residual disk emission could change the interferometric signal and alter the determination of the photospheric parameters.

In order to characterize the densest possible residual disk around Achernar within the observational constrains available and how such disk might affect the interferometric measurements, simulations were performed with the HDUST code. For that, we used the synthetic photosphere parameters determined by CHARRON code and the VDD description for the disk.

Fig. 5.3, containts the B-band polarization and the standard deviation of difference Hα profile as a function of disk base density (ρ_0) on the residual disk models from Carciofi and Bjorkman (2008). That set the maximum base density of $\sim 0.52 \times 10^{-13}$ g cm^{-3} for the disk to be detectable. A comparison between (pure) photometric model with the residual disk set with the upper density limit were carefully conducted to (i) Hα line profile; the interferometric observables (ii) squared visibilities (V^2) in the H band, and (iii) Brγ

differential phases. We concluded that the residual disk could not considerably change the PIONIER data without first alter other observables available, notably polarimetry. So, no further component was needed to validated the CHARRON determination of the photosphere.

The von Zeipel coefficient variation with rotation

As the photosphere of stars starting been resolved by interferometry, it became clear that the stars do not follow the von Zeipel prescription to the gravity darkening effect, namely, $\beta = 0.25$ or $T_{\rm eff} \propto g_{\rm eff}^{1/4}$. The von Zeipel's β appears to decrease the fastest the star rotates.

Espinosa Lara and Rieutord (2011) (ELR) model predicted the dependence of the β parameter as a function of stellar rotation, assuming that the energy flux is a divergence-free vector, antiparallel to the effective gravity. So, the flux $\vec{F}$ has the dependence $\vec{F} = -f(r,\theta)\vec{g}_{\rm eff}$, where f is a function of stellar surface position. In doing so, it allows the ratio $\|\vec{F}\|/\|\vec{g}_{\rm eff}\|$ to vary with latitude. The prescription was tested using fully two-dimensional models of rotating stars produced by the ESTER code.

The first Achernar parameters reconstruction (Domiciano de Souza et al., 2012) was done with von Zeipel's β parameter fixed in 0.20. This was done, essentially, due to the weak dependence of the differential phases signal with respect to this parameter. That is not the case when looking at visibilities with closure phase information. The PIONIER information allows fitting β simultaneously with the other photospheric parameters.

The derived β value for Achernar, $0.166\,(^{+0.012}_{-0.010})$, matches very well the predicted value by the ELR model to its rotational rate. The derived temperature structure for the photosphere is illustrated in the Fig. 1.1. Slight differences between the RVZ and the ELR models exists, but they are much smaller that the derived uncertaints. Achernar is the fastest and more massive star with detailed photospheric information, and the results supports this linear dependence of the emitted flux and the local effective gravity in rotating stars as shown in Fig. 5.4.

The model-independent image reconstruction

Once the closure phases information are present, it is possible to apply regular image reconstruction techniques and compare with the employed methodology of model fitting.

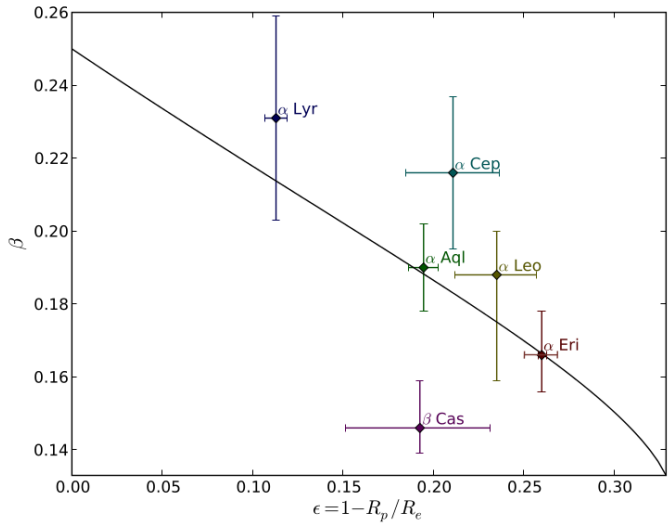

Figure 5.4: Gravity darkening coefficient β estimated from the ELR model (Espinosa Lara and Rieutord, 2011) as a function of the rotation flattening compared to values measured from interferometric observations of six rapidly rotating stars (Table 1.2), Achernar being the flattest one. The estimation of β is obtained from a fit to the $T_{\rm eff}$ vs. $g_{\rm eff}$ curves directly predicted by the ELR model. The ELR model predictions and interferometric measurements have a good general agreement (Domiciano de Souza et al., 2014).

This model-independent study was then applied to the PIONIER data of Achernar, using MIRA software (Multi-aperture Image Reconstruction Algorithm; Thiébaut, 2008) and using the parametric modeling as the prior image. Fig. 5.5, shows the reconstruction image of Achernar and its difference to the best-fit CHARRON image. The final images agreed within $\sim \pm 1\%$ of the intensity level, indicating that essentially only the photosphere of Achernar is contributing to the PIONIER data, without any additional circumstellar component. It also asserts the precision of the employed methods and the corresponding derived parameters.

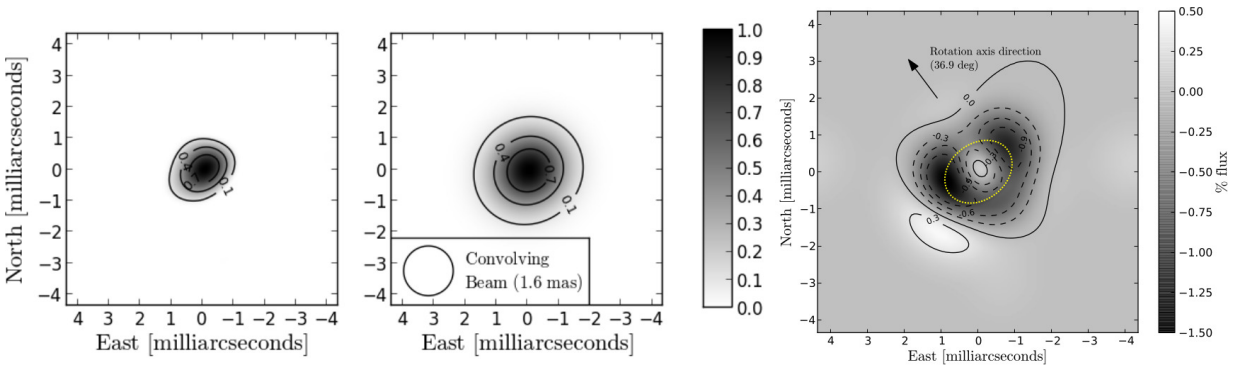

Figure 5.5: Left: Image reconstruction of Achernar obtained by applying the MIRA software to the *H* band VLTI/PIONIER observations. *Middle*: Convolution of this reconstructed MIRA image convolved by a Gaussian beam of FWHM = 1.6 mas $\left(= 0.61\lambda/\|\vec{B}^{\max}_{\text{proj}}\|\right)$ corresponding to the diffraction limit of the PIONIER observations. *Right*: Reconstructed MIRA image minus the best-fit CHARRON image (convolved by the Gaussian diffraction limit beam to match the resolution of reconstructed image). The difference between the images is very small ($\lesssim 1.5\%$ in modulus, relative to the total MIRA image flux), indicating that essentially only the photosphere of Achernar is contributing to the PIONIER data, without any additional circumstellar component. The dotted ellipse represents roughly the border of the apparent photosphere of Achernar given by the best-fit CHARRON RVZ model.

5.4 Chapter summary

The possibility of angularly resolving main sequence stars was achieved in the beginning of this century with optical interferometry. This opens new windows to the stellar astrophysics study, as the origin, role and impact of rotation on stars. For example, the discover that Vega is a rapid rotating star (Aufdenberg et al., 2006) lead to significantly revises our view of this fundamental standard (Rieke et al., 2008).

Both interferometric quantities, visibilities and phases, can be used to the photospheric parameters determination, while its reconstruction independent of models required the combination of both. Since the absolute phase information is destroyed by the atmosphere, the combined phase information of three telescopes can be recovered with the closure phases information - enabling the interferometric reconstruction techniques.

Here we show the results to the photospheric properties determination of Achernar for three different techniques, namely parametric minimization of (i) differential phases signal; (ii) visibilites and closure phases; and (iii) model-independent image reconstruction.

The differential phases method shown as useful proof-of-concept while determining the photospheric parameters. However, it is based on a differential quantity and strong assumptions are imposed when determining stellar parameters. In the specific case of

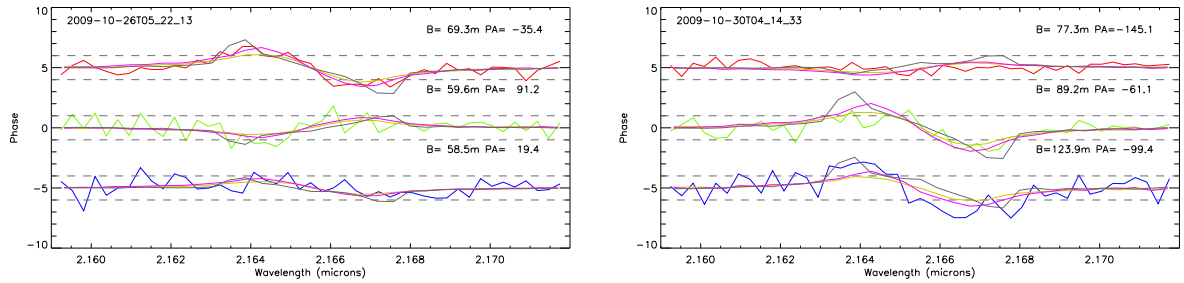

Figure 5.6: AMBER-VLTI pure photospheric observations of Achernar compared to (i) photospheric model of Domiciano de Souza et al. (2012) (purple line), (ii) photopheric model of Domiciano de Souza et al. (2014) (yellow line) and (iii) the latter model with a VDD steady-state residual disk with $R = 1.75 R_{\rm eq}$ and volumetric particle density of $n_0 = 5\,10^{12}$ cm^{-3} ($\rho_0 \sim 4.2\,10^{12}$ g cm^{-3}).

Achernar, it resulted in a quite big star ($R_p \sim 9\ R_\odot$, by both Domiciano de Souza et al., 2012; Hadjara et al., 2014) and could not constraint the gravity darkening coefficient β. Fig. 5.6 ilustrates the degeneracy of the photometric models derived from AMBER and PIONIER data.

The methods based on visibilities and closure phases, namely the parameters fitting and the image reconstruction, are fully compatible with each other and precisely determine the stellar photospheric properties of Achernar. The MCMC minimization tools were shown to be very useful when minimizing multiple parameters simultaneously, allowing to infer the uncertainties on their determination and the dependence between parameters.

The photospheric characterization of Achernar is important in many aspects. As a Be star, it is the first characterization of a Be central star photosphere. This assures, for example, that the rigid rotation with Roche geometry is a good assumption to this stellar type. And, since it is not rotating too close to the critical velocity, adds constraints to the mass loss mechanism in this kind of star. Also, it showed no signal of polar wind, contrary to previous interferometric results. These and other circumstellar features are further discussed in Chapter 6.

In the context of fast rotating stars, Achernar is the fastest and also the more massive star with known photospheric information. This is an important point to the investigation of these stars. For example, the derived von Zeipel β coefficient is fully compatible with the ELR model (Espinosa Lara and Rieutord, 2011), model which could explain the coefficient variation among of most stars with resolved photospheres.

5.5 Publication: Beyond the diffraction limit of optical/IR interferometers; I. Angular diameter and rotation parameters of Achernar from differential phases

A&A 545, A130 (2012)
DOI: 10.1051/0004-6361/201218782

Astronomy & Astrophysics

Beyond the diffraction limit of optical/IR interferometers⋆,⋆⋆,⋆⋆⋆

I. Angular diameter and rotation parameters of Achernar from differential phases

A. Domiciano de Souza[1], M. Hadjara[1,2], F. Vakili[1], P. Bendjoya[1], F. Millour[1], L. Abe[1], A. C. Carciofi[3], D. M. Faes[1,3], P. Kervella[4], S. Lagarde[1], A. Marconi[5], J.-L. Monin[6], G. Niccolini[1], R. G. Petrov[1], and G. Weigelt[7]

[1] Laboratoire J.-L. Lagrange, UMR 7293, Observatoire de la Côte d'Azur (OCA), Université de Nice-Sophia Antipolis (UNS), Centre National de la Recherche Scientifique (CNRS), Campus Valrose, 06108 Nice Cedex 2, France
e-mail: Armando.Domiciano@oca.eu
[2] Centre de Recherche en Astronomie, Astrophysique et Géophysique (CRAAG), Route de l'Observatoire, BP 63, Bouzareah 16340, Alger, Algérie
[3] Instituto de Astronomia, Geofísica e Ciências Atmosféricas, Universidade de São Paulo (USP), Rua do Matão 1226, Cidade Universitária, São Paulo 05508-900, Brazil
[4] LESIA, Observatoire de Paris, CNRS UMR 8109, UPMC, Université Paris Diderot, 5 Place Jules Janssen, 92195 Meudon, France
[5] INAF-Osservatorio Astrofisico di Arcetri, Largo E. Fermi 5, 50125 Firenze, Italy
[6] UJF-Grenoble 1 / CNRS-INSU, Institut de Planétologie et d'Astrophysique de Grenoble (IPAG) UMR 5274, 38041 Grenoble, France
[7] Max-Planck-Institut für Radioastronomie, Auf dem Hügel 69, 53121 Bonn, Germany

Received 6 January 2012 / Accepted 26 July 2012

ABSTRACT

Context. Spectrally resolved long-baseline optical/IR interferometry of rotating stars opens perspectives to investigate their fundamental parameters and the physical mechanisms that govern their interior, photosphere, and circumstellar envelope structures.
Aims. Based on the signatures of stellar rotation on observed interferometric wavelength-differential phases, we aim to measure angular diameters, rotation velocities, and orientation of stellar rotation axes.
Methods. We used the AMBER focal instrument at ESO-VLTI in its high-spectral resolution mode to record interferometric data on the fast rotator Achernar. Differential phases centered on the hydrogen Br γ line (K band) were obtained during four almost consecutive nights with a continuous Earth-rotation synthesis during ~5 h/night, corresponding to ~60° position angle coverage per baseline. These observations were interpreted with our numerical code dedicated to long-baseline interferometry of rotating stars.
Results. By fitting our model to Achernar's differential phases from AMBER, we could measure its equatorial radius $R_{\rm eq} = 11.6 \pm 0.3\,R_\odot$, equatorial rotation velocity $V_{\rm eq} = 298 \pm 9\,{\rm km\,s^{-1}}$, rotation axis inclination angle $i = 101.5 \pm 5.2°$, and rotation axis position angle (from North to East) $\mathrm{PA_{rot}} = 34.9 \pm 1.6°$. From these parameters and the stellar distance, the equatorial angular diameter $\oslash_{\rm eq}$ of Achernar is found to be 2.45 ± 0.09 mas, which is compatible with previous values derived from the commonly used visibility amplitude. In particular, $\oslash_{\rm eq}$ and $\mathrm{PA_{rot}}$ measured in this work with VLTI/AMBER are compatible with the values previously obtained with VLTI/VINCI.
Conclusions. The present paper, based on real data, demonstrates the super-resolution potential of differential interferometry for measuring sizes, rotation velocities, and orientation of rotating stars in cases where visibility amplitudes are unavailable and/or when the star is partially or poorly resolved. In particular, we showed that differential phases allow the measurement of sizes up to ~4 times smaller than the diffraction-limited angular resolution of the interferometer.

Key words. stars: rotation – stars: individual: Achernar – methods: observational – methods: numerical – techniques: interferometric

1. Introduction

By combining high angular and high spectral resolution, differential interferometry (DI; i.e., the measurement of wavelength-differential phases or wavelength-differential visibilities) yields physical parameters of sources with important wavelength-dependent spatial structures, even in cases where these sources are only poorly or partially resolved by the telescope (single-aperture) or the interferometer (multi-aperture).

Because they are self-calibrated and essentially seeing-independent, DI observables are usually more reliable than absolute visibility amplitude, which is the classical observable used to measure stellar angular diameters. Moreover, visibility amplitudes below ≃0.7 (well-resolved objects) are typically required to attain useful constraints (a few percent) on the angular diameters. This demands access to relatively long baselines (≃100−300 m) for optical/IR interferometers in order to measure angular diameters of ≃0.5−2 mas, a typical range of values for many bright stars. These observational constraints are relaxed in DI, where more precise and accurate stellar parameters can be measured for stars only slightly to partially resolved,

⋆ Based on observations performed at ESO, Chile under AMBER-consortium GTO programme ID 084.D-0456.
⋆⋆ Full Fig. 5 is available in electronic form at http://www.aanda.org
⋆⋆⋆ The FITS tables of the reduced data are only available at the CDS via anonymous ftp to cdsarc.u-strasbg.fr (130.79.128.5) or via http://cdsarc.u-strasbg.fr/viz-bin/qcat?J/A+A/545/A130

corresponding to relatively high visibility amplitudes ≃0.6–0.9. Recently, Le Bouquin et al. (2009) used DI to measure the position angle (orientation on the plane of the sky) of the rotation axis of the fast rotator Fomalhaut.

Chelli & Petrov (1995) performed a theoretical study showing that DI can be used to measure stellar angular diameters, rotation velocities, and position angle of rotation axes. However, their study was based on a model of rotating spherical stars with homogeneous effective temperature and gravity, implying a constant local photospheric profile. Such formalism is thus more adapted to slowly rotating stars. It cannot be applied for fast rotators because the effective temperature and gravity, as well as the local profile, vary over the rotationally distorted stellar surface due to rotational flattening and gravity-darkening (also called von Zeipel effect; von Zeipel 1924). To interpret DI observations of rapidly rotating stars, it is thus necessary to use models including these two physical effects caused by high rotation velocities. In this work, we use our model for fast rotators CHARRON (Code for High Angular Resolution of Rotating Objects in Nature; Domiciano de Souza et al. 2012, 2002) to interpret differential phases of the rapidly rotating star Achernar (α Eridani). The observations were performed with the ESO VLTI/AMBER beam combiner (Petrov et al. 2007) centered on the hydrogen Br γ line (K band).

Achernar is a fast rotating Be star ($V_{\rm eq}\sin i \simeq 225\,{\rm km\,s^{-1}}$ from spectroscopy; e.g., Vinicius et al. 2006) presenting a strong rotational flattening directly measured from VLTI/VINCI interferometry (Domiciano de Souza et al. 2003; Kervella & Domiciano de Souza 2006), which indicates that its rotation rate is close to the critical limit. Differential rotation (Jackson et al. 2004) and/or a small residual disk (Carciofi et al. 2008) are additional effects invoked to explain the very strong flattening observed on Achernar. In any case, the rapid stellar rotation is mainly responsible for this flattening.

Because Achernar is bright and well-studied with an angular diameter interferometrically measured, it is an ideal target to investigate, from real observations, how differential phases can be used to measure sizes, rotation velocities, and orientation of rotating stars. In this work, we thus interpret AMBER differential phases of Achernar under the hypothesis that its strong geometrical deformation is essentially due to a fast (near-critical) uniform rotation. This hypothesis is supported by the fact that the Br γ line observed with AMBER is in clear absorption; also, linear polarimetry obtained at the Pico dos Dias Observatory, Brazil, produced a null result within the observational errors ($P \lesssim 0.01\%$; Faes & Carciofi 2012, priv. comm.) Both observables, obtained at contemporaneous epochs, indicate that Achernar had no disk (or a very tenuous one at most) during our AMBER observations.

Our model for fast rotators is briefly presented in Sect. 2 while the observations and data reduction are described in Sect. 3. The data analysis followed by the discussion and conclusions of this study are presented in Sects. 4 and 5.

2. Differential phase modeling for fast rotating stars

We investigate here the dependence of the differential phase $\phi_{\rm diff}$, close to and within the Br γ line, on the relevant physical parameters of a model for fast rotating stars.

Thanks to the Van Cittert-Zernike theorem (e.g., Born & Wolf 1980), the interferometric observables can be derived from the monochromatic intensity maps of the studied object. In the present work, these intensity maps are computed with the numerical program CHARRON (Domiciano de Souza et al. 2012). This code is an IDL[1]-based, faster (~0.5 min per model) version of the interferometry-oriented code for rotating stars presented by Domiciano de Souza et al. (2002).

The $\phi_{\rm diff}$ obtained with the AMBER data reduction algorithm are related to the object's Fourier phase $\phi_{\rm obj}$ by (e.g., Millour et al. 2011, 2006)

$$\phi_{\rm diff}(u,v) = \phi_{\rm obj}(u,v) - a(u,v) - b(u,v)/\lambda, \quad (1)$$

where the spatial frequency coordinates u and v depend on the wavelength λ, the projected baseline length $B_{\rm proj}$ and the baseline position angle PA (from north to east; $u = B_{\rm proj}\sin({\rm PA})/\lambda$ and $v = B_{\rm proj}\cos({\rm PA})/\lambda$). The parameters a and b correspond to an offset and a slope, given in appropriate units.

The high spectral resolution mode of AMBER ($\lambda/\Delta\lambda \simeq 10^4$) leads to a velocity resolution of $\simeq 30\,{\rm km\,s^{-1}}$. Projected equatorial rotational velocities $V_{\rm eq}\sin i$ above $\sim 150\,{\rm km\,s^{-1}}$ would ensure that observations show ~10 individual $\phi_{\rm diff}$ values inside Br γ. In such cases, rapid rotation effects need to be accounted for when modeling phase signatures in order to be consistent with the physics of the studied star.

Many previous works have shown that the geometrical flattening and gravity-darkening are the main consequences of fast rotation measured by interferometry. Based on these works, the model of a uniformly rotating, gravity-darkened star in the Roche approximation was adopted in the present study (Domiciano de Souza et al. 2002). The most relevant physical parameters defining the model are: the rotation axis inclination angle i, the equatorial rotation velocity $V_{\rm eq}$ (or alternatively $V_{\rm eq}\sin i$), the equatorial radius $R_{\rm eq}$, the stellar mass M, the mean stellar effective temperature on the stellar surface $\overline{T}_{\rm eff}$, and the gravity-darkening coefficient β. This set of input parameters defines the co-latitudinal (θ) dependent surface radius $r(\theta)$, the local effective gravity $g(\theta)$, the local effective temperature $T(\theta)$, the geometrical flattening (ratio of equatorial to polar radii) $R_{\rm eq}/R_{\rm p} = 1 + V_{\rm eq}^2 R_{\rm eq}/2GM$, the stellar surface area S, the luminosity $L = S\,\sigma\overline{T}_{\rm eff}^4$ (σ is the Stefan-Boltzmann constant), among other quantities. The local effective temperature and gravity are related by the von Zeipel law: $T(\theta) \propto g(\theta)^\beta$.

Two additional geometrical parameters required for calculating interferometric observables are the distance d and the position angle of the sky-projected rotation axis ${\rm PA_{rot}}$. Further details on the adopted fast rotator model are given by Domiciano de Souza et al. (2002).

To study the dependence of $\phi_{\rm diff}$ on the model parameters, we define a reference stellar model similar to Achernar: $R_{\rm eq} = 11\,R_\odot$, $d = 50\,{\rm pc}$, $V_{\rm eq}\sin i = 250\,{\rm km\,s^{-1}}$, $i = 60°$, $M = 6.1\,M_\odot$, $\overline{T}_{\rm eff} = 15\,000\,{\rm K}$, ${\rm PA_{rot}} = 0°$ (north direction), $\beta = 0.25$ (theoretical value for radiative stellar envelopes; von Zeipel 1924). These parameters correspond to $V_{\rm eq}$ equal to 90% of the critical velocity $V_{\rm crit}$, $R_{\rm eq}/R_{\rm p} = 1.4$ and an equatorial angular diameter $\oslash_{\rm eq} = 2R_{\rm eq}/d = 2\,{\rm mas}$. To be compatible with the AMBER observations presented in Sect. 3, the simulations were performed around the hydrogen Br γ line, considering an uncertainty in $\phi_{\rm diff}$ of $\sigma_\phi = 0.5°$, $B_{\rm proj} = 75\,{\rm m}$ and $150\,{\rm m}$, PA = 45° and 90°, and $\lambda/\Delta\lambda = 12\,000$.

Figures 1 to 3 show several plots comparing $\phi_{\rm diff}$ from the reference model with those from models where the input parameters have been varied one by one. The characteristic s-shaped signature of rotation is seen at all $\phi_{\rm diff}$ curves inside Br γ. Our

[1] Interactive Data Language.

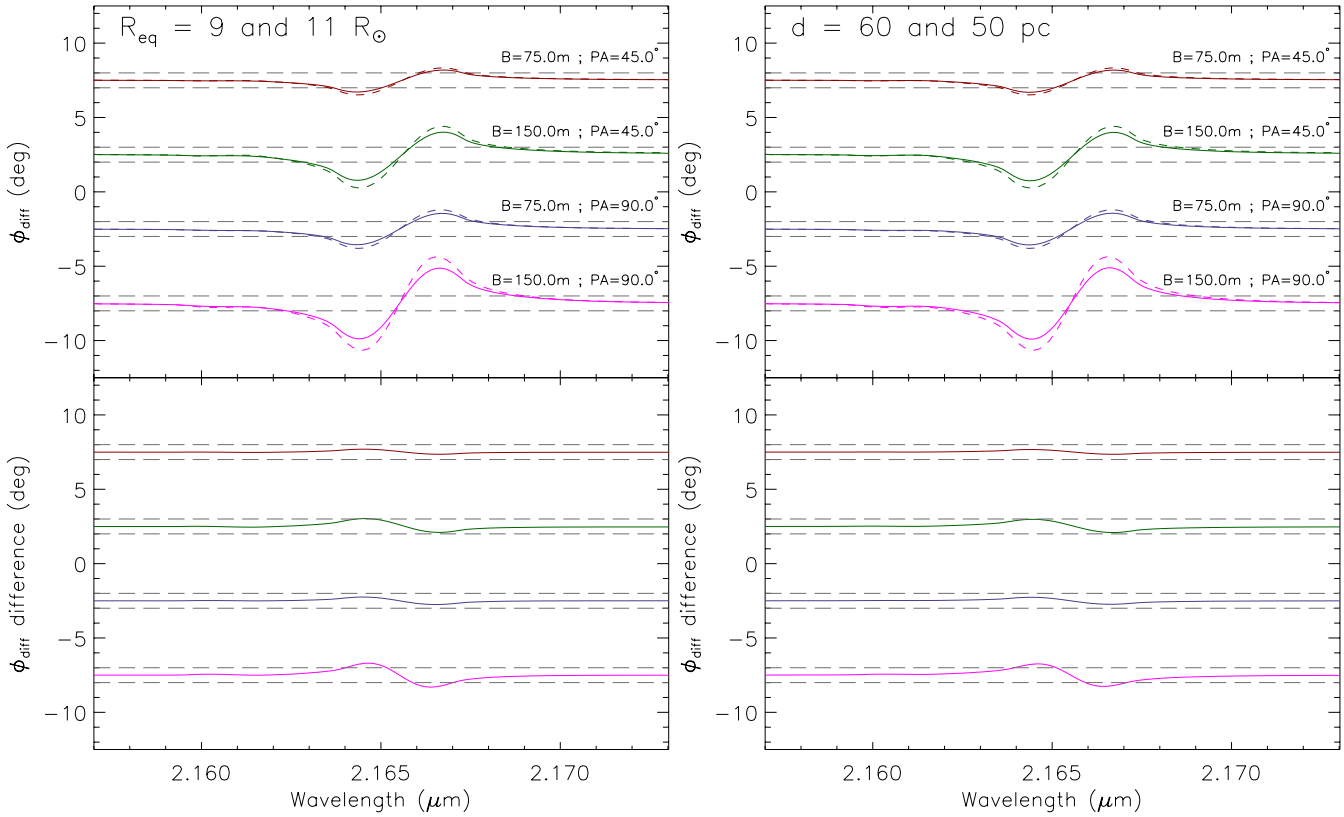

Fig. 1. *Top*: dependence of simulated differential phases $\phi_{\rm diff}$ on $R_{\rm eq}$ and on d (solid line: tested model; dashed line: reference model as described in Sect. 2). The parameters of the tested model are identical to those of the reference model, except that $R_{\rm eq} = 9\,R_\odot$ (*left*) and $d = 60$ pc (*right*). The values of the tested and reference models differ by ≃20%; they are indicated in the upper left part of the figures. All $\phi_{\rm diff}$ models were calculated across the Br γ line with a spectral resolution of 12 000 at four projected baselines ($B_{\rm proj}$ = 75 m and 150 m, and PA = 45° and 90°), which are typical values attained with VLTI/AMBER. These wavelengths and baselines result in visibility amplitudes between 0.6 and 0.9 for the studied stellar models, corresponding to a partially resolved star. The horizontal dashed gray lines indicate the typical error bar of AMBER $\phi_{\rm diff}$ ($\sigma_\phi = \pm 0.5°$). The $\phi_{\rm diff}$ signature of stellar rotation appears as an s-shaped curve well visible inside Br γ, with an amplitude higher than σ_ϕ at all baselines. *Bottom*: difference between $\phi_{\rm diff}$ of the tested and reference models (solid minus dashed curves in the *top panel*). The continuum of all curves is equal to zero, but they were shifted for better readability.

simulations indicate that $\phi_{\rm diff}$ is mostly sensitive to $R_{\rm eq}$ and d (defining the equatorial angular diameter $\oslash_{\rm eq}$), and to $V_{\rm eq} \sin i$ (or $V_{\rm eq}$). For the adopted σ_ϕ and stellar model, these parameters can be determined within a ≃20% precision for a few observations, with the longest baselines at different PA. Figures 2 and 3 show that $\phi_{\rm diff}$ is also sensitive to i, $\overline{T}_{\rm eff}$, and β, but to a lesser extent when compared to $R_{\rm eq}$, d, and $V_{\rm eq} \sin i$.

The strong dependence of $\phi_{\rm diff}$ on $\rm PA_{rot}$ can equally be seen in Figs. 1 to 3, which show that, for a given baseline, the amplitude of the s-shaped $\phi_{\rm diff}$ inside the line is stronger for PA = 90° (perpendicular to $\rm PA_{rot}$) and weaker for PA = 45° (45° from $\rm PA_{rot}$). Indeed, for uniform rotation, the $\phi_{\rm diff}$ amplitude decreases to zero when PA is parallel to $\rm PA_{rot}$. This indicates that only the angular sizes in the equatorial directions are constrained directly from $\phi_{\rm diff}$ data alone and, consequently, this interferometric observable is not strongly sensitive to the apparent flattening of the star.

Of course, the uncertainties of the model parameters mentioned above are only indicative values. The actual precisions of the model parameters depend on the available baselines, observation errors, and parameter values. In the next section, we analyze real VLTI/AMBER observations using CHARRON and the results from the simulations presented above.

3. VLTI/AMBER observations and data reduction

VLTI/AMBER observations of Achernar in high spectral resolution ($\lambda/\Delta\lambda \approx 12\,000$) centered on the Br γ line were carried out from October 25th to November 1th, 2009, during four nights with a different Auxiliary Telescope (AT) triplet configuration in each night (D0-H0-K0, D0-H0-G1, A0-G1-K0, and E0-G0-H0), providing good (u, v) coverage (Fig. 4). The calibrator δ Phe was observed interleaved with Achernar's observations. δ Phe is a bright (K = 1.7) K0IIIb single star with a K band uniform-disk angular diameter of $\oslash_{\rm UD} = 2.180 \pm 0.023$ mas (Bordé et al. 2002). Previous works showed that it is a trustable interferometric calibrator (e.g., Kervella & Domiciano de Souza 2006). The fringe tracker FINITO was used, providing a good locking ratio and fringe tracking performance. Individual exposure times ranged from 360 ms to 735 ms. The seeing varied from 0.8″ to 1.2″. The log of the observations with details on the dates, times, and baselines is given in Table 1.

Data were reduced with amdlib software (version 3.1; Chelli et al. 2009; Tatulli et al. 2007). We adopted a frame selection based on fringe SNR and kept the 50% best frames. Data were calibrated using a dedicated script from Millour et al. (2008). Wavelength calibration was performed by fitting a Gaussian function to the line center of the AMBER spectra and correcting to the rest wavelength of Br γ.

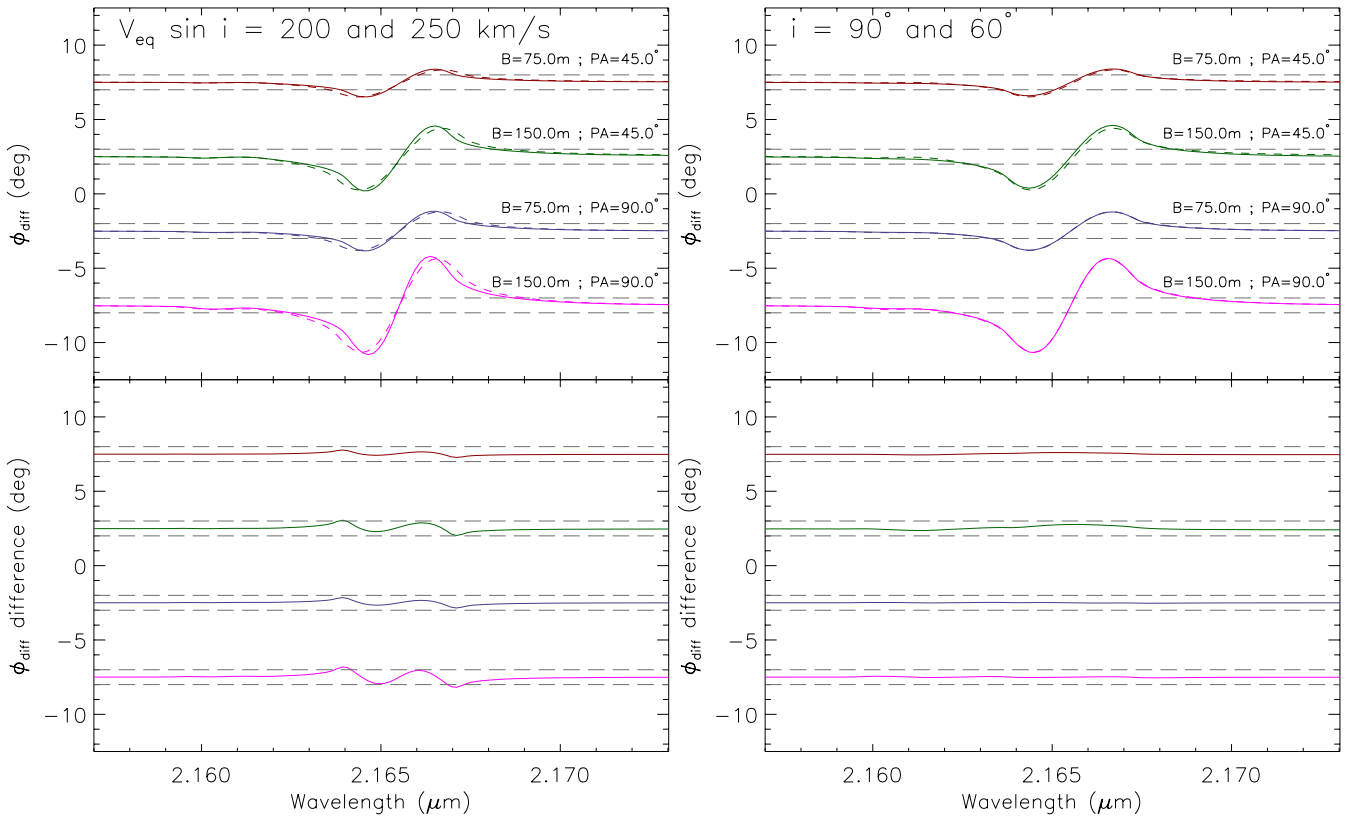

Fig. 2. Similar to Fig. 1 but for the dependence of $\phi_{\rm diff}$ on $V_{\rm eq}\sin i$ and i. The *left panel* shows that $\phi_{\rm diff}$ in Brγ is sensitive to a variation of 20% in $V_{\rm eq}\sin i$ (= 200 km s^{-1} for the tested model). The *right panel* shows that $\phi_{\rm diff}$ also depends on i (changing from 60° to 90°), but to a lesser extent when compared to $R_{\rm eq}$, d, and $V_{\rm eq}\sin i$.

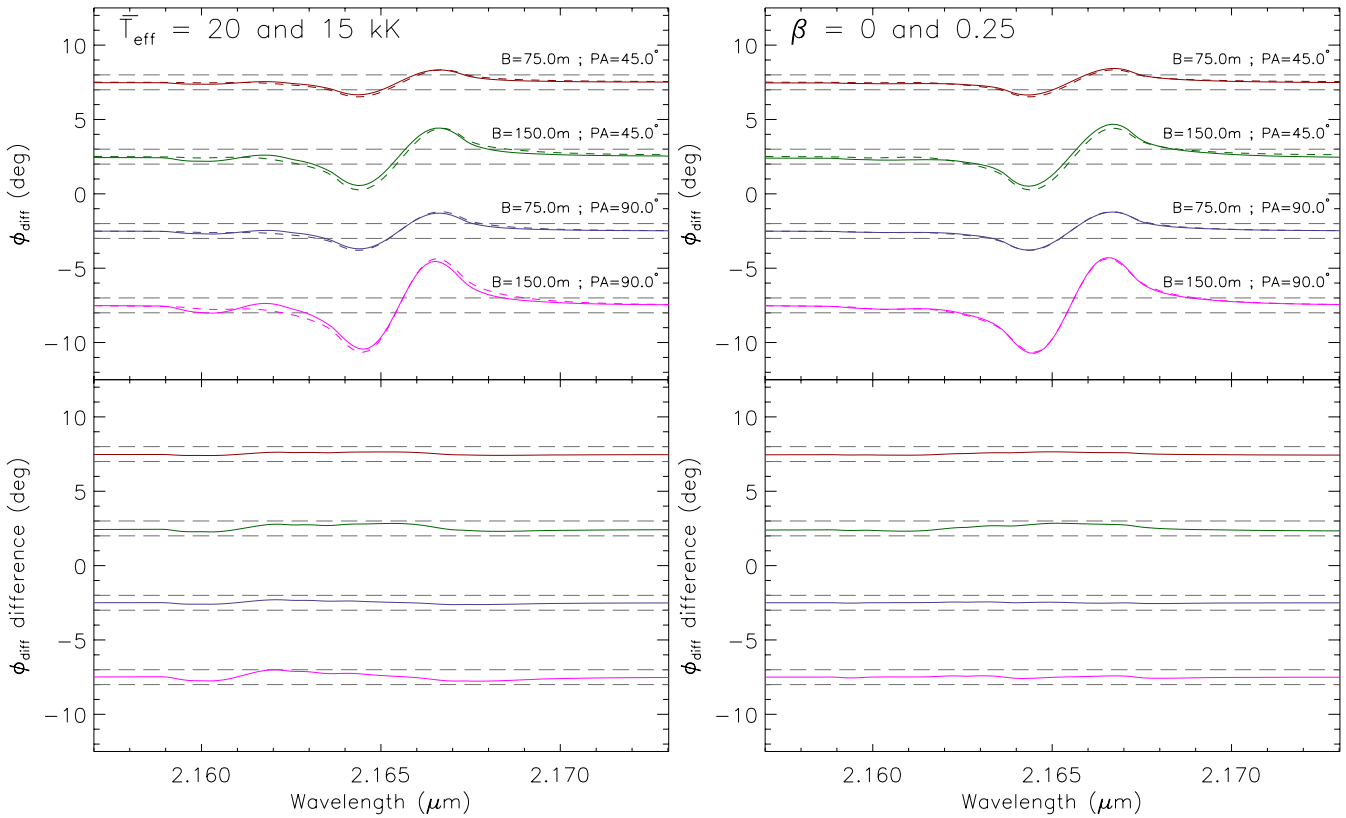

Fig. 3. Similar to Fig. 1 but for the dependence of $\phi_{\rm diff}$ on $\overline{T}_{\rm eff}$ and β. $\overline{T}_{\rm eff}$ changed from 15 000 K to 20 000 K, and β changed from 0.25 (von Zeipel value) to 0.0 (no gravity-darkening). $\phi_{\rm diff}$ in Brγ is not strongly sensitive to these parameters.

Table 1. Log of the 28 VLTI/AMBER observations of Achernar with details on the dates, times, and baseline triplets.

Object	Date and time	Baseline length $B_{\rm proj}$ (m)	Baseline PA PA (°)
Observations with AT triplet D0-H0-K0:			
δ Phe	2009-10-25T01:51	63, 31, 94	48, 48, 48
Achernar	2009-10-25T02:10	64, 32, 96	50, 50, 50
δ Phe	2009-10-25T02:27	64, 32, 96	55, 55, 55
δ Phe	2009-10-25T03:59	63, 32, 95	73, 73, 73
Achernar	2009-10-25T04:15	63, 31, 94	76, 76, 76
δ Phe	2009-10-25T04:32	62, 31, 93	79, 79, 79
Achernar	2009-10-25T04:50	61, 31, 92	84, 84, 84
δ Phe	2009-10-25T05:11	60, 30, 90	86, 86, 86
Achernar	2009-10-25T05:28	60, 30, 89	92, 92, 92
δ Phe	2009-10-25T05:48	58, 29, 87	93, 93, 93
Achernar	2009-10-25T06:04	57, 29, 86	99, 99, 99
δ Phe	2009-10-25T06:21	55, 27, 83	100, 100, 100
Observations with AT triplet G1-D0-H0:			
δ Phe	2009-10-25T23:53	44, 60, 63	−85, 22, −20
Achernar	2009-10-26T00:11	45, 62, 58	−93, 24, −20
Achernar	2009-10-26T01:01	51, 63, 60	−83, 35, −14
δ Phe	2009-10-26T01:18	56, 62, 65	−71, 42, −10
Achernar	2009-10-26T01:38	55, 64, 60	−76, 44, −9
δ Phe	2009-10-26T01:58	60, 63, 66	−66, 50, −5
Achernar	2009-10-26T02:29	60, 64, 61	−67, 55, −3
δ Phe	2009-10-26T03:14	66, 64, 66	−54, 65, 4
Achernar	2009-10-26T03:29	65, 64, 61	−56, 67, 5
δ Phe	2009-10-26T03:52	68, 63, 65	−49, 72, 8
Achernar	2009-10-26T04:09	67, 63, 60	−49, 76, 10
δ Phe	2009-10-26T04:27	70, 62, 65	−43, 79, 12
Achernar	2009-10-26T04:45	68, 62, 60	−43, 83, 15
δ Phe	2009-10-26T05:04	71, 61, 64	−37, 85, 16
Achernar	2009-10-26T05:22	69, 60, 59	−36, 91, 19
δ Phe	2009-10-26T05:43	71, 58, 63	−30, 93, 20
Achernar	2009-10-26T06:01	70, 57, 57	−29, 99, 24
δ Phe	2009-10-26T06:18	71, 56, 61	−24, 100, 24
Observations with AT triplet K0-G1-A0:			
δ Phe	2009-10-30T03:11	85, 88, 128	−155, −71, −112
Achernar	2009-10-30T03:32	80, 87, 127	−151, −70, −108
δ Phe	2009-10-30T03:54	83, 90, 126	−149, −63, −104
Achernar	2009-10-30T04:15	77, 89, 124	−145, −62, −100
δ Phe	2009-10-30T04:35	81, 90, 123	−144, −56, −97
Achernar	2009-10-30T04:55	75, 90, 121	−139, −54, −92
δ Phe	2009-10-30T06:00	73, 90, 110	−134, −39, −81
Achernar	2009-10-30T06:20	67, 90, 110	−128, −36, −73
δ Phe	2009-10-30T06:40	69, 89, 102	−130, −31, −72
Achernar	2009-10-30T07:00	62, 90, 104	−123, −27, −63
δ Phe	2009-10-30T07:20	63, 88, 93	−127, −22, −62
Achernar	2009-10-30T07:42	55, 90, 97	−117, −18, −52
δ Phe	2009-10-30T07:59	57, 87, 85	−123, −13, −52
Achernar	2009-10-30T08:16	50, 89, 92	−113, −10, −42
δ Phe	2009-10-30T08:32	51, 86, 78	−121, −5, −41
Achernar	2009-10-30T08:56	43, 89, 87	−107, −1, −29
Observations with AT triplet H0-G0-E0:			
δ Phe	2009-11-01T00:22	31, 15, 46	−145, −145, −145
Achernar	2009-11-01T00:50	32, 16, 47	−141, −141, −141
δ Phe	2009-11-01T01:08	31, 16, 47	−135, −135, −135
Achernar	2009-11-01T01:25	32, 16, 48	−133, −133, −133
δ Phe	2009-11-01T01:47	32, 16, 48	−127, −127, −127
Achernar	2009-11-01T02:04	32, 16, 48	−125, −125, −125
δ Phe	2009-11-01T02:22	32, 16, 48	−120, −120, −120
Achernar	2009-11-01T02:40	32, 16, 48	−117, −117, −117
δ Phe	2009-11-01T02:59	32, 16, 48	−113, −113, −113
Achernar	2009-11-01T03:16	32, 16, 48	−110, −110, −110
δ Phe	2009-11-01T03:34	32, 16, 48	−106, −106, −106
Achernar	2009-11-01T03:50	31, 16, 47	−103, −103, −103

Notes. The calibration star is δ Phe.

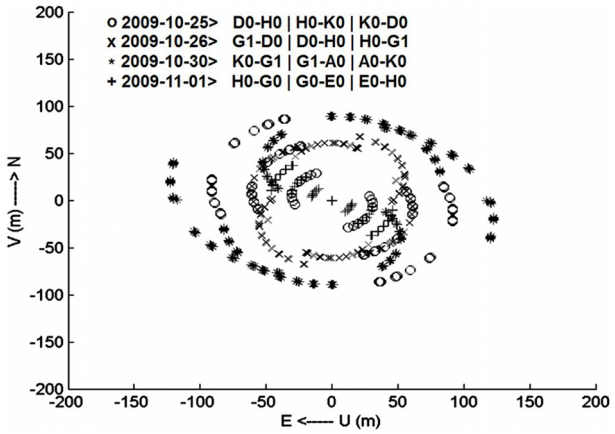

Fig. 4. Used VLTI baselines and (u, v) coverage of our VLTI/AMBER observations of Achernar. Earth-rotation synthesis spanning ~5 h/night provided this good (u, v) coverage.

After this initial data reduction, we obtain several VLTI/AMBER spectro-interferometric observables: source spectra, absolute and differential visibilities, differential phases, and closure phases. A high-frequency beating in wavelength was present in the calibrated data of all measurements (spectrum, visibilities, phases) due to a dichroic plate in the VLTI optical train in front of AMBER, routing the H band light to the IRIS image-tracker camera. Since this beating appears in a narrow frequency range in the wave-number domain, we removed it by applying a Fourier filtering to that specific wave-number domain. Moreover, a low-frequency beating was also present in our data due to the polarizing prisms of AMBER. This second beating was removed by subtracting a single sine wave fitted to the continuum close to Br γ.

Once the described data reduction steps are done, the differential phases $\phi_{\rm diff}$ show a clear signal in the Br γ line region corresponding to the expected s-shaped signature caused by stellar rotation (Fig. 5). Unfortunately, the commonly used visibility amplitudes could not be reliably calibrated due to a very chaotic transfer function. Additionally, no clear stellar signal was present in the Br γ line region in the differential visibilities. Finally, the closure phases are compatible with zero within the observational errors at all AT triplets and wavelengths (Br γ line included), not revealing any strong signatures of stellar rotation and/or asymmetries in the intensity distribution. At each AT triplet, the wavelength-averaged closure phase is always <0.8° (in absolute value), with a corresponding standard deviation several (~3−10) times higher. Such lack of stellar signatures in the closure phases is in agreement with (1) the Achernar's inclination angle i being close to 90° (centrally-symmetric object; see Sect. 4) and with (2) the closure phases being less sensitive to the spatial intensity distribution than the differential phases for partially resolved objects. This last point is a consequence of the fact that, for poorly resolved objects, the closure phase is a third-order term of the Fourier transform of the spatial intensity distribution, while the differential phase is a first-order term (e.g., Lachaume 2003).

We thus concentrate hereafter our data analysis on the differential phase $\phi_{\rm diff}$ alone, which is the only available spectro-interferometric observable presenting a signal-to-noise ratio high enough to constrain the physical parameters of Achernar with a model-fitting algorithm. Most model-fitting algorithms, including the Levenberg-Marquardt algorithm used in the next section, assume that all data points are independent. To be

consistent with this assumption, we did not use the $\phi_{\rm diff}$ observations at all wavelengths. Instead, we used only each third point (one wavelength over three), which ensures that all observations are independent with respect to the finite resolution of the AMBER spectrograph.

Our final data set consists of 84 (=28 × 3 baselines) $\phi_{\rm diff}(\lambda)$ curves centered on Brγ (from 2.159 to 2.172 μm) and presents ≃45 $\phi_{\rm diff}$ points for each of the 84 individual projected baselines. The median uncertainty of this data set is $\sigma_{\phi,\rm median} = 0.6°$.

4. Stellar parameters from VLTI/AMBER $\phi_{\rm diff}$

The VLTI/AMBER $\phi_{\rm diff}$ observations of Achernar were analyzed with the numerical model CHARRON presented in Sect. 2. A χ^2 minimization was performed using an IDL implementation of the Levenberg-Marquardt (LM) algorithm (Markwardt 2009, and references therein).

The free parameters for the model-fitting are $R_{\rm eq}$, $V_{\rm eq}$, i, and $\rm PA_{rot}$. Based on measurements from previous works and on the results of Sect. 2, the remaining model parameters were held fixed, namely:

- d = 44.1 pc. For a consistent comparison of our results with previous works, we adopted the Hipparcos distance d = 44.1 pc from Perryman et al. (1997), instead of the more recent value of d = 42.7 pc from van Leeuwen (2007).
- β = 0.20. Since Achernar is a hot B star with a mostly radiative envelope, the gravity-darkening parameter β should be close to 0.25. Recent interferometric observations of fast rotators (Che et al. 2011) and theoretical works (Claret 2012) suggest that the value β = 0.20 would be more adapted to Achernar's spectral type. Gravity-darkening models from Espinosa Lara & Rieutord (2011) also indicate that $\beta < 0.25$ for fast rotators. Based on these works and on our results showing that $\phi_{\rm diff}$ is not strongly sensitive to β (Fig. 3), this parameter was fixed to 0.20 throughout the data analysis.
- M = 6.1 $M_\odot$. Value from Harmanec (1988), which was adopted by Domiciano de Souza et al. (2003) for Achernar.
- $\overline{T}_{\rm eff}$ = 15 000 K. We adopt the value given by Vinicius et al. (2006), corresponding to the apparent temperature of Achernar. As shown in Fig. 3, $\phi_{\rm diff}$ does not depend strongly on $\overline{T}_{\rm eff}$.

Figure 5 show the best-fit $\phi_{\rm diff}$, together with the corresponding observations. The best-fit values of the free parameters found with the LM algorithm are given in Table 2. The uncertainties of the parameters estimated by the LM algorithm are ∼1%. However, previous works have shown that the LM errors derived from the fit of spectro-interferometric data are often too optimistic and should be considered as lower limits (e.g., Niccolini et al. 2011; Domiciano de Souza et al. 2011). To obtain a more realistic estimation of the parameter uncertainties, we applied a Monte Carlo method, which consists in the analysis of artificial data sets generated from the real observations (Press et al. 2002). These artificial data sets have a random Gaussian distribution with a standard deviation given by the observed σ_ϕ and an average value given by the observed $\phi_{\rm diff}$. By generating 300 artificial $\phi_{\rm diff}$ data sets and by performing a LM model-fit on each of these data sets, we determined the histogram distribution of each fitted parameter, which allowed us to estimate its uncertainty. The limits of the parameter distribution defining the uncertainties of the best-fit parameters given in Table 2 were chosen to correspond to the 68% confidence level of the commonly used standard deviation for normal distributions. We also present in Table 2 several stellar parameters derived from the best-fit parameters.

Table 2. Parameters and uncertainties estimated from a Levenberg-Marquardt fit of our model to the VLTI/AMBER $\phi_{\rm diff}$ observed on Achernar.

Best-fit parameter	**Best-fit value and error**
Equatorial radius $R_{\rm eq}$	11.6 ± 0.3 $R_\odot$
Equatorial rotation velocity $V_{\rm eq}$	298 ± 9 km s^{-1}
Rotation-axis inclination angle i	101.5 ± 5.2°
Rotation-axis position angle $\rm PA_{rot}$	34.9 ± 1.6°
Fixed parameter	**Value**
Distance d	44.1 pc
Mass M	6.1 $M_\odot$
Surface mean temperature $\overline{T}_{\rm eff}$	15 000 K
Gravity-darkening coefficient β	0.20
Derived parameter	**Value and error**
Equatorial angular diameter $\oslash_{\rm eq}$	2.45 ± 0.09 mas
Equatorial-to-polar radii $R_{\rm eq}/R_{\rm p}$	1.45 ± 0.04
$V_{\rm eq} \sin i$	292 ± 10 km s^{-1}
$V_{\rm eq}/V_{\rm crit}$	0.96 ± 0.03
Polar temperature $T_{\rm pol}$	$18\,013^{+141}_{-171}$ K
Equatorial temperature $T_{\rm eq}$	$9955^{+1\,115}_{-2\,339}$ K
Luminosity $\log L/L_\odot$	3.654 ± 0.028

Notes. The minimum reduced χ^2 of the fit is $\chi^2_{\rm min,r}$ = 1.22. The Hipparcos distance d = 44.1 ± 1.1 pc from Perryman et al. (1997) was adopted to convert from linear to angular sizes.

5. Discussion and conclusions

The stellar parameters derived from the Achernar's $\phi_{\rm diff}$ mostly agree with those from previous results. Our equatorial angular diameter $\oslash_{\rm eq}$ = 2.45 ± 0.09 mas (or, alternatively, $R_{\rm eq}$) is between the values reported by Kervella & Domiciano de Souza (2006, $\oslash_{\rm eq}$ = 2.13 ± 0.05 mas) and by Domiciano de Souza et al. (2003, $\oslash_{\rm eq}$ = 2.53 ± 0.06 mas), which were based on VLTI/VINCI observations. The relatively small differences between these three values can be explained, at least partially, by the fact that different approaches and models were used to interpret the interferometric observations. In particular, the smaller $\oslash_{\rm eq}$ from Kervella & Domiciano de Souza (2006) is due to the use of a uniform brightness ellipse model, which is known to give smaller angular sizes than more realistic models, such as the one used in this work. The comparison with previous works also suggests that the uncertainty of $\oslash_{\rm eq}$ derived from $\phi_{\rm diff}$ is of the same order as the uncertainties attained from visibility amplitudes.

The $\rm PA_{rot}$ derived here is ≃6° smaller than the values reported in these two previous works, meaning that these results agree within ≃3−4 sigma. The fact that the AMBER (u, v) coverage is more complete than the VLTI/VINCI (u, v) coverage suggests that the $\rm PA_{rot}$ from the present work is probably somewhat more accurate.

The derived $V_{\rm eq} \sin i$ is larger than those obtained in other works based on spectroscopic data (e.g., Vinicius et al. 2006). These differences can be explained by gravity-darkening, which tends to decrease the $V_{\rm eq} \sin i$ estimated from spectroscopy alone (e.g., Frémat et al. 2005). In any case, the derived rotation rate ($V_{\rm eq}/V_{\rm crit}$ = 0.96 ± 0.03) agrees with the value reported by Carciofi et al. (2008), who obtained a lower limit for the rotational speed of $V_{\rm eq}/V_{\rm crit} > 0.93$, based on interferometric, spectroscopic, and polarimetric data.

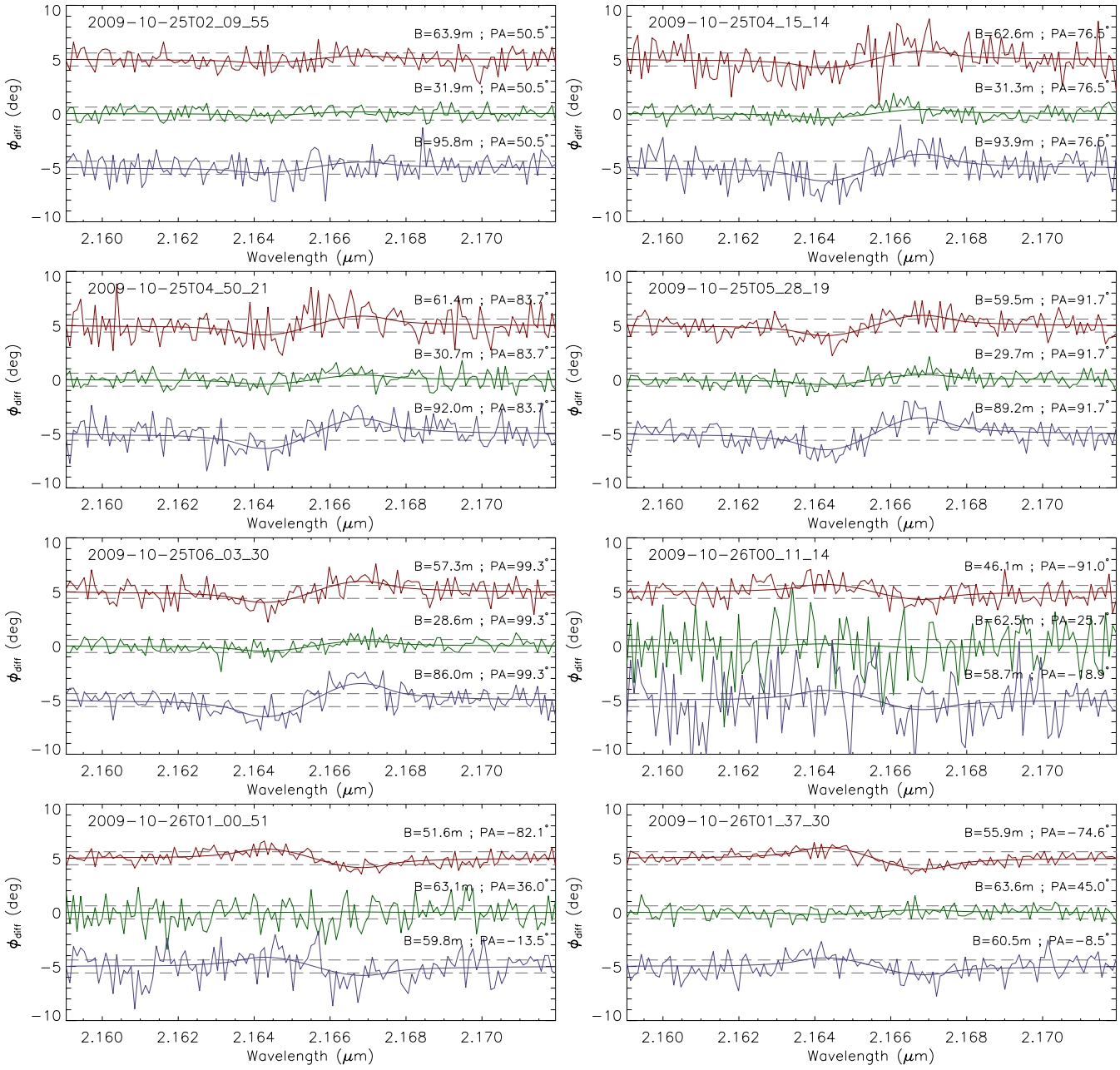

Fig. 5. The 84 VLTI/AMBER $\phi_{\rm diff}(\lambda)$ measured on Achernar around Brγ at 28 different observing times (format YYYY-MM-DDTHH_MM_SS) and, for each time, three different projected baselines and baseline position angles, as indicated in the plots. The dashed gray horizontal lines indicate the median $\pm\sigma_\phi = \pm 0.6°$ of all observations. The smooth curves superposed to the observations are the best-fit $\phi_{\rm diff}$ obtained with a uniform-rotation, gravity-darkened Roche model, as described in Sect. 4. All the observed $\phi_{\rm diff}$ points are shown here, even if the fit has been performed using only each third wavelength point (cf. Sect. 4). All $\phi_{\rm diff}$ curves are equal to zero in the continuum, but they were shifted for better readability. The other panels are available in the electronic edition.

The measured i (=101.5 ± 5.2°) is compatible with previous results, suggesting that $65° \leq i \leq 115°$ (Vinicius et al. 2006; Carciofi et al. 2007). We note that, although $i = 101.5°$ and $i = 78.5°$ (= 180°−101.5°) are indistinguishable from spectroscopic observations, they have different $\phi_{\rm diff}$ signatures when gravity-darkening is present. The measured inclination close to 90° (nearly a centrally-symmetric intensity distribution) is totally consistent with the observed closure phases, which show values compatible with zero within the error bars.

Following Vinicius et al. (2006), a somewhat higher $\overline{T}_{\rm eff}$ value could be adopted in our models, since this quantity is dependent on the rotation rate of the star and on the inclination angle i. We have thus checked the robustness of our results by performing an additional model-fitting fixing $\overline{T}_{\rm eff} = 16\,000$ K, which corresponds to the average effective temperature of the visible stellar hemisphere given by Vinicius et al. (2006). In agreement with what was expected from Fig. 3, the values of the parameters obtained from the best fits with $\overline{T}_{\rm eff} = 15\,000$ K (Table 2) and with $\overline{T}_{\rm eff} = 16\,000$ K are compatible within the parameter uncertainties.

Finally, we also checked that compatible results, within uncertainties, are obtained from a fit performed over all wavelengths, instead of one-third of the $\phi_{\rm diff}(\lambda)$ points.

The present work shows that $\phi_{\rm diff}$ can be used to measure several parameters in fast rotators, in particular $\mathcal{D}_{\rm eq}$ (or $R_{\rm eq}$),

PA_{rot}, V_{eq}, and i. This is very useful, notably in cases when the visibility amplitude is too high (partially resolved objects), when it is poorly determined (large errors), and/or when it cannot be calibrated (as in the case of Achernar's data). By analyzing VLTI/AMBER ϕ_{diff} of Achernar, we have shown, using real observations, that the combination of high spatial and high spectral resolution allows one to go beyond diffraction-limited angular resolution of the interferometer, commonly defined as λ/B_{proj}^{max}. The equatorial angular diameter of Achernar of $\oslash_{eq} = 2.45 \pm 0.09$ mas was measured from ϕ_{diff} alone on B_{proj} between $B_{proj}^{min} \simeq 15$ m and $B_{proj}^{max} \simeq 128$ m at $\lambda \simeq 2.2\,\mu$m. The derived $\oslash_{eq}$ is therefore $\simeq$1.5 times smaller than the maximum available diffraction-limited angular resolution. Furthermore, our observations show that the Achernar's diameter is already resolved at shorter baselines, with a clear signature of rotation seen (ϕ_{diff} amplitudes $\gtrsim\sigma_\phi$) at B_{proj} above $\simeq$45 m (Fig. 5). Therefore, in these observations with $B_{proj} \simeq 45$ m, the measured diameter is even $\simeq$4 times smaller than the corresponding diffraction-limited resolution of 10 mas.

This super-resolution capacity provided by ϕ_{diff} can be further improved if the observational uncertainties are smaller than those attained in the present work. In such cases, the angular diameters of even smaller and slower rotators can be measured, thanks to this powerful technique. The results obtained in this work from VLTI/AMBER differential phases open new perspectives to measure angular sizes of faint and/or angularly small stars, beyond the diffraction limit of optical/IR interferometers.

Acknowledgements. This research has made use of the SIMBAD database, operated at the CDS, Strasbourg, France, of NASA Astrophysics Data System Abstract Service, and of the Jean-Marie Mariotti Center `Aspro` service[2]. A.D.S. and A.C.C. thank the CNRS-PICS program for supporting our Brazilian-French collaboration and the present work. This research received the support of PHASE, the high angular resolution partnership between ONERA, Observatoire de Paris, CNRS, and University Denis Diderot Paris 7. A.C.C. acknowledges support from CNPq (grant 308985/2009-5) and Fapesp (grant 2010/19029-0). M.H. acknowledges the CRAAG and the EII/OPTICON Fizeau program for supporting his PhD thesis. We acknowledge the anonymous referee for her/his constructive comments and suggestions that helped us to improve this work.

References

Bordé, P., Coudé du Foresto, V., Chagnon, G., & Perrin, G. 2002, A&A, 393, 183
Born, M., & Wolf, E. 1980, Principles of Optics Electromagnetic Theory of Propagation, Interference and Diffraction of Light, 6th edn.
Carciofi, A. C., Domiciano de Souza, A., Magalhães, A. M., Bjorkman, J. E., & Vakili, F. 2008, ApJ, 676, L41
Carciofi, A. C., Magalhães, A. M., Leister, N. V., Bjorkman, J. E., & Levenhagen, R. S. 2007, ApJ, 671, L49
Che, X., Monnier, J. D., Zhao, M., et al. 2011, ApJ, 732, 68
Chelli, A., & Petrov, R. G. 1995, A&AS, 109, 401
Chelli, A., Utrera, O. H., & Duvert, G. 2009, A&A, 502, 705
Claret, A. 2012, A&A, 538, A3
Domiciano de Souza, A., Bendjoya, P., Niccolini, G., et al. 2011, A&A, 525, A22
Domiciano de Souza, A., Kervella, P., Jankov, S., et al. 2003, A&A, 407, L47
Domiciano de Souza, A., Vakili, F., Jankov, S., Janot-Pacheco, E., & Abe, L. 2002, A&A, 393, 345
Domiciano de Souza, A., Zorec, J., & Vakili, F. 2012, SF2A Proc., in press
Espinosa Lara, F., & Rieutord, M. 2011, A&A, 533, A43
Frémat, Y., Zorec, J., Hubert, A., & Floquet, M. 2005, A&A, 440, 305
Harmanec, P. 1988, Bull. Astron. Inst. Czechoslovakia, 39, 329
Jackson, S., MacGregor, K. B., & Skumanich, A. 2004, ApJ, 606, 1196
Kervella, P., & Domiciano de Souza, A. 2006, A&A, 453, 1059
Lachaume, R. 2003, A&A, 400, 795
Le Bouquin, J., Absil, O., Benisty, M., et al. 2009, A&A, 498, L41
Markwardt, C. B. 2009, in Astronomical Data Analysis Software and Systems XVIII, eds. D. A. Bohlender, D. Durand, & P. Dowler, ASP Conf. Ser., 251
Millour, F., Vannier, M., Petrov, R. G., et al. 2006, in EAS Publ. Ser. 22, eds. M. Carbillet, A. Ferrari, & C. Aime, 379
Millour, F., Petrov, R. G., Vannier, M., & Kraus, S. 2008, in SPIE Conf. Ser., 7013, 41
Millour, F., Meilland, A., Chesneau, O., et al. 2011, A&A, 526, A107
Niccolini, G., Bendjoya, P., & Domiciano de Souza, A. 2011, A&A, 525, A21
Perryman, M. A. C., Lindegren, L., Kovalevsky, J., et al. 1997, A&A, 323, L49
Petrov, R. G., Malbet, F., Weigelt, G., et al. 2007, A&A, 464, 1
Press, W., Teukolsky, S., Vetterling, W., & Flannery, B. 2002, Numerical Recipes in C: The art of scientific computing, 2nd edn. (Cambridge University Press)
Tatulli, E., Millour, F., Chelli, A., et al. 2007, A&A, 464, 29
van Leeuwen, F. 2007, A&A, 474, 653
Vinicius, M. M. F., Zorec, J., Leister, N. V., & Levenhagen, R. S. 2006, A&A, 446, 643
von Zeipel, H. 1924, MNRAS, 84, 665

Pages 9 to 10 are available in the electronic edition of the journal at http://www.aanda.org

[2] Available at http://www.jmmc.fr/aspro

5.6 *Publication: The environment of the fast rotating star Achernar; III. Photospheric parameters revealed by the VLTI.*

Astronomy & Astrophysics manuscript no. Achernar_PIONIER
May 6, 2014

The environment of the fast rotating star Achernar.⋆

III. Photospheric parameters revealed by the VLTI.

A. Domiciano de Souza[1,⋆⋆], P. Kervella[2], D. Moser Faes[2,3], G. Dalla Vedova[1], A. Mérand[4], J.-B. Le Bouquin[6,7], F. Espinosa Lara[8,9], M. Rieutord[8,9], P. Bendjoya[1], A.C. Carciofi[3], M. Hadjara[1,10], F. Millour[1], and F. Vakili[1]

[1] Laboratoire Lagrange, UMR 7293, Université de Nice-Sophia Antipolis (UNS), CNRS, Observatoire de la Côte d'Azur, 06300 Nice, France
[2] LESIA, Observatoire de Paris, CNRS UMR 8109, UPMC, Université Paris Diderot, 5 Place Jules Janssen, F-92195 Meudon, France
[3] Instituto de Astronomia, Geofísica e Ciências Atmosféricas, Universidade de São Paulo (USP), Rua do Matão 1226, Cidade Universitária, São Paulo, SP - 05508-900, Brazil
[4] European Southern Observatory, Alonso de Córdova 3107, Casilla 19001, Santiago 19, Chile
[5] UJF-Grenoble 1/CNRS-INSU, Institut de Planétologie et d'Astrophysique de Grenoble (IPAG) UMR 5274, F-38041 Grenoble, France
[6] Univ. Grenoble Alpes, IPAG, F-38000 Grenoble, France
[7] CNRS, IPAG, F-38000 Grenoble, France
[8] Université de Toulouse, UPS-OMP, IRAP, Toulouse, France
[9] CNRS, IRAP, 14, avenue Edouard Belin, 31400 Toulouse, France
[10] Centre de Recherche en Astronomie, Astrophysique et Géophysique (CRAAG), Route de l'Observatoire, B.P. 63, Bouzareah, 16340, Alger, Algérie

Received ; accepted

ABSTRACT

Context. Rotation significantly impacts on the structure and life of stars. At phases where rotation velocity is high (close to critical), the photospheric structure can be highly modified, in particular presenting geometrical deformation (rotation flattening) and latitudinal dependent flux (gravity darkening). Being the fastest known rotators (non-degenerate stars close to the main sequence), the Be stars are key targets to study the effects of fast rotation on the stellar photosphere.
Aims. We seek to determine the purely photospheric parameters of Achernar based on observations recorded during an emission-free phase (normal B phase).
Methods. Several recent works proved that optical/IR long-baseline interferometry the only technique able to sufficiently spatially resolve and to measure photospheric parameters of fast rotating stars. We thus analyze ESO-VLTI (PIONIER and AMBER) interferometric observations of Achernar to measure its photospheric parameters by the fit of our physical model CHARRON using a Markov Chain Monte Carlo method. This analysis has also been complemented by spectroscopic, polarimetric, and photometric observations to investigate the status of the circumstellar environment of Achernar during the VLTI observations and to cross check our model fitting results.
Results. Based on VLTI observations able to partially resolve Achernar, we measured simultaneously 5 photospheric parameters of a Be star for the first time: equatorial radius (equatorial angular diameter), equatorial rotation velocity, polar inclination, position angle of the rotation axis projected on the sky, and the gravity darkening β coefficient (effective temperature distribution). The close circumstellar environment of Achernar was also investigated based on contemporaneous polarimetry, spectroscopy, and interferometry, including image reconstruction. This analysis did not reveal any important circumstellar contribution, so that Achernar was essentially in a normal B phase at least from mid-2009 to end-2012 and the model parameters derived in this work provide a fair description of its photosphere. Finally, because Achernar is the flattest interferometrically resolved fast rotator to-date, the measured β and flattening, combined with values from previous works, provide a crucial test for the gravity darkening model of Espinosa Lara & Rieutord (2011). This model offers a promising explanation to the fact that the measured β parameter decreases with flattening, exhibiting values significantly smaller than the classical von Zeipel prediction (von Zeipel 1924).

Key words. Stars: rotation – Stars: individual: Achernar – Methods: observational, numerical – Techniques: interferometric, high angular resolution, polarimetric, spectroscopic, photometric

1. Introduction

The rapidly rotating Be star Achernar (α Eridani, HD10144) is a key target in stellar physics for a deeper understanding of (1) the physical structure and evolution of fast rotators, and (2) the physical mechanism(s) connected to the Be phenomenon (e.g. episodic mass and angular momentum losses, disk formation and dissipation). It is thus crucial to determine a realistic model of Achernar's photosphere, by measuring its main relevant physical parameters such as radius, rotation velocity, temperature distribution (gravity darkening), mass, inclination. Being the closest

⋆ Based on observations performed at ESO, Chile under VLTI PIONIER and AMBER programme IDs 087.D-0150 and 084.D-0456.
⋆⋆ e-mail: Armando.Domiciano@oca.eu

and brightest Be star in the sky, the photosphere of Achernar and its close vicinity can be at least partially resolved by modern high angular resolution instruments able to probe spatial scales ranging from ∼ 1 to ∼ 100 mas.

In particular, the ESO-VLTI (Very Large Telescope Interferometer Haguenauer et al. 2010) instruments are well-adapted to this study. Observations performed in 2002 with the commissioning beam-combiner VLTI/VINCI revealed a strong apparent oblateness (rotational flattening) and suggested an extended structure accounting to a few percent of the photospheric flux (Domiciano de Souza et al. 2003; Kervella & Domiciano de Souza 2006). This strong flattening could not be explained by the commonly adopted stellar rotation models and two possibilities were proposed to account for it: differential rotation (Jackson et al. 2004) and a residual circumstellar disk (Carciofi et al. 2008). By studying the time variation of Hα line profiles, Vinicius et al. (2006) showed that a weak but measurable emission (relative to a reference spectra) was detectable at the epoch of the VLTI/VINCI observations, supporting the residual disk hypothesis.

In addition, direct high angular resolution imaging revealed a faint, lower-mass companion orbiting the Be star at angular distances of ∼ 50 − 300 mas (Kervella & Domiciano de Souza 2007; Kervella et al. 2008, Kervella, Domiciano de Souza, et al., *in prep.*).

These works show that studying Achernar as a simple fast rotator in order to extract its photospheric parameters is a delicate task, since one has to consider its B⇆Be cycle as well the possible influence of the binary companion. In this paper we seek to determine the purely photospheric parameters of Achernar based on a physical model of rapidly rotating stars and on VLTI observations recorded during a quiescent, emission-free phase (normal B phase).

The VLTI observations and data reduction are described in Sect. 2. In Sect. 3 we present a detailed investigation of the possible influence of a circumstellar disk and/or the binary companion on the interferometric observations. The adopted model and the photospheric parameters of Achernar measured from a model-fitting procedure are presented in Sects. 4 and 5. Deviations from the photospheric model and the photosphere vicinity of Achernar possibly revealed by the VLTI observations are investigated in Sect. 6, in particular using interferometric image reconstruction. Finally, the conclusions of this work are given in Sect. 7.

2. Interferometric observations and data reduction

2.1. VLTI/PIONIER

Near-infrared interferometric data of Achernar were obtained in 2011/Aug.-Sep. and 2012/Sep. with the PIONIER beam combiner (Le Bouquin et al. 2011) at the ESO-VLTI (Haguenauer et al. 2010). We used the largest quadruplet available with the Auxiliary Telescopes at that time (A1-G1-K0-I1) in order to resolve as much as possible the stellar photosphere. The resulting *uv* coverage is shown in Fig. 1.

Depending on the night, the data were dispersed over three or seven spectral channels across the H band. Table 1 summarizes the log of observations. Data were reduced and calibrated with the `pndrs` package (Le Bouquin et al. 2011). Each observation provides six squared visibilities V^2 and four closure phases CP. This dataset is available upon request in the standard OIFITS format.

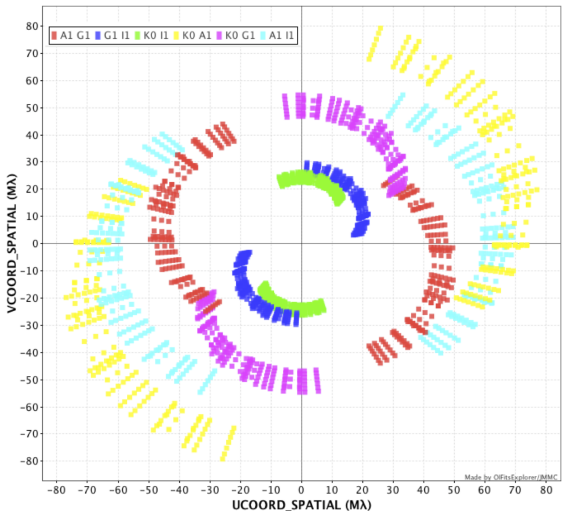

Fig. 1. *uv* coverage of VLTI/PIONIER observations of Achernar. AT baselines used are identified with different colors. Image adapted from the OIFITSExplorer/JMMC tool.

Table 1. Log of VLTI/PIONIER observations of Achernar.

Date	nb observations	nb spec. channels
2011-08-06	4	3
2011-09-22	10	7
2011-09-23	9	7
2012-09-16	9	3
2012-09-17	3	3

2.2. VLTI/AMBER

Domiciano de Souza et al. (2012a) described and analyzed VLTI/AMBER HR differential phase observations of Achernar around the Brγ line. The observations were recorded in 2009 (Oct. 25th, Oct. 26th, Oct. 30th, and Nov. 1st) with the high spectral resolution mode and using the FINITO fringe tracker. In this paper we reanalyze these AMBER differential phases together with the PIONIER data, since they were both taken during a diskless phase, as demonstrated in the next section.

3. Disk and companion status during the VLTI observations

The Be and binary nature of Achernar may imply temporal variabilities of observables with possible detectable spectro-interferometric signatures. It is thus important to check which physical components should be included in the models in order to interpret VLTI observations from a given epoch. Indeed, Carciofi et al. (2008) showed that the presence of a residual circumstellar disk is a promising explanation to the strong flattening measured on the 2002 VLTI/VINCI observations (Domiciano de Souza et al. 2003). The presence of this residual disk is supported by a 2002 Hα profile showing a weak but measurable emission superposed to the stronger photospheric absorption (Vinicius et al. 2006).

Based on our observations of Achernar (Kervella, Domiciano de Souza, et al., *in prep.*), the binary companion was located close to apastrom (separation ∼ 200 − 300 mas) during the PIONIER observations, which is outside the field of view of this instrument. Concerning the possible influence of a Be circumstellar disk, a more thorough analysis is required as described in the following.

Table 2. Summary of broad-band polarization data contemporaneous to the VLTI observations. These data are plotted in Fig. 2.

Date	Band	Polarization(%)
2009-09-21	B	0.008 ± 0.011
2009-11-18	B	0.014 ± 0.026
2011-06-29	B	0.016 ± 0.038
2011-09-02	B	0.014 ± 0.036
2011-09-02	V	0.025 ± 0.015
2011-09-09	B	0.027 ± 0.018
2011-09-09	V	0.023 ± 0.017
2011-09-29	B	0.008 ± 0.030
2011-09-29	V	0.013 ± 0.018
2011-10-19	B	0.026 ± 0.039
2011-10-19	V	0.013 ± 0.016
2011-11-03	V	0.015 ± 0.036
2012-07-01	V	0.017 ± 0.015
2012-11-21	V	0.035 ± 0.050

3.1. Search for polarimetric and spectroscopic signatures of a Be circumstellar disk

In order to investigate the presence and strength of a possible circumstellar disk during the VLTI (PIONIER and AMBER) observations (Sect. 2), we analyzed contemporaneous broadband polarimetry (B and V) and hydrogen line profiles (Hα and Hβ). These observations span from July 2009 to November 2012.

Imaging polarimetry in the B and V bands was obtained using the IAGPOL polarimeter attached to the 0.6 m Boller & Chivens telescope at OPD/LNA[1], Brazil. We used a CCD camera with a polarimetric module described by Magalhães et al. (1996), consisting of a rotating half-wave plate and a calcite prism placed in the telescope beam. A typical observation consists of 16 consecutive wave plate positions separated by 22.5°. In each observing run at least one polarized standard star HD41117 or HD187929 was observed in order to calibrate the observed position angle. Details of the data reduction can be found in Magalhães et al. (1984). A summary of our polarimetric data is presented in Table 2.

The IAGPOL data, shown in Fig. 2, exhibit values compatible with no intrinsic polarization, having a weighted average polarization of only $0.019 \pm 0.012\%$ during the observed period. This average is used in Sect. 3.2 as an upper limit to the polarization from a possible residual disk. Such low polarization level contrasts with the measurements from a period of stellar activity in 2006, where the presence of circumstellar material lead to a polarization 10 times higher (up to 0.19% in B band), as shown by Carciofi et al. (2007). These authors also report a clear spectroscopic signal with an Hα emission to continuum (E/C) ratio of ~ 1.06. The polarization values shown here also suggest no significant contribution from the interstellar medium to this quantity.

In addition to the polarimetric data, Hα and Hβ spectra of Achernar contemporaneous to the VLTI observations have also been analyzed in search for possible signatures of a circumstellar disk. We obtained 7 spectra at OPD/LNA, using the Cassegrain spectrograph (ECass) with 600 groove mm^{-1} grating blazed at 6563 Å in first order, resulting in a reciprocal dispersion of 1.0 Å pixel^{-1}. FEROS and HARPS spectra have also been used to complement the OPD data. The spectroscopic observations are summarized in Table 3.

[1] Observatório Pico dos Dias/Laboratório Nacional de Astrofísica.

Table 3. Summary of spectroscopic data of Achernar contemporaneous to the VLTI observations; typical S/N ratio is 300. The Hα and Hβ spectra are shown in Fig. 3.

Date	H line	Instrument	Min. Resolution
2000-01-11	Hα + Hβ	ESO/FEROS	54000
2009-07-01	Hα + Hβ	ECass/OPD	3400
2009-11-18	Hβ	ECass/OPD	3400
2011-06-27	Hα	ECass/OPD	5400
2011-09-28	Hα + Hβ	ECass/OPD	3400
2011-12-12	Hα + Hβ	ESO/HARPS	109000
2012-08-07	Hα	ECass/OPD	5400
2012-10-14	Hβ	ECass/OPD	3400
2012-11-20	Hα	ECass/OPD	5400

Following (Rivinius et al. 2013), we adopt the FEROS spectra from early 2000 as a reference photospheric spectrum for Achernar. In Fig. 3 we plot the Hα and Hβ line profiles (top panels) and the difference profiles, computed as the difference between the observed profiles and the reference FEROS spectrum (bottom panels). All difference profiles are completely featureless, with difference values typically comprised between -0.012 and 0.012.

Thus, the polarimetric and spectroscopic data above suggest that the presence of a strong Be disk contemporaneous to the interferometric data can be discarded. In the follwoing we quantify this assumption based on physical models of Be disks constrained by the observational limits imposed by the contemporaneous polarimetry (below $0.019 \pm 0.012\%$) and spectroscopy (disk signatures below 0.012 in absolute values relative to a photospheric profile).

3.2. Residual disk

We investigate here whether the presence a weak residual disk that is hard to detect from non-angularly resolved observations could still affect the interferometric observations of Achernar. Such weak disk is constrained by the limits imposed by contemporaneous polarimetric and spectroscopic data determined in the previous section.

Using radiative transfer simulations from the HDUST code (Carciofi & Bjorkman 2006) we computed a grid of models based on our previous grid used to investigate the 2002 phase of Achernar (Carciofi et al. 2008): a large and dense disk in hydrostatic equilibrium (i.e., geometrically thin) and a smaller and more tenuous disk with enhanced scale height (i.e., geometrically thick). We adopt a power-law radial density profile:

$$\rho(r) = \rho_0 \left(\frac{R_{\rm eq}}{r} \right)^m \quad , \tag{1}$$

where $R_{\rm eq}$ is the stellar equatorial radius where the disk starts (inner disk radius), ρ_0 is the density of the disk at $R_{\rm eq}$ (density scale), and m is chosen as 3.5 corresponding to the steady-stade regime of a viscous decretion disk (VDD) model (c.f. Haubois et al. 2012, and references therein). To study the influence of the disk on the different observables we vary ρ_0 considering two sets of disk size $R_{\rm d}$ and scale height H_0 at the inner disk radius. Table 4 details the parameters of these two sets of VDD models. In addition to these VDD models, we have also used HDUST to compute a reference ellipsoidal photospheric model of Achernar compatible with the more physical photospheric model determined in Sect. 4.

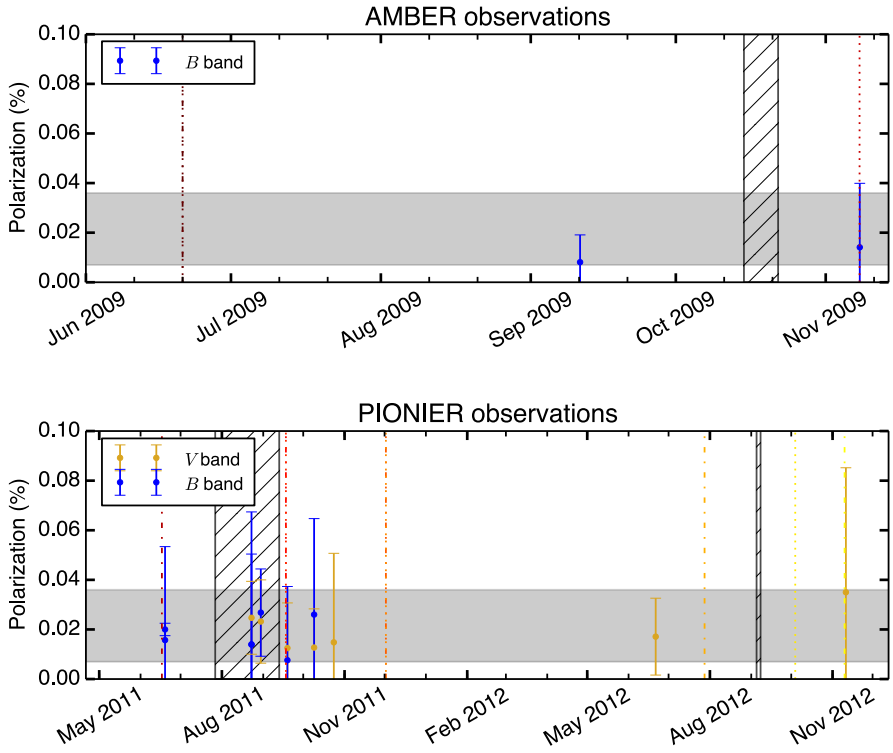

Fig. 2. Polarimetric observations at the epochs of ESO-VLTI AMBER and PIONIER data of Achernar analyzed in this work (vertical hatched bars). All the measurements are compatible with null/negligible polarization. The horizontal grey bars indicate the weighted average of the polarization: $0.019 \pm 0.012\%$. Vertical lines correspond to epochs of Hα (dotted) and Hβ (dot-dashed) data observations with colors corresponding to the spectra shown in Fig. 3. The spectroscopic and polarimetric data are thus contemporaneous and embrace the interferometric observations in time.

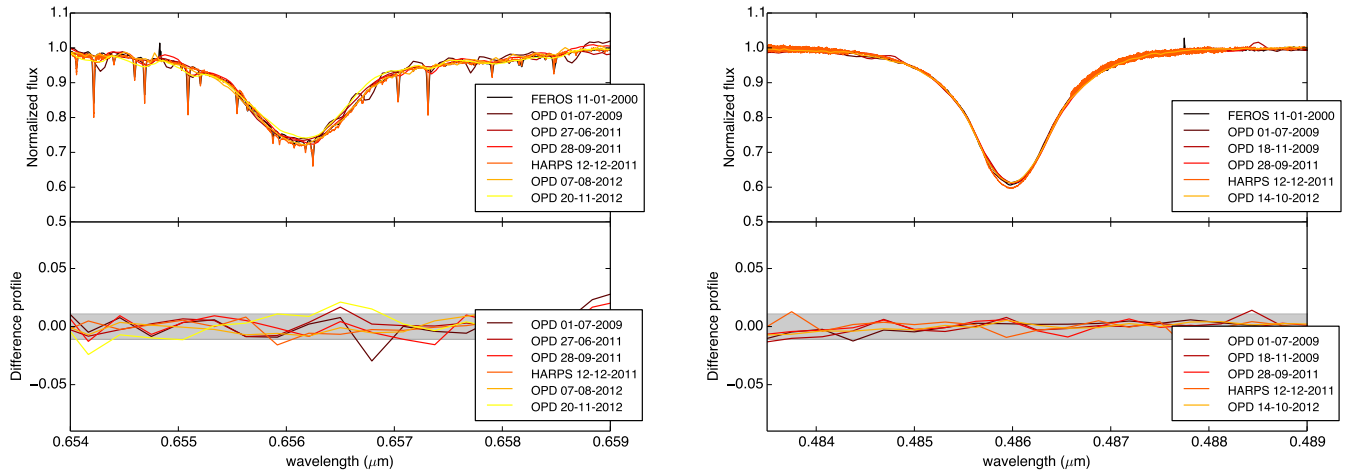

Fig. 3. Top: Hα (left) and Hβ (right) line profiles of Achernar at the epoch of interferometric observations. **Bottom:** Difference in flux of the line profiles with respect to the reference FEROS spectrum from 11-01-2000. This spectrum can be considered as a good approximation to the pure photospheric profile of Achernar (Rivinius et al. 2013). Whenever possible (enough spectral resolution) the telluric lines seen in some spectra have been removed before computing the differences. The horizontal shaded areas indicate the typical error on the difference profiles also setting a limit to them.

The dependence of the polarimetric and spectroscopic observables on the density ρ_0 for the two VDD models are shown in Fig. 4, where the quantities predicted from the models are compared to our observational constraints. By comparing the modeled and observed limits determined in Sect. 3 for the polarization and difference Hα spectra we can set strict upper limits to ρ_0: $\rho_0 < 0.52\times10^{-12}$ g cm^{-3} (thin disk) and $\rho_0 < 0.65\times10^{-12}$ g cm^{-3} (thick disk). As shown in Fig. 4 these limits are mainly imposed by the polarimetric data.

Table 4. Parameters of the two geometrical configurations of residual disk (VDD) models studied. The photospheric parameters are kept constant for simulations. For a given density ρ_0 the total mass of the disk is the same for both models.

Disk Model	ρ_0 range (10^{-12} g cm^{-3})	R_d ($R_\odot$)	H_0 ($R_\odot$)
1 (thin)	0.2 – 7.5	11.0	0.37
2 (thick)	0.2 – 7.5	10.1	0.73

Figure 5 shows a detailed comparison of the VDD modeled Hα line profiles for these two ρ_0 limits with the photospheric profile. As expected, the difference profiles have almost everywhere values within the ±0.012 limit determined from the observed difference profiles (Sect. 3). Only at the wings of the Hα profiles the VDD models could present weak signatures when compared to the pure photospheric profile. This detailed investigation of Hα profiles combined to the results from Fig. 4 thus shows that the limits to ρ_0 imposed by polarimetry are also reliable upper limits to hydrogen spectral lines.

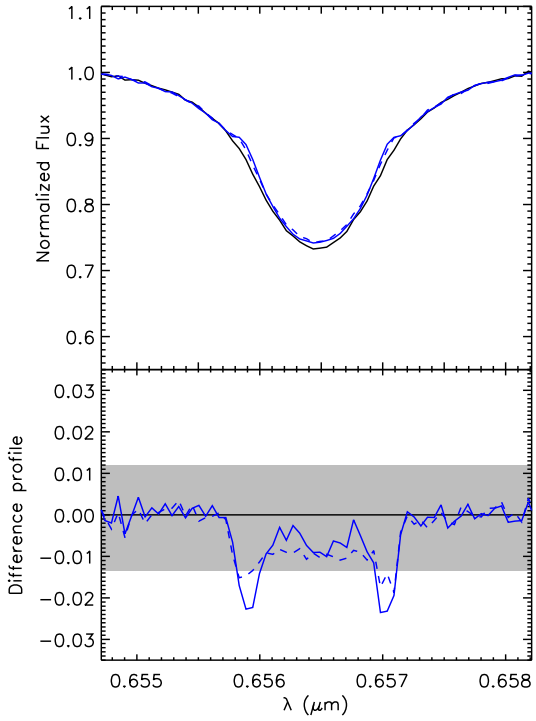

Fig. 5. *Top:* Hα line profile for the pure photospheric model (black solid line) and at the presence of a residual disk as defined in Table 4 and computed for the upper limit values of ρ_0 (c.f. Fig. 4): 0.52×10^{-12} g cm^{-3} (thin disk; blue solid line) and 0.65×10^{-12} g cm^{-3} (thick disk; blue dashed line). *Bottom:* The difference between the disk models relative to the photospheric model. The observational limit set to the difference profiles defined in Sect. 3 is indicated by the shaded area.

By adopting these limits to ρ_0 we now evaluate the signatures that a possible residual disk might have on our interferometric observations of Achernar. These evaluations are shown in Fig. 6, which compares the H band squared visibilities V^2, and Brγ differential phases computed with the two VDD models (Table 4) to the expected values for the purely photospheric model. All deviations from the photospheric model are well within the typical observational errors on these interferometric quantities.

Therefore, in the following analysis we can safely rule out any effects of the known companion and of a significant residual disk around Achernar on our interferometric observations.

4. Achernar's photospheric parameters from VLTI observations

Based on the results from the previous section we adopt as a starting point a model of a fast rotating, single B star without circumstellar environment to interpret the interferometric data of Achernar.

4.1. Photospheric model of fast rotating stars

Most recent works describe the photospheric structure of rapidly rotating, non-degenerate, single stars of intermediate to high masses by adopting a Roche model (rigid rotation and mass concentrated in the stellar center) with a generalized form of the von Zeipel's gravity darkening (von Zeipel 1924). We adopt this model since it has proven to well reproduce many distinct observables on rapid rotators (e.g. this work on Achernar and the cited references on other stars). Whether this is the only/best representation for their photospheres could be tested based on future and more precise observations.

Many codes exist providing similar numerical implementations of this model, hereafter called RVZ model. The reference numerical code for the RVZ model used here is the IDL-based program CHARRON (Code for High Angular Resolution of Rotating Objects in Nature). We present below a short description of CHARRON in the context the present work. A more detailed description is given by Domiciano de Souza et al. (2012a,b, 2002).

The stellar photospheric shape follows the colatitude θ dependent equipotential $\Psi(\theta)$ given by the Roche potential (gravitational plus centrifugal):

$$\Psi(\theta) = -\frac{GM}{R(\theta)} - \frac{\Omega^2 R^2(\theta)\sin^2\theta}{2} = -\frac{GM}{R_{\rm eq}} - \frac{V_{\rm eq}^2}{2} \quad , \tag{2}$$

where M is the stellar mass, $R_{\rm eq}$ and $V_{\rm eq}$ are the equatorial radius and rotation velocity. Solving this cubic equation provides the colatitude dependent stellar radius $R(\theta)$.

Gravity darkening is considered by relating the local effective gravity $g_{\rm eff}(\theta) = |\nabla\Psi(\theta)|$ to the local effective temperature $T_{\rm eff}(\theta)$ by:

$$T_{\rm eff}(\theta) = \left(\frac{C}{\sigma}\right)^{0.25} g_{\rm eff}^{\beta}(\theta) \quad , \tag{3}$$

where σ is the Stefan-Boltzmann constant and β is the gravity darkening coefficient, which is more general than the $\beta = 0.25$ value from von Zeipel (1924), but still assumed constant over the stellar surface. We note that for the spectral type of Achernar we can neglect any radiative acceleration effects since it is far from the Eddington limit. The proportionality constant C can be derived from stellar physical parameters such as mass and luminosity (e.g. Maeder & Meynet 2000) or related to a fixed point on the photosphere (the stellar pole for example). In this work, the constant C and the stellar luminosity L are related to the average effective temperature $\overline{T}_{\rm eff}$ over the total stellar surface $S_\star$ (area of the Roche photosphere):

$$L = \sigma \int T_{\rm eff}^4(\theta)\, dS = \sigma \overline{T}_{\rm eff}^4 S_\star = C \int g_{\rm eff}^{4\beta}(\theta)\, dS \quad . \tag{4}$$

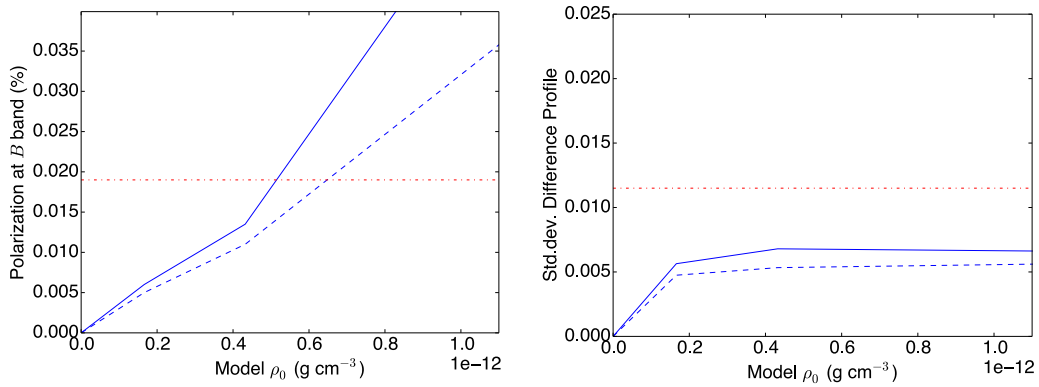

Fig. 4. B-band polarization (*left*) and standard deviation of difference Hα profile (*right*) as a function of disk base density ρ_0 for the residual disk models from Table 4 (model 1: full line; model 2: dashed line). The standard deviation is the root mean square of the disk model spectrum minus the pure photospheric profile. The horizontal dot-dashed lines represent the observational limits of average polarization and difference profile determined from observations performed at the epoch of interferometric observations as explained in Sect. 3. While the measured Hα difference profile level does not impose a limit to ρ_0, the measured average polarization sets a strict upper limit to this quantity: $\rho_0 < 0.52 \times 10^{-12}$ g cm^{-3} for the thin disk model and $\rho_0 < 0.65 \times 10^{-12}$ g cm^{-3} for the thick disk model.

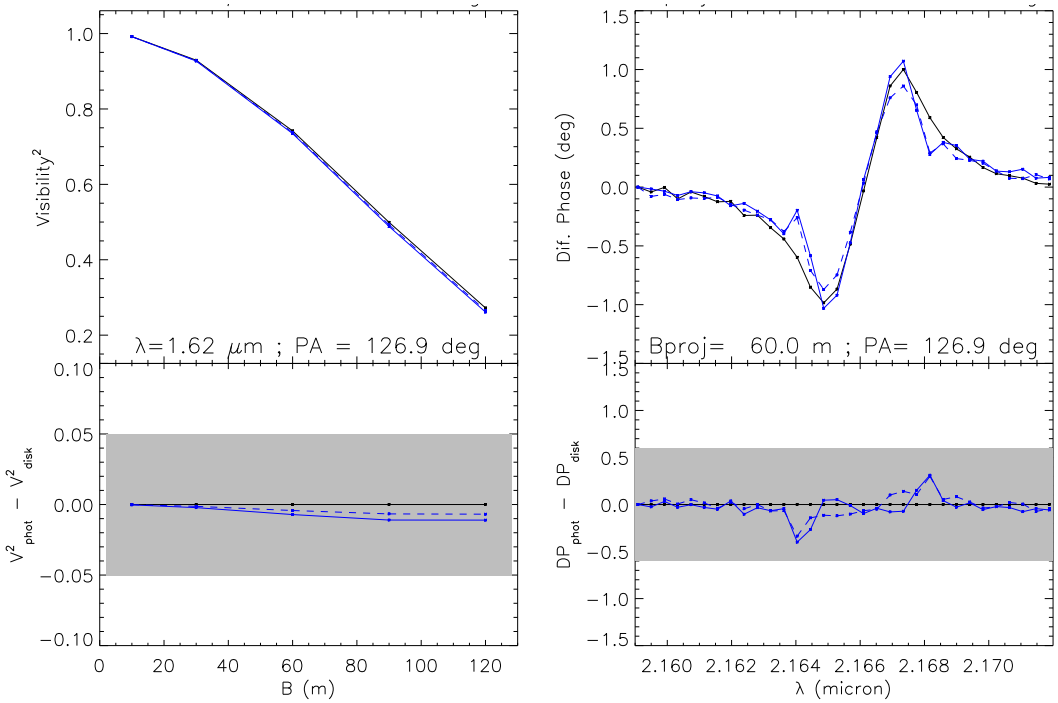

Fig. 6. Interferometric observables, squared visibilities V^2 in the H band (*left*) and Brγ differential phases (*right*), computed for the pure photospheric model (black solid line) and for the two residual disk models as defined in Table 4 at the upper limit values of ρ_0 (c.f. Fig. 4): 0.52×10^{-12} g cm^{-3} (thin disk; blue solid line) and 0.65×10^{-12} g cm^{-3} (thick disk; blue dashed line). The baseline position angle PA was chosen along stellar equator (c.f. Sect. 4.2), so that the effects of the residual disk are maximized on these comparisons. The baseline length for the differential phase calculations roughly corresponds to half of the maximum available length. *Bottom:* The difference between the interferometric observables from the disk models relative to the photospheric model. The shaded areas correspond to the typical observational errors from our PIONIER and AMBER observations. These difference plots show that the disk contribution to the interferometric observables is only a small fraction of the observation errors even at the upper limit ρ_0, discarding any detectable influence of a circumstellar disk on the present interferometric observations of Achernar.

$\overline{T}_{\rm eff}$ can be directly related to the bolometric flux $F_{\rm bol}$ and to the mean angular diameter $\overline{\oslash}$ (diameter of spherical star having a surface area $S_\star$) by:

$$F_{\rm bol} = \sigma \overline{T}^4_{\rm eff} \frac{S_\star}{4\pi d^2} = \sigma \overline{T}^4_{\rm eff} \frac{\overline{\oslash}^2}{4} \quad , \tag{5}$$

where d is the distance to the star.

In our numerical implementation of the RVZ model the stellar surface is divided in a predefined grid with nearly identical surface area elements (typically $\sim$ 50 000 surface elements). From $T_{\rm eff}(\theta)$ and $g_{\rm eff}(\theta)$ defined in the above equations, a local specific intensity from a plane-parallel atmosphere $I = I(g_{\rm eff}, T_{\rm eff}, \lambda, \mu)$ is associated to each surface element, where λ is the wavelength and μ is the cosine between the normal to

the surface grid element and the line-of-sight (limb-darkening is thus automatically included in the model). The local specific intensities I are interpolated from a grid of specific intensities precalculated using the spectral synthesis code SYNSPEC (Hubeny & Lanz 2011) and the ATLAS9 stellar atmosphere models (Kurucz 1979). For Achernar, we adopted atmosphere models with turbulent velocity of $2\,\mathrm{km\,s^{-1}}$ and solar abundance in agreement with its spectral type and short distance.

From the local specific intensities we obtain wavelengh-dependent intensity maps of the visible stellar surface at the chosen spectral domain and resolution, such as the image given in Fig. 11. The interferometric observables (e.g. squared visibilities, closure phases, differential phases) are then directly obtained from the Fourier transform of these sky-projected photospheric intensity maps, which for a given star in the sky also depend on its rotation-axis inclination angle i and on the position angle of its sky-projected rotation axis $PA_{\rm rot}$ (counted from North to East until the visible stellar pole).

Thus, the main input parameters of the photospheric RVZ model for fast rotators used to interpret the interferometric observations of Achernar are: M, $R_{\rm eq}$, $V_{\rm eq}$, β, $\overline{T}_{\rm eff}$, i, $PA_{\rm rot}$, and d.

4.2. Fitting of CHARRON model to VLTI/PIONIER data with a MCMC method

Here we use the CHARRON model to constrain several photospheric parameters of Achernar from the PIONIER observations (described in Sect. 2.1), which consists of a homogenous data set obtained with the same beam combiner instrument at VLTI. To be compatible with the observations, the CHARRON intensity maps were calculated over the H band with a spectral resolution of $\sim 20-40$. We note that, in broad-band observations, the effect of bandwidth smearing (mixing of different spatial frequencies in a given wavelength bin) can lead to a decrease of visibility contrast and should in principle be considered. However, we checked that the bandwidth smearing effect does not need to be considered in the present analysis because (1) the squared visibilities are higher than $0.3-0.4$, which minimizes this effect (Kervella et al. 2003), and (2) the data spans a few wavelength bins over the H band so that the range of spatial frequencies mixed is small. Based on results from previous works M, $\overline{T}_{\rm eff}$, and d were fixed:

- $M = 6.1\,M_{\odot}$. Value from Harmanec (1988), previously adopted by Domiciano de Souza et al. (2012a). This mass is also in agreement (1) with the estimation from Jerzykiewicz & Molenda-Zakowicz (2000) ($M = 6.22 \pm 0.16\,M_{\odot}$) based on evolutionary tracks and (2) with mass estimates from an ongoing work on Achernar's binary system (Kervella, Domiciano de Souza, et al., *in prep.*);
- $\overline{T}_{\rm eff} = 15\,000$ K. Value adopted by Domiciano de Souza et al. (2012a) following Vinicius et al. (2006). A critical discussion on this value and comparisons with other works are presented in Sect. 5;
- $d = 42.75$ pc. We adopted the updated distance derived from the new reduction of the Hipparcos astrometric data and provided by van Leeuwen (2007).

The free parameters are thus: $R_{\rm eq}$, $V_{\rm eq}$, i, β, and $PA_{\rm rot}$.

The model-fitting was performed using the emcee code (Foreman-Mackey et al. 2013), which is a Python implementation of a Markov Chain Monte Carlo (MCMC) method proposed by Goodman & Weare (2010). This code has been recently used by Monnier et al. (2012) to interpret interferometric observations.

From a given likelihood function of the parameters, emcee provides histograms of the model free parameters (samplings of the posterior probability) from which one can estimate the best parameter values and associate uncertainties. In the present work, the measurement errors on V^2 and CP are assumed to be all independent and normally distributed so that the likelihood function is proportional to $\exp(-\chi^2)$, where χ^2 has its usual definition and is composed by $\chi^2 = \chi^2_{V^2} + \chi^2_{CP}$ (sum of χ^2 from the V^2 and CP data, respectively). To equally explore an homogenous range of initial values, we adopted initial uniform distribution for the 5 free CHARRON parameters, covering a wide range of physically consistent values.

The emcee algorithm explored the defined parameter space using 800 walkers in a 200 steps initial phase (burn-in) and 150 steps in the final phase, starting from the last state of the burn-in chain (for details using the code see Foreman-Mackey et al. 2013). Convergence of the parameters distribution was typically attained within $\lesssim 100$ steps during the burn-in phase (an example for $R_{\rm eq}$ is shown in the electronically available Fig. 7).

The final histograms of the five free parameters and their two-by-two correlations are shown in Fig. 8 (available electronically). The best-fit values of the free parameters are the mean of these histograms. The uncertainties on the parameters were defined as corresponding to a range enclosing $\pm 34.15\%$ of the parameter distribution relative to the mean value (this corresponds to the commonly used rule for normal distributions). The reduced χ^2 of the best-fit model is $\chi^2_{\rm r} = 1.9$ (for 1777 degrees of freedom DOF and 5 free parameters).

Table 5 summarizes the best-fit parameter values and uncertainties measured on Achernar from the MCMC fit of CHARRON RVZ model to the VLTI/PIONIER data. Other derived stellar parameters are also given in the table. The V^2 and CP corresponding to this best-fit model are plotted together with the observations in Figs. 9 and 10. The sky-projected intensity map of the visible stellar photosphere for this model is shown in Fig. 11.

As a completely independent check of the results above, we have also performed a Levenberg-Marquardt fit to the PIONIER data using a different RVZ model developed by one of us (A. Mérand). The best-fit parameter values obtained are in good agreement (within the emcee error bars) with the values derived from the emcee fit of the CHARRON RVZ model.

5. Discussion

5.1. Radius and angular diameter

Long-baseline interferometry is traditionally known to deliver stellar angular diameters (and radii if distances are available). These size measurements are directly dependent on the chosen photospheric model and on how fairly this model can represent the stellar photosphere. As shown in Sect. 4, for fast rotators the stellar radius is a function of the co-latitude, and the apparent stellar photosphere is dependent on additional parameters such as gravity darkening, effective temperature, rotation velocity, and polar inclination (discussed in the following sub-sections).

As explained in the previous sections, the equatorial radius $R_{\rm eq}$ determined here (or more generally the photospheric $R(\theta)$) is based on a physical model fitted to observations taken on a normal B phase of Achernar. As expected, the $R_{\rm eq}$ measured in this work is smaller than the previous results derived from VLTI/VINCI observations, obtained in an epoch with a small, but non negligible influence of a residual disk (Domiciano de

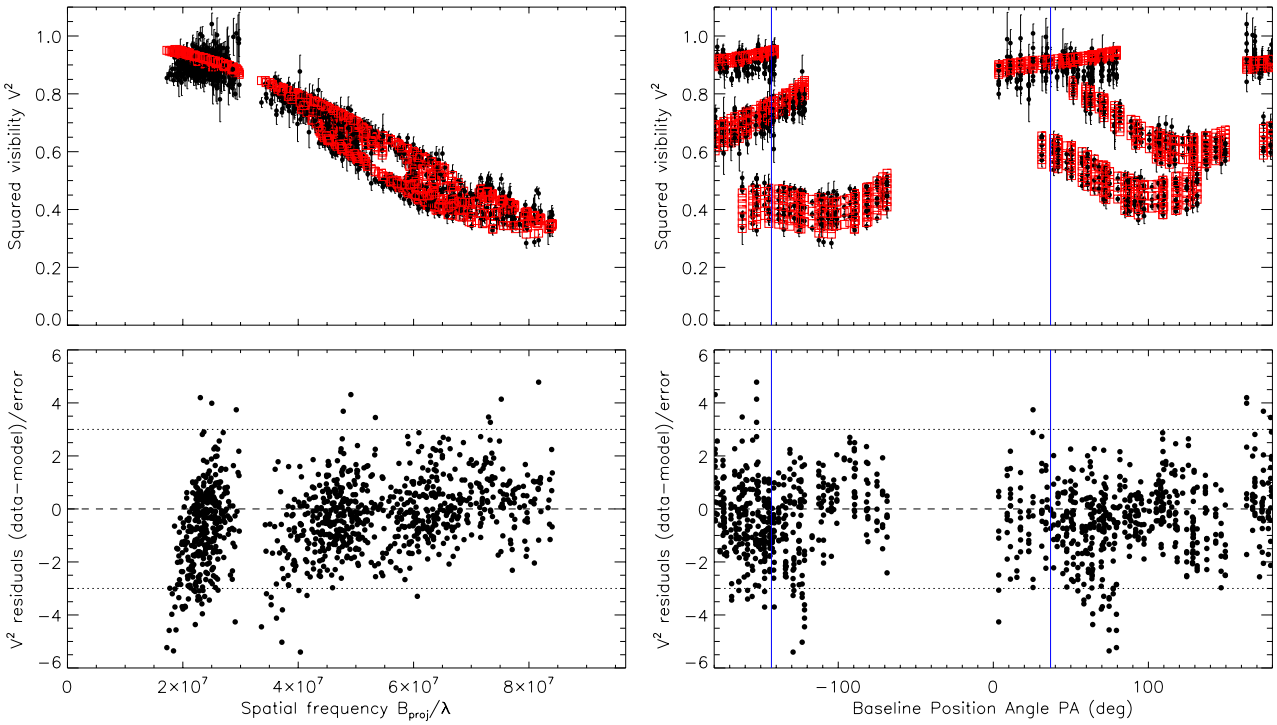

Fig. 9. *Top:* Squared visibilities V^2 observed on Achernar (filled circles and error bars) and computed (opened squares) from the best-fit CHARRON model (Table 5) as a function of spatial frequency (left column) and baseline *PA* (right column). *Bottom:* V^2 residuals from observations relative to the best-fit model in units of corresponding uncertainties. Vertical solid lines indicate the position angles of the visible (216.9° ≡ −143.1°) and hidden (16.9° = 216.9° − 180°) stellar poles. The horizontal dotted lines delimit the $\pm 3\sigma$ region around zero (dashed line).

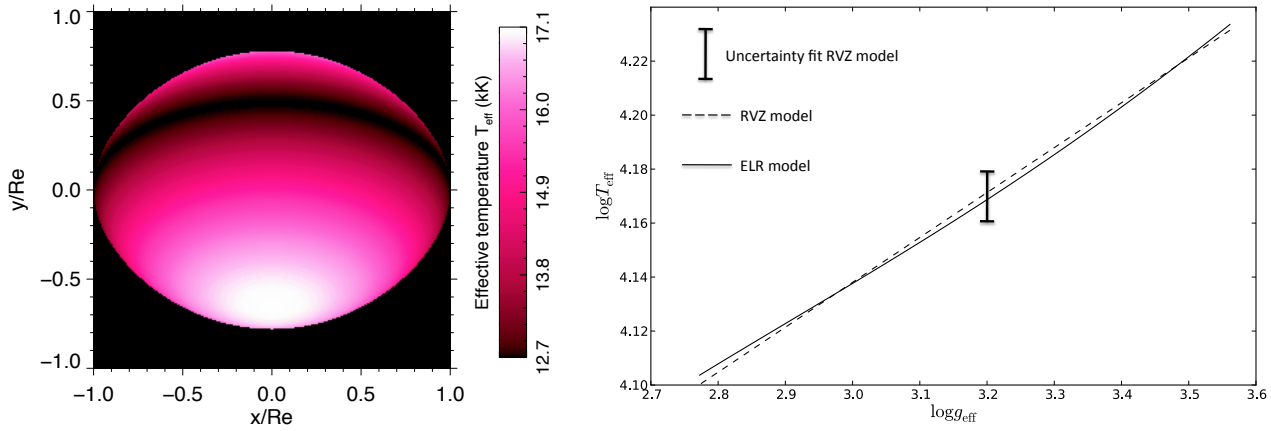

Fig. 12. *Left:* Effective temperature map of Achernar corresponding to the best-fit of the CHARRON RVZ model to the VLTI/PIONIER H band observations (model parameters in Table 5). The spatial coordinates are normalized to the measured equatorial radius $R_{\rm eq} = 9.16\,R_\odot$. The polar and equatorial effective temperatures of Achernar are $T_{\rm p} = 17\,124$ K (white) and $T_{\rm eq} = 12\,673$ K (black). *Right:* $\log T_{\rm eff}$ as a function of $\log g_{\rm eff}$ of Achernar for the ELR model (solid line Espinosa Lara & Rieutord 2011). The calculations were performed considering a Roche model with the same stellar parameters as in Table 5, except the gravity darkening, which is directly obtained from the ELR model. The dashed straight line shows the $\log T_{\rm eff}$ *versus* $\log g_{\rm eff}$ corresponding to the best-fit RVZ model with the measured gravity darkening coefficient $\beta\,(= 0.166^{+0.012}_{-0.010})$. The vertical bar indicates the uncertainty in $T_{\rm eff}$ associated to the measured uncertainty in this best-fit β value alone. We also note that by fitting a straight line to the ELR model (solid curve) results in an identical $\beta\,(= 0.166)$ as measured with the CHARRON RVZ model, matching exactly the dashed straight line. Thus, although the ELR model predicts a slightly more complex gravity darkening relation than the RVZ model (Eq. 3), these two gravity darkening models agree within the uncertainties derived from the RVZ model fit to the PIONIER observations.

Souza et al. 2003; Kervella & Domiciano de Souza 2006; Carciofi et al. 2008).

Considering the stellar size derived from the VLTI/AMBER observations by Domiciano de Souza et al. (2012a), we postpone the discussion to Sect. 5.5, where we consider the whole set of model parameters.

5.2. Photometry and effective temperature

The photometric magnitudes in the UBVJHK bands and the bolometric flux derived from the CHARRON best-fit model are compared with measurements reported in the literature in Table 6. We first note form the table that these observed magnitudes and bolometric fluxes show uncertainties and/or dispersion of measured values of the order of 10% − 20%, which are at least

Table 5. Physical parameters of Achernar derived from the fit of the RVZ model (CHARRON code) to VLTI/PIONIER H band data using the MCMC method (emcee code). Details of the fit are given in Sect. 4.2.

Model free parameters fitted	**Values and uncertainties**
Equatorial radius: $R_{\rm eq}$ ($R_\odot$)[a]	9.16 (+0.23; −0.23)
Equatorial rotation velocity: $V_{\rm eq}$ (km s^{-1})	298.8 (+6.9; −5.5)
Rotation-axis inclination angle: i (°)	60.6 (+7.1; −3.9)
Gravity-darkening coefficient: β	0.166 (+0.012; −0.010)
Position angle of the visible pole: $PA_{\rm rot}$ (°)	216.9 (+0.4; −0.4)
Derived parameters	**Values**
Equatorial angular diameter: $\oslash_{\rm eq} = 2R_{\rm eq}/d$ (mas)	1.99
Polar radius: $R_{\rm p}$ ($R_\odot$)	6.78
$R_{\rm eq}/R_{\rm p}$; $\epsilon \equiv 1 - R_{\rm p}/R_{\rm eq}$	1.352; 0.260
Apparent flattening (major to minor axis ratio)	1.30
Mean angular diameter: $\overline{\oslash}$ (mas)	1.77
$V_{\rm eq} \sin i$ (km s^{-1})	260.3
Critical rotation rate[b]: $V_{\rm eq}/V_{\rm c}$; $\Omega/\Omega_{\rm c}$	0.883; 0.980
Keplerian rotation rate[c]: $V_{\rm eq}/V_{\rm k}$; $\Omega/\Omega_{\rm k}$	0.838; 0.838
Polar temperature: $T_{\rm p}$ (K)	17 124
Equatorial temperature: $T_{\rm eq}$ (K)	12 673
Luminosity: $\log L/L_\odot$	3.480
Equatorial gravity: $\log g_{\rm eq}$	2.772
Polar gravity: $\log g_{\rm p}$	3.561
Rotation period: $P_{\rm rot}$ (h)	37.25
Rotation frequency: $\nu_{\rm rot}$ (d^{-1})	0.644

[a] The uncertainty in the distance d from van Leeuwen (2007) was added quadratically to the fit uncertainty on $R_{\rm eq}$.
[b] Critical (Roche model) linear ($V_{\rm c}$) and angular ($\Omega_{\rm c}$) velocities: $V_{\rm c} = \Omega_{\rm c} R_{\rm eq,c} = \sqrt{GM/R_{\rm eq,c}}$, with $R_{\rm eq,c} = 1.5R_{\rm p}$ (critical Roche equatorial radius).
[c] Keplerian (orbital) linear ($V_{\rm k}$) and angular ($\Omega_{\rm k}$) velocities: $V_{\rm k} = \Omega_{\rm k} R_{\rm eq} = \sqrt{GM/R_{\rm eq}}$.

partially caused by a combination of instrumental and intrinsic effects from the star. Indeed, Achernar is known to present multiple flux variabilities at time scales from hours to years, which are caused for example by pulsations (Goss et al. 2011), binarity (Kervella & Domiciano de Souza 2007), and the B⇆Be cycle (e.g. Vinicius et al. 2006). Thus, the observed magnitudes and bolometric flux should not be considered as tight constraints to the model fitting, although they provide an important consistency check on the best-fit model parameters. Indeed, the modeled magnitudes and bolometric flux given in Table 6 agree with the observations within their uncertainties and/or dispersion of measured values.

By using Eq. 5 we can cross-check the consistency between the adopted mean effective temperature $\overline{T}_{\rm eff}$, the measured bolometric flux $F_{\rm bol}$, and the mean angular diameter $\overline{\oslash}$ reported in Tables 5 and 6. From the $F_{\rm bol}$ provided by Code et al. (1976) and Nazé (2009) one thus obtain $\overline{T}_{\rm eff} = 15094$ K and 14703 K, respectively. We note that the temperature of 14 510 K estimated by Code et al. (1976) is somewhat lower than the value estimated here because they considered the higher angular diameter (1.92 mas) reported by Hanbury Brown et al. (1974), based on intensity interferometry observations at the Narrabri Observatory. As expected, this diameter is between the major and minor diameters derived in the present work. However the measurements from Hanbury Brown did not allow to take into account the angular size variation with the baseline position angle caused by the rotational flattening of Achernar. Thus, recalling that the average effective temperature of $\simeq$ 15 000 K reported by Vinicius et al. (2006) was derived from different methods, the adopted $\overline{T}_{\rm eff} = 15\,000$ K is good agreement with several independent measurements (bolometric fluxes, photometry, spectroscopy, interferometry).

5.3. Inclination and rotation velocity

The inclination angle i ($= 60.6^{+7.1}_{-3.9}$) measured in this work is compatible (within $\simeq 1.5\sigma$) with the values ($i \sim 65 - 70°$) estimated by Vinicius et al. (2006) and Carciofi et al. (2007).

Different values have been previously reported on the projected rotation velocity $V_{\rm eq} \sin i$ of Achernar, with mainly three distinct range of values: $V_{\rm eq} \sin i \sim 223 - 235$ km s^{-1} (e.g. Slettebak 1982; Chauville et al. 2001; Vinicius et al. 2006), $V_{\rm eq} \sin i = 292 \pm 10$ km s^{-1} (Domiciano de Souza et al. 2012a), and $V_{\rm eq} \sin i \sim 410$ km s^{-1} (e.g. Hutchings & Stoeckley 1977; Jaschek & Egret 1982).

In this work we determine $V_{\rm eq} \sin i = 260.3^{+19}_{-12}$ km s^{-1}, where these uncertainties were computed by properly adding the individual uncertainties estimated on i and $V_{\rm eq}$ (c.f. Table 5 and Fig. 8). This estimated $V_{\rm eq} \sin i$ lies between the lower and intermediate values found in the literature, as mentioned above, and it is compatible with them within 2σ to 3σ, i.e. $\simeq 30-40$ km s^{-1}.

Some clues to explain the discrepancies in the measured $V_{\rm eq} \sin i$ may be given by the fact that different methods to estimate this quantity can lead to different results depending on their sensitivity to the non-uniform photospheric intensity distribution caused by the gravity darkening. For example, it is known that, because of gravity darkening, the $V_{\rm eq} \sin i$ obtained from visible/IR spectroscopy are generally underestimated in fast rotating stars (Townsend et al. 2004; Frémat et al. 2005). Moreover, the actual $V_{\rm eq} \sin i$ of Achernar seems to significantly vary in time, as recently showed by Rivinius et al. (2013), who put in evidence $V_{\rm eq} \sin i$ variations with amplitudes $\lesssim 35$ km s^{-1} that are correlated to the B⇆Be phase transitions. Interestingly, this amplitude of $V_{\rm eq} \sin i$ variations is of the same order of the differences of $V_{\rm eq} \sin i$ values measured in this work and by several other authors as discussed above.

Table 6. Observed and modeled UBVJHK photometry and bolometric flux $F_{\rm bol}$ of Achernar. The model values are based on the parameters given in Table 5 for the best emcee fit of CHARRON RVZ model to PIONIER data. For comparison, we also show the values derived from the model given by Domiciano de Souza et al. (2012a), based on the AMBER differential phases.

Catalogue or reference	U	B	V	J	H	K	$F_{\rm bol}$ (10^{-9} W m^{-2})
2MASS [a]				0.815 ± 0.254	0.865 ± 0.320	0.880 ± 0.330	
NOMAD Tycho-2 [b]		0.473	0.527				
Johnson et al. (1966)		0.32	0.47				
Code et al. (1976)							54.4 ± 4.3
Jaschek & Egret (1982)	-0.36	0.30	0.46				
Nazé (2009)							48.98
CHARRON RVZ model	-0.279	0.339	0.472	0.783	0.828	0.886	53.05
Model in 2012 paper	-0.387	0.215	0.333	0.596	0.631	0.684	62.90

[a] Cutri et al. (2003); Skrutskie et al. (2006).
[b] Hog et al. (2000); Zacharias et al. (2005).

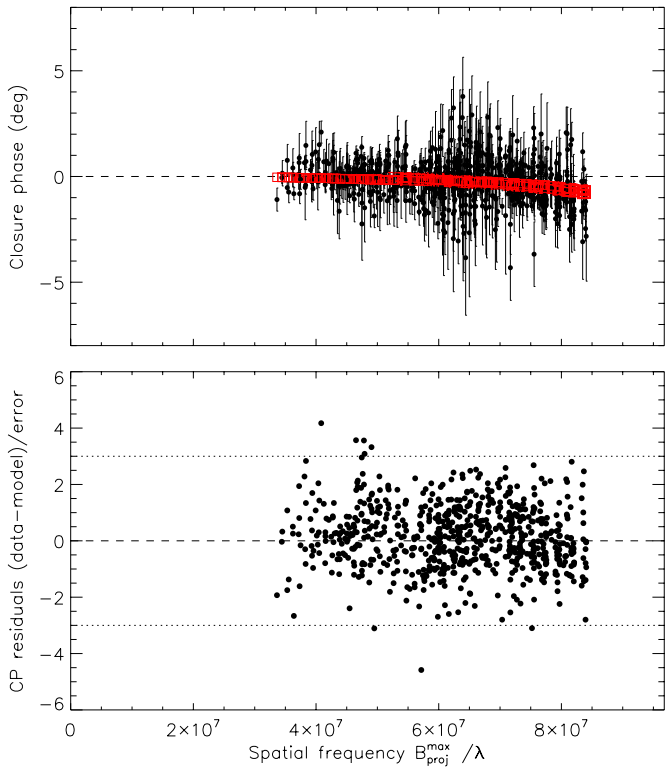

Fig. 10. *Top:* Closure phases (*CP*) observed on Achernar and computed from the best-fit CHARRON model (Table 5) as a function of the spatial frequency (for the longest projected baseline $B^{\rm max}_{\rm proj}$ in the corresponding triangle configuration). *Bottom: CP* residuals from observations relative to the best-fit model in units of corresponding uncertainties. The horizontal dotted lines delimit the $\pm 3\sigma$ region around zero (dashed line). Since the photosphere is only partially resolved, the *CP* signatures of fast rotation are small (within $\sim \pm 1°$).

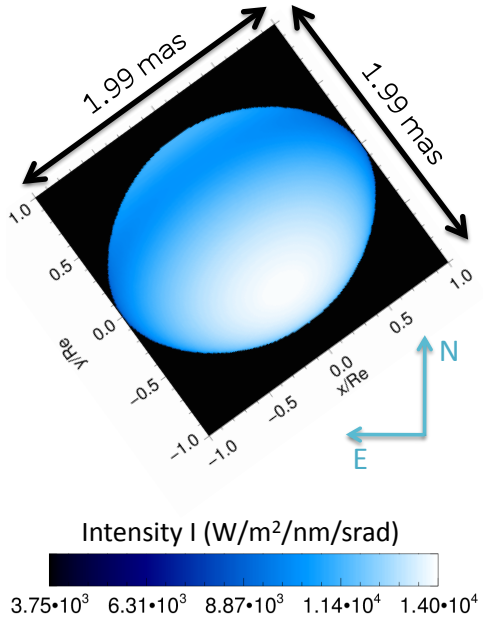

Fig. 11. Intensity map of Achernar corresponding to the best-fit of the CHARRON RVZ model to the VLTI/PIONIER H band observations. The spatial coordinates indicated in angular milliarcseconds (mas) units and also normalized to the equatorial radius $R_{\rm eq} = 9.16\,R_\odot$. The complete list of the measured stellar parameters is given in Table 5.

Finally, we note that, from the three frequencies detected by Goss et al. (2011), based on time series analysis of photometric light curves of Achernar, the low amplitude frequency of $0.680\,{\rm d}^{-1}$ is the closest (but still $\sim 2.5\sigma$ above) to the rotation frequency $\nu_{\rm rot} = 0.644 \pm 0.015\,{\rm d}^{-1}$ derived in the present work (uncertainty was estimated by properly adding quadratically the relative maximum individual uncertainties on $R_{\rm eq}$ and $V_{\rm eq}$).

5.4. Gravity darkening

The gravity darkening parameter β determined in this work is significantly lower than the von Zeipel law ($\beta = 0.25$), a result in agreement with β values derived from recent interferometric observations of fast rotating stars (see for example the recent review from van Belle 2012, and references therein).

These low β (< 0.25) are explained theoretically by Espinosa Lara & Rieutord (2011), who derive an alternative gravity darkening law (ELR model hereafter) by relaxing the assumption of barotropicity leading to the von Zeipel law. The ELR model includes a divergence-free flux vector and the ratio $T^4_{\rm eff}/g_{\rm eff}$ is allowed to vary with latitude leading to an analytical relation between $T_{\rm eff}$ and $g_{\rm eff}$ without the need to assume a constant β parameter as in Eq. 3. Let us compare in more detail the gravity darkening derived from the best-fit of the CHARRON RVZ model with the ELR model prediction. Both models adopt the Roche approximation so that they consider an identical photo-

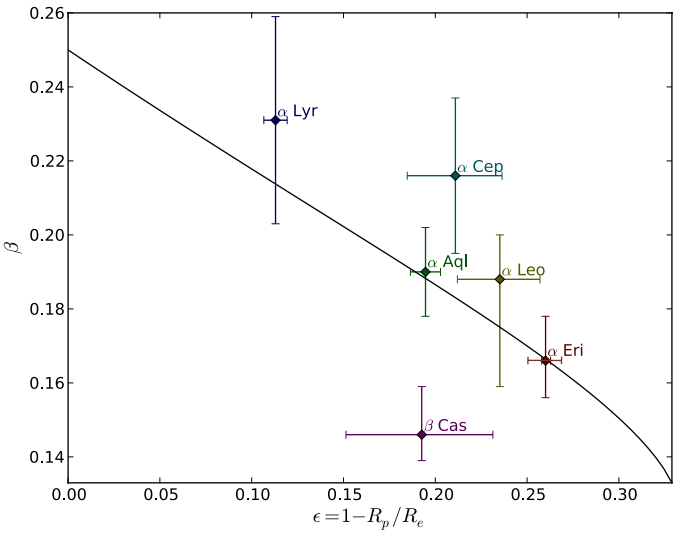

Fig. 13. Gravity darkening coefficient β estimated from the ELR model (Espinosa Lara & Rieutord 2011) as a function of the rotation flattening ϵ compared to values measured from interferometric observations of six rapidly rotating stars (references in Sect. 5.4), Achernar (α Eri) being the flattest one. The estimation of β is obtained from a fit to the $\log T_{\rm eff}$ *versus* $\log g_{\rm eff}$ curves directly predicted by the ELR model, such as in Fig. 12 (right). The ELR model predictions and interferometric measurements have a good general agreement (see Sect. 5.4 for a more detailed discussion).

spheric shape $R(\theta)$. Based on the best-fit parameters in Table 5, Fig. 12 compares the $\log T_{\rm eff}$ *versus* $\log g_{\rm eff}$ relations for the two gravity darkening models. The $T_{\rm eff}$ map of the RVZ model is also illustrated in Fig. 12. As shown in the figure, the two models agree within the parameter uncertainties but the present observation errors do not allow yet to probe the small differences in $T_{\rm eff}(\theta)$ predicted by the models.

Although the detailed $T_{\rm eff}(\theta)$ cannot be investigated, it is clear that the ELR model reproduces an average $T_{\rm eff}(\theta)$ dependence totally compatible with measurements from the RVZ model, but without the need to use a β parameter. Indeed, by estimating an equivalent β value (e.g. from $\log(T_{\rm eq}/T_{\rm p})/\log(g_{\rm eq}/g_{\rm p})$), Espinosa Lara & Rieutord (2011, in their Fig. 4) show a good agreement between their predictions and the β coefficients measured on four fast rotators as a function of flattening $\epsilon\,(=1-R_{\rm p}/R_{\rm eq})$.

In Fig. 13 we extend this comparison by adding α Lyr (Vega; Monnier et al. 2012) and Achernar (α Eri; present work). These two new stars provide a crucial test for the ELR model since they have, respectively, the lowest and highest flattening in the sample. Fig. 13 thus compares β and ϵ from the ELR model with values measured on six fast rotators (listed from hotter to colder spectral types): α Eri (Achernar, B3-6Vpe; this work), α Leo (Regulus, B8IVn; Che et al. 2011), α Lyr (Vega, A0V; Monnier et al. 2012), α Aql (Altair, A7IV-V; Monnier et al. 2007), α Cep (Alderamin, A7IV; Zhao et al. 2009), β Cas (Caph, F2IV; Che et al. 2011).

Five out of the six stars are in relatively good agreement with the ELR model (in particular Altair and Achernar), considering the observational uncertainties. The only exception is β Cas and a more detailed study would be required do decide if the discrepancy is due to a bias in the measured flattening related to its low inclination (as discussed by Espinosa Lara & Rieutord 2011) and/or maybe related to the fact that this is star is the coldest one in the sample. This agreement between observational and theoretical results are thus a promising perspective for a more profound understanding of the gravity darkening effect in fast rotating stars.

Based on the curve β *versus* flattening $\epsilon\,(=1-R_{\rm p}/R_{\rm eq})$ given in Fig. 13 and derived from the ELR model, we can deduce a linear relation that roughly follows this curve:

$$\beta \simeq 0.25 - 0.328\epsilon \quad (6)$$

This linear approximation reproduces the curve in Fig. 13 within 1% (3%) for $\epsilon \lesssim 0.27\,(0.30)$. We recall however that the use of a β parameter is not required nor compatible with the ELR model, which does not describe the gravity darkening by a power law as in Eq. 3.

5.5. Comparison with the VLTI/AMBER differential phases

Let us now compare the best-fit CHARRON model determined from the PIONIER data (Table 5) with the AMBER differential phases, described in Sect. 2.2 and by Domiciano de Souza et al. (2012a). The differential phases computed directly from the PIONIER best-fit model already well reproduce the AMBER observations, resulting in $\chi^2_{\rm r} = 1.3$ (DOF = 3808). This $\chi_{\rm r}$ is only slightly higher than the 1.2 value found by Domiciano de Souza et al. (2012a) from the same model, but with a somewhat different set of parameters. Indeed, for all AMBER baselines and wavelengths considered, the absolute differences between both sets of modeled differential phases are smaller than 0.5°, which is lower than the typical uncertainties in the differential phases for these AMBER observations (median value of 0.6°).

Conversely, the photospheric model parameters derived from the AMBER differential phases (Domiciano de Souza et al. 2012a) are far from reproducing the PIONIER observations, resulting in a 10 times higher $\chi^2_{\rm r}$ (= 19.2). Moreover, the model from Domiciano de Souza et al. (2012a) presents a worse agreement with the photometric observations as shown in Table 6 (brighter star in particular due to the higher β and size). Thus, the CHARRON RVZ photospheric model with parameters as in Table 5, provides the best general agreement with the whole set of polarimetric, spectroscopic, photometric and interferometric (PIONIER and AMBER) observations of Achernar considered in this work.

6. Beyond the photospheric model ?

We have shown in Sect. 3 that the interferometric data analyzed in this work are not influenced by a strong circumstellar disk or by the known binary companion. This conclusion is in agreement with the good quality of the fit obtained by adopting a single photospheric fast rotator RVZ model in Sect. 4. In spite of this satisfactory result, and relying on the relatively high precision PIONIER data, let us push the analysis a step further in order to search for possible more subtle components in the close environment of Achernar and/or indications of small deviations from the adopted fast rotator RVZ model. To this aim two complementary approaches were adopted: (1) model fitting of the RVZ model plus an additional analytical component and (2) image reconstruction.

6.1. Photospheric physical model plus analytical component

We used the emcee code to fit a model consisted by the photospheric best-fit RVZ model determined in Sect. 4 plus an analytical 2D Gaussian ellipse. The free parameters of the 2D Gaussian

ellipse and their initial range of values (initial uniform distribution of values) are:

- major axis FWHM $a_{\rm GE}$: 0.5 mas to 20 mas
- minor to major axis ratio $r_{\rm GE}$: 0.1 to 1
- position angle of the major axis $PA_{\rm GE}$: 0° to 180°
- flux ratio (relative to the stellar total flux) $F_{\rm GE}$: 0% to 10%
- horizontal (equatorial direction) shift relative to the center of the star $x_{\rm GE}$: −15 mas to 15 mas
- vertical (polar direction) shift relative to the center of the star $y_{\rm GE}$: −15 mas to 15 mas

This approach is similar to, but more general than the one adopted by Kervella & Domiciano de Souza (2006) since it allows to simultaneously test different faint circumstellar structures such as a faint companion or a weak polar wind or equatorial disk.

As before, the emcee algorithm explored the entire parameter space (within the above defined boundaries) using 800 walkers in a 200 steps burn-in phase and 150 steps in the final phase. Since the RVZ model already provide a good fit to the data, the parameters of the additional 2D Gaussian ellipse are not expected to be strongly constrained, leading to $\chi^2_{\rm r} = 1.79$, which is only slightly lower than the value obtained for the RVZ model alone. Two parameters of the 2D Gaussian ellipse were nevertheless relatively well constrained: $a_{\rm GE} = 5.2 \pm 2.4$ mas and $F_{\rm GE} = 0.7\% \pm 0.1\%$. It also comes out from the fit that the position of this possible additional component is roughly centered on the star, with a shift uncertainty smaller than $\sim$ 5 mas for both directions ($x_{\rm GE}$ and $y_{\rm GE}$). The remaining parameters are not well constrained by the data.

6.2. Image reconstruction

As a model independent study of the PIONIER data we have also performed an image reconstruction of Achernar using the MIRA[2] software (Thiébaut 2008). MIRA is based on an iterative process, aimed at finding the image that minimizes a joint criterion under constraints of positivity and normalization:

$$f(\mathbf{x}) = f_{\rm data}(\mathbf{x}) + \mu f_{\rm prior}(\mathbf{x}) \ , \tag{7}$$

where $\mathbf{x}$ are the set of image pixels, $f_{\rm data}(\mathbf{x})$ is the penalty function of the measurements, $f_{\rm prior}(\mathbf{x})$ is a term that enforces additional *a priori* constraints, and $\mu\,(\geq 0)$ is the hyper-parameter, i.e. the weight of the priors.

The hyper-parameter has to be chosen as large as possible in order to maximize the weight of the constraints arising from physical modeling and to ensure the convergence of the reconstruction at a minimal value of the penalty χ^2. As we dispose of a model of the target, we used an elliptical Lorentzian *a priori* ($f_{\rm prior}(\mathbf{x})$) with (1) the same minor axis position angle as Achernar, 216.9° (≡ 36.9° for a centrally-symmetrical ellipse), (2) a major to minor axis ratio of 1.3 corresponding to the apparent flattening, and (3) a FWHM = 3.2 mas in the major axis direction, corresponding to a size slightly bigger than Achernar's angular diameter, to avoid missing possible structures close to the photosphere.

In order to determine the best value of the hyper-parameter, we performed several ($\sim 10^3$) independent reconstructions with 200 iterations and random μ values ranging from 1 to 10^9. In Fig. 14 (available electronically), we show the distribution of χ^2 for converged reconstructions as a function of μ for each reconstruction. This procedure revealed that there is a plateau of minimum $\chi^2 (= 1.4)$, reached for values of μ lower than $\hat{\mu} \sim 630$.

Once the parameters of the reconstruction have been determined, we followed the procedure described by Millour et al. (2012) to create the reconstructed image of Achernar as the weighted average of several hundred converged reconstructed images:

$$\bar{I}(\mathbf{x}) = \frac{\sum_i 1/\chi^2_i I_i(\mathbf{x} - \bar{\mathbf{x}}_i)}{\sum_i 1/\chi^2_i} \ , \tag{8}$$

where each image i was centered on its photocenter position $\bar{\mathbf{x}}_i$ before summation. The weight of each reconstruction is $1/\chi^2_i$, with a limit penalty value of $\chi^2_i \leq 5$ to reject low quality reconstructed images.

Figure 15 shows the reconstructed image of Achernar, both given by MIRA with a 0.07 mas resolution pixel (over-resolved image) and convolved by a Gaussian beam of FWHM = 1.6 mas (diffraction limit of the PIONIER observations). Although this diffraction limit does not provide a highly resolved image of the photosphere, it is enough to investigate the close circumstellar environment. Indeed, the reconstructed MIRA image clearly shows the presence of a compact object (stellar photosphere) without any signature of extended circumstellar component. This is more clearly seen in the right panel of Fig. 15, which shows the subtraction of the MIRA and best-fit CHARRON images, convolved by the 1.6 mas Gaussian beam. The difference between these images is at most 1.5% in modulus (relative to the total flux of the MIRA image) and below $\sim$ 0.5% almost everywhere.

Both results from the image reconstruction and the fit of the RVZ model plus an analytical 2D Gaussian ellipse presented in this section show that no additional component is present in the PIONIER data within $\sim$ ±1% level of intensity. This is in well agreement with the conclusions based on polarimetric and spectroscopic data and modeling shown in Sect. 3.

7. Conclusions

Based on ESO-VLTI interferometric observations of Achernar obtained in a normal B star phase we derived its photospheric parameters by the fit of our physical model CHARRON using a Markov Chain Monte Carlo (MCMC) method. A best-fit photospheric model was derived from squared visibilities and phase closures recorded with the PIONIER beam combiner in the H band. This model is also in good agreement with AMBER HR differential phase observations around the Brγ line.

The interferometric observations were complemented by spectroscopic, polarimetric, and photometric data to investigate the status of the circumstellar environment of Achernar during the VLTI observing runs, to cross check our model fitting results, and to set constraints into the model parameter space (photosphere and possible residual disk). In particular, polarimetry was crucial to constrain the disk density, imposing quite well-defined upper limits.

We note that our photospheric model of Achernar is in agreement with many observations from distinct techniques: PIONIER V^2 and CP, AMBER differential phases, V and B band polarimetry, Hα and Hβ line profiles, UBJHK photometry. Moreover, our results are compatible with the theoretical ELR model of gravity darkening proposed by Espinosa Lara & Rieutord (2011), which we also show to be consistent with previously published results from different fast rotators over a large range of

[2] Multi-aperture Image Reconstruction Algorithm.

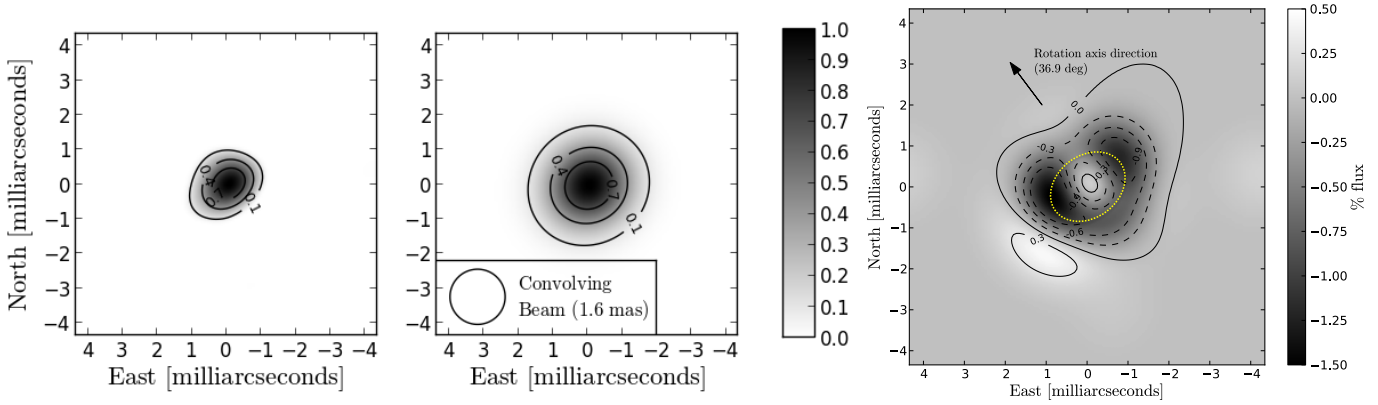

Fig. 15. *Left:* Image reconstruction of Achernar obtained by applying the MIRA software to the H band VLTI/PIONIER observations. *Middle:* Convolution of this reconstructed MIRA image convolved by a Gaussian beam of FWHM = 1.6 mas (= $0.61\lambda/B_{\rm max}$) corresponding to the diffraction limit of the PIONIER observations. *Right:* Reconstructed MIRA image minus the best-fit CHARRON image (Fig. 11 convolved by the Gaussian diffraction limit beam to mach the resolution of reconstructed image). The difference between the images is very small, < 1.5% in modulus, relative to the total MIRA image flux), indicating that essentially only the photosphere of Achernar is contributing to the PIONIER data, without any additional circumstellar component. The dotted ellipse represents roughly the border of the apparent photosphere of Achernar given by the best-fit CHARRON RVZ model.

rotational flattening (Achernar being the flattest one in the sample). Observational validation of gravity darkening models such as the ELR model is an important step in the understanding of rapidly rotating stars since it has the great advantage of reducing the number of free parameters (β coefficient is not needed anymore). Indeed, by relying on few input parameters and hypothesis, the ELR model reproduces five out of the six measured gravity darkening, which is motivating and promising for a more profound understand of this important effect in stellar physics.

Taking advantage of the good quality and uv coverage of the PIONIER observations we have also pushed the analysis a little further and performed an interferometric image reconstruction that did not reveal any signatures of additional circumstellar components and/or deviations from the photospheric Roche-von Zeipel (RVZ) model within a $\sim \pm 1\%$ level of intensity. This result is also in agreement with a fit of an addition analytical component to the RVZ model. We note that, although the spatial resolution of the image is rather low (spatial frequencies restricted to the first visibility lobe) this is, to our knowledge, the first reconstructed image of the photosphere of a Be star.

The results of this work thus provide the first determination of the pure photospheric parameters of a Be star in a normal B phase. The measured photospheric parameters are $R_{\rm eq}$, $V_{\rm eq}$, i, β, and $PA_{\rm rot}$. Concerning Achernar specifically, these parameters can be used as a reference input photospheric model for future studies based on modeling including circumstellar disk and photosphere.

Acknowledgements. PIONIER is funded by the Université Joseph Fourier (UJF), the Institut de Planétologie et d'Astrophysique de Grenoble (IPAG), the Agence Nationale pour la Recherche (ANR-06-BLAN-0421 and ANR-10-BLAN-0505), and the Institut National des Science de l'Univers (INSU PNP and PNPS). The integrated optics beam combiner is the result of a collaboration between IPAG and CEA-LETI based on CNES R&T funding. This research has made use of the SIMBAD database, operated at the CDS, Strasbourg, France, of NASA Astrophysics Data System Abstract Service, and of the Jean-Marie Mariotti Center (JMMC) services. This work has made use of the computing facilities of the Laboratory of Astroinformatics (IAG/USP and NAT/Unicsul, Brazil), whose purchase was made possible by the Brazilian agency FAPESP (grant 2009/54006-4) and the INCT-A. We thank the CNRS-PICS (France) program 2010-2012 for supporting our Brazilian-French collaboration and the present work. We acknowledge D. Mary and D. Foreman-Mackey for their enlightening suggestions on MCMC methods and on the emcee code. We also thank E. Alecyan and T. Rivinius for providing the reduced HARPS and FEROS visible spectra of Achernar.

References

Carciofi, A. C. & Bjorkman, J. E. 2006, ApJ, 639, 1081
Carciofi, A. C., Domiciano de Souza, A., Magalhães, A. M., Bjorkman, J. E., & Vakili, F. 2008, ApJ, 676, L41
Carciofi, A. C., Magalhães, A. M., Leister, N. V., Bjorkman, J. E., & Levenhagen, R. S. 2007, ApJ, 671, L49
Chauville, J., Zorec, J., Ballereau, D., et al. 2001, A&A, 378, 861
Che, X., Monnier, J. D., Zhao, M., et al. 2011, ApJ, 732, 68
Code, A. D., Bless, R. C., Davis, J., & Brown, R. H. 1976, ApJ, 203, 417
Cutri, R. M., Skrutskie, M. F., van Dyk, S., et al. 2003, VizieR Online Data Catalog, 2246, 0
Domiciano de Souza, A., Hadjara, M., Vakili, F., et al. 2012a, A&A, 545, A130
Domiciano de Souza, A., Kervella, P., Jankov, S., et al. 2003, A&A, 407, L47
Domiciano de Souza, A., Vakili, F., Jankov, S., Janot-Pacheco, E., & Abe, L. 2002, A&A, 393, 345
Domiciano de Souza, A., Zorec, J., & Vakili, F. 2012b, in SF2A-2012: Proceedings of the Annual meeting of the French Society of Astronomy and Astrophysics, ed. S. Boissier, P. de Laverny, N. Nardetto, R. Samadi, D. Valls-Gabaud, & H. Wozniak, 321–324
Espinosa Lara, F. & Rieutord, M. 2011, A&A, 533, A43
Foreman-Mackey, D., Hogg, D. W., Lang, D., & Goodman, J. 2013, PASP, 125, 306
Frémat, Y., Zorec, J., Hubert, A., & Floquet, M. 2005, A&A, 440, 305
Goodman, J. & Weare, J. 2010, Communications in Applied Mathematics and Computational Science, 5, 65
Goss, K. J. F., Karoff, C., Chaplin, W. J., Elsworth, Y., & Stevens, I. R. 2011, MNRAS, 411, 162
Haguenauer, P., Alonso, J., Bourget, P., et al. 2010, in Society of Photo-Optical Instrumentation Engineers (SPIE) Conference Series, Vol. 7734, Society of Photo-Optical Instrumentation Engineers (SPIE) Conference Series
Hanbury Brown, R., Davis, J., & Allen, L. R. 1974, MNRAS, 167, 121
Harmanec, P. 1988, Bulletin of the Astronomical Institutes of Czechoslovakia, 39, 329
Haubois, X., Carciofi, A. C., Rivinius, T., Okazaki, A. T., & Bjorkman, J. E. 2012, ApJ, 756, 156
Hog, E., Fabricius, C., Makarov, V. V., et al. 2000, VizieR Online Data Catalog, 1259, 0
Hubeny, I. & Lanz, T. 2011, Synspec: General Spectrum Synthesis Program, astrophysics Source Code Library
Hutchings, J. B. & Stoeckley, T. R. 1977, PASP, 89, 19
Jackson, S., MacGregor, K. B., & Skumanich, A. 2004, ApJ, 606, 1196
Jaschek, M. & Egret, D. 1982, in IAU Symposium, Vol. 98, Be Stars, ed. M. Jaschek & H.-G. Groth, 261
Jerzykiewicz, M. & Molenda-Zakowicz, J. 2000, Acta Astron., 50, 369
Johnson, H. L., Mitchell, R. I., Iriarte, B., & Wisniewski, W. Z. 1966, Communications of the Lunar and Planetary Laboratory, 4, 99
Kervella, P. & Domiciano de Souza, A. 2006, A&A, 453, 1059
Kervella, P. & Domiciano de Souza, A. 2007, A&A, 474, L49
Kervella, P., Domiciano de Souza, A., & Bendjoya, P. 2008, A&A, 484, L13
Kervella, P., Thévenin, F., Morel, P., Bordé, P., & Di Folco, E. 2003, A&A, 408, 681

Kurucz, R. L. 1979, ApJS, 40, 1
Le Bouquin, J.-B., Berger, J.-P., Lazareff, B., et al. 2011, A&A, 535, A67
Maeder, A. & Meynet, G. 2000, ARA&A, 38, 143
Magalhães, A. M., Benedetti, E., & Roland, E. H. 1984, PASP, 96, 383
Magalhães, A. M., Rodrigues, C. V., Meade, M., et al. 1996, in Astronomical Society of the Pacific Conference Series, Vol. 97, Polarimetry of the Interstellar Medium, ed. W. G. Roberge & D. C. B. Whittet, 202
Millour, F. A., Vannier, M., & Meilland, A. 2012, in Society of Photo-Optical Instrumentation Engineers (SPIE) Conference Series, Vol. 8445, Society of Photo-Optical Instrumentation Engineers (SPIE) Conference Series
Monnier, J. D., Che, X., Zhao, M., et al. 2012, ApJ, 761, L3
Monnier, J. D., Zhao, M., Pedretti, E., et al. 2007, Science, 317, 342
Nazé, Y. 2009, A&A, 506, 1055
Rivinius, T., Baade, D., Townsend, R. H. D., Carciofi, A. C., & Štefl, S. 2013, A&A, 559, L4
Skrutskie, M. F., Cutri, R. M., Stiening, R., et al. 2006, AJ, 131, 1163
Slettebak, A. 1982, ApJS, 50, 55
Thiébaut, E. 2008, in Society of Photo-Optical Instrumentation Engineers (SPIE) Conference Series, Vol. 7013, Society of Photo-Optical Instrumentation Engineers (SPIE) Conference Series
Townsend, R. H. D., Owocki, S. P., & Howarth, I. D. 2004, MNRAS, 350, 189
van Belle, G. T. 2012, A&A Rev., 20, 51
van Leeuwen, F. 2007, A&A, 474, 653
Vinicius, M. M. F., Zorec, J., Leister, N. V., & Levenhagen, R. S. 2006, A&A, 446, 643
von Zeipel, H. 1924, MNRAS, 84, 665
Zacharias, N., Monet, D. G., Levine, S. E., et al. 2005, VizieR Online Data Catalog, 1297, 0
Zhao, M., Monnier, J. D., Pedretti, E., et al. 2009, ApJ, 701, 209

Chapter 6

The Be star Achernar and the 2013 outburst

Achernar is a key star to investigate the Be phenomenon. Its importance derives from its proximity, enabling the detailed investigation of the CS emission of a star whose photospheric parameters are very well known (as seen in Chap. 5).

In the beginning of 2013 the star entered a new outburst phase (Tasso Napoleão, priv. comm.) after about 7 years of quiescence during which it was mostly a normal B star. Triggered by this exciting possibility, we started a broad-scope, multi-technique campaign to follow the disk evolution. Coordinating this campaign, gathering, reducing, analyzing and organizing the data took much of my time since then.

Here we report on the observational results and the initial modeling of the disk evolution. The analysis combine multi-technique data, including broadband polarimetry (OPD/LNA), spectroscopy (FEROS and others) and interferometry (VLTI-AMBER and PIONIER). The inteferometric survey, that includes 79 individual observations since 2013, corresponds to the first high-cadence interferometric survey of a Be star to date.

These data will allow us to test the VDD predictions in conditions hitherto not explored. For instance, the high cadence of the observations offers a rare opportunity to evaluate the evolution of a just formed Be disk in detail and derive the relevant physical quantities governing the system.

6.1 Star overview

Achernar displays important features that are related to the Be phenomenon: (i) a fast rotating central star; (ii) quasi-cyclic disk formation/dissipation, with both long- and short-term variations; (iii) episodic mass disk injections; and (iv) binarity. In addition,

there has been suggestions in the literature about a possible polar wind emission, that still remains to be verified. Before detailing the new data, we review Achernar's characteristics known previously to the current active phase.

The photospheric determination by interferometry

We discussed the consistent determination of multiple photospheric parameters of Achernar (radius, rotational velocity, inclination angle and on-sky orientation) by Domiciano de Souza et al. (2012) in Section 5.2. That work was based on AMBER spectro-interferometric differential phases along the Brγ line, a differential quantity.

A quantitative jump was given by Domiciano de Souza et al. (2014, Sect. 5.3). The study was based on PIONIER 4 beam combiner observations, including high precision visibility measurements with closure phase information. The stellar diameter ratio $R_{\rm eq}/R_p$ was found to be 1.352, which corresponds to a not so high rotation rate ($W = 0.838$). Still, it is the highest rotation rate observed in a angularly resolved star so far.

Evolutionary stage

Different estimations for the mass of Achernar points to the value of $\sim$6.2 $M_\odot$ (see references in Table 6.1). The photospheric parameters obtained from interferometry show that Achernar is a considerably large star and has a higher luminosity than a main sequence star of same mass (Table 6.1).

In Appendix D we apply the BeAtlas photospheric models of main-sequence stars to ultraviolet observations of Achernar. The results points to a star with $M \gtrsim 7.2 M_\odot$, but the quality of the fitting confirms that it is not a typical main sequence star.

These elements indicate that Achernar is likely at the end of the main sequence or in the early post-main sequence phases, as already proposed in literature (e.g., Rieutord and Espinosa, 2013).

6.1.1 Circumstellar activity

The variable circumstellar disk and photosphere

Vinicius et al. (2006) report both long-and short-term Hα variations in Achernar. The authors argue about the existence of a 14-15 year cyclic B-Be phase transition. These

Table 6.1 - Main sequence stellar parameters compared to the ones of Achernar derived from interferometry (Domiciano de Souza et al., 2014). The main sequence data assumes $W = 0.894$.

X_c	$M(M_\odot)$	$R_p(R_\odot)$	$L(L_\odot)$
0.54	5.50	3.21	845.18
0.30	5.50	4.14	1153.50
0.08	5.50	5.38	1480.41
0.54	6.40	3.55	1497.22
0.30	6.40	4.45	1953.61
0.08	6.40	5.75	2521.98
0.54	7.70	3.71	2564.45
0.30	7.70	4.93	3726.03
0.08	7.70	6.37	4827.72
Achernar	6.22[a]	6.78	3019.95

[a] $M = 6.1 M_\odot$ (Harmanec, 1988); $M = 6.22 M_\odot$ (Jerzykiewicz and Molenda-Zakowicz, 2000).

variations are understood as the recurrent formation/dissipation of the equatorial CS disk, and the 2013 activity is part of one of these cycles. This cycle, however, should be viewed with reservations. The authors only had detailed spectra for a period of 11 years (1991 to 2002), and the cycle period was extrapolated with data from literature. The existence of activity in the years 2006-2007 and now in 2013-2015 shows that this is not a regular frequency.

The short-term variability and disk feeding

Goss et al. (2011) reported a high-precision (~ 0.001) magnitude observations of Achernar. Solar Mass Ejection Imager (SMEI) satellite observations were done at optical wavelengths, centered at 700 nm and covering roughly from 350 to 1100 nm. The observational period of Achernar covered June 2003 to November 2008, spanning 1,993 days. SMEI covered a period of great changes in disk activity, both active and quiescent phases seen through the Hα profile (Rivinius et al., 2013).

The authors found two main photometric frequencies, $0.775\,\mathrm{d}^{-1}$ (F1) and $0.725\,\mathrm{d}^{-1}$ (F2), where the amplitude of this last frequency changed considerably over time. The nature of F2 appears to be associated with stellar outbursts, while the main frequency F1 with $\lesssim 0.04$ mag amplitude had already been reported by Balona et al. (1987), Vinicius

Table 6.2 - Identified photometric frequencies in Achernar by Goss et al. (2011). The starred (*) frequencies indicate with no previous published results in literature. These are frequencies for the entire observation timeseries, from 2003 up to 2008.

	Frequency (d^{-1})	Amplitude (mag)	SNR
F1	0.775177(5)	0.0165(3)	27.09
F2*	0.724854(6)	0.0129(3)	19.05
F3*	0.68037(3)	0.0027(3)	4.11

et al. (2006) and Rivinius et al. (2003), the last with amplitude of 0.02 mag. Other frequencies reported by Vinicius et al. (2006), namely 0.49 d^{-1}, 1.27 d^{-1} and 1.72 d^{-1} were not found. Goss et al. (2011) frequencies are listed in Table 6.2. The third low-amplitude frequency reported is 0.680 d^{-1} (F3), described as a "pulsation or transient frequency".

Analyzing Hα and high-precision photometric measurements, Rivinius et al. (2013) argue that Achernar's photospheric lines profiles indicate a stellar spin-up by as much as $\Delta v \sin i \approx 35$ km s^{-1} at epochs prior to stellar activity. The photospheric line widths also increase correlated with a photometric variability of 0.775 d^{-1} up to ~ 0.04 magnitudes in visible. At the end of the activity, the apparent stellar rotational speed declines to the value at quiescence after Hα returns to its photospheric configuration, when the photometric variability is minimum. Such change at the stellar surface must be compensated by internal momentum angular changes, whose precise mechanism is unknown (see Sect. 6.2).

From polarimetry, Carciofi et al. (2007) report polarization PA changes between 26° and 31°, where the polarization level changed from 0.12% to 0.17% within 2 hours (uncertainties $\leq 2°$ and $\leq 0.01\%$). The linear polarization observations were taken in 2006 at the B band. This variability (within a few hours) was interpreted as a signature of a large mass ejection from the photosphere, in a timescale $\sim 15\times$ shorter than the the frequencies listed in Table 6.2.

Variations of this time scale should in principle be detected by high-precision photometry (as in Goss et al., 2011). However, these ejections may not have a strong correspondent photometric signal given the inclination angle on which Achernar is seen. As shown by Haubois et al. (2012), as the disk density grows in Be stars seen at $i \approx 70°$, almost no photometric changes are detected. Around this inclination angle the emitted flux at visible wavelengths by the disk is almost exactly compensated by disk absorption of photospheric light. This is the likely scenario occurring to Achernar and, if occurring, it would be an

evidence that the circumstellar material is distributed until regions very close to the stellar photosphere.

The binary companion

High angular resolution images revealed a close-in faint ($\sim 30 - 50\times$ fainter in the infrared) A1-3V companion star orbiting the Be star (Kervella and Domiciano de Souza, 2007). In a following work (Kervella et al., 2008), the authors estimated the orbital period of ~ 15 years, close to the Hα spectroscopic variability found by Vinicius et al. (2006).

The orbital period of Achernar is currently been refined by Kervella et al. and can contribute to define the role of the companion on Achernar's activity, and the link to the Be phenomenon. For example, during the PIONIER observations of Achernar in 2010-2011, those authors estimate that the companion star was in the apastron (Domiciano de Souza et al., 2014). This means that the recent outburst started when the both stars were still very far apart, which suggest that there is no relation between binary and disk activity - at least for Achernar.

The polar wind emission in Achernar and Be stars

The presence of a dense polar wind in Be stars is commonly cited in literature (e.g., Georgy et al., 2011; Meilland et al., 2012), including textbooks of stellar rotation (Maeder, 2009). Although a polar wind with the characteristics of a O-type star is expected when a B star is rotating close to its critical limit ($W \approx 1$; Maeder, 2002), this wind would not explain the densities ($\gtrsim 10^{-13}$ g cm^{-3}) claimed by observations. The term dense here refers to densities higher than the ones expected by traditional stellar wind theory (e.g., CAK). However, these densities are low when compared to the typical densities of the circumstellar disks ($\approx 10^{-11}$ g cm^{-3}).

The interferometric evidence of polar winds appear to exist for only two Be's stars, namely α Ara and Achernar, as pointed out in the recent review of Rivinius et al. (2013). According to these authors, the evidence for α Ara is very fragile: based on a single interferometric measurement in which a single calibration bias in the data would result in the alleged characteristics for such wind. Thus, it is unlikely that these features were actually present. The only case pointed out by the authors that deserves further investigation is the case of Achernar.

Although the interferometric imaging of Domiciano de Souza et al. (2014) discard the presence of a polar wind during 2010-2011 in Achernar, its presence can be associated with disk activity. The investigation in the current active phase can provide important information about this feature.

6.2 The multiperiodicity of Achernar and other Be stars

Let us now investigate whether there is any relation between the photometric frequencies reported by Goss et al. (2011) and the spin-up speeds discovered by Rivinius et al. (2013). The reported spin-up velocity (~ 35 km s^{-1}) is very roughly the difference between the stellar rotational and critical velocities

$$\Delta v = (v_{\rm crit} - v_{\rm rot}) \times \sin i = 34.3 \text{ km s}^{-1}\,, \tag{6.1}$$

indicating that Achernar is rotating critically during its active phases (at least, in its equatorial region). Another interesting fact is that the very stable and known F1~ 0.775 day^{-1} frequency is very closely the orbital frequency of material just above the stellar equator (F4)

$$F4 = \frac{v_{\rm orb}}{2\pi R_{\rm eq}} = \frac{v_{\rm orb}}{2\pi 1.352 R_p} \sim 0.769 \text{ d}^{-1}\,, \tag{6.2}$$

where $R_{\rm eq}$ used was the value obtained by Domiciano de Souza et al. (2014). The close match between F1 and F4 suggests that F1 may be (i) a rotational frequency, perhaps associated with material freshly ejected by the star that is in an orbit very close to the equatorial radius; (ii) a non-radial pulsation frequency that naturally matches the frequency of an equatorial orbit. Note that this match could only be identified now that the photospheric parameters of Achernar are accurately known.

We also found two possible orbital frequencies with a less accurate match involving the transient frequency F3~ 0.680 day^{-1}. They are: (i) the period around the critically rotating star (F5)

$$F5 = \frac{v_{\rm crit}}{2\pi 1.5 R_p} \sim 0.657 \text{ d}^{-1}\,, \tag{6.3}$$

and (ii) the rotational period (F6)

$$F6 = \frac{v_{\rm rot}}{2\pi 1.352 R_p} \sim 0.644 \text{ d}^{-1}. \tag{6.4}$$

Be stars have three naturally arising frequencies. One of them is the rotation frequency (F6, above), which would be associated with purely photospheric phenomena such as stellar

Table 6.3 - NRP pulsation and transient frequencies of Achernar and other Be stars listed in Rivinius et al. (2003).

Star	F3 (d^{-1})	F1 (d^{-1})	F3/F1 (d^{-1})
α Eri	0.68037	0.775177	0.878
κ CMa	1.62075	1.824818	0.888
ω CMa	0.68027	0.728863	0.933
μ Cen	$\approx$1.60772	1.988072	0.809
η Cen	1.55521	1.733102	0.897

spots, non-radial pulsation, etc. The second is the critical frequency, when the rotation at stellar equatorial radius balances gravity (F5). The third is the orbital period at the stellar equator (F4). If the first and third periods are known, somehow, the stellar rotation rate could be easily estimated by

$$W = \frac{v_{\rm rot}}{v_{\rm orb}} = \frac{\rm F6}{\rm F4}\,, \tag{6.5}$$

If the last two frequencies are known,

$$\frac{v_{\rm rot}}{v_{\rm crit}} = \frac{\rm F5}{\rm F4}. \tag{6.6}$$

If we make the associations above between the observed periods of Achernar (F1 $\equiv$ F4 and F3 $\equiv$ F6), we find $W = 0.878$, that is $\sim 5\%$ higher than the one determined by Domiciano de Souza et al. (2014, $W = 0.838$). Assuming F3 $\equiv$ F5, the value of 0.878 is less than 1% of the ratio $v_{\rm rot}/v_{\rm crit}$ determined by in the same work ($v_{\rm rot}/v_{\rm crit} = 0.883$).

Observationally, Rivinius et al. (2003) state that "the presence of these secondary [transient] periods is enhanced in the outburst phases". The enhancement of F3 with activity was also found in Goss et al. (2011) observations of Achernar. If the material ejected by the star causes an asymmetry in the stellar photosphere or it accumulates in the critical rotation radius, the frequencies related to these processes are, respectively, F6 and F5.

Applying this method to the objects in Table 4 of Rivinius et al. (2003), we find a (near-)constant value of $F3/F1 \sim 0.9$ (Table 6.3; at least, $F3/F1 > 0.8$ if we do not exclude μ Cen for which the transient frequency was poorly determined).

The correlation between pulsations and the ejections of matter into the circumstellar disk of Be stars was first proposed by Rivinius et al. (2001), firmly established by Huat et al.

(2009) using CoRoT observations and are confirmed by Goss et al. (2011). The theoretical foundations for these correlations are discussed by Neiner and Mathis (2014), with the transport of angular momentum from the core to the surface due to the κ mechanism applied for fast rotating stars. According to these authors, "the accumulation of angular momentum just below the surface of Be stars increases the surface velocity. The surface then reaches the critical velocity so that material gets ejected from the star". This is a suggestive interpretation of the spin-up observation in Achernar. Evidence of spin-up in other Be stars would enhance the likelihood of this model. The stars listed in in Table 6.3 are good candidates to the presence of this phenomenon.

A speculative resonant scenario based on the frequencies derived to Achernar is developed in Appendix E. Although based on strong ad-hoc assumptions, it could bring insights into the origin of the Be phenomenon.

6.3 Observations of the active phase

After the activity report in 2013, our interferometric observations of Achernar started in August that year with a Director's Discretionary Time (DDT) proposal to AMBER 091.D-0107. They were followed by the proposal 093.D-0399, with observations from June 24th 2014 to January 19th 2015. These proposals were complemented by observations from collaborators, both from AMBER and PIONIER interferometers. The interferometric observations where complemented by high cadence polarimetric (OPD/LNA) and spectroscopic observations. Here we present the observational data obtained as well as the results of an initial modeling effort.

Spectroscopy

Our spectroscopic campaign covers 50 nights and 163 individual spectra. Table 6.4 contains a summary of the observations. The observations contains data from the following instruments: PUCHEROS (PUC-Chile; Vanzi et al., 2012), X-SHOOTER in experimental mode (ESO, Martayan, priv. comm.), FEROS (ESO; Kaufer et al., 1999), ECASS and MUSICOS (OPD/LNA; both described in Sect. 2.1.1). The complete list of observations are in appendix (Table F.1).

The observed spectra are shown in Figs. 6.1 and 6.2. They include observations from all

Table 6.4 - Summary of the spectroscopic data available for the 2013 outburst of Achernar. For an extended list of observations see the appendix (Table F.1).

Instrument	Approx. Resolution	Number of spectra	First date	Last date
ECASS	5000	1	2012-11-20	2012-11-20
PUCHEROS	20000	5	2013-01-18	2014-01-30
Amateur	5000	11	2013-01-22	2015-01-18
XSHOOTER	15000	1	2013-07-18	2013-07-18
FEROS	48000	136	2013-09-06	2014-02-25
MUSICOS	30000	7	2013-11-12	2014-11-19
BeSS	5000[a]	2	2014-11-26	2014-11-28

[a] The average value of observations used.

instruments except from FEROS, due to the large number of observations and their high cadence. These spectra are also presented in the appendix overplotted and as difference to the purely photospheric reference (Figs. F.1 to F.4, respectively). The reference profile was observed in January 2000 and was selected by Rivinius et al. (2013). FEROS spectra are presented in Figs. F.5 to F.14.

One problem we faced in our analysis was to combine spectra from multiple sources. Since Achernar has an extremely wide Hα profile, with wings extending at speeds greater than $\sim$ 1000 km s^{-1} from line center, in some instruments that can be mistaken as the continuous emission. This is particularly important for Echelle spectrographs that do not have a large spectral coverage at the different orders. In this case, the small difference in the level of the wings can be easily confused with the the instrumental response between the orders.

The solution was to perform the analyzes only for the center of the lines, ignoring the wings. The level on the continuum was determined by shifting the center line limits until their values correspond to the values of the purely photospheric profile. The criterion used to determine the best value for the core size was to minimize the difference of the EW values between different instruments but from a similar observational epoch, where no substantial changes were expected. The value that best described the line evolution was $\Delta v = 750$ km s^{-1}. As a consequence of the criterion adopted, the photospheric equivalent widths have systematically higher values of ~ 2 Å since it is does not consider absorption in the line wings.

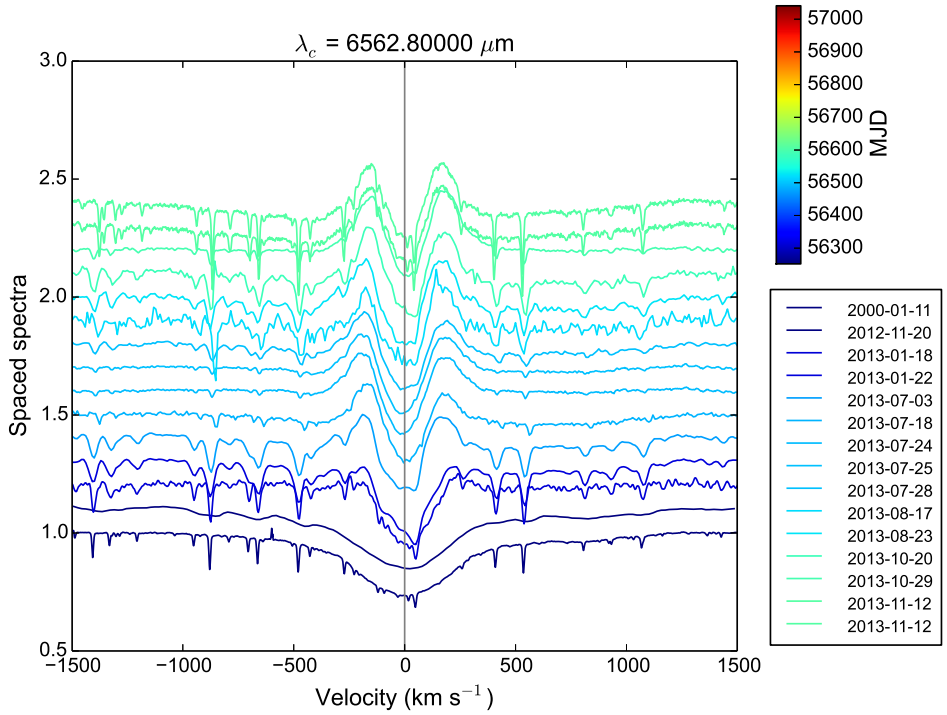

Figure 6.1: Hα line profiles of Achernar between November, 2012 and November, 2013. The color corresponds to the observation date. The (purely) photospheric reference profile of Rivinius et al. (2013) is also shown. It contains the observations from all instruments presented in Sec. 6.3, except for FEROS/ESO, due to its high cadence.

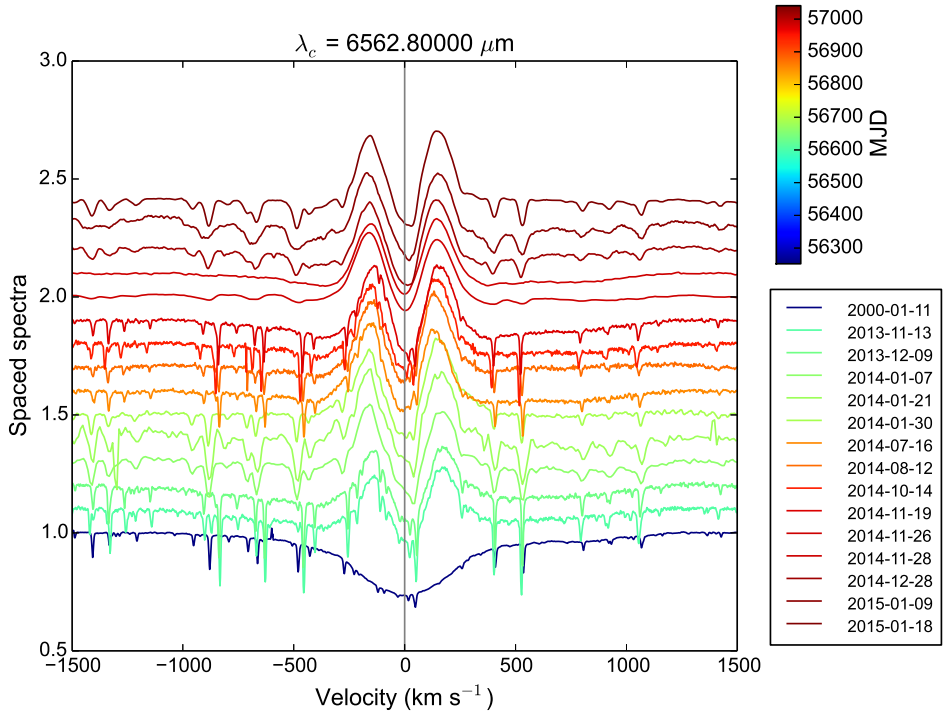

Figure 6.2: The same as previous figure, for observations between November 2013 to January 2015.

The main spectroscopic secular characteristics are: (i) Hα line profile is characterized by a central absorption, surrounded by emission peaks with large separation ($\Delta v >$ 300 km s^{-1}). (ii) the evolution of the profiles is slow (much slower the the polarization variations, see below) and only reach a (near-)constant regime after $\sim$ 1.6 years; The items (i) and (ii) can be seen in Fig. 6.3 and are discussed in more detail in the next section.

An interesting phenomenon that was observed was the transition from the photospheric profile to a shell-star profile at the beginning of the activity (F0 quantity in Fig. 6.4 and the first three profiles of Fig. 6.1). This occurrence was previously reported by Rivinius et al. (2013) in the 2006 towards the end of a disk formation phase, when the disk had reached maximum emission. This effect indicates that at the start of the activity (i) the ejected material was dense enough to absorb a considerable part of the stellar flux, (ii) the photospheric temperature changed considerably, or (iii) a combination of both effects occurred. The effect is even more intriguing since the last determination of Achernar's viewing angle $i \simeq 60.6°$ by Domiciano de Souza et al. (2014) points to a angle far from the equator-on, expected for shell stars.

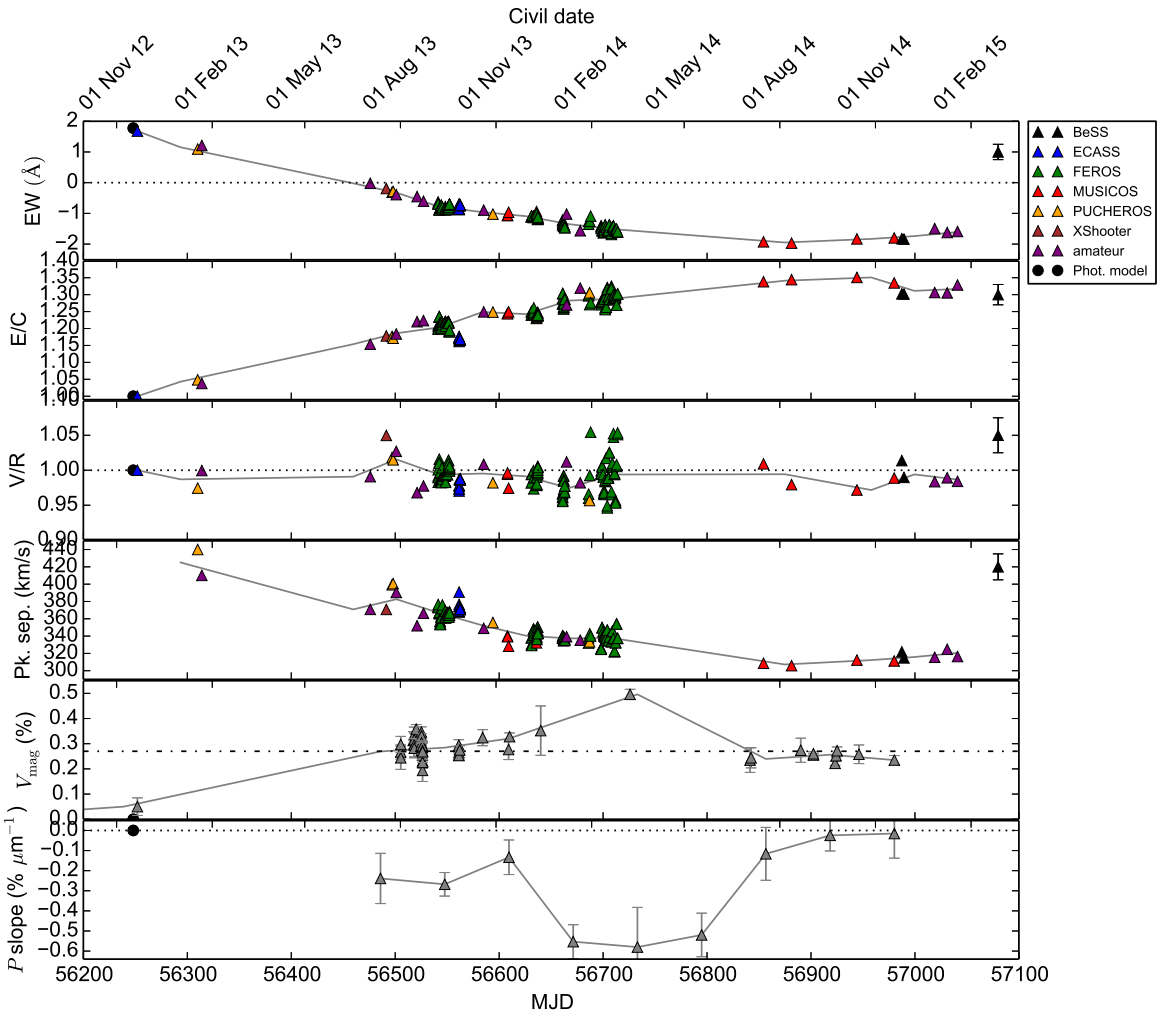

Figure 6.3: Secular evolution of Achernar after the 2013 outburst. Observations cover the period from November 2012 (purely photospheric observables) to February 2015. *From top to bottom:* Hα line profile equivalent width (EW), emission/continuum (E/C) ratio, V/R peaks ratio, and peak separation; V band polarization and BVR polarization slope (or *color*). The typical error of the measurements are indicated at the top right corners. The straight lines refer to the data binning in intervals of 45 days (interpolated when data is absent in the bin interval). The spectrographs used are indicated. The polarization data is from OPD/LNA (Brazil). The dotted lines indicate reference values EW$=0$, $V/R=1$ and flat polarized spectrum. The polarization value $P\sim0.27\%$ is also indicated by the dash-dotted line. The EW measurements consider only the core of the line, in a width of 750 km s^{-1}.

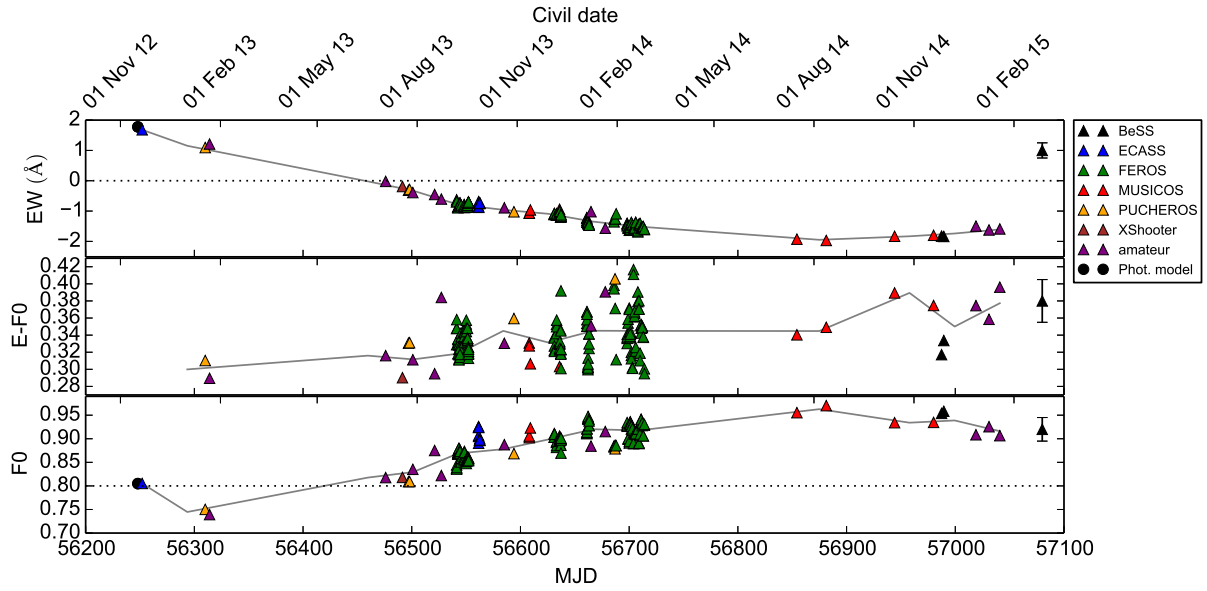

Figure 6.4: Secular evolution of selected spectroscopic quantities of Achernar in the 2013 outburst. *From top to bottom:* Hα line profile equivalent width (EW), emission-absorption depth (at rest wavelength; E-F0), and the absorption depth (F0). Observations cover the period from November 2012 (purely photospheric observables) to February 2015. The typical error of the measurements is indicated at the top right corners. The straight line refers to the interpolation of data at intervals of 45 days, interpolated when absent in the interval. The spectrographs used are indicated. The dotted lines indicate reference values EW = 0 and F0 at the purely photospheric level. The EW measurements consider only the core of the line, in a width of 750 km s^{-1}.

Polarimetry

Our polarimetric campaign covers 35 nights and 108 individual observations. The observations consist of imaging polarimetry in the B, V, R and I bands obtained using the IAGPOL polarimeter attached to the 0.6 m Boller & Chivens telescope at OPD/LNA, Brazil. The observational setup and reduction procedure are described in Sect. 2.1.1. The complete list of polarimetric observations are in the appendix (Table F.3).

The evolution of polarization at $BVRI$ bands are show in Fig. 6.5. The data of BVR bands were used to obtain the polarization color of Fig. 6.3. The color is calculated as following: data intervals were selected within which no large variations were detected. For each interval the data for each filter was binned and then the resulting BVR values were fitted with a linear function. I band was not considered for the color fitting. As discussed in Sect. 1.8.1, the I band contains wavelengths beyond the Paschen series limit ($n = 3$, i.e., $\lambda > 8204$ Å). This region can have a much lower absorption opacity, since photons beyond these frequencies cannot ionized electrons at orbits $n \leq 3$. Thus, this region has an abrupt increase of the polarized light once photos at these wavelengths are scattered

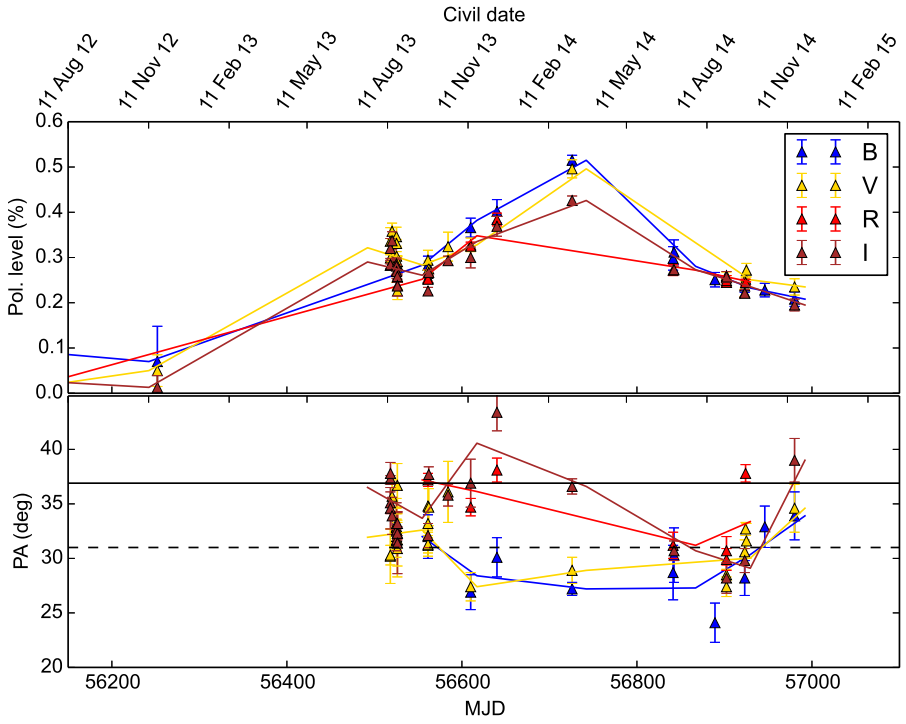

Figure 6.5: Broad-band linear polarization of Achernar ($BVRI$ filters). The observational data is binned in order to increase each epoch mean precision.

instead of been absorbed.

The linear polarization level at all observed filters are between $0.20 - 0.35\%$ for most of the considered period, starting in July 2013 up to the end of 2014. This is not true for the period around March 2014, where the linear polarization reaches a peak of $\approx 0.50\%$ at B and V filters. Although based on observations of a single night, these do not seem to be data of bad accuracy since all observed filters indicate such increased polarization level, and the derived on-sky polarization orientation are the expected values (Fig. 6.5, bottom panel). After the maximum seen in March 2014, the star reach a level similar to what was seen in the second half of 2013 ($\approx 0.27\%$ in all filters), with slight downward trend.

Interestingly, this variation observed in polarization in March 2014 does not have a spectroscopic correspondence. This is indicative that the polarization originates from a smaller and closer to the star region than the spectroscopic line, which does not directly reflects short-term variations in the inner disk.

In Figs. 6.6 and are displayed the QU polarization diagrams of the V band. The majority of the observations are located between the on-sky orientation angles 31° and 37°. At the start of the outburst to polarization seems to point to $\{Q, U\} = \{0.12, 0.27\}\%$. The

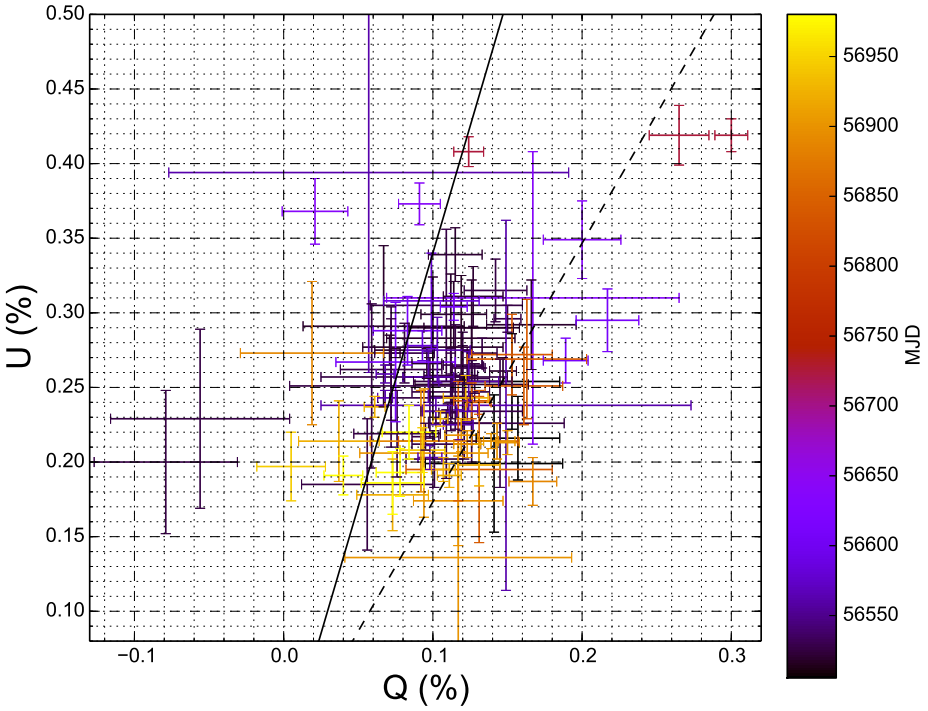

Figure 6.6: Polarimetric QU plane of V band observations of the 2013 outburst of Achernar. The straight line corresponds to a (fixed) polarization orientation of 36.9° and the dashed line to 31.0°.

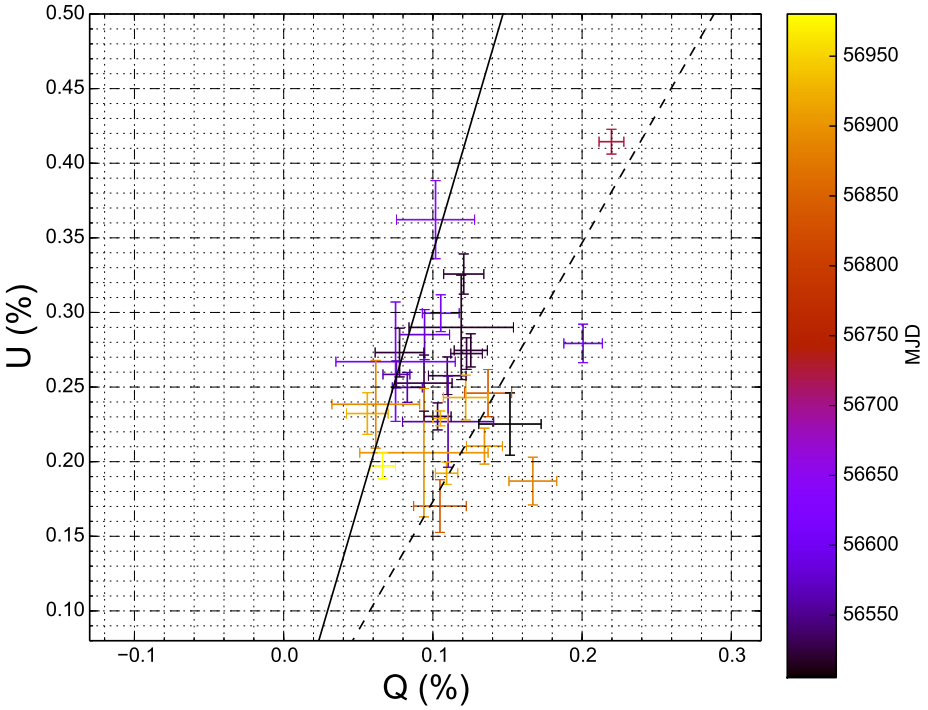

Figure 6.7: Same as previous figure, but data binned in time.

maximum point is reaches in March 2014 at $\{0.21, 0.41\}\%$, and the late period of 2014 it returns to $\{0.10, 0.21\}\%$. The variations in the polarization angle can be interpreted as inhomogeneities in the inner disk. This allows speculating that the injection of matter in the disk does not occur with an azimuthal symmetry. Oddly, the epoch of highest polarization level ($\sim$ March 2014, i.e., approx. epoch of highest mass injection) was preceded by the measurements of highest V/R variations (February 2014).

6.3.1 Secular evolution

Our data reveals both long- (months) and short-term (weeks) variability. We start discussing the evolution of observational quantities since the start of active phase to describe the long-term variations. The precise starting date of the outburst is unknown, however spectroscopic measurements from late November 2012 (20^{th}) show no sign of activity whereas in late January 2013 (18^{th}) a significant activity is present. This restricts the beginning of the activity between early December 2012 and early January 2013.

The main quantities chosen to characterize the disk evolution are based on Hα spectroscopy and broad band linear polarization and are presented in Fig. 6.3. Hα Equivalent Width (EW) departs from its maximum (positive) value, known to be photospheric-only, to smaller values. The decrease reveals the absorption profile been filled by disk emission, until eventually the emission overcomes the absorption (EW > 0), something that occurred around July 2013. Disk emission can also be traced by the Emission/Continuum (E/C) ratio. An E/C> 0 means that the emission component is higher than the continuum level, a condition quickly reached (February 2013). The Hα profile of Achernar exhibits a peak-separation decreasing with the increase of EW. This decrease of peak separation with time is consistent with a progressively larger disk; assuming Keplerian rotation, the fact that the peak separations decreases confirms that the emission originates in progressively larger regions.

The double peak line profile allows to measure asymmetries on the circumstellar emission through the V/R quantity, or the ratio between the Violet and Red peak values. In the considered period, the average V/R value was 0.991, with standard deviation of 0.020, i .e., completely consistent with a axisymmetric disk, for which $V/R = 1$. The maximum asymmetries records are $V/R = 0.946$ and 1.054.

Polarization is the most sensitive quantity to detect circumstellar activity (Sect. 5.3).

This, and the null polarization value ($\lesssim 0.02\%$) reported by Domiciano de Souza et al. (2014), measured in the pre-outburst phase, indicates no considerable ISM polarization towards Achernar. For this reason no ISM correction was applied to the data. Achernar departs from its minimum (null) polarimetric value in November 2012 to a high value of $\gtrsim 0.27\%$ at the first polarimetric observation in the active phase (late July 2013) until December 2013. Then, an increase in polarization occurs with peak around mid-March 2014, an in July 2014 the polarization returns to a lower value. The V-band polarization value of 0.27%, approximate value which polarimetry of Achernar is located most of the time, is twice that detected by Carciofi et al. (2007) in the 2006 activity.

The polarization of the 2013 active phase at V band is presented in Fig. 6.3, as well as the polarization color (i.e., the spectral slope of the polarization across the B, V and R bands). The polarization color is indicative of the disk density: the larger the disk, the larger in modulus (i.e., the more negative) the slope (see, e.g., Haubois et al., 2014, Fig. 4). As the polarization level, that presented three clear phases (nearly constant in 2013, increase in 2014 and back to the 2013 value in August 2014) the polarization color is nearly constant in 2013, decreases sharply in the first half of 2014 and then goes back to a smaller value. These facts alone allows us to conclude that the disk was denser between December 2013 and July 2014, and in 2013 the disk was slightly denser than in late 2014.

6.4 Interferometry

In this section we describe the rich interferometric dataset obtained by us. In order to make an initial comparison between this data and the VDD, we developed a simple reference model. Based on the stability of the star observed between August 2014 and, at least, December 2014, we performed a modeling of Achernar based on the VDD prescription of a steady-stable disk. Our aim was to describe the spectroscopic and polarimetric quantities, and them apply it to the interferometric data. This model will set constraints on a future dynamical evolution analysis. As seen in Sect. 6.3.1, a negative slope in the polarized (visible) spectrum is indicative of high densities in the inner disk, thus suggesting a large mass injection rate. Conversely, a zero slope indicates a much smaller density, possibly related to a smaller or even zero disk feeding rate.

The steady-state (SS) assumption is likely valid for Achernar at the considered period

(August 2014 - December 2014) since no big changes in the Hα spectroscopy were recorded. Running a small grid of SS disks for Achernar, the value of $\Sigma_0 = 0.06$ g cm^{-2} were found to be able to reproduce the observables, mainly $P \simeq 0.27\%$ and EW ~ -2 Å.

To get an estimation of the disk mass injection $\dot{M}$ from this value, (and that is representative of the activity), we relate the surface density value Σ_0 with $\dot{M}$ by Eq. 1.44,

$$\frac{\dot{M}R_0^{1/2}}{\alpha} = \frac{\Sigma_0 3\pi c_s^2 R_{\rm eq}^2}{(GM)^{1/2}},$$

$$\frac{\dot{M}R_0^{1/2}}{\alpha} \simeq \frac{0.06 \times 3\pi \times 1.413 \cdot 10^{12} \times (9.16R_\odot)^2}{(G \cdot 6.2M_\odot)^{1/2}}. \tag{6.7}$$

This results in $\frac{\dot{M}R_0^{1/2}}{\alpha} \simeq 1.13 \times 10^{22}$ g s^{-1} cm$^{1/2}$. To have an order of magnitude estimation, we impose that $R_0 \approx 100R_{\rm eq}$, yielding $\frac{\dot{M}}{\alpha} \sim 2.25 \times 10^{-11}\ M_\odot$ yr^{-1}.

6.4.1 Interferometric results

Our interferometric campaign with AMBER covers 38 nights and has 79 individual observations. The observations where performed in high-resolution (HR) mode around the Brγ line, make use of the FINITO fringe tracker. Because of its brightness, observation attempts were made in adverse weather conditions and for this reason a number have a low S/N and others were lost due to bad weather. Appendix Table F.2 contains the list of observed nights, indicating for them the amount of individual observations. The data reduction was made with the software AMDLIB (e.g., Chelli et al., 2009). During the reduction process it was attempted to perform the absolute calibration of visibilities from the standard star's observations of each night. However the visibilities were not reliable and we chose to normalize visibilities to the continuum level.

When comparing the temporal series of (spectro-)interferometric observations, differences among them can be given for two reasons: (i) changes in the configuration of the interferometer, and (ii) the disk evolution itself. In order to distinguish between the two effects, we grouped the observation on equivalent interferometric settings (i.e., similar $\vec{B}_{\rm proj}$), and analyzed the groups that had the largest number of observations. The criterion was to group observations within $\Delta\|\vec{B}_{\rm proj}\| \leq 20$ m and ΔPA $\leq 10°$. Table 6.5 contains the list of selected interferometers configurations. Fig. 6.8 show the data grouped by $\{\|\vec{B}_{\rm proj}\|$, PA$\}$. Below, we show some of the grouped observations, guiding our discussion based on

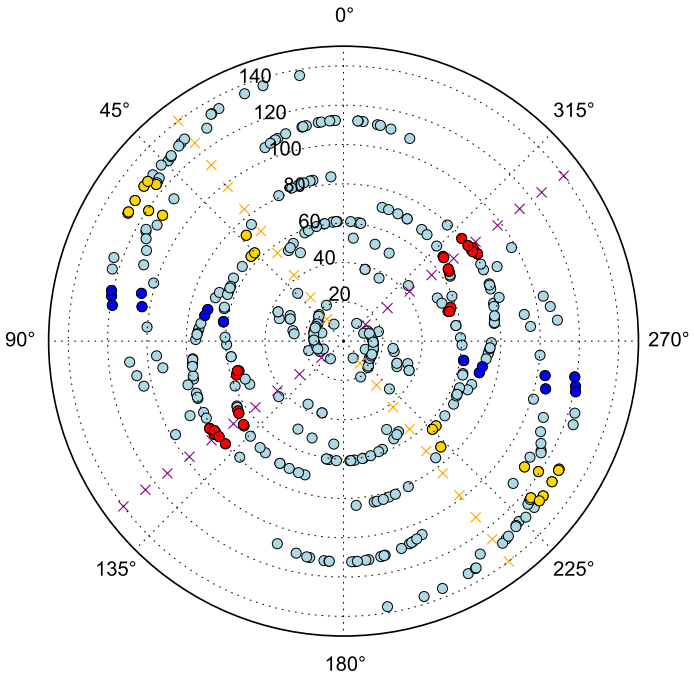

Figure 6.8: AMBER observations of Achernar between August 2013 and January 2015. The radial scale sets $\|\vec{B}_{\rm proj}\|$ up to 140 m, and the angle is the observed PA (deg). The selected groups in Table 6.5 are marked according to their orientation. The bottom right box indicate Achernar's polar direction (orange, PA = 216.9°) and its equatorial direction (purple crosses, PA = 126.9°), values from Domiciano de Souza et al. (2014).

Table 6.5 - Selected groups of AMBER observations displaying similar $\vec{B}_{\rm proj}$.

PA (deg)	$\vec{B}_{\rm proj}$ (m)	Number of observations	MJD0	MJDF	Appox. Direction (pole, interm., disk)
45	72	4	56518.27	56929.34	pole
55	122	12	56518.36	56928.25	pole
80	62	4	56518.39	56931.25	interm.
80	112	5	56920.30	56924.30	interm.
105	52	4	56518.27	56920.32	disk
127	72	6	56558.30	56924.21	disk

the their orientation: close to the equator, to the pole, and intermediate directions. The numbers above each observation box are, respectively, its Modified Julian Day (MJD) and the days count since January 1$^{\rm st}$ 2013, used as a reference to the activity starting date.

Equatorial directions

As in polarimetry, interferometric observations first occurred in August 2013. This is approximately 200 days after the beginning of the activity, where the disk in its inner regions was already well developed (as the constant polarization value indicates). For convenience, we employ the expression "day n" as the $n^{\rm th}$ day since January 1$^{\rm st}$ 2013 to refer to the observations dates.

In Fig. 6.9 we show the AMBER observations from days 225 to 636, where the disk growth can be observed both in visibilities and phases: the V^2 minimum decreases from ~ 0.8 until ~ 0.6, and the phase amplitudes increases from $\sim 5.5°$ up to $\sim 8.5°$. Assuming that the target brightness distribution is roughly similar in shape, a lower visibility corresponds to a angularly larger object, i.e., a larger disk, as expected from the VDD model. The same applies to the phases, if the photocenter-phase relation is valid. These observations were executed with $\|\vec{B}_{\rm proj}\| \simeq 52$ m. Although being a relatively small baseline, $\nu_{\rm obs} \simeq 1.22$, indicating that the observations are in the limit of the astrometric regime. This can also be seen by the visibilities values: Fig. 4.3 shows that the astrometric regime ends when $V^2 \sim 0.6$, the same value registered in the latter observation. A very promissing result is the fact that our simple steady-state VDD model (red lines in Figs. 6.9 to 6.14) is already capable of reproducing most of the observed features.

Fig. 6.10 contains an extensive list of observations with a similar configuration, where

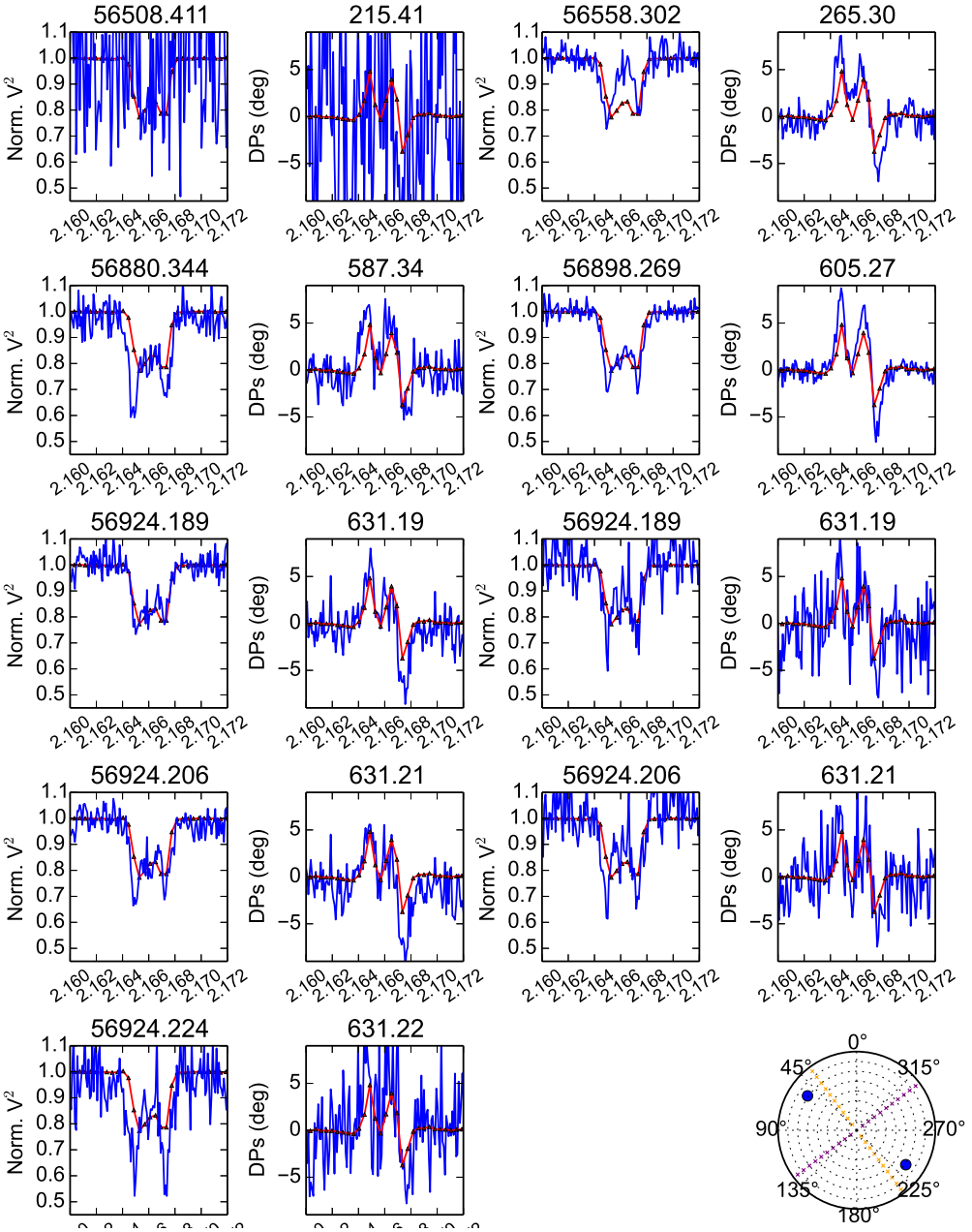

Figure 6.9: AMBER-VLTI Intereferometric observations. Normalized visibilities (first and third columns) and differential phases (DPs; second and fourth columns). Observations are the blue curves and the steady-state VDD disk model are the red curves. Above the visibility boxes, is the Modified Julian Day of the observation. Above DPs, the amount of days since January 1st 2013. The bottom right box indicate Achernar's polar direction (orange) and its equatorial direction (purple crosses). They were grouped according to telescopes configuration indicated by the blue points (projected PA = 105° and $\|\vec{B}_{\rm proj}\| = 52$ m).

variations of time scales of weeks to months can be studied. The V^2 minimum is progressively lower and the DPs show a rich morphology: from a (roughly) symmetric S-phases in at $\sim$ 200 days, and incursion appears on phase peaks ($\sim$ 300 and 635 days) to a very complex modulation in $\sim$ 600 days. As the direction of this base is very close to the expected to the equator (PA = 127°), deviations of phase symmetry are result of disk asymmetric emission.

Intermidiate directions

For the rotating disk, as the Be stars, disk kinematic component is present and dominates the photocenter displacement in the astrometric regimes for most of the baseline orientations (Faes et al., 2013, Fig. 9). This only does not apply to PAs very close to the polar orientation. Fig. 6.11 shows the interferometric signal for a direction midway between the equator and the pole of the star at different epochs. The decrease of the visibilities and increase of the phases is readily noticed. In the first observations ($\sim$ 200 days) there is a substructure in the center of the phase profile.

An illustrative example of the over-resolution effects on the phase signal is at Fig. 6.12. These are observations for exactly the same orientation of the previous figure, but for a longer baseline. The previous S-shaped profile almost disappears, remaining only a very irregular profile and a lower V^2 minimum. The displayed noise is due to bad weather conditions. Note that these complex phase profiles will like not present any challenge for the VDD model, since our initial reference model can reproduce the profiles qualitatively well.

Polar direction

Fig. 6.13 contains observations in a PA very close do the polar direction. Different from observations shown until here, this configuration exhibits both low amplitude phases and visibilities (minimum $V^2 \sim 0.9$), but which also displays a slight evolution.

Fig. 6.14 contains other observations towards the polar directions, but slightly misaligned. The effects on the amplitude of the phases is clear, as pointed out in the discussion of PA's between the poles and the disk.

In conclusion to this inspection of the interferometric data, the observables exhibit a detectable evolution in the period (day $\sim$ 250 up to 700). As occurred to the polarimetric

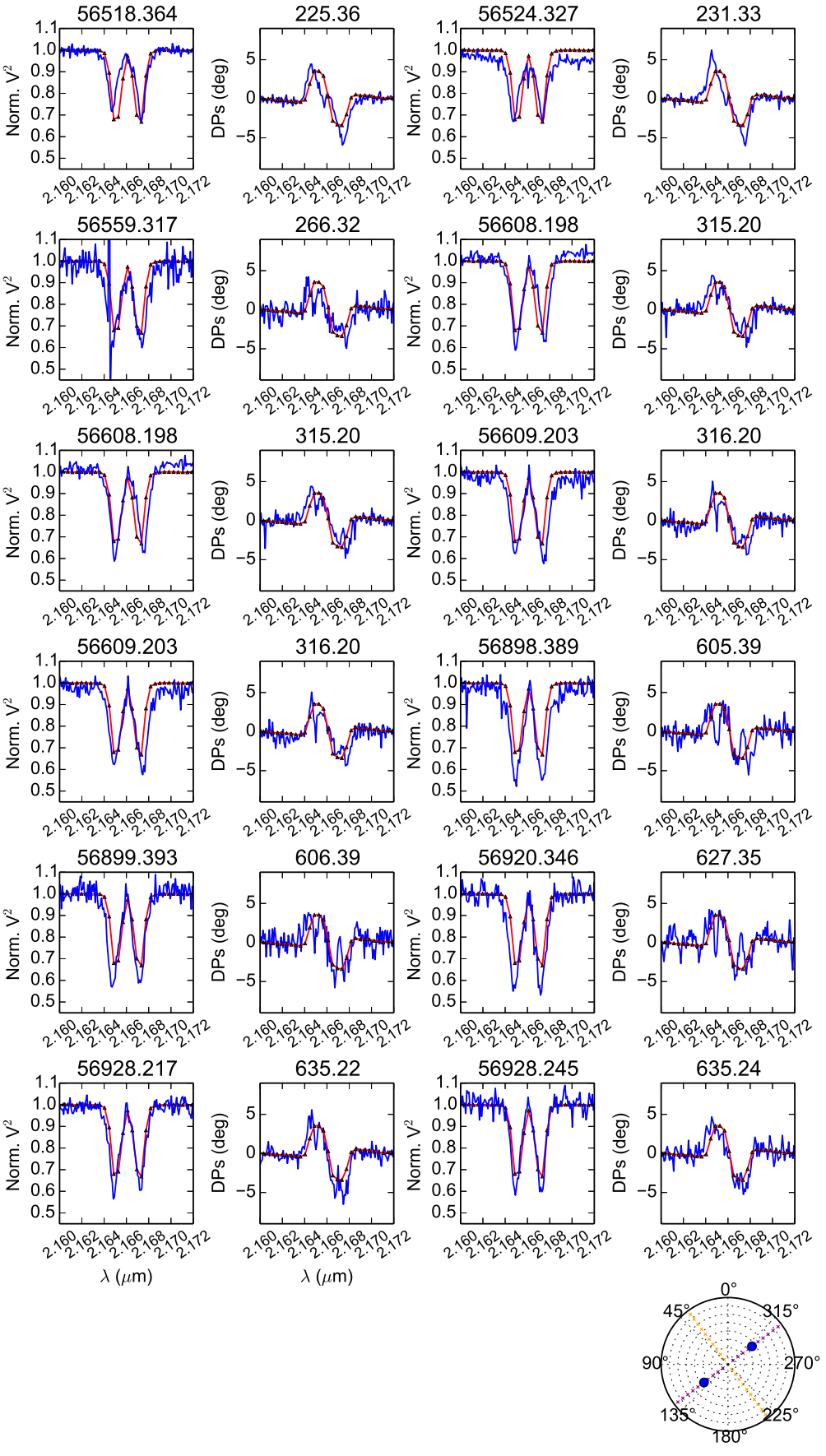

Figure 6.10: The same as previous figure, for PA = 127° and $\|\vec{B}_{\rm proj}\| = 72$ m.

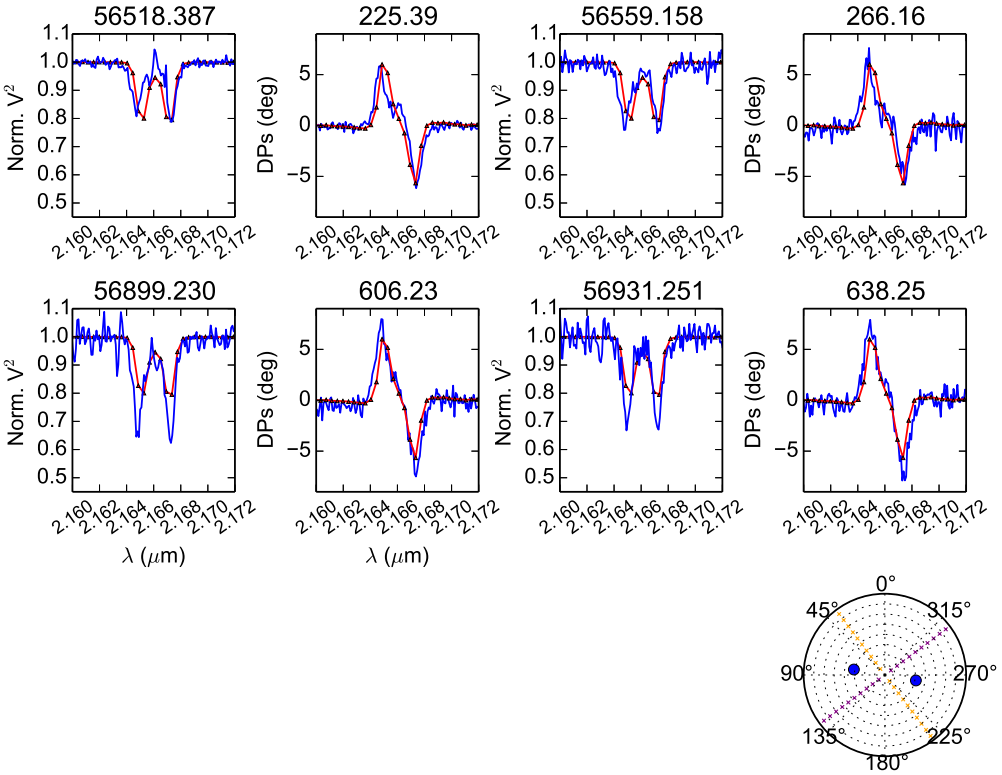

Figure 6.11: The same as previous figure, for PA = 80° and $\|\vec{B}_{\rm proj}\| = 62$ m.

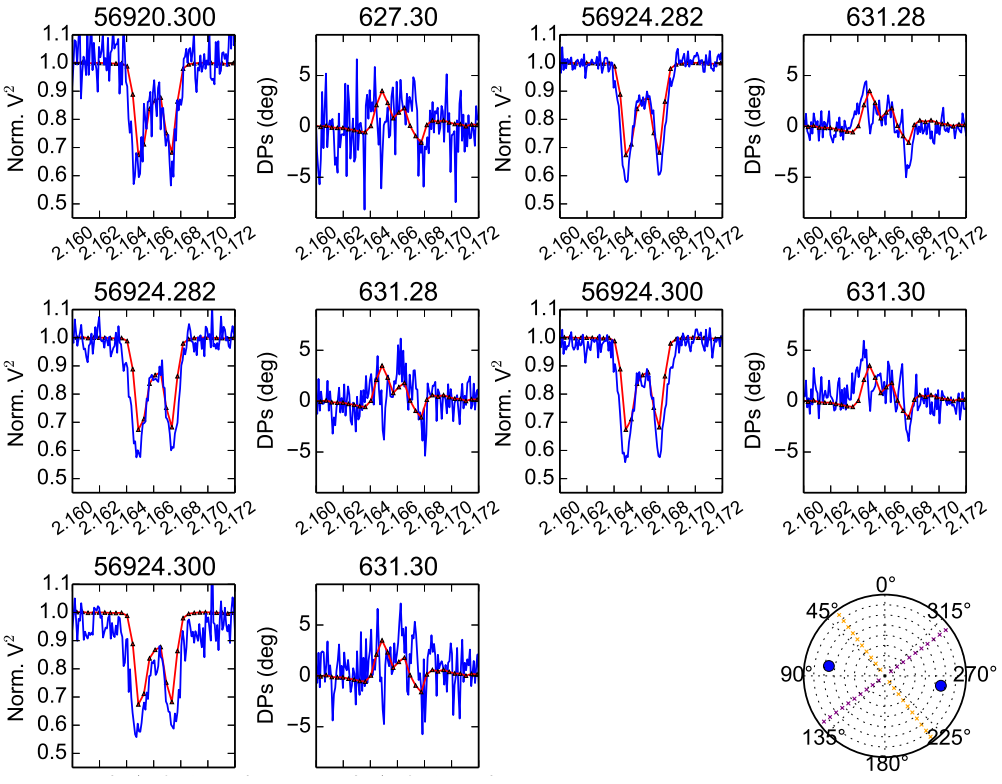

Figure 6.12: The same as previous figure, for PA = 80° and $\|\vec{B}_{\rm proj}\| = 112$ m.

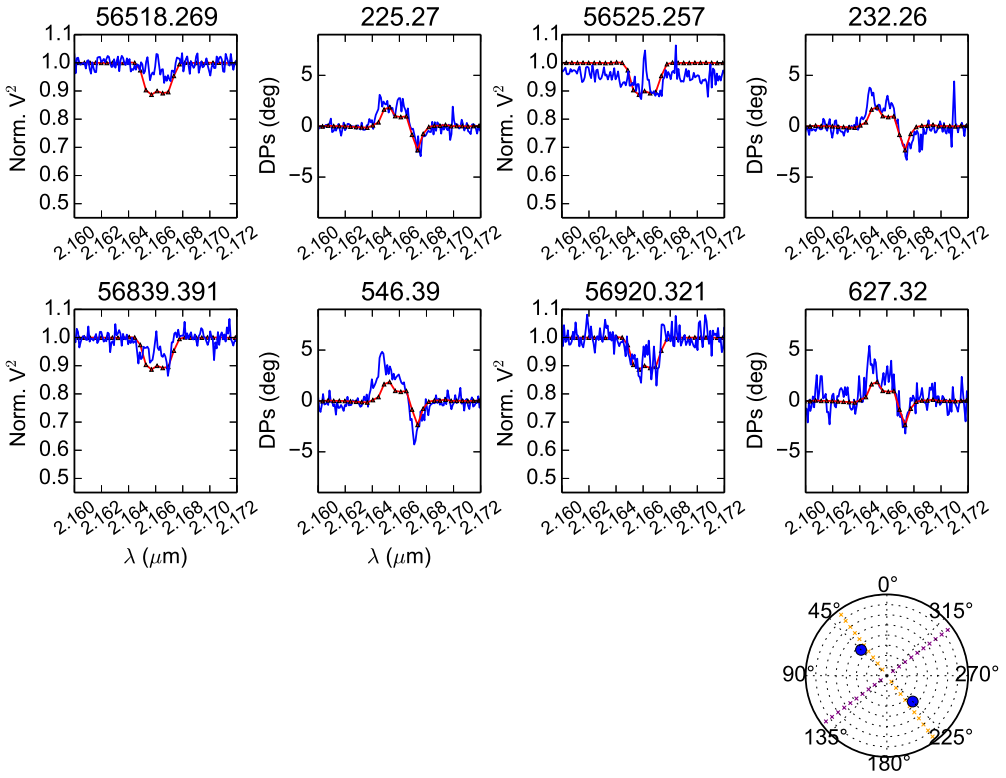

Figure 6.13: The same as previous figure, for PA=45° and $\|\vec{B}_{\rm proj}\| = 72$ m.

data, the emission in Brγ appears to have evolved quickly, less than 6 months after the start of the activity. Unfortunately, no interferometric observations where performed between October 2013 and May 2014, period on which an increase of polarization was observed.

We also highlight that almost of the data of Achernar are outside of the astrometric regime, which makes it difficult to isolate the over-resolution features of those predicted by the CQE-PS (Chapter 4). Several phase profiles observed have a distinct shoulder in the rest wavelength (see, e.g., the profile for 266.16 days in Fig. 6.12). These profiles suggest that the CQE-PS have been detected for the first time, however a more careful modeling is needed to reach this conclusion.

For the modeling, we considered the parameters from Domiciano de Souza et al. (2014), i.e., $d = 42.75$ pc and $i = 60.6°$. The VDD provides a good description of the interferometric data for all considered directions. Difference between model and observations likely arise from the fact that we used a time-invariable model to fit time-variable observations. As a next step, we will study these observations with a dynamical VDD model. The main unexpected observed feature consists of the incursions near the phase peaks when the interferometer is aligned to the disk direction. Simulating different values of $\vec{B}_{\rm proj}$ and d we

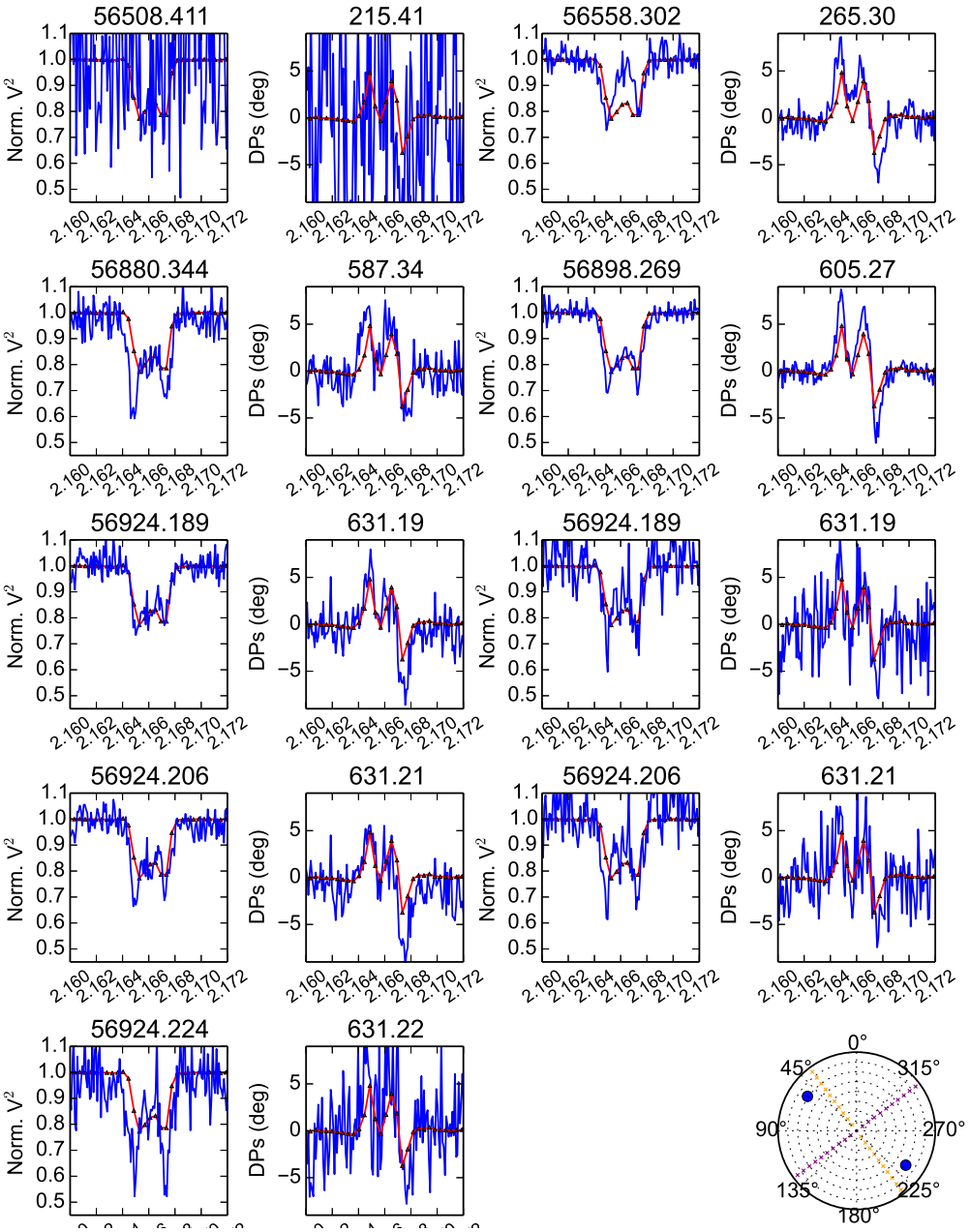

Figure 6.14: The same as previous figure, for PA=55° and $\|\vec{B}_{\rm proj}\| = 122$ m.

were not able to reproduce this phenomenon.

6.5 Chapter summary

In this chapter we presented the singular characteristics of the Be Achernar and our running observational campaign that aims at a multi-technique characterization of its current active phase.

We started analyzing some observational phenomena, such as the $v \sin i$ variations and photometric and spectroscopic frequencies with very high precision data obtained by photospheric reconstruction. This led to an interesting speculation between the relationship of these frequencies observed for Be stars, traditionally attributed to non-radial pulsations, and their turnover rates.

An observational characterization of the activity was made, including Hα spectroscopy, broad-band polarimetry, and spectro-interferometry AMBER. The observational results include: (i) variability in different time scales; (ii) variation V/R and QU polarimetric diagram shows that the disk is not symmetric; (iii) polarization shows periods of large-scale variation and also periods of relative stability; (iv) $H\alpha$ spectroscopy presents a slow and gradual evolution, and reaches a near stationary regime to only $\sim$1.6 years after the beginning of the activity.

Interferometry is sensitive to the brightness distribution of a observed target. The relation of physical properties of Be stars and the interferometric data can only be directly determined if they are analyzed by realistic emission models. Both interferometry and spectrointerferometry allowed establishing the viscous decretion disk (VDD) model, solved by radiative transfer, as the most likely scenario to explain the Be star disks.

The solutions provided by radiative transfer can both determine the structure as well the emergent observables of the Be stars. This enables, for instance, the study of second order effects that may be present on these systems. Multi-technique studies, combining integrated quantities (such as photometry or spectroscopy) with ones containing spatial information (such as polarimetry or interferometry) are an important way of constraining the multiple parameters that characterized the systems in a consistent way.

In interferometry, it is seen that the VDD model performs a good description of all baselines, ensuring that our estimates of the physical conditions of the system (such as gas density, scale high, etc.) are appropriate and that can lead to accurate estimations of parameters such as the mass loss rate. Some profile features, such as narrow cusps in

visibility and phases at high speeds wavelengths, or incursions in the S-shaped driven by the disk need to be investigated.

Bibliography

Aufdenberg J. P., Mérand A., Coudé du Foresto V., Absil O., Di Folco E., Kervella P., Ridgway S. T., Berger D. H., ten Brummelaar T. A., McAlister H. A., Sturmann J., Sturmann L., Turner N. H., First Results from the CHARA Array. VII. Long-Baseline Interferometric Measurements of Vega Consistent with a Pole-On, Rapidly Rotating Star, ApJ, 2006, vol. 645, p. 664

Baade D., Rivinius T., Štefl S., Nonradial Pulsations and Magnetic Fields in Be Stars. In Magnetic Fields in O, B and A Stars: Origin and Connection to Pulsation, Rotation and Mass Loss , vol. 305 of Astronomical Society of the Pacific Conference Series, 2003, p. 269

Balbus S. A., Enhanced Angular Momentum Transport in Accretion Disks, ARA&A, 2003, vol. 41, p. 555

Balbus S. A., Hawley J. F., On the Nature of Angular Momentum Transport in Nonradiative Accretion Flows, ApJ, 2002, vol. 573, p. 749

Balona L. A., Engelbrecht C. A., Marang F., Achernar, MNRAS, 1987, vol. 227, p. 123

Baudrand J., Bohm T., MUSICOS - A fiber-fed spectrograph for multi-site observations, A&A, 1992, vol. 259, p. 711

Bjorkman J. E., Circumstellar Disks. In Stellar Atmospheres: Theory and Observations , vol. 497 of Lecture Notes in Physics, Berlin Springer Verlag, 1997, p. 239

Bjorkman J. E., Bjorkman K. S., The effects of gravity darkening on the ultraviolet continuum polarization produced by circumstellar disks, ApJ, 1994, vol. 436, p. 818

Bjorkman J. E., Carciofi A. C., Modeling the Structure of Hot Star Disks. In The Nature and Evolution of Disks Around Hot Stars , vol. 337 of Astronomical Society of the Pacific Conference Series, 2005, p. 75

Borra E. F., Landstreet J. D., The magnetic field of the helium-strong stars, ApJ, 1979, vol. 228, p. 809

Brown J. C., McLean I. S., Polarisation by Thomson Scattering in Optically Thin Stellar Envelopes. I. Source Star at Centre of Axisymmetric Envelope, A&A, 1977, vol. 57, p. 141

Carciofi A. C., Bjorkman J. E., Non-LTE Monte Carlo Radiative Transfer. I. The Thermal Properties of Keplerian Disks around Classical Be Stars, ApJ, 2006, vol. 639, p. 1081

Carciofi A. C., Bjorkman J. E., Non-LTE Monte Carlo Radiative Transfer. II. Nonisothermal Solutions for Viscous Keplerian Disks, ApJ, 2008, vol. 684, p. 1374

Carciofi A. C., Domiciano de Souza A., Magalhães A. M., Bjorkman J. E., Vakili F., On the Determination of the Rotational Oblateness of Achernar, ApJ, 2008, vol. 676, p. L41

Carciofi A. C., Faes D. M., Townsend R. H. D., Bjorkman J. E., Polarimetric Observations of σ Orionis E, ApJ, 2013, vol. 766, p. L9

Carciofi A. C., Magalhães A. M., Leister N. V., Bjorkman J. E., Levenhagen R. S., Achernar: Rapid Polarization Variability as Evidence of Photospheric and Circumstellar Activity, ApJ, 2007, vol. 671, p. L49

Carciofi A. C., Okazaki A. T., Le Bouquin J.-B., Štefl S., Rivinius T., Baade D., Bjorkman J. E., Hummel C. A., Cyclic variability of the circumstellar disk of the Be star ζ Tauri. II. Testing the 2D global disk oscillation model, A&A, 2009, vol. 504, p. 915

Castor J. I., Abbott D. C., Klein R. I., Radiation-driven winds in Of stars, ApJ, 1975, vol. 195, p. 157

Catanzaro G., Spectroscopic atlas of Hα and Hβ in a sample of northern Be stars, A&A, 2013, vol. 550, p. A79

Che X., Monnier J. D., Zhao M., Pedretti E., Thureau N., Mérand A., ten Brummelaar T., McAlister H., Ridgway S. T., Turner N., Sturmann J., Sturmann L., Colder and Hotter: Interferometric Imaging of β Cassiopeiae and α Leonis, ApJ, 2011, vol. 732, p. 68

Chelli A., Utrera O. H., Duvert G., Optimised data reduction for the AMBER/VLTI instrument, A&A, 2009, vol. 502, p. 705

Claret A., A new non-linear limb-darkening law for LTE stellar atmosphere models. Calculations for -5.0 <= log[M/H] <= +1, 2000 K <= T_{eff} <= 50000 K at several surface gravities, A&A, 2000, vol. 363, p. 1081

Collins II G. W., Harrington J. P., Theoretical H-Beta Line Profiles and Related Parameters for Rotating B Stars, ApJ, 1966, vol. 146, p. 152

Davis Jr. L., Greenstein J. L., The Polarization of Starlight by Aligned Dust Grains., ApJ, 1951, vol. 114, p. 206

Dolginov A. Z., Mitrofanov I. G., Orientation of cosmic dust grains, Ap&SS, 1976, vol. 43, p. 291

Domiciano de Souza A., Hadjara M., Vakili F., Bendjoya P., Millour F., Abe L., Carciofi A. C., Faes D. M., Kervella P., Lagarde S., Marconi A., Monin J.-L., Niccolini G., Petrov R. G., Weigelt G., Beyond the diffraction limit of optical/IR interferometers. I. Angular diameter and rotation parameters of Achernar from differential phases, A&A, 2012, vol. 545, p. A130

Domiciano de Souza A., Kervella P., Faes D. M., Dalla Vedova G., Mérand A., Le Bouquin J.-B., Espinosa Lara F., Rieutord M., Bendjoya P., Carciofi A. C., Hadjara M., Millour F., Vakili F., The environment of the fast rotating star Achernar, A&A, 2014, vol. 569, p. A10

Domiciano de Souza A., Kervella P., Jankov S., Abe L., Vakili F., di Folco E., Paresce F., The spinning-top Be star Achernar from VLTI-VINCI, A&A, 2003, vol. 407, p. L47

Domiciano de Souza A., Vakili F., Jankov S., Janot-Pacheco E., Abe L., Modelling rapid rotators for stellar interferometry, A&A, 2002, vol. 393, p. 345

Domiciano de Souza A., Zorec J., Jankov S., Vakili F., Abe L., Janot-Pacheco E., Stellar differential rotation and inclination angle from spectro-interferometry, A&A, 2004, vol. 418, p. 781

Domiciano de Souza A., Zorec J., Vakili F., CHARRON: Code for High Angular Resolution of Rotating Objects in Nature. In SF2A-2012: Proceedings of the Annual meeting of the French Society of Astronomy and Astrophysics , 2012, p. 321

Donati J.-F., Landstreet J. D., Magnetic Fields of Nondegenerate Stars, ARA&A, 2009, vol. 47, p. 333

Donati J.-F., Semel M., Carter B. D., Rees D. E., Collier Cameron A., Spectropolarimetric observations of active stars, MNRAS, 1997, vol. 291, p. 658

Ekström S., Meynet G., Maeder A., Barblan F., Evolution towards the critical limit and the origin of Be stars, A&A, 2008, vol. 478, p. 467

Espinosa Lara F., Rieutord M., The dynamics of a fully radiative rapidly rotating star enclosed within a spherical box, A&A, 2007, vol. 470, p. 1013

Espinosa Lara F., Rieutord M., Gravity darkening in rotating stars, A&A, 2011, vol. 533, p. A43

Faes D. M., Modelagem de nebulosas planetárias com morfologia bipolar, Universidade de São Paulo, 2011, Master thesis

Faes D. M., Carciofi A. C., Rivinius T., Štefl S., Baade D., Domiciano de Souza A., On the CQE Phase Signature Feature in High-Resolution Spectro-Interferometry of Be Stars. In PASPC , vol. 464 of Circumstellar Dynamics at High Resolution, 2012, p. 141

Faes D. M., Carciofi A. C., Rivinius T., Štefl S., Baade D., Domiciano de Souza A., Differential interferometric phases at high spectral resolution as a sensitive physical diagnostic of circumstellar disks, A&A, 2013, vol. 555, p. A76

Faes D. M., Domiciano de Souza A., Carciofi A. C., Bendjoya P., The photosphere and circumstellar environment of the Be star Achernar. In IAU Symposium , vol. 307 of IAU Symposium, 2015, p. 261

Foreman-Mackey D., Hogg D. W., Lang D., Goodman J., emcee: The MCMC Hammer, PASP, 2013, vol. 125, p. 306

Franco G. A. P., MUSICOS: dos Pirineus para a Mantiqueira, 2010 , LNA em dia, 12, p. 6

Frisch P. C., Redfield S., Slavin J. D., The Interstellar Medium Surrounding the Sun, ARA&A, 2011, vol. 49, p. 237

Georgy C., Ekström S., Granada A., Meynet G., Mowlavi N., Eggenberger P., Maeder A., Populations of rotating stars. I. Models from 1.7 to 15 $M_{\odot}$ at Z = 0.014, 0.006, and 0.002 with Ω/Ω_{crit} between 0 and 1, A&A, 2013, vol. 553, p. A24

Georgy C., Meynet G., Maeder A., Effects of anisotropic winds on massive star evolution, A&A, 2011, vol. 527, p. A52

Goss K. J. F., Karoff C., Chaplin W. J., Elsworth Y., Stevens I. R., Variations of the amplitudes of oscillation of the Be star Achernar, MNRAS, 2011, vol. 411, p. 162

Granada A., Ekström S., Georgy C., Krtička J., Owocki S., Meynet G., Maeder A., Populations of rotating stars. II. Rapid rotators and their link to Be-type stars, A&A, 2013, vol. 553, p. A25

Granada A., Haemmerlé L., Evolution of single B-type stars with a large angular momentum content, A&A, 2014, vol. 570, p. A18

Grunhut J. H., Rivinius T., Wade G. A., Townsend R. H. D., Marcolino W. L. F., Bohlender D. A., Szeifert T., Petit V., Matthews J. M., Rowe J. F., Moffat A. F. J., Kallinger T., Kuschnig R., Guenther D. B., Rucinski S. M., Sasselov D., Weiss W. W., HR 5907: Discovery of the most rapidly rotating magnetic early B-type star by the MiMeS Collaboration, MNRAS, 2012, vol. 419, p. 1610

Hadjara M., Domiciano de Souza A., Vakili F., Jankov S., Millour F., Meilland A., Khorrami Z., Chelli A., Baffa C., Hofmann K.-H., Lagarde S., Robbe-Dubois S., Beyond the diffraction limit of optical/IR interferometers. II. Stellar parameters of rotating stars from differential phases, A&A, 2014, vol. 569, p. A45

Hadjara M., Vakili F., Domiciano de Souza A., Millour F., Petrov R., Jankov S., Bendjoya P., SCIROCCO+: Simulation Code of Interferometric-observations for ROtators and

CirCumstellar Objects including Non-Radial Pulsations. In EAS Publications Series , vol. 59 of EAS Publications Series, 2013, p. 131

Haemmerlé L., Eggenberger P., Meynet G., Maeder A., Charbonnel C., Star formation with disc accretion and rotation. I. Stars between 2 and 22 $M_{\odot}$ at solar metallicity, A&A, 2013, vol. 557, p. A112

Haguenauer P., Abuter R., Andolfato L., Alonso J., Blanchard G., Berger J.-P., Bourget P., Brillant S., Derie F., Delplancke F., Di Lieto N., Dupuy C., et al. The Very Large Telescope Interferometer v2012+. In Society of Photo-Optical Instrumentation Engineers (SPIE) Conference Series , vol. 8445 of Society of Photo-Optical Instrumentation Engineers (SPIE) Conference Series, 2012, p. 0

Hall J. S., Observations of the Polarized Light from Stars, Science, 1949, vol. 109, p. 166

Hanuschik R. W., Shell lines in disks around Be stars. 1: Simple approximations for Keplerian disks, A&A, 1995, vol. 295, p. 423

Harmanec P., Stellar masses and radii based on modern binary data, Bulletin of the Astronomical Institutes of Czechoslovakia, 1988, vol. 39, p. 329

Harmanec P., Long-term monitoring of the complex variations of Be stars. In NATO ASIC Proc. 436: The Impact of Long-Term Monitoring on Variable Star Research: Astrophysics , 1994, p. 55

Haubois X., Carciofi A. C., Rivinius T., Okazaki A. T., Bjorkman J. E., Dynamical Evolution of Viscous Disks around Be Stars. I. Photometry, ApJ, 2012, vol. 756, p. 156

Haubois X., Mota B. C., Carciofi A. C., Draper Z. H., Wisniewski J. P., Bednarski D., Rivinius T., Dynamical Evolution of Viscous Disks around Be Stars. II. Polarimetry, ApJ, 2014, vol. 785, p. 12

Hesser J. E., Ugarte P. P., Moreno H., On the period and luminosity stability of sigma Orionis E, ApJ, 1977, vol. 216, p. L31

Hiltner W. A., Polarization of Light from Distant Stars by Interstellar Medium, Science, 1949, vol. 109, p. 165

Hoffleit D., Warren Jr. W. H., VizieR Online Data Catalog: Bright Star Catalogue, 5th Revised Ed. (Hoffleit+, 1991), VizieR Online Data Catalog, 1995, vol. 5050, p. 0

Huang W., Gies D. R., McSwain M. V., A Stellar Rotation Census of B Stars: From ZAMS to TAMS, ApJ, 2010, vol. 722, p. 605

Huat A.-L., Hubert A.-M., Baudin F., Floquet M., Neiner C., Frémat Y., Gutiérrez-Soto J., Andrade L., de Batz B., Diago P. D., Emilio M., Espinosa Lara F., Fabregat J., Janot-Pacheco E., et al. The B0.5IVe CoRoT target HD 49330. I. Photometric analysis from CoRoT data, A&A, 2009, vol. 506, p. 95

Hubeny I., A computer program for calculating non-LTE model stellar atmospheres, Computer Physics Communications, 1988, vol. 52, p. 103

Jaschek M., Slettebak A., Jaschek C., Be star terminology., 1981 Be Star Newsletter

Jerzykiewicz M., Molenda-Zakowicz J., Empirical Luminosities and Radii of Early-Type Stars after Hipparcos, Acta Astron., 2000, vol. 50, p. 369

Kanaan S., Meilland A., Stee P., Zorec J., Domiciano de Souza A., Frémat Y., Briot D., Disk and wind evolution of Achernar: the breaking of the fellowship, A&A, 2008, vol. 486, p. 785

Kaufer A., Stahl O., Tubbesing S., Nørregaard P., Avila G., Francois P., Pasquini L., Pizzella A., Commissioning FEROS, the new high-resolution spectrograph at La-Silla., The Messenger, 1999, vol. 95, p. 8

Kemp J. C., Herman L. C., The polarization of Sigma Orionis E - A curious eclipsing binary, ApJ, 1977, vol. 218, p. 770

Kervella P., Domiciano de Souza A., The polar wind of the fast rotating Be star Achernar. VINCI/VLTI interferometric observations of an elongated polar envelope, A&A, 2006, vol. 453, p. 1059

Kervella P., Domiciano de Souza A., The environment of the fast rotating star Achernar. High-resolution thermal infrared imaging with VISIR in BURST mode, A&A, 2007, vol. 474, p. L49

Kervella P., Domiciano de Souza A., Bendjoya P., The close-in companion of the fast rotating Be star Achernar, A&A, 2008, vol. 484, p. L13

Klement R., Carciofi A. C., Rivinius T., Panoglou D., Vieira R. G., Bjorkman J. E., Stefl S., Tycner C., Faes D. M., Korcakova D., Muller A., Zavala R. T., Curé M., Multi-technique testing of the viscous decretion disk model. I. The stable and tenuous disk of the late-type Be star Beta CMi., A&A, 2015, vol. in press

Kraus S., Monnier J. D., Che X., Schaefer G., Touhami Y., Gies D. R., Aufdenberg J. P., Baron F., Thureau N., ten Brummelaar T. A., McAlister H. A., Turner N. H., Sturmann J., Sturmann L., Gas Distribution, Kinematics, and Excitation Structure in the Disks around the Classical Be Stars β Canis Minoris and ζ Tauri, ApJ, 2012, vol. 744, p. 19

Kudritzki R.-P., Puls J., Winds from Hot Stars, ARA&A, 2000, vol. 38, p. 613

Kurucz R. L., Model atmospheres for G, F, A, B, and O stars, ApJS, 1979, vol. 40, p. 1

Lamers H. J. G. L. M., Cassinelli J. P., Introduction to Stellar Winds, 1999

Landi Degl'Innocenti E., Landi Degl'Innocenti M., A Perturbative Solution of the Transfer Equations for the Stokes Parameters in a Magnetic Field, Sol. Phys., 1973, vol. 31, p. 299

Landstreet J. D., Borra E. F., The magnetic field of Sigma Orionis E, ApJ, 1978, vol. 224, p. L5

Le Bouquin J.-B., Berger J.-P., Lazareff B., Zins G., Haguenauer P., Jocou L., Kern P., Millan-Gabet R., Traub W., Absil O., Augereau J.-C., et al. PIONIER: a 4-telescope visitor instrument at VLTI, A&A, 2011, vol. 535, p. A67

Ledrew G., The Real Starry Sky, JRASC, 2001, vol. 95, p. 32

Lee U., Osaki Y., Saio H., Viscous excretion discs around Be stars, MNRAS, 1991, vol. 250, p. 432

Leitherer C., Robert C., Drissen L., Deposition of mass, momentum, and energy by massive stars into the interstellar medium, ApJ, 1992, vol. 401, p. 596

Lucy L. B., Gravity-Darkening for Stars with Convective Envelopes, ZAp, 1967, vol. 65, p. 89

Lucy L. B., Solomon P. M., Mass Loss by Hot Stars, ApJ, 1970, vol. 159, p. 879

Maciel W. J., Introdução à Estrutura e Evolução Estelar, 1999

Maeder A., Stellar evolution with rotation. IX. The effects of the production of asymmetric nebulae on the internal evolution, A&A, 2002, vol. 392, p. 575

Maeder A., Physics, Formation and Evolution of Rotating Stars, 2009

Magalhães A. M., Benedetti E., Roland E. H., A Photoelectric Polarimeter with Tilt-Scanning Capability, PASP, 1984, vol. 96, p. 383

Magalhães A. M., Rodrigues C. V., Margoniner V. E., Pereyra A., Heathcote S., High Precision CCD Imaging Polarimetry. In Polarimetry of the Interstellar Medium , vol. 97 of Astronomical Society of the Pacific Conference Series, 1996, p. 118

Mariotti J.-M., Adaptive Optics for Long Baseline Optical Interferometry. In NATO Advanced Science Institutes (ASI) Series C , vol. 423 of NATO Advanced Science Institutes (ASI) Series C, 1994, p. 309

Marquardt D. W., An algorithm for least-squares estimation of nonlinear parameters, SIAM Journal on Applied Mathematics, 1963, vol. 11, p. 431

Martayan C., Frémat Y., Hubert A.-M., Floquet M., Zorec J., Neiner C., Effects of metallicity, star-formation conditions, and evolution in B and Be stars. I. Large Magellanic Cloud, field of NGC 2004, A&A, 2006, vol. 452, p. 273

Martayan C., Frémat Y., Hubert A.-M., Floquet M., Zorec J., Neiner C., Effects of metallicity, star-formation conditions, and evolution in B and Be stars. II. Small Magellanic Cloud, field of NGC 330, A&A, 2007, vol. 462, p. 683

Mason B. D., Hartkopf W. I., Gies D. R., Henry T. J., Helsel J. W., The High Angular Resolution Multiplicity of Massive Stars, AJ, 2009, vol. 137, p. 3358

McGill M. A., Sigut T. A. A., Jones C. E., The Thermal Structure of Gravitationally Darkened Classical Be Star Disks, ApJ, 2011, vol. 743, p. 111

McLean I. S., Clarke D., Separation of the intrinsic and interstellar linear polarization components of southern hemisphere early-type emission-line stars, MNRAS, 1979, vol. 186, p. 245

Meilland A., Millour F., Kanaan S., Stee P., Petrov R., Hofmann K.-H., Natta A., Perraut K., First spectro-interferometric survey of Be stars. I. Observations and constraints on the disk geometry and kinematics, A&A, 2012, vol. 538, p. A110

Meilland A., Stee P., Vannier M., Millour F., Domiciano de Souza A., Malbet F., Martayan C., Paresce F., Petrov R. G., Richichi A., Spang A., First direct detection of a Keplerian rotating disk around the Be star α Arae using AMBER/VLTI, A&A, 2007, vol. 464, p. 59

Mihalas D., Athay R. G., The Effects of Departures from LTE in Stellar Spectra, ARA&A, 1973, vol. 11, p. 187

Monnier J. D., Astrophysics with Closure Phases. In EAS Publications Series , vol. 6 of EAS Publications Series, 2003, p. 213

Monnier J. D., Zhao M., Pedretti E., Thureau N., Ireland M., Muirhead P., Berger J.-P., Millan-Gabet R., Van Belle G., ten Brummelaar T., McAlister H., Ridgway S., Turner N., Sturmann L., Sturmann J., Berger D., Imaging the Surface of Altair, Science, 2007, vol. 317, p. 342

Mourard D., Clausse J. M., Marcotto A., Perraut K., Tallon-Bosc I., Bério P., Blazit A., Bonneau D., Bosio S., Bresson Y., Chesneau O., Delaa O., Hénault F., Hughes Y., Lagarde S., Merlin G., et al. VEGA: Visible spEctroGraph and polArimeter for the CHARA array: principle and performance, A&A, 2009, vol. 508, p. 1073

Neiner C., Mathis S., Making a Be star: the role of rotation and pulsations. In IAU Symposium , vol. 301 of IAU Symposium, 2014, p. 465

Okazaki A. T., Viscous Transonic Decretion in Disks of Be Stars, PASJ, 2001, vol. 53, p. 119

Okazaki A. T., Theory vs. Observation of Circumstellar Disks and Their Formation. In Active OB-Stars: Laboratories for Stellare and Circumstellar Physics , vol. 361 of Astronomical Society of the Pacific Conference Series, 2007, p. 230

Okazaki A. T., Bate M. R., Ogilvie G. I., Pringle J. E., Viscous effects on the interaction between the coplanar decretion disc and the neutron star in Be/X-ray binaries, MNRAS, 2002, vol. 337, p. 967

Oksala M. E., Wade G. A., Marcolino W. L. F., Grunhut J., Bohlender D., Manset N., Townsend R. H. D., Mimes Collaboration Discovery of a strong magnetic field in the rapidly rotating B2Vn star HR 7355, MNRAS, 2010, vol. 405, p. L51

Pauls T. A., Young J. S., Cotton W. D., Monnier J. D., A Data Exchange Standard for Optical (Visible/IR) Interferometry, PASP, 2005, vol. 117, p. 1255

Pereyra A., Dust and Magnetic Field in Dense Regions of the Interstellar Medium, University of São Paulo, 2000, Ph.D. Thesis

Peterson D. M., Hummel C. A., Pauls T. A., Armstrong J. T., Benson J. A., Gilbreath G. C., Hindsley R. B., Hutter D. J., Johnston K. J., Mozurkewich D., Schmitt H. R., Vega is a rapidly rotating star, Nature, 2006, vol. 440, p. 896

Petit V., Owocki S. P., Wade G. A., Cohen D. H., Sundqvist J. O., Gagné M., Maíz Apellániz J., Oksala M. E., Bohlender D. A., Rivinius T., Henrichs H. F., Alecian E., Townsend R. H. D., ud-Doula A., MiMeS Collaboration A magnetic confinement versus rotation classification of massive-star magnetospheres, MNRAS, 2013, vol. 429, p. 398

Petrov R. G., Malbet F., Weigelt G., Antonelli P., Beckmann U., Bresson Y., Chelli A., Dugué M., Duvert G., Gennari S., Glück L., Kern P., et al. AMBER, the near-infrared spectro-interferometric three-telescope VLTI instrument, A&A, 2007, vol. 464, p. 1

Porter J. M., Rivinius T., Classical Be Stars, PASP, 2003, vol. 115, p. 1153

Prates Campos R., Domicini T. P., LNA/OPD Recebe o Espectrógrafo MUSICOS, 2010 , LNA em dia, 16, p. 10

Pringle J. E., Accretion discs in astrophysics, ARA&A, 1981, vol. 19, p. 137

Puls J., Vink J. S., Najarro F., Mass loss from hot massive stars, A&A Rev., 2008, vol. 16, p. 209

Quirrenbach A., Bjorkman K. S., Bjorkman J. E., Hummel C. A., Buscher D. F., Armstrong J. T., Mozurkewich D., Elias II N. M., Babler B. L., Constraints on the Geometry of Circumstellar Envelopes: Optical Interferometric and Spectropolarimetric Observations of Seven Be Stars, ApJ, 1997, vol. 479, p. 477

Rieke G. H., Blaylock M., Decin L., Engelbracht C., Ogle P., Avrett E., Carpenter J., Cutri R. M., Armus L., Gordon K., Gray R. O., Hinz J., Su K., Willmer C. N. A., Absolute Physical Calibration in the Infrared, AJ, 2008, vol. 135, p. 2245

Rieutord M., Espinosa L. F., Present status of two-dimensional ESTER models: Application to Be stars. In SF2A-2013: Proceedings of the Annual meeting of the French Society of Astronomy and Astrophysics , 2013, p. 101

Rivinius T., Baade D., Townsend R. H. D., Carciofi A. C., Štefl S., Variable rotational line broadening in the Be star Achernar, A&A, 2013, vol. 559, p. L4

Rivinius T., Baade D., Štefl S., Non-radially pulsating Be stars, A&A, 2003, vol. 411, p. 229

Rivinius T., Baade D., Štefl S., Townsend R. H. D., Stahl O., Wolf B., Kaufer A., Stellar and circumstellar activity of the Be star mu Centauri. III. Multiline nonradial pulsation modeling, A&A, 2001, vol. 369, p. 1058

Rivinius T., Carciofi A. C., Grunhut J., Wade G., Baade D., Štefl S., Faes D. M., The interferometric signature of the rapidly corotating magnetosphere of HR 59071. In American Institute of Physics Conference Series , vol. 1429 of American Institute of Physics Conference Series, 2012, p. 102

Rivinius T., Carciofi A. C., Martayan C., Classical Be stars. Rapidly rotating B stars with viscous Keplerian decretion disks, A&A Rev., 2013, vol. 21, p. 69

Rivinius T., Szeifert T., Barrera L., Townsend R. H. D., Štefl S., Baade D., Magnetic field detection in the B2Vn star HR 7355, MNRAS, 2010, vol. 405, p. L46

Rivinius T., Townsend R. H. D., Kochukhov O., Štefl S., Baade D., Barrera L., Szeifert T., Basic parameters and properties of the rapidly rotating magnetic helium-strong B star HR 7355, MNRAS, 2013, vol. 429, p. 177

Rivinius T., Štefl S., Baade D., Central quasi-emission peaks in shell spectra and the rotation of disks of Be stars, A&A, 1999, vol. 348, p. 831

Rivinius T., Štefl S., Baade D., Bright Be-shell stars, A&A, 2006, vol. 459, p. 137

Salpeter E. E., The Luminosity Function and Stellar Evolution., ApJ, 1955, vol. 121, p. 161

Sana H., Evans C. J., The multiplicity of massive stars. In IAU Symposium , vol. 272 of IAU Symposium, 2011, p. 474

Semel M., Zeeman-Doppler imaging of active stars. I - Basic principles, A&A, 1989, vol. 225, p. 456

Serkowski K., Mathewson D. S., Ford V. L., Wavelength dependence of interstellar polarization and ratio of total to selective extinction, ApJ, 1975, vol. 196, p. 261

Shakura N. I., Sunyaev R. A., Black holes in binary systems. Observational appearance., A&A, 1973, vol. 24, p. 337

Shultz M., Wade G., Rivinius T., Townsend R., the MiMeS Collaboration Emission from the Centrifugal Magnetospheres of Magnetic B-type Stars, ArXiv e-prints, 2014

Stee P., On the kinematics of the envelope of γ Cassiopeiae., A&A, 1996, vol. 311, p. 945

Thiébaut E., MIRA: an effective imaging algorithm for optical interferometry. In Society of Photo-Optical Instrumentation Engineers (SPIE) Conference Series , vol. 7013 of Society of Photo-Optical Instrumentation Engineers (SPIE) Conference Series, 2008, p. 1

Thiébaut É., Principles of Image Reconstruction in Interferometry. In EAS Publications Series , vol. 59 of EAS Publications Series, 2013, p. 157

Tody D., IRAF in the Nineties. In Astronomical Data Analysis Software and Systems II , vol. 52 of Astronomical Society of the Pacific Conference Series, 1993, p. 173

Townsend R. H. D., Exploring the photometric signatures of magnetospheres around helium-strong stars, MNRAS, 2008, vol. 389, p. 559

Townsend R. H. D., Owocki S. P., A rigidly rotating magnetosphere model for circumstellar emission from magnetic OB stars, MNRAS, 2005, vol. 357, p. 251

Townsend R. H. D., Owocki S. P., Groote D., The Rigidly Rotating Magnetosphere of σ Orionis E, ApJ, 2005, vol. 630, p. L81

Townsend R. H. D., Rivinius T., Rowe J. F., Moffat A. F. J., Matthews J. M., Bohlender D., Neiner C., Telting J. H., Guenther D. B., Kallinger T., Kuschnig R., Rucinski S. M., Sasselov D., Weiss W. W., MOST Observations of σ Ori E: Challenging the Centrifugal Breakout Narrative, ApJ, 2013, vol. 769, p. 33

Ud-Doula A., Owocki S. P., Townsend R. H. D., Dynamical simulations of magnetically channelled line-driven stellar winds - II. The effects of field-aligned rotation, MNRAS, 2008, vol. 385, p. 97

Štefl S., Rivinius T., Baade D., Carciofi A., AMBER High-Spectral Resolution Interferometry of Be Stars: More Than Just Stars and Disks?. In Resolving The Future Of Astronomy With Long-Baseline Interferometry , vol. 487 of Astronomical Society of the Pacific Conference Series, 2014, p. 377

van Belle G. T., Interferometric observations of rapidly rotating stars, A&A Rev., 2012, vol. 20, p. 51

van Belle G. T., Ciardi D. R., Thompson R. R., Akeson R. L., Lada E. A., Altair's Oblateness and Rotation Velocity from Long-Baseline Interferometry, ApJ, 2001, vol. 559, p. 1155

van Cittert P. H., Die Wahrscheinliche Schwingungsverteilung in Einer von Einer Lichtquelle Direkt Oder Mittels Einer Linse Beleuchteten Ebene, Physica, 1934, vol. 1, p. 201

van Leeuwen F., Validation of the new Hipparcos reduction, A&A, 2007, vol. 474, p. 653

Vanzi L., Chacon J., Helminiak K. G., Baffico M., Rivinius T., Štefl S., Baade D., Avila G., Guirao C., PUCHEROS: a cost-effective solution for high-resolution spectroscopy with small telescopes, MNRAS, 2012, vol. 424, p. 2770

Vinicius M. M. F., Zorec J., Leister N. V., Levenhagen R. S., α Eridani: rotational distortion, stellar and circumstellar activity, A&A, 2006, vol. 446, p. 643

von Zeipel H., The radiative equilibrium of a rotating system of gaseous masses, MNRAS, 1924, vol. 84, p. 665

Wade G. A., Alecian E., Bohlender D. A., Bouret J.-C., Cohen D. H., Duez V., Gagné M., Grunhut J. H., Henrichs H. F., Hill N. R., Kochukhov O., et al. The MiMeS project: overview and current status. In IAU Symposium , vol. 272 of IAU Symposium, 2011, p. 118

Wade G. A., Petit V., Grunhut J., Neiner C., Magnetic fields of Be stars: preliminary results from a hybrid analysis of the MiMeS sample, ArXiv e-prints, 2014

Wheelwright H. E., Bjorkman J. E., Oudmaijer R. D., Carciofi A. C., Bjorkman K. S., Porter J. M., Probing the properties of Be star discs with spectroastrometry and NLTE radiative transfer modelling: β CMi, MNRAS, 2012, vol. 423, p. L11

Wilking B. A., Lebofsky M. J., Kemp J. C., Martin P. G., Rieke G. H., The wavelength dependence of interstellar linear polarization, ApJ, 1980, vol. 235, p. 905

Wood K., Bjorkman K. S., Bjorkman J. E., Deriving the Geometry of Be Star Circumstellar Envelopes from Continuum Spectropolarimetry. I. The Case of ζ Tauri, ApJ, 1997, vol. 477, p. 926

Zernike F., The concept of degree of coherence and its application to optical problems, Physica, 1938, vol. 5, p. 785

Zhao M., Monnier J. D., Pedretti E., Thureau N., Mérand A., ten Brummelaar T., McAlister H., Ridgway S. T., Turner N., Sturmann J., Sturmann L., Goldfinger P. J., Farrington C., Imaging and Modeling Rapidly Rotating Stars: α Cephei and α Ophiuchi, ApJ, 2009, vol. 701, p. 209

Appendix

Appendix A

Keplerian disks relations

Here we present some structure equations for Keplerian discs with isothermal scale height is steady-state regime. Steady state is defined when $\frac{\partial \Sigma}{\partial t} = 0$.

A.1 Surface density

The integration of the mass conservation equation results

$$\dot{M} = 2\pi r \Sigma v_r = \text{constant}. \tag{A.1}$$

Relating the decretion rate $\dot{M}$ and the torque momentum equation

$$\Sigma(r) = \frac{\dot{M} R_{\rm eq}^{1/2}}{3\pi\alpha c_s^2} \frac{v_{\rm orb}}{r^{3/2}} \left[\left(\frac{R_0}{r} \right)^{1/2} - 1 \right], \tag{A.2}$$

where $v_{\rm orb} = \sqrt{GM/R_{\rm eq}}$ and R_0 is the "disk truncation" radius obtained from momentum equation integration[1]. Under the assumption that $R_0 \gg R_d$, Eq. A.2 becomes

$$\Sigma(r)_{R_0 \gg R_d} = \frac{\dot{M}(GMR_0)^{1/2}}{3\pi\alpha c_s^2 R_{\rm eq}^2} \left(\frac{R_{\rm eq}}{r} \right)^2 = \Sigma_0 \left(\frac{R_{\rm eq}}{r} \right)^2. \tag{A.3}$$

Once the disk is in vertically in hydrostatic equilibrium, the steady-state volumetric density $\rho(r, z)$ can be determined as

$$\rho(r, z) = \rho_0'(r) \exp\left(-\frac{1}{2} \frac{z^2}{H^2(r)} \right), \tag{A.4}$$

$$H(r) = H_0 r^{1.5} = c_s \left(\frac{GM}{r} \right)^{-1/2} r. \tag{A.5}$$

[1] R_0 can not be zero, otherwise it generates inconsistent quantities that and equivalent to a "viscous disk without torque".

Parametrically, m is the exponent of $\rho_0'(r) = \rho_0 \left(\frac{R_{\rm eq}}{r}\right)^m$. The surface density $\Sigma(r)$ can be written as

$$\Sigma(r) = \int_{-\infty}^{\infty} \rho(r,z)dz = \int_{-\infty}^{\infty} \rho_0 \left(\frac{R_{\rm eq}}{r}\right)^m \exp\left(-\frac{1}{2}\frac{z^2}{H^2(r)}\right) ; \tag{A.6}$$

using the identity

$$\int_{-\infty}^{\infty} \exp -\frac{(x-x_0)^2}{a^2} dx = |a|\sqrt{\pi}\,, \tag{A.7}$$

$$\Sigma(r) = \sqrt{\frac{2\pi}{GM}} c_s \rho_0 R_{\rm eq}^{3/2} \left(\frac{R_{\rm eq}}{r}\right)^2 , \tag{A.8}$$

where $m = 7/2$ is equivalent to steady-state solution. Parametrically, n is the exponent of $\Sigma(r) = \Sigma_0 (R_{\rm eq}/r)^n$ and since the scale-height $H(r) \propto r^{3/2}$,

$$n = m - \frac{3}{2}. \tag{A.9}$$

A.2 Disk mass injection rate $\dot{M}$

Equaling Eq. A.3 and Eq. A.8 at $r = R_{\rm eq}$,

$$\left(\frac{2\pi}{GM}\right)^{1/2} c_s \rho_0 R_{\rm eq}^{3/2} = \frac{\dot{M}(GMR_0)^{1/2}}{3\pi\alpha c_s^2 R_{\rm eq}^2}\,, \tag{A.10}$$

$$\dot{M}_{R_0 \gg R_d} = \left(\frac{2\pi}{R_0}\right)^{1/2} \frac{3\pi\alpha c_s^3 R_{\rm eq}^{7/2}}{GM} \rho_0. \tag{A.11}$$

For reference, Eq. A.2 and Eq. A.8 at $r = R_{\rm eq}$,

$$\dot{M} = \frac{\sqrt{2\pi} 3\pi\alpha c_s^3 \rho_0 R_{\rm eq}^3}{GM} \left[\left(\frac{R_0}{R_{\rm eq}}\right)^{1/2} - 1\right]^{-1}. \tag{A.12}$$

A.3 Disk total mass

Disk mass $M_d = M_d(c_s, M, \rho_0, R_{\rm eq}, R_d)$ is

$$M_{d,R_0 \gg R_d} = \int_0^{2\pi} \int_{R_{\rm eq}}^{R_d} \Sigma(r) r dr d\phi = 2\pi R_{\rm eq}^2 \Sigma_0 \ln\left(\frac{R_d}{R_{\rm eq}}\right) \tag{A.13}$$

For reference, $M_d = M_d(R_0, \alpha, c_s, M, \dot{M}, R_{\rm eq}, R_d)$ is

$$M_d = (2\pi)^{3/2} \int_{R_{\rm eq}}^{R_d} \rho(r) H(r) dr\,, \tag{A.14}$$

$$M_d = \frac{2\dot{M}\sqrt{GM}}{3\alpha c_s^3} \left[\sqrt{R_0} \ln\left(\frac{R_d}{R_{\rm eq}}\right) + 2(\sqrt{R_{\rm eq}} - \sqrt{R_0})\right]. \tag{A.15}$$

A.4 BeAtlas *surface density equivalence*

For each stellar mass M and a given rotational rate, the base surface density Σ_0 is a function of (at least) two variables. In the case of Eq. A.8, it is $\Sigma_0(c_s, \rho_0)$. To set the two parameters simultaneously, another equation needs to be satisfied. The criterion for the project was to equal the disk mass-injection rate loss equation ($\dot{M}$, Eq. A.11), assuming that $R_0 = kR_{\rm eq}$ with k constant.

Thus, for two stars of different rotation rates, equality of the above mentioned equations yields, respectively,

$$\frac{\rho_0}{\rho_0'} = \frac{c_s'}{c_s}\frac{R_{\rm eq}'^{3/2}}{R_{\rm eq}^{3/2}}\,, \tag{A.16}$$

$$\frac{\rho_0}{\rho_0'} = \frac{c_s'^3}{c_s^3}\frac{R_{\rm eq}'^3}{R_{\rm eq}^3}. \tag{A.17}$$

The relationship between disk temperature and equatorial radii is

$$c_s'^2 = \frac{R_{\rm eq}^{3/2}}{R_{\rm eq}'^{3/2}}c_s^2\,, \tag{A.18}$$

where the reference value is $c_s = c_s(W = 0.447) = 0.72\,T_p(W = 0.447)$. The adopted criterion results in a decrease of disk scale height H with the stellar rotation, something expected from initial studies (e.g., McGill et al., 2011).

A.5 *Relation between numerical and mass densities*

The chemical composition of a gas is often defined as mass fractions of H, He and other elements, respectively X, Y and Z. By definition,

$$X + Y + Z = 1. \tag{A.19}$$

The X fraction can be written as

$$X = \frac{n_H m_H}{n_H m_H + n_{He} m_{He} + \sum n_i m_i}. \tag{A.20}$$

A more convenient way of is write the mass fractions in terms of the relative abundance to the hydrogen. Considering A_i be the mass number of an element i

$$X = \frac{1}{1 + 4(n_{He}/n_H) + \sum A_i (n_i/n_H)}\,, \tag{A.21}$$

$$Y = \frac{4(n_{He}/n_H)}{1 + 4(n_{He}/n_H) + \sum A_i(n_i/n_H)}\,, \tag{A.22}$$

$$Z = \frac{\sum A_i(n_i/n_H)}{1 + 4(n_{He}/n_H) + \sum A_i(n_i/n_H)}. \tag{A.23}$$

Neutral atoms

The relationship between numerical and mass density for a neutral gas with a given chemical composition is

$$n = \frac{\rho}{\mu m_H} \approx \frac{\rho}{m_H}\left(X + \frac{Y}{4} + \frac{Z}{\langle A\rangle}\right)\,, \tag{A.24}$$

where $\langle A\rangle$ is the mean atomic weight of the gas, excluding H and He. Removing the dependence with Z

$$\mu = \frac{\langle A\rangle}{1 + (\langle A\rangle - 1)X + (\langle A\rangle/4 - 1)Y}. \tag{A.25}$$

Full ionized atoms

For a fully ionized gas,

$$n \approx \frac{\rho}{m_H}\left(2X + \frac{3}{4}Y + \frac{Z}{2}\right)\,, \tag{A.26}$$

where $2.0 \geq \mu \geq 0.5$,

$$\mu = \frac{2}{1 + 3X + Y/2}. \tag{A.27}$$

In terms of electronic density, n_e,

$$n_e\mu_e \equiv n\mu\,, \tag{A.28}$$

$$n_e = \frac{\rho}{\mu_e m_H} \approx \frac{\rho}{m_H}\left(X + \frac{Y}{2} + \frac{Z}{2}\right)\,, \tag{A.29}$$

where $2.0 \geq \mu_e \geq 1.0$,

$$\mu_e \approx \frac{2}{1 + X}. \tag{A.30}$$

Appendix B

Useful equations for interferometry

B.1 Fourier transform

There are several conventions for defining the Fourier transform $\hat{f}$ of an integrable function f. We will use the definition

$$\hat{f}(\xi) = \frac{1}{(2\pi)^{n/2}} \int_{-\infty}^{\infty} f(x) \exp(-ix\xi)\, dx \tag{B.1}$$

for every real number ξ.

When the independent variable x represents a unit (let's say, *time*, with SI unit of seconds), the transform variable ξ represents its inverse (in this case, *frequency*, in Hertz). Under typical smooth conditions, f can be reconstructed from $\hat{f}$ by the inverse transform:

$$f(x) = \frac{1}{(2\pi)^{n/2}} \int_{-\infty}^{\infty} \hat{f}(\xi) \exp(i\xi x)\, d\xi \tag{B.2}$$

for every real number x; n is the dimension of the vectors ξ and x (in our example, $n = 1$).

The Fourier transform $\hat{f}$ measures how much of an individual frequency is present in a function f. If we know $\hat{f}(\omega)$ for all possible frequencies ω, we can perfectly approximate our function f. And that's what the Fourier transform does.

Fourier transform takes some function $f(t)$ of time and returns some other function $\hat{f}(\omega) = \mathscr{F}(f)$, it's Fourier transform, that describes how much of any given frequency is present in f. It's just another representation of $f(t)$, of equal information but with over a different domain. And we can go the other way. Given a Fourier transform, we can integrate over its all frequencies, and get the original $f(t)$ again, which we call inverse Fourier transform $\mathscr{F}(f)^{-1}$.

That is important in this context is that Fourier transform has many interesting mathematical properties (e.g., convolution is just a multiplication). Indeed, in 1807 Fourier in-

troduced his for the purpose of solving the heat equation in a metal plate (heat equation is a partial differential equation).

A classical example of the utility of the Fourier transform is noise reduction on a digital image (or a sound wave). Rather than manipulating a function image(*Pixel-Brightness*), we transform it and work with $\mathscr{F}$(image; *Frequency-Amplitude*). Let suppose those party of high frequency that cause the noise. It can simply be cut off with $\mathscr{F}$(image; ω)=0, when $\omega > w_{\text{cut}}$. We transform it back, and have the image without noise.

B.2 Bessel functions

The Bessel functions are frequently defined as solutions to the differential equation:

$$x^2\frac{d^2y}{dx^2} + x\frac{dy}{dx} + (x^2 - k^2)y = 0. \tag{B.3}$$

They are generally refereed as $J_k(x)$, where k is the function index:

$$J_k(x) = \sum_{m=0}^{\infty} \frac{(-1)^m}{m!\,\Gamma(m+k+1)} \left(\frac{x}{2}\right)^{2m+k}, \tag{B.4}$$

where $\Gamma(y)$ is the gamma function. k is usually taken as an integer number, but Eq. B.4 is also valid for real numbers. There are other definitions of the Bessel functions, for examples, in form of power series. An interesting problem on mathematics is to find the roots of the Bessel Functions. Since interferometry make use of them for simple brightness distributions that can be treated analytically, we list the initial root values in Tables B.1 and B.2. Table B.3 contains a list of useful brightness distribution models.

Table B.1 - The first few roots of Bessel functions J_k

k	$J_0(x)$	$J_1(x)$	$J_2(x)$
1	2.4048	3.8317	5.1356
2	5.5201	7.0156	8.4172
3	8.6537	10.1735	11.6198
4	11.7915	13.3237	14.7960
5	14.9309	16.4706	17.9598

An useful relation dealing with half integer indexes of Bessel functions are:

$$J_{n/2-1}(x) + J_{n/2+1}(x) = \frac{2n}{x} J_{n/2}(x)\,, \tag{B.5}$$

$$J_{-n}(x) = (-1)^n J_n(x). \tag{B.6}$$

Table B.2 - The first few roots of the derivative of Bessel functions $J'_k(x)$

k	$J'_0(x)$	$J'_1(x)$	$J'_2(x)$
1	3.8317	1.8412	3.0542
2	7.0156	5.3314	6.7061
3	10.1735	8.5363	9.9695
4	13.3237	11.7060	13.1704
5	16.4706	14.8636	16.3475

B.3 Other valuable information

Properties of the Fourier transform:

- **linearity**: $\mathscr{F}(f+g) = \mathscr{F}(f) + \mathscr{F}(g)$
- **translation**: $\mathscr{F}[f(x-x_0, y-y_0)] = \mathscr{F}[f(u,v)\exp i2\pi(ux_0+vy_0)]$
- **similarity**: $\mathscr{F}[f(ax,by)] = \frac{1}{ab}\mathscr{F}\left[f\left(\frac{u}{a},\frac{v}{b}\right)\right]$
- **convolution**: $\mathscr{F}(f\otimes g) = \mathscr{F}(f)\times\mathscr{F}(g)$

The optical interferometry data should be stored according to the IAU standards. In this case, it is the OIFITS format defined by Pauls et al. (2005). Routines to deal with this format in Python programing language are available in the PYHDUST library.

The relation between angle units can be obtained as

$$\frac{\text{radian}}{\text{arcsecond}} = \frac{2\pi}{360°60”60'} \approx \frac{1}{206264.8} \tag{B.7}$$

So, we have the factor of $\approx 4.848\times10^{-9}$ rad per mas.

Table B.3 - Simple interferometric reference models

Shape	Brightness distribution	Visibility
Point source	$\delta(\vec{r})$	1
Background	I_0	0
Binary star	$I_0[\delta(\vec{r_1}) + R\delta(\vec{r_1} - \vec{r_2})]$	$\sqrt{\frac{V_1^2+R^2V_2^2+2R\lvert V_1\rvert\lvert V_2\rvert\cos[2\pi\vec{u}\cdot(\vec{r_1}-\vec{r_2})]}{(1+R)^2}}$
Gaussian	$I_0\sqrt{\frac{2\sigma}{\pi}} \times \exp\left(-\frac{r^2}{\sigma^2}\right)$	$\exp(-\pi\sigma\lvert\vec{u}\rvert)^2$
Uniform disk	$\frac{4}{\pi\phi^2}$ if $\lvert\vec{r}\rvert < \frac{\phi}{2}$; 0 else	$\left[\frac{2J_1(\pi\phi\lvert\vec{u}\rvert)}{\pi\phi\lvert\vec{u}\rvert}\right]$
Ring	$\frac{1}{\pi\phi}\delta\left(\lvert\vec{r}\rvert - \frac{\phi}{2}\right)$	$J_0(\pi\phi\lvert\vec{u}\rvert)$
Exponential	$\exp(-k_0\lvert\vec{r}\rvert), k_0 \geq 0$	$\left(\frac{k_0^2}{1+k_0^2\vec{u}^2}\right)$
Circularly symmetric	$I(r)$	$2\pi\int_0^\infty I(r)J_0(2\pi\vec{r}\cdot\vec{u})r\,dr$
Rectangle (xy coord.)	$1/lL$ if $x < l$ and $y < L$; 0 else	$\left[\frac{\sin(\pi xl)\sin(\pi yL)}{\pi^2 xylL}\right]$
Limb-darkened (linearly) disk	$I_0[1 = a_k(1-\mu)]$ if $\lvert\vec{r}\rvert < \frac{\phi}{2}$; 0 else; $\mu = \cos\left(\frac{2\lvert\vec{r}\rvert}{\phi}\right)$	$\frac{\left[\alpha\frac{J_1(x)}{x} + \beta\sqrt{\frac{\pi}{2}}\frac{J_{3/2}(x)}{x^{3/2}}\right]^2}{\left(\frac{\alpha}{2}+\frac{\beta}{3}\right)^2}$ $\alpha = 1 - a_k;\ \beta = a_k\lambda;$ $x = \pi\theta_{\mathrm{LD}}\lvert\vec{u}\rvert$

Appendix C

Polarimetric observations of magnetospheres

Table C.1 - V-band polarization measurements of σ Ori E.

MJD	P (%)	Q (%)	U (%)	θ (deg)	σ_P (%)	σ_θ (deg)
55808.325654	0.292	-0.286	0.061	83.9	0.015	0.4
55808.325654	0.292	-0.286	0.061	83.9	0.015	0.4
55814.297218	0.362	-0.362	-0.015	91.2	0.021	0.6
55814.297218	0.362	-0.362	-0.015	91.2	0.021	0.6
55808.347460	0.365	-0.364	0.025	88.1	0.044	1.3
55808.347460	0.365	-0.364	0.025	88.1	0.044	1.3
55427.338335	0.349	-0.349	-0.024	92.0	0.047	1.3
55427.338335	0.349	-0.349	-0.024	92.0	0.047	1.3
55813.268611	0.354	-0.354	-0.005	90.4	0.005	0.1
55813.268611	0.354	-0.354	-0.005	90.4	0.005	0.1
55813.309468	0.357	-0.357	0.001	90.0	0.010	0.3
55813.309468	0.357	-0.357	0.001	90.0	0.010	0.3
55813.348828	0.335	-0.335	-0.006	90.5	0.013	0.4
55426.341288	0.346	-0.345	-0.033	92.7	0.036	1.0
55499.133779	0.311	-0.310	-0.022	92.1	0.005	0.1
55499.156024	0.323	-0.322	-0.022	91.9	0.004	0.1
55499.184219	0.309	-0.309	-0.010	91.0	0.004	0.1
55499.205862	0.310	-0.310	0.000	90.0	0.006	0.2
55499.227656	0.310	-0.310	0.007	89.4	0.006	0.2

Continued on next page

Table C.1 – continued from previous page.

MJD	P (%)	Q (%)	U (%)	θ (deg)	σ_P (%)	σ_θ (deg)
55443.334203	0.312	-0.312	0.004	89.6	0.015	0.4
55443.352942	0.312	-0.312	0.019	88.2	0.012	0.3
55498.137529	0.333	-0.332	0.015	88.7	0.006	0.2
55498.160515	0.327	-0.326	0.024	87.9	0.004	0.1
55498.182436	0.329	-0.328	0.025	87.8	0.005	0.2
55498.231777	0.336	-0.336	0.016	88.6	0.004	0.1
55442.284060	0.326	-0.324	0.034	87.0	0.013	0.4
55498.253605	0.332	-0.332	0.012	89.0	0.006	0.2
55442.307880	0.321	-0.321	0.014	88.8	0.032	0.9
55498.278038	0.337	-0.337	0.016	88.6	0.005	0.1
55498.299809	0.328	-0.328	0.007	89.4	0.007	0.2
55442.333760	0.328	-0.328	0.001	89.9	0.030	0.8
55497.135596	0.350	-0.350	0.008	89.4	0.008	0.2
55497.157448	0.331	-0.331	-0.006	90.5	0.004	0.1
55497.180341	0.331	-0.331	-0.004	90.3	0.009	0.2
55497.201615	0.323	-0.323	-0.002	90.2	0.004	0.1
55497.223744	0.324	-0.323	-0.009	90.8	0.007	0.2
55497.245943	0.317	-0.317	-0.003	90.2	0.011	0.3
55441.293938	0.287	-0.287	-0.020	92.0	0.016	0.5
55497.268212	0.330	-0.330	-0.008	90.7	0.009	0.3
55441.320951	0.306	-0.299	-0.068	96.4	0.035	1.0
55441.320951	0.306	-0.299	-0.068	96.4	0.035	1.0
55497.290446	0.328	-0.328	-0.007	90.6	0.015	0.4
55497.290446	0.328	-0.328	-0.007	90.6	0.015	0.4
55441.348127	0.299	-0.298	-0.019	91.8	0.011	0.3
55441.348127	0.299	-0.298	-0.019	91.8	0.011	0.3
55496.151719	0.327	-0.326	-0.018	91.6	0.008	0.2
55496.151719	0.327	-0.326	-0.018	91.6	0.008	0.2
55496.174196	0.323	-0.322	-0.027	92.4	0.008	0.2

Continued on next page

Table C.1 – continued from previous page.

MJD	P (%)	Q (%)	U (%)	θ (deg)	σ_P (%)	σ_θ (deg)
55496.174196	0.323	-0.322	-0.027	92.4	0.008	0.2
55496.195573	0.337	-0.336	-0.027	92.3	0.010	0.3
55496.195573	0.337	-0.336	-0.027	92.3	0.010	0.3
55496.230110	0.335	-0.334	-0.026	92.2	0.009	0.3
55496.230110	0.335	-0.334	-0.026	92.2	0.009	0.3
55808.226678	0.328	-0.327	0.013	88.8	0.019	0.5
55808.226678	0.328	-0.327	0.013	88.8	0.019	0.5
55496.251962	0.329	-0.328	-0.008	90.7	0.013	0.4
55496.251962	0.329	-0.328	-0.008	90.7	0.013	0.4
55808.260854	0.335	-0.335	0.010	89.2	0.013	0.4
55808.260854	0.335	-0.335	0.010	89.2	0.013	0.4
55496.272980	0.335	-0.335	0.002	89.8	0.006	0.2
55496.272980	0.335	-0.335	0.002	89.8	0.006	0.2
55496.294508	0.337	-0.337	0.005	89.6	0.009	0.3
55496.294508	0.337	-0.337	0.005	89.6	0.009	0.3
55814.245312	0.294	-0.291	-0.044	94.3	0.022	0.6
55814.245312	0.294	-0.291	-0.044	94.3	0.022	0.6
55808.295159	0.363	-0.360	0.045	86.5	0.030	0.9
55808.295159	0.363	-0.360	0.045	86.5	0.030	0.9
55496.316047	0.338	-0.338	0.005	89.6	0.014	0.4
55496.316047	0.338	-0.338	0.005	89.6	0.014	0.4

Table C.2 - V-band polarization measurements of HR 7355.

MJD	P (%)	Q (%)	U (%)	θ (deg)	σ_P (%)	σ_θ (deg)
55354.316111	0.029	-0.018	0.023	243.5	0.040	1.1
55355.292959	0.017	0.010	-0.013	153.7	0.024	0.7
55355.301703	0.025	-0.021	0.014	253.4	0.024	0.7

Continued on next page

Table C.2 – continued from previous page.

MJD	P (%)	Q (%)	U (%)	θ (deg)	σ_P (%)	σ_θ (deg)
55355.307623	0.026	0.025	0.006	186.9	0.015	0.4
55426.231794	0.024	0.003	0.024	220.9	0.011	0.3
55428.166076	0.048	-0.022	0.042	58.5	0.021	0.6
55428.178906	0.021	-0.012	-0.017	116.9	0.020	0.6
55441.163588	0.043	-0.042	0.010	83.3	0.010	0.3
55443.088255	0.130	0.102	-0.080	161.0	0.041	1.2
55443.098516	0.022	0.019	0.012	196.3	0.023	0.6
55443.108735	0.006	-0.002	0.006	56.1	0.027	0.8
55443.118956	0.033	0.007	-0.032	141.0	0.013	0.4
55443.134418	0.072	0.035	-0.063	149.5	0.022	0.6
55443.149899	0.079	-0.020	-0.076	127.5	0.091	2.6
55443.160963	0.115	-0.097	-0.061	106.2	0.069	2.0
55496.978263	0.018	-0.015	0.011	72.5	0.008	0.2
55496.986972	0.025	-0.024	0.007	81.7	0.003	0.1
55727.204879	0.039	0.004	0.038	41.9	0.021	0.6
55727.225370	0.011	-0.011	0.004	80.6	0.019	0.5
55727.246904	0.016	-0.008	0.014	59.6	0.019	0.5
55727.271788	0.019	0.001	0.019	43.7	0.012	0.4
55741.279656	0.044	-0.036	-0.025	107.6	0.049	1.4
55741.293545	0.040	0.011	0.038	36.8	0.031	0.9
55741.306698	0.017	-0.009	0.015	60.1	0.036	1.0
55741.319470	0.019	-0.001	-0.019	133.5	0.053	1.5
55741.332028	0.050	0.021	-0.045	147.6	0.019	0.6
56923.051934	0.017	-0.016	0.004	83.2	0.012	0.3
56923.055012	0.049	-0.044	-0.022	-76.7	0.033	0.9
56923.058097	0.026	-0.026	0.004	86.1	0.026	0.7
56923.061178	0.005	-0.002	-0.005	-54.4	0.005	0.1
56923.064259	0.019	-0.009	-0.017	-59.5	0.012	0.3
56923.067303	0.013	0.012	-0.006	-12.5	0.007	0.2

Continued on next page

Table C.2 – continued from previous page.

MJD	P (%)	Q (%)	U (%)	θ (deg)	σ_P (%)	σ_θ (deg)
56923.070385	0.032	0.008	0.031	38.1	0.020	0.6
56923.073446	0.071	0.046	0.053	24.5	0.049	1.4

Table C.3 - V-band polarization measurements of HR 5907.

MJD	P (%)	Q (%)	U (%)	θ (deg)	σ_P (%)	σ_θ (deg)
55355.130869	0.599	-0.262	0.539	238.0	0.007	0.2
55355.135273	0.621	-0.254	0.566	237.1	0.021	0.6
55355.142235	0.601	-0.264	0.540	238.1	0.011	0.3
55395.960399	0.620	-0.324	0.528	60.8	0.034	1.0
55397.050492	0.606	-0.333	0.506	-118.3	0.040	1.1
55397.057344	0.622	-0.284	0.553	-121.4	0.008	0.2
55425.061678	0.588	-0.302	0.504	60.5	0.042	1.2
55425.073536	0.698	-0.343	0.608	59.7	0.011	0.3
55426.984575	0.606	-0.265	0.545	58.0	0.026	0.7
55426.999847	0.627	-0.335	0.530	61.1	0.009	0.2
55427.914965	0.613	-0.305	0.531	60.0	0.029	0.8
55427.923258	0.616	-0.311	0.532	60.1	0.013	0.4
55441.915871	0.620	-0.282	0.552	58.5	0.007	0.2
55727.053359	0.631	-0.309	0.550	59.7	0.022	0.6
55727.103608	0.617	-0.251	0.563	57.0	0.019	0.5
55741.046923	0.613	-0.354	0.501	62.7	0.011	0.3
55741.083277	0.600	-0.351	0.487	62.9	0.033	1.0
55812.957300	0.651	-0.310	0.573	59.2	0.026	0.7
55812.969586	0.566	-0.270	0.497	59.2	0.045	1.3
55812.981409	0.625	-0.308	0.544	59.8	0.030	0.8
56027.133345	0.585	-0.297	0.504	60.3	0.026	0.8
56027.146435	0.579	-0.305	0.492	60.9	0.015	0.4

Continued on next page

Table C.3 – continued from previous page.

MJD	P (%)	Q (%)	U (%)	θ (deg)	σ_P (%)	σ_θ (deg)
56027.160550	0.634	-0.316	0.549	60.0	0.020	0.6
56027.175729	0.626	-0.321	0.538	60.4	0.012	0.3
56922.938028	0.613	-0.275	0.548	58.3	0.027	0.8
56922.952285	0.603	-0.308	0.518	60.4	0.025	0.7
56922.971061	0.666	-0.342	0.571	60.5	0.072	2.1
56922.985319	0.672	-0.313	0.595	58.9	0.021	0.6

Appendix D

IUE data fitting to Achernar with BeAtlas

As an example of the work being conducted with BeAtlas models, we applied our photospheric models to the ultra-violet observations of the IUE satellite on Achernar. The IUE (International Ultraviolet Explorer) satellite was launched in 1978 and operated until 1996. During this period, the satellite observed Achernar in different epochs, resulting in observations over different circumstellar activity phases.

The IUE observations analyzed here were grouped according to the circumstellar activity at the time of the observations (Table D.1). The work of Vinicius et al. (2006) contains detailed information of Hα line profile that can be used to assess the activity from 1991 up to 2003. It also contains the authors qualitative estimations of the emission strength before 1990 from the literature, which allows us infer the level of Achernar activity since the first observations until 1991.

The BeAtlas MCMC minimization for the different level of circumstellar activity are shown in Figs. D.1 to D.3. The constraints, used priors in the likelyhood probability, were: (i) the oblateness $1.3 \leq R_{\rm eq}/R_p \leq 1.45$, (ii) the inclination angle $50^\circ \leq i \leq 80^\circ$, and (iii) the distance value from van Leeuwen (2007, $d = 42.8(1.0)$ pc). The interestellar extinction value was fixed in $E(B-V) = 0$, based on the stellar unpolarized spectrum at the disk quiescent phase and its nearby position, inside the interestellar local bubble (Frisch et al., 2011).

As results of this minimization, we highlight: (i) the disk activity little changed the parameters determination; (ii) within the considered ranges, no clear trend exist for stellar oblateness, inclination angle, or evolutionary stage ($X_{\rm c}$) itself; (iii) the most probable stellar mass would have $\sim$7.2 $M_\odot$, correlated with and late evolurionary age ($X_{\rm c} \lesssim 0.2$), where most of H present in the core was already consumed by the star.

Table D.1 - IUE observations of Achernar grouped according to the circunstellar activity at the time of observations.

Disk activity (Hα)	Group 1 None/Small	Group 2 Intermediate	Group 3 Full
Dates	Â 1983-09-24	1992-08-03	1993-09-06
	1988-05-14	1995-09-07	1993-09-24
	1989-12-14	1995-09-08	1993-10-16
	1990-09-30	1995-09-09	1993-11-14
		1994-06-15	1994-06-14
			1994-07-26

According to Mota et al. (in prep.), the IUE spectra has the capacity of precise constrain the multiple photospheric parameters of main sequence stars, even if the interstellar extinction is present. This allows us to state that Achernar is not a typical main-sequence star. Different estimations for Achernar points to a stellar mass around the value of $\sim$6.2 $M_{\odot}$ (Domiciano de Souza et al., 2014). Comparing to the BeAtlas models, the photospheric parameters derived from interferometry mimics a main sequence star with a higher mass (Table 6.1). It is also known that the radius and luminosity of the star typically increase along the main sequence (e.g., Georgy et al., 2013). These elements show that Achernar likely is a star leaving the main sequence, as discussed by Rieutord and Espinosa (2013).

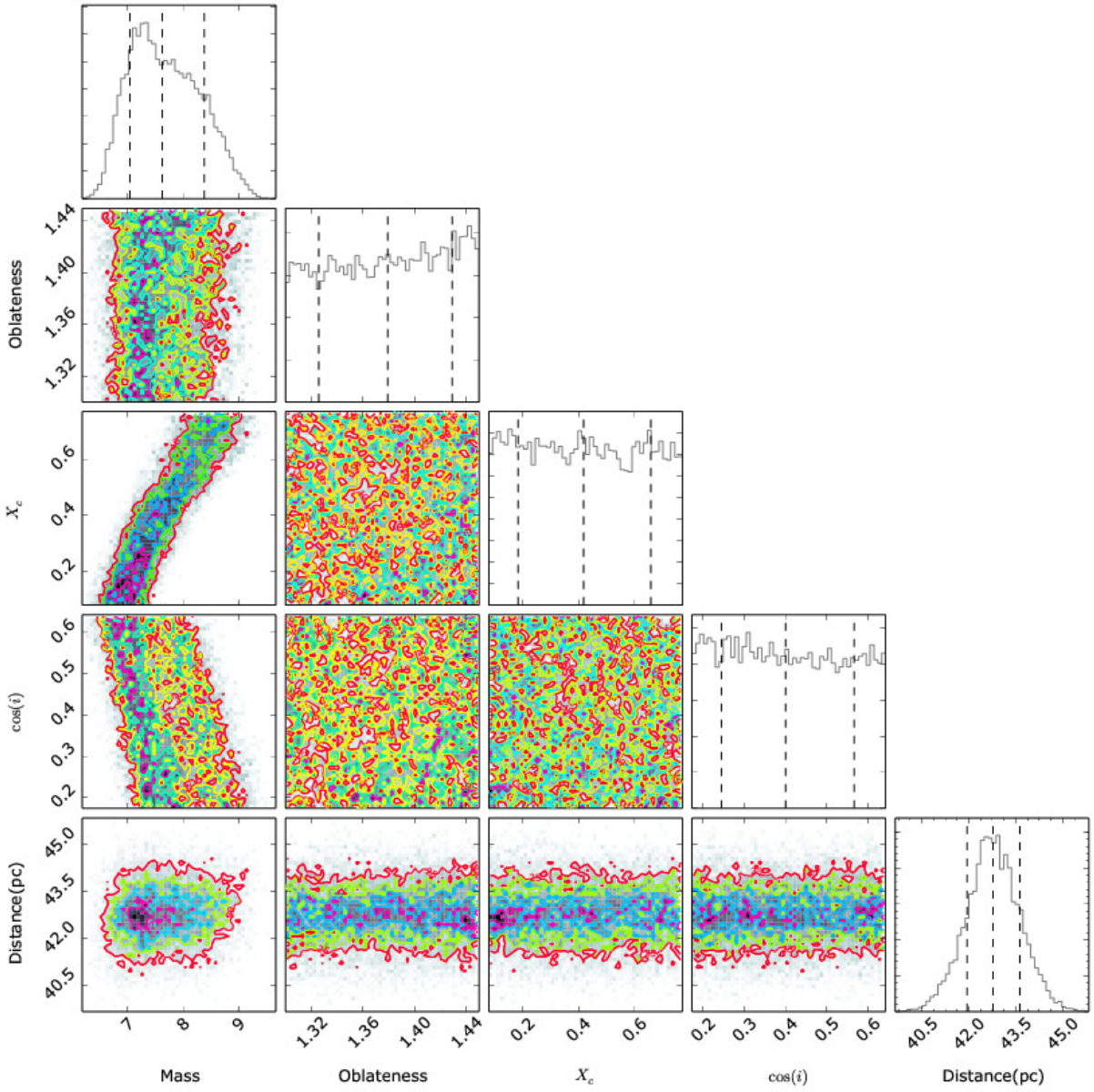

Figure D.1: Probability density functions of the derived stellar parameters for Achernar and their correlation maps. It corresponds to the set 1 of IUE observations (none or very small disk activity; Table D.1) sampled with BEATLAS models. The rainbow-like color map indicates the isocontour of highest probabilities (blue) to the lowest (red). *From left to right (or top-bottom):* mass (Solar masses), oblateness, H fraction at stellar core, cosine of the inclination angle and distance (in parsec). The dashed vertical lines in the histograms indicate the percentile of 16% (-1σ), the median and the percentile of 84% (1σ) of each distribution.

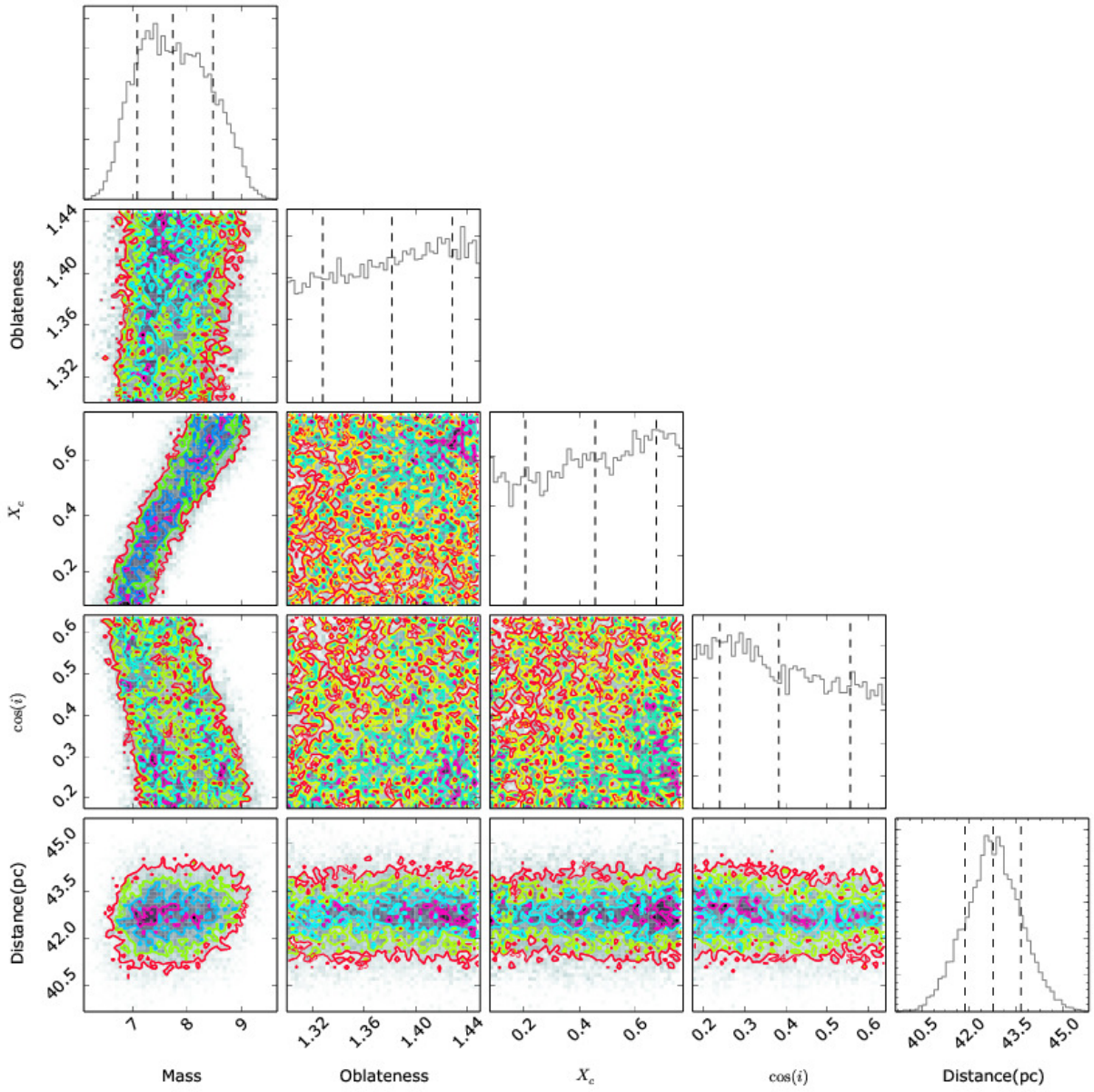

Figure D.2: Same as previous figure, but for set 2 of IUE data (intermediate disk activity).

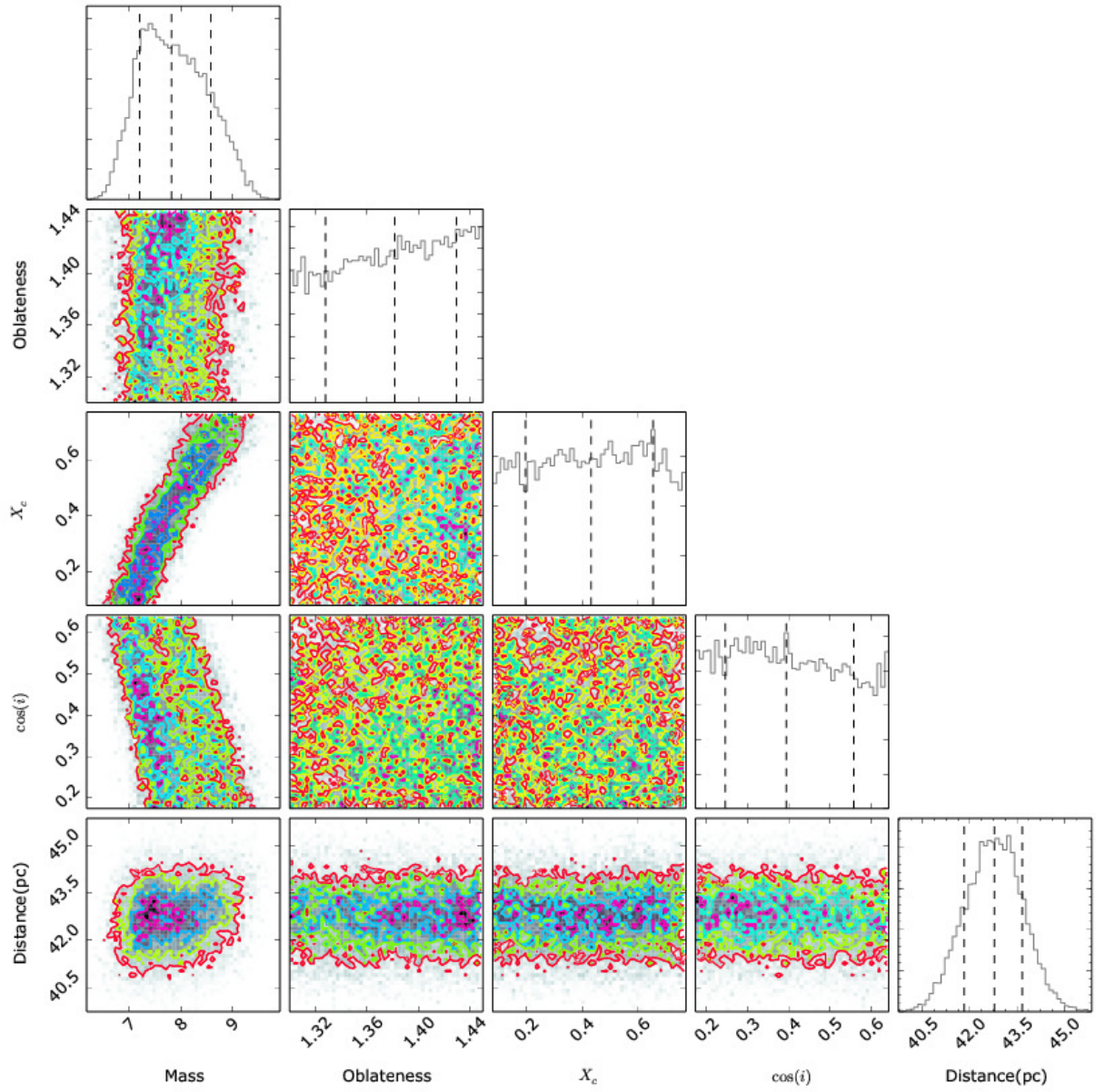

Figure D.3: Same as previous figure, but for set 3 of IUE data (full disk activity).

Appendix E

The Be phenomenon: a resonance effect?

The proximity between the orbital, rotational and critical frequencies deducted for Achernar based on the parameters from Domiciano de Souza et al. (2014) and known observational frequencies draws attention. Indeed, it points to a interesting effect on massive stars and that could be necessary for the occurrence of the Be phenomenon.

It is known to resonance that smallest is the difference between the oscillating frequency ω and the resonant frequency Ω bigger is the intensity (I, or squared amplitude) of the oscillations:

$$I(\omega) \propto \frac{\left(\frac{\Gamma}{2}\right)^2}{(\omega-\Omega)^2+\left(\frac{\Gamma}{2}\right)^2}\,, \tag{E.1}$$

where Γ is a parameter dependent on the damping of the oscillator, and is known as the linewidth of the resonance.

For a given star at W rotational rate, it is possible to define three frequencies: F4, the equatorial orbital frequency; F5, the critical frequency; and F6, the equatorial rotational frequency (if the star is a rigid rotator, F6 is the stellar rotational frequency). If $W<1$, then F4 > F5 > F6. If the star rotates critically ($W=1$), F4 = F5 = F6.

Keeping the W fixed, the difference between all these frequencies ($\Delta\mathrm{F}^*$) satisfies

$$\Delta\mathrm{F}^* \propto \sqrt{\frac{M}{R_p^3}}\,, \tag{E.2}$$

in the three possible cases

$$\Delta\mathrm{F} = \mathrm{F4}-\mathrm{F5} = \frac{v_{\rm orb}}{2\pi r R_p} - \frac{v_{\rm crit}}{2\pi 1.5 R_p} = \frac{(GM)^{1/2}}{2\pi R_p^{3/2}}\left(\frac{1}{r^{3/2}} - \frac{1}{1.5^{3/2}}\right)\,, \tag{E.3}$$

$$\Delta\mathrm{F}' = \mathrm{F4}-\mathrm{F6} = \frac{v_{\rm orb}}{2\pi r R_p} - \frac{W v_{\rm orb}}{2\pi r R_p} = \frac{(GM)^{1/2}}{2\pi R_p^{3/2}}\left(\frac{1-W}{r^{3/2}}\right)\,, \tag{E.4}$$

Table E.1 - Main sequence masses and radius values from Maciel (1999).

Sp	$M/M_\odot$	$R/R_\odot$	M/R^3 (Solar units)
05V	60	12	0.035
06V	37	10	0.037
08V	23	8.5	0.037
B0V	17.5	7.4	0.043
B3V	7.6	4.8	0.069
B5V	5.9	3.9	0.099
B8V	3.8	3.0	0.141
A0V	2.9	2.4	0.210
A5V	2.0	1.7	0.407
F0V	1.6	1.5	0.474
F5V	1.4	1.3	0.637

$$\Delta \mathrm{F}'' = \mathrm{F5} - \mathrm{F6} = \frac{W v_{\rm orb}}{2\pi r R_p} - \frac{v_{\rm crit}}{2\pi 1.5 R_p} = \frac{(GM)^{1/2}}{2\pi R_p^{3/2}} \left(\frac{1}{1.5^{3/2}} - \frac{W}{r^{3/2}} \right) , \tag{E.5}$$

where $1 \leq r \leq 1.5$ is the radius ratio $R_{\rm eq}/R_p$ for a specific W value (e.g., Eq. 1.30).

If the Be phenomenon is a resonance effect in the critical frequency then the lower the $\Delta \mathrm{F}^*$ differences, most likely is its occurrence. Indeed, it is know that the ratio M/R^3 decreases as the mass increases along the main sequence. Taking, for example, the stellar parameters from Maciel (1999), $\Delta \mathrm{F}^*$ is smaller the more massive is the main-sequence star, with $M/R^3 \lesssim 0.2$ from A0V subtypes (solar units; Table E.1).

This resonance could also indicates with early-type B stars have denser disks than late-type B, and rotational perturbations (inducing $\Delta \mathrm{F}^*$) could easy be originate by tide effects from a binary companion star (or other process in stellar interior). However, this do not explain why the Be phenomenon is not present in O-type stars as it is in B0 ones. One possibility to be investigated the interaction of the ejected material with the stronger winds of these stars. Other, more likely, is the presence of NRP frequencies occurring only in B stars that are similar to near-critical equatorial orbits, working as triggers to mass-loss episodes, as the proximity between Goss et al. (2011) frequency F1 and F4 for Achernar suggests. If the κ mechanism if the origin of these pulsations and the transport of angular momentum as proposed by Neiner and Mathis (2014), the hotter temperatures or physical dimensions of O-type stars could completely block the mechanism.

Table E.2 - Rotational and orbital frequencies for Achernar. ^{c} denote values at critical rotation.

Fn	Frequency Description	Value (d^{-1})	Closest observed frequency (d^{-1})	Diff. to closest obs. freq. (d^{-1})	Vel. ($km\,s^{-1}$)	Radius (R_p)
F4	Equatorial orbit	0.769	F1	0.0066	356.4	1.352
F4^c	Equatorial orbit	0.657	F3	0.0234	338.2	1.5
F5	Critic rotation	0.657	F3	0.0234	338.2	1.5
F6^c	Rotation	0.657	F3	0.0234	338.2	1.5
F6	Rotation	0.644	F3	0.0356	298.8	1.352
F7	Keplerian ($R \lesssim R_{eq}$)	0.777	F1	0.0003	357.8	1.3405
F8	Keplerian ($R > R_{eq}$)	0.725	F2	0.0002	349.5	1.405
F9	Keplerian ($R > R_{eq}$)	0.681	F3	0.0003	342.2	1.465

E.1 Achernar frequencies

Let us consider the following scenario: Achernar has a NRP frequency matching the orbital the equatorial orbital frequency (F4). The F4 frequency could also be associated with a tenuous residual disk (Carciofi and Bjorkman, 2008; Domiciano de Souza et al., 2014), leaving a low magnitude orbiting signature. However, its stability is hard to be explained since viscosity would dissipated the ejected material. At epochs of stellar activity, a transient period appears with the photospheric rotational frequency (F6) due to material ejection by the star, for example, associated with the presence of photospheric spots. Table E.2 contains a list of orbital frequencies calculated for Achernar, that are compared to the observed frequencies by Goss et al. (2011, Table 6.2).

Having the two frequencies (F4 and F6) in the scenario described above one have a direct measurement of the stellar rotation rate (Eq. 6.5). The facts that (i) the transient period F3 of Achernar is roughly its critical frequency (F5; since it is a fast rotating star, F5 $\approx$ F6); (ii) the observed F1 frequency coincides with the orbital frequency F4; and (iii) the observed spin-up velocity in Achernar's line profile is exactly the one required to F4 reach F5; they together strongly suggests that the Be phenomenon can be seen as a resonant effect of these frequencies. NRP pulsations at frequency F1 $\approx$ F4 could act as a trigger to the stellar mechanical mass-loss to orbits around the equatorial radius previously its spin-up. The role of observed frequency F2 to Achernar should be determined but it could, in principle, be associate with other non-stable pulsation modes or a Keplerian orbit at radius $R > R_{eq}$.

Appendix F

Achernar 2013+ active phase observational log

F.1 Spectroscopy

Table F.1 - List of spectroscopic observations covering Hα wavelengths available after the 2013 outburst of Achernar.

Instument	**Resolution**	**Date**	**MJD**
ECass	5000	2012-11-20	56251.9942
PUCHEROS	20000	2013-01-18	56310.0
Amateur	5000	2013-01-22	56314.0
Amateur	5000	2013-07-03	56476.0
XSHOOTER	15000	2013-07-18	56491.4418
PUCHEROS	20000	2013-07-24	56497.0
PUCHEROS	20000	2013-07-25	56498.0
Amateur	5000	2013-07-28	56501.0
Amateur	5000	2013-08-17	56521.0360
Amateur	5000	2013-08-23	56527.2199
FEROS	48000	2013-09-06	56541.2938
FEROS	48000	2013-09-06	56541.2948
FEROS	48000	2013-09-06	56541.2968
FEROS	48000	2013-09-06	56541.3519
FEROS	48000	2013-09-07	56542.3922
FEROS	48000	2013-09-07	56542.3930
FEROS	48000	2013-09-07	56542.3940
FEROS	48000	2013-09-07	56542.3952
FEROS	48000	2013-09-08	56543.1813
FEROS	48000	2013-09-08	56543.1822
FEROS	48000	2013-09-08	56543.3196

Continue on next page

Tabela F.1 – table from previous page

Instument	Resolution	Date	MJD
FEROS	48000	2013-09-08	56543.3218
FEROS	48000	2013-09-08	56543.4230
FEROS	48000	2013-09-08	56543.4238
FEROS	48000	2013-09-09	56544.2428
FEROS	48000	2013-09-09	56544.2436
FEROS	48000	2013-09-09	56544.3869
FEROS	48000	2013-09-09	56544.4148
FEROS	48000	2013-09-09	56544.4156
FEROS	48000	2013-09-10	56545.1311
FEROS	48000	2013-09-10	56545.4103
FEROS	48000	2013-09-13	56548.1172
FEROS	48000	2013-09-13	56548.1179
FEROS	48000	2013-09-13	56548.2305
FEROS	48000	2013-09-13	56548.2312
FEROS	48000	2013-09-13	56548.4111
FEROS	48000	2013-09-13	56548.4118
FEROS	48000	2013-09-15	56550.1151
FEROS	48000	2013-09-15	56550.1159
FEROS	48000	2013-09-15	56550.1169
FEROS	48000	2013-09-15	56550.1783
FEROS	48000	2013-09-15	56550.1793
FEROS	48000	2013-09-15	56550.1809
FEROS	48000	2013-09-16	56551.2722
FEROS	48000	2013-09-16	56551.2729
FEROS	48000	2013-09-16	56551.3209
FEROS	48000	2013-09-16	56551.3217
FEROS	48000	2013-09-16	56551.3914
FEROS	48000	2013-09-16	56551.3922
FEROS	48000	2013-09-17	56552.1087
FEROS	48000	2013-09-17	56552.1095
FEROS	48000	2013-09-17	56552.1826
FEROS	48000	2013-09-17	56552.1839
FEROS	48000	2013-09-17	56552.1846
FEROS	48000	2013-09-17	56552.2549
FEROS	48000	2013-09-17	56552.2562

Continue on next page

Tabela F.1 – table from previous page

Instument	Resolution	Date	MJD
Amateur	5000	2013-10-20	56585.1473
PUCHEROS	20000	2013-10-29	56594.0
ECass	30000	2013-11-12	56608.0633
ECass	30000	2013-11-12	56608.0661
ECass	30000	2013-11-13	56609.0978
FEROS	48000	2013-12-05	56631.0286
FEROS	48000	2013-12-05	56631.0297
FEROS	48000	2013-12-05	56631.1607
FEROS	48000	2013-12-05	56631.1616
FEROS	48000	2013-12-05	56631.2506
FEROS	48000	2013-12-07	56633.0184
FEROS	48000	2013-12-07	56633.1470
FEROS	48000	2013-12-07	56633.2091
FEROS	48000	2013-12-07	56633.3095
ECass	30000	2013-12-09	56635.9693
FEROS	48000	2013-12-10	56636.0266
FEROS	48000	2013-12-10	56636.0273
FEROS	48000	2013-12-10	56636.1609
FEROS	48000	2013-12-10	56636.1615
FEROS	48000	2013-12-10	56636.2349
FEROS	48000	2013-12-10	56636.2356
FEROS	48000	2013-12-11	56637.0190
FEROS	48000	2013-12-11	56637.0197
FEROS	48000	2013-12-11	56637.1407
FEROS	48000	2013-12-11	56637.1414
FEROS	48000	2013-12-11	56637.2620
FEROS	48000	2013-12-11	56637.2626
FEROS	48000	2013-12-11	56637.2633
FEROS	48000	2013-12-11	56637.2640
FEROS	48000	2014-01-04	56661.0262
FEROS	48000	2014-01-04	56661.0269
FEROS	48000	2014-01-04	56661.0995
FEROS	48000	2014-01-04	56661.1002
FEROS	48000	2014-01-04	56661.1940
FEROS	48000	2014-01-04	56661.1947

Continue on next page

Tabela F.1 – table from previous page

Instument	Resolution	Date	MJD
FEROS	48000	2014-01-05	56662.0422
FEROS	48000	2014-01-05	56662.0429
FEROS	48000	2014-01-05	56662.1181
FEROS	48000	2014-01-05	56662.1192
FEROS	48000	2014-01-05	56662.1200
FEROS	48000	2014-01-05	56662.1945
FEROS	48000	2014-01-05	56662.1951
FEROS	48000	2014-01-06	56663.0088
FEROS	48000	2014-01-06	56663.0096
FEROS	48000	2014-01-06	56663.0913
FEROS	48000	2014-01-06	56663.0920
Amateur	5000	2014-01-07	56664.875
Amateur	5000	2014-01-21	56678.0027
FEROS	48000	2014-01-29	56686.0261
FEROS	48000	2014-01-29	56686.1033
PUCHEROS	20000	2014-01-30	56687.0
FEROS	48000	2014-01-30	56687.1304
FEROS	48000	2014-01-31	56688.0346
FEROS	48000	2014-02-10	56698.1137
FEROS	48000	2014-02-10	56698.1143
FEROS	48000	2014-02-10	56698.1150
FEROS	48000	2014-02-10	56698.1156
FEROS	48000	2014-02-10	56698.9999
FEROS	48000	2014-02-11	56699.0009
FEROS	48000	2014-02-12	56700.0709
FEROS	48000	2014-02-12	56700.0718
FEROS	48000	2014-02-12	56700.9995
FEROS	48000	2014-02-13	56701.0003
FEROS	48000	2014-02-13	56701.0016
FEROS	48000	2014-02-13	56701.0023
FEROS	48000	2014-02-13	56701.0029
FEROS	48000	2014-02-13	56701.0036
FEROS	48000	2014-02-13	56701.0043
FEROS	48000	2014-02-13	56701.9933
FEROS	48000	2014-02-13	56701.9941

Continue on next page

Tabela F.1 – table from previous page

Instument	Resolution	Date	MJD
FEROS	48000	2014-02-13	56701.9948
FEROS	48000	2014-02-15	56703.0050
FEROS	48000	2014-02-15	56703.0057
FEROS	48000	2014-02-16	56704.0037
FEROS	48000	2014-02-16	56704.0043
FEROS	48000	2014-02-16	56704.9957
FEROS	48000	2014-02-16	56704.9964
FEROS	48000	2014-02-16	56704.9973
FEROS	48000	2014-02-16	56704.9979
FEROS	48000	2014-02-18	56706.0047
FEROS	48000	2014-02-18	56706.0053
FEROS	48000	2014-02-19	56707.9940
FEROS	48000	2014-02-19	56707.9947
FEROS	48000	2014-02-20	56708.9942
FEROS	48000	2014-02-20	56708.9962
FEROS	48000	2014-02-20	56708.9969
FEROS	48000	2014-02-21	56709.9972
FEROS	48000	2014-02-21	56709.9979
FEROS	48000	2014-02-22	56710.9950
FEROS	48000	2014-02-22	56710.9957
FEROS	48000	2014-02-22	56710.9980
FEROS	48000	2014-02-22	56710.9987
FEROS	48000	2014-02-23	56711.9895
FEROS	48000	2014-02-23	56711.9911
FEROS	48000	2014-02-23	56711.9918
FEROS	48000	2014-02-24	56712.9847
FEROS	48000	2014-02-24	56712.9854
FEROS	48000	2014-02-25	56713.9918
FEROS	48000	2014-02-25	56713.9924
ECass	30000	2014-07-16	56854.2982
ECass	30000	2014-10-14	56944.1713
ECass	30000	2014-11-19	56980.0376
BeSS	5000	2014-11-26	56987.3834
BeSS	100000	2014-11-28	56989.4437
Amateur	5000	2014-12-28	57019.0116

Continue on next page

Tabela F.1 – table from previous page

Instument	Resolution	Date	MJD
Amateur	5000	2015-01-09	57031.0142
Amateur	5000	2015-01-18	57040.9596

F.2 Interferometry

Table F.2 - List of VLTI-AMBER observations (K band, high resolution mode) of the 2013 outburst of Achernar.

Date	MJD	Dataset
2013-08-01	56506.2863503	2
2013-08-02	56507.4056214	1
2013-08-03	56508.4106953	1
2013-08-04	56509.3647363	1
2013-08-13	56518.2686651	5
2013-08-19	56524.327139	1
2013-08-20	56525.2566051	3
2013-09-22	56558.3015531	1
2013-09-23	56559.1584479	4
2013-11-11	56608.197591	1
2013-11-12	56609.2032108	1
2013-11-15	56612.3060189	1
2014-06-24	56833.4330857	1
2014-06-30	56839.3910707	1
2014-07-13	56852.3893149	2
2014-08-04	56874.4086259	1
2014-08-05	56875.4041884	1
2014-08-10	56880.3435603	1
2014-08-16	56886.0635461	1
2014-08-28	56929.2058108	2
2014-08-29	56899.3931993	3
2014-09-08	56909.2860173	1
2014-09-09	56910.27	0

Continue on next page

Tabela F.2 – table from previous page

Date	MJD	Dataset
2014-09-10	56911.2660414	2
2014-09-11	56912.25	0
2014-09-19	56920.119566	9
2014-09-23	56924.1887453	8
2014-09-24	56925.3043003	4
2014-09-27	56928.2170004	2
2014-09-28	56898.3894947	3
2014-09-30	56931.2513042	1
2014-10-01	56932.3477905	1
2014-10-18	56949.3	0
2014-10-28	56958.9977269	5
2014-10-29	56960.0185591	5
2014-10-30	56961.2078147	1
2015-01-12	57035.057242	1
2015-01-18	57041.0526772	1

F.3 Polarimetry

Table F.3 - List of linear polarimetric observations of the 2013 outburst of Achernar.

MJD	Band	Date	P(%)	Q(%)	U	$\theta(^\circ)$	σ_P	σ_θ
56500.350732	V	2013-07-26	0.293	0.154	0.249	29.1	0.033	1.0
56500.372017	V	2013-07-26	0.251	0.080	0.238	35.7	0.038	1.1
56503.228983	R	2013-07-29	0.284	0.065	0.277	38.4	0.004	0.1
56503.295401	R	2013-07-29	0.288	0.062	0.281	38.8	0.006	0.2
56504.290627	B	2013-07-30	0.283	-0.018	0.283	46.8	0.078	2.2
56504.300175	V	2013-07-30	0.227	0.109	0.199	30.7	0.029	0.8
56504.317043	I	2013-07-30	0.253	0.071	0.243	36.9	0.031	0.9
56504.326981	B	2013-07-30	0.292	0.188	0.223	24.9	0.049	1.4
56504.335748	V	2013-07-30	0.218	0.090	0.199	32.9	0.014	0.4
56504.343907	R	2013-07-30	0.247	0.097	0.227	33.4	0.011	0.3
56504.350724	I	2013-07-30	0.257	0.114	0.230	31.8	0.030	0.9
56504.357889	V	2013-07-30	0.258	0.134	0.220	29.4	0.031	0.9

Continue on next page

Tabela F.3 – table from previous page

MJD	Band	Date	$P(\%)$	$Q(\%)$	$U(\%)$	$\theta(^\circ)$	σ_P	σ_θ
56504.365586	V	2013-07-30	0.243	0.119	0.213	30.4	0.012	0.3
56504.372831	V	2013-07-30	0.229	0.097	0.208	32.5	0.024	0.7
56505.349694	V	2013-07-31	0.273	0.137	0.236	30.0	0.027	0.8
56505.358549	V	2013-07-31	0.289	0.134	0.256	31.2	0.012	0.3
56505.367669	V	2013-07-31	0.272	0.147	0.228	28.6	0.024	0.7
56517.348524	V	2013-08-12	0.266	0.163	0.210	26.1	0.071	2.0
56518.184862	V	2013-08-13	0.336	0.148	0.302	31.9	0.030	0.8
56518.222449	I	2013-08-13	0.305	0.112	0.283	34.2	0.043	1.2
56518.258924	V	2013-08-13	0.299	0.132	0.269	31.9	0.009	0.3
56518.267888	I	2013-08-13	0.293	0.095	0.277	35.5	0.024	0.7
56518.278444	I	2013-08-13	0.320	0.114	0.299	34.6	0.022	0.6
56518.293757	V	2013-08-13	0.316	0.109	0.297	34.9	0.032	0.9
56518.304335	V	2013-08-13	0.295	0.084	0.282	36.7	0.047	1.3
56518.313461	I	2013-08-13	0.299	0.067	0.291	38.5	0.054	1.5
56518.333942	I	2013-08-13	0.278	0.089	0.264	35.7	0.026	0.7
56518.344150	V	2013-08-13	0.282	0.111	0.259	33.4	0.038	1.1
56518.357009	I	2013-08-13	0.265	0.099	0.246	34.0	0.030	0.8
56520.197235	V	2013-08-15	0.358	0.107	0.342	36.3	0.018	0.5
56520.208849	I	2013-08-15	0.337	0.127	0.311	33.9	0.020	0.6
56520.220840	V	2013-08-15	0.327	0.099	0.312	36.2	0.017	0.5
56520.229844	I	2013-08-15	0.290	0.097	0.273	35.2	0.015	0.4
56520.238658	V	2013-08-15	0.303	0.089	0.290	36.5	0.021	0.6
56520.247414	I	2013-08-15	0.287	0.073	0.277	37.6	0.027	0.8
56520.256031	V	2013-08-15	0.299	0.089	0.286	36.4	0.017	0.5
56520.264931	I	2013-08-15	0.275	0.081	0.263	36.4	0.021	0.6
56520.281870	I	2013-08-15	0.297	0.081	0.286	37.1	0.012	0.4
56520.290238	V	2013-08-15	0.321	0.074	0.312	38.3	0.013	0.4
56520.299005	I	2013-08-15	0.309	0.023	0.308	42.9	0.048	1.4
56520.308137	V	2013-08-15	0.270	0.071	0.261	37.4	0.021	0.6
56520.316621	I	2013-08-15	0.295	0.036	0.293	41.5	0.036	1.0
56520.325469	V	2013-08-15	0.330	0.074	0.321	38.6	0.045	1.3
56520.334445	I	2013-08-15	0.289	0.049	0.285	40.1	0.033	0.9
56520.343392	V	2013-08-15	0.305	0.074	0.296	38.0	0.007	0.2
56520.351650	I	2013-08-15	0.305	0.067	0.298	38.7	0.009	0.2
56520.359966	V	2013-08-15	0.310	0.050	0.306	40.3	0.015	0.4

Continue on next page

Tabela F.3 – table from previous page

MJD	Band	Date	$P(\%)$	$Q(\%)$	$U(\%)$	$\theta(^\circ)$	σ_P	σ_θ
56520.368195	I	2013-08-15	0.300	0.045	0.297	40.7	0.021	0.6
56525.227304	V	2013-08-20	0.327	0.141	0.295	32.2	0.007	0.2
56525.235956	I	2013-08-20	0.289	0.119	0.264	32.9	0.038	1.1
56525.247628	V	2013-08-20	0.343	0.192	0.285	28.0	0.019	0.5
56525.264190	I	2013-08-20	0.324	0.109	0.305	35.1	0.051	1.5
56525.281748	V	2013-08-20	0.341	0.120	0.319	34.7	0.031	0.9
56525.288762	I	2013-08-20	0.326	0.147	0.292	31.6	0.061	1.8
56525.298369	V	2013-08-20	0.287	0.117	0.262	33.0	0.022	0.6
56525.317969	V	2013-08-20	0.334	0.140	0.303	32.6	0.026	0.7
56525.339694	V	2013-08-20	0.303	0.124	0.276	32.9	0.042	1.2
56525.348207	I	2013-08-20	0.281	0.115	0.257	32.9	0.035	1.0
56525.355788	V	2013-08-20	0.298	0.127	0.270	32.4	0.012	0.3
56525.363791	I	2013-08-20	0.328	0.178	0.276	28.6	0.061	1.8
56526.194579	V	2013-08-21	0.284	0.081	0.273	36.7	0.020	0.6
56526.203473	I	2013-08-21	0.267	0.072	0.257	37.2	0.047	1.3
56526.212322	V	2013-08-21	0.256	0.121	0.226	30.9	0.024	0.7
56526.255973	V	2013-08-21	0.291	0.124	0.263	32.3	0.011	0.3
56526.265342	I	2013-08-21	0.253	0.072	0.243	36.7	0.019	0.5
56526.274266	V	2013-08-21	0.272	0.072	0.262	37.3	0.034	1.0
56526.284301	I	2013-08-21	0.262	0.098	0.243	34.1	0.027	0.8
56526.299261	V	2013-08-21	0.231	0.076	0.219	35.4	0.029	0.8
56526.301019	I	2013-08-21	0.258	0.059	0.251	38.4	0.055	1.6
56526.319659	I	2013-08-21	0.238	0.109	0.212	31.4	0.023	0.7
56526.321651	V	2013-08-21	0.194	0.056	0.185	36.6	0.044	1.2
56526.341934	I	2013-08-21	0.174	0.023	0.172	41.2	0.042	1.2
56526.342246	V	2013-08-21	0.226	0.101	0.202	31.7	0.019	0.5
56526.360707	I	2013-08-21	0.266	0.126	0.234	30.9	0.034	1.0
56526.360829	V	2013-08-21	0.268	0.145	0.226	28.7	0.043	1.2
56561.214752	B	2013-09-25	0.282	0.140	0.245	30.1	0.028	0.8
56561.226332	V	2013-09-25	0.277	0.108	0.255	33.5	0.020	0.6
56561.233259	R	2013-09-25	0.252	0.068	0.243	37.2	0.005	0.1
56561.242530	I	2013-09-25	0.284	0.103	0.265	34.4	0.007	0.2
56561.249179	I	2013-09-25	0.221	0.065	0.212	36.5	0.011	0.3
56561.249457	V	2013-09-25	0.215	0.112	0.184	29.4	0.020	0.6
56561.255805	I	2013-09-25	0.224	0.095	0.203	32.5	0.007	0.2

Continue on next page

Tabela F.3 – table from previous page

MJD	Band	Date	$P(\%)$	$Q(\%)$	$U(\%)$	$\theta(^\circ)$	σ_P	σ_θ
56561.262674	V	2013-09-25	0.251	0.102	0.229	33.0	0.022	0.6
56561.276627	V	2013-09-25	0.244	0.116	0.215	30.9	0.018	0.5
56561.352431	V	2013-09-25	0.294	0.152	0.252	29.4	0.039	1.1
56561.358791	I	2013-09-25	0.284	0.119	0.258	32.6	0.051	1.5
56562.090557	B	2013-09-26	0.275	0.175	0.212	25.2	0.023	0.7
56562.100996	V	2013-09-26	0.270	0.105	0.248	33.5	0.012	0.3
56562.108728	R	2013-09-26	0.261	0.120	0.232	31.3	0.011	0.3
56562.116656	I	2013-09-26	0.245	0.054	0.239	38.7	0.025	0.7
56584.163867	V	2013-10-18	0.315	0.115	0.293	34.3	0.022	0.6
56584.172344	I	2013-10-18	0.284	0.098	0.267	34.9	0.025	0.7
56609.097206	V	2013-11-12	0.277	0.079	0.266	36.7	0.040	1.2
56610.018897	V	2013-11-13	0.328	0.190	0.268	27.3	0.015	0.4
56610.034451	B	2013-11-13	0.371	0.221	0.298	26.7	0.010	0.3
56610.035586	I	2013-11-13	0.300	0.087	0.287	36.6	0.023	0.7
56610.049168	R	2013-11-13	0.311	0.118	0.288	33.9	0.018	0.5
56640.016320	V	2013-12-13	0.372	0.157	0.337	32.5	0.027	0.8
56640.040400	R	2013-12-13	0.384	0.100	0.371	37.5	0.014	0.4
56640.048971	I	2013-12-13	0.369	0.021	0.368	43.4	0.022	0.6
56640.059214	B	2013-12-13	0.442	0.191	0.398	32.2	0.095	2.7
56725.928754	B	2014-03-09	0.566	0.313	0.472	28.2	0.047	1.3
56725.939636	V	2014-03-09	0.458	0.222	0.401	30.5	0.023	0.7
56725.946704	I	2014-03-09	0.423	0.089	0.413	38.9	0.029	0.8
56841.327645	B	2014-07-02	0.268	0.175	0.202	24.5	0.020	0.6
56841.334865	V	2014-07-02	0.232	0.133	0.189	27.4	0.043	1.2
56841.339711	R	2014-07-02	0.272	0.126	0.241	31.2	0.012	0.3
56842.355721	B	2014-07-03	0.380	0.197	0.326	29.4	0.056	1.6
56842.362876	V	2014-07-03	0.256	0.115	0.228	31.6	0.050	1.4
56842.368099	R	2014-07-03	0.315	0.163	0.269	29.4	0.040	1.1
56842.375059	I	2014-07-03	0.284	0.120	0.258	32.5	0.035	1.0
56889.193547	B	2014-08-19	0.258	0.158	0.204	26.1	0.017	0.5
56889.294155	B	2014-08-19	0.201	0.122	0.160	26.4	0.040	1.1
56889.300386	B	2014-08-19	0.329	0.309	0.113	10.0	0.113	3.2
56889.325231	V	2014-08-19	0.292	0.187	0.224	25.1	0.008	0.2
56889.335314	R	2014-08-19	0.279	0.172	0.220	26.0	0.018	0.5
56889.342774	I	2014-08-19	0.268	0.187	0.192	22.9	0.010	0.3

Continue on next page

Tabela F.3 – table from previous page

MJD	Band	Date	$P(\%)$	$Q(\%)$	$U(\%)$	$\theta(^\circ)$	σ_P	σ_θ
56890.111175	I	2014-08-20	0.233	0.092	0.214	33.4	0.034	1.0
56890.120916	V	2014-08-20	0.285	0.039	0.282	41.1	0.039	1.1
56890.201550	V	2014-08-20	0.292	0.168	0.239	27.5	0.031	0.9
56890.210932	V	2014-08-20	0.316	0.174	0.263	28.3	0.031	0.9
56890.221297	V	2014-08-20	0.262	0.159	0.209	26.4	0.027	0.8
56890.231776	V	2014-08-20	0.249	0.140	0.206	27.9	0.023	0.7
56890.324839	B	2014-08-20	0.249	0.178	0.173	22.1	0.077	2.2
56890.333295	V	2014-08-20	0.280	0.179	0.216	25.1	0.022	0.6
56890.341413	R	2014-08-20	0.276	0.182	0.207	24.3	0.007	0.2
56890.353331	V	2014-08-20	0.275	0.175	0.213	25.3	0.011	0.3
56890.356256	V	2014-08-20	0.285	0.198	0.206	23.1	0.015	0.4
56890.359180	V	2014-08-20	0.262	0.202	0.166	19.7	0.044	1.3
56890.362105	V	2014-08-20	0.276	0.179	0.211	24.9	0.007	0.2
56890.365029	V	2014-08-20	0.270	0.174	0.207	25.0	0.007	0.2
56902.286837	B	2014-09-01	0.239	0.015	0.238	43.2	0.039	1.1
56902.299653	B	2014-09-01	0.207	0.139	0.154	24.0	0.020	0.6
56902.313673	V	2014-09-01	0.267	0.145	0.224	28.5	0.011	0.3
56902.318603	V	2014-09-01	0.259	0.154	0.208	26.8	0.005	0.1
56902.324711	R	2014-09-01	0.245	0.123	0.212	29.9	0.009	0.3
56902.329641	R	2014-09-01	0.230	0.134	0.187	27.2	0.009	0.2
56902.336581	I	2014-09-01	0.241	0.142	0.195	27.0	0.015	0.4
56902.342029	I	2014-09-01	0.210	0.117	0.174	28.0	0.030	0.9
56923.161809	V	2014-09-22	0.222	0.066	0.212	36.4	0.009	0.3
56923.169206	B	2014-09-22	0.238	0.179	0.157	20.7	0.088	2.5
56923.176906	R	2014-09-22	0.192	0.073	0.178	33.9	0.024	0.7
56923.184689	I	2014-09-22	0.226	0.121	0.191	28.8	0.006	0.2
56923.193235	V	2014-09-22	0.203	0.067	0.192	35.4	0.043	1.2
56923.199211	V	2014-09-22	0.245	0.101	0.223	32.8	0.015	0.4
56923.205194	V	2014-09-22	0.252	0.094	0.233	34.0	0.014	0.4
56923.211175	V	2014-09-22	0.250	0.102	0.228	32.9	0.015	0.4
56923.220260	B	2014-09-22	0.172	-0.004	0.172	45.7	0.105	3.0
56923.227873	R	2014-09-22	0.237	0.137	0.194	27.4	0.014	0.4
56923.235107	I	2014-09-22	0.238	0.144	0.189	26.3	0.027	0.8
56923.243851	V	2014-09-22	0.231	0.127	0.193	28.3	0.064	1.8
56923.250751	V	2014-09-22	0.241	0.099	0.220	32.8	0.018	0.5

Continue on next page

Tabela F.3 – table from previous page

MJD	Band	Date	$P(\%)$	$Q(\%)$	$U(\%)$	$\theta(^\circ)$	σ_P	σ_θ
56923.257654	V	2014-09-22	0.226	0.101	0.203	31.8	0.018	0.5
56923.273918	B	2014-09-22	0.279	0.219	0.173	19.1	0.085	2.4
56923.282788	R	2014-09-22	0.222	0.117	0.188	29.1	0.006	0.2
56923.289502	I	2014-09-22	0.233	0.125	0.196	28.7	0.025	0.7
56923.296570	V	2014-09-22	0.220	0.097	0.198	32.0	0.008	0.2
56923.304646	V	2014-09-22	0.230	0.105	0.204	31.4	0.014	0.4
56924.151246	V	2014-09-23	0.256	0.077	0.244	36.2	0.037	1.1
56924.158357	B	2014-09-23	0.268	0.190	0.189	22.4	0.023	0.7
56924.165095	R	2014-09-23	0.245	0.061	0.237	37.8	0.007	0.2
56924.172355	I	2014-09-23	0.254	0.108	0.229	32.4	0.037	1.1
56924.178851	V	2014-09-23	0.244	0.098	0.223	33.2	0.006	0.2
56925.111848	V	2014-09-24	0.272	0.122	0.243	31.6	0.015	0.4
56946.111394	I	2014-10-15	0.192	-0.004	0.191	45.6	0.029	0.8
56946.125236	B	2014-10-15	0.225	0.083	0.209	34.2	0.014	0.4
56980.150634	V	2014-11-18	0.235	0.097	0.214	32.8	0.018	0.5
56980.157276	I	2014-11-18	0.195	0.040	0.191	39.0	0.013	0.4
56980.163592	R	2014-11-18	0.199	0.072	0.186	34.4	0.021	0.6
56980.173516	B	2014-11-18	0.208	0.078	0.193	33.9	0.016	0.5

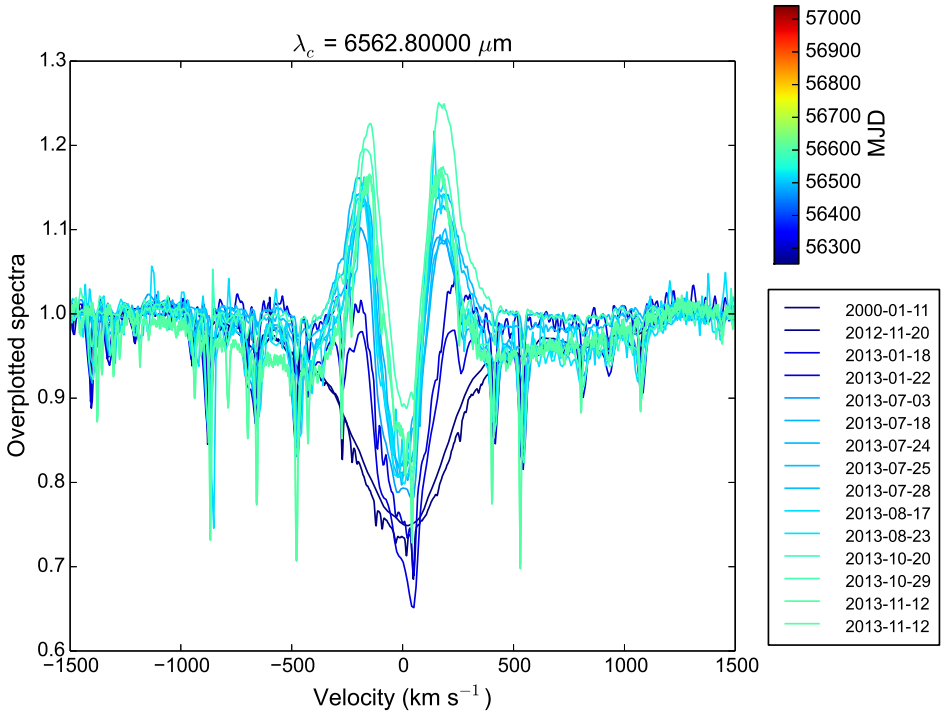

Figure F.1: Hα overplotted line profiles of Achernar during the 2013 outburst. The color corresponds to the observation date. The (pure) photospheric reference profile Rivinius et al. (2013) is also shown. It contains the observations from all instruments presented in Sec. 6.3, except for FEROS/ESO, due to its with frequency.

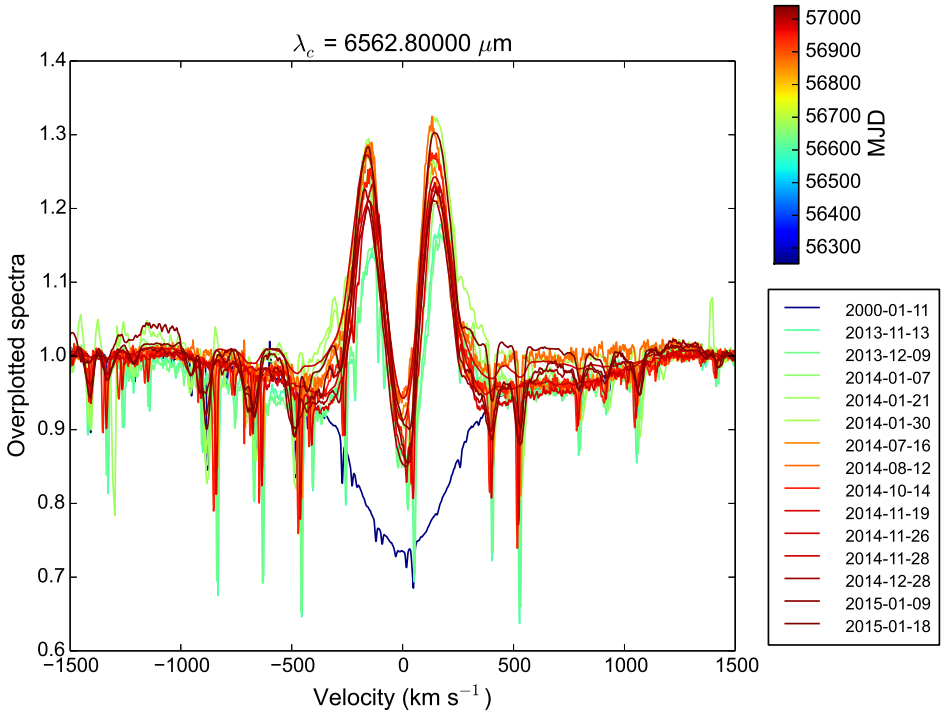

Figure F.2: The same as previous figure, for posterior observations.

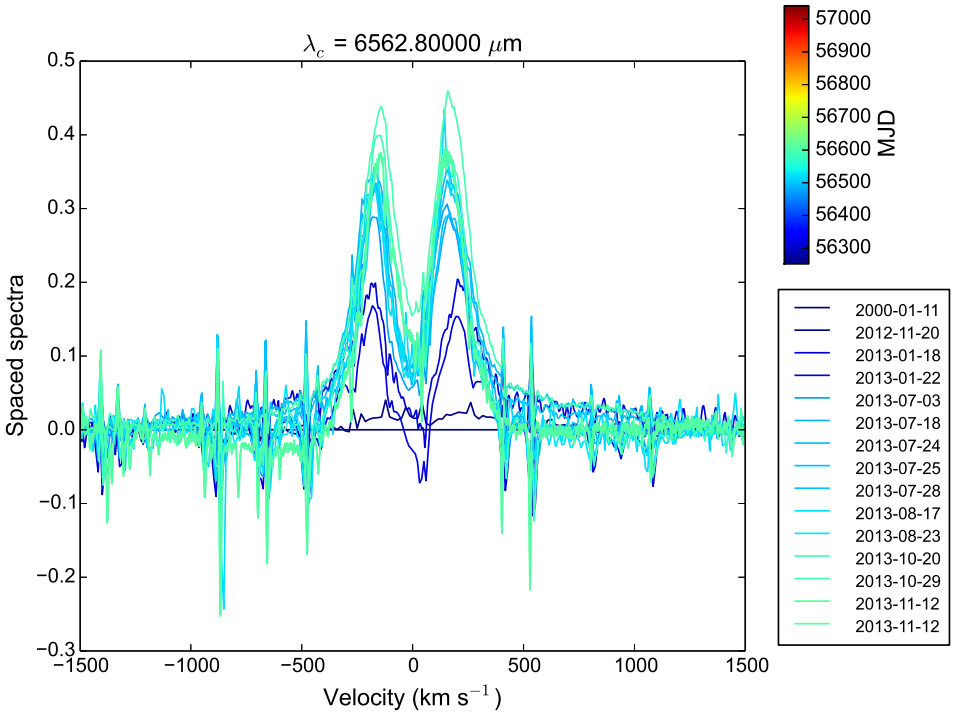

Figure F.3: Hα difference profiles of Achernar during the 2013 outburst, in relation to the (pure) photospheric reference profile Rivinius et al. (2013). The color corresponds to the observation date. It contains the observations from all instruments presented in Sec. 6.3, except for FEROS/ESO, due to its with frequency.

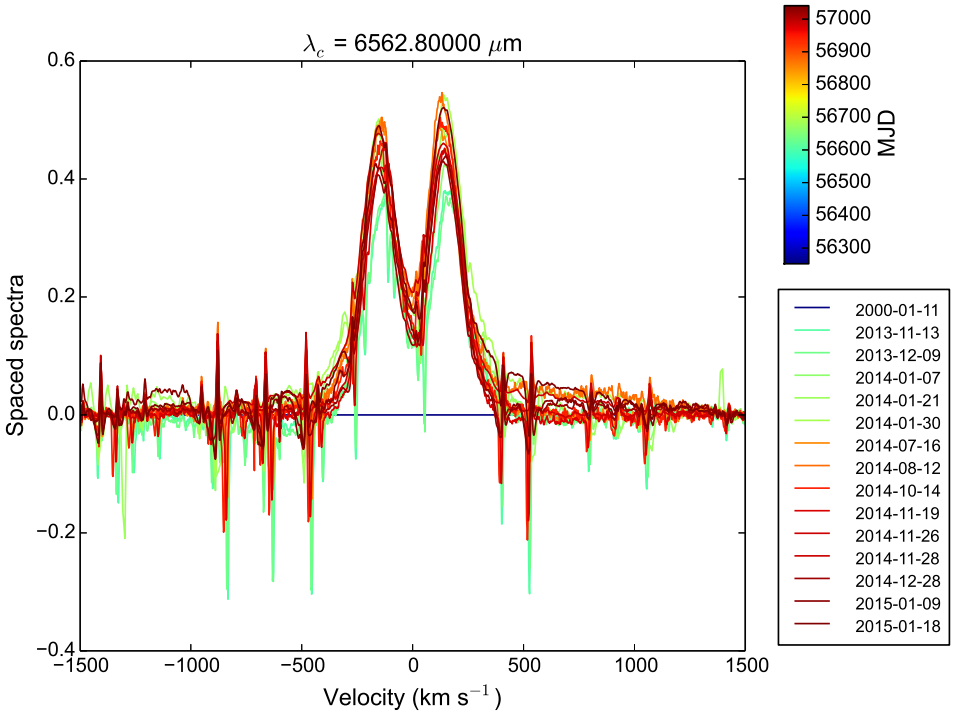

Figure F.4: The same as previous figure, for posterior observations.

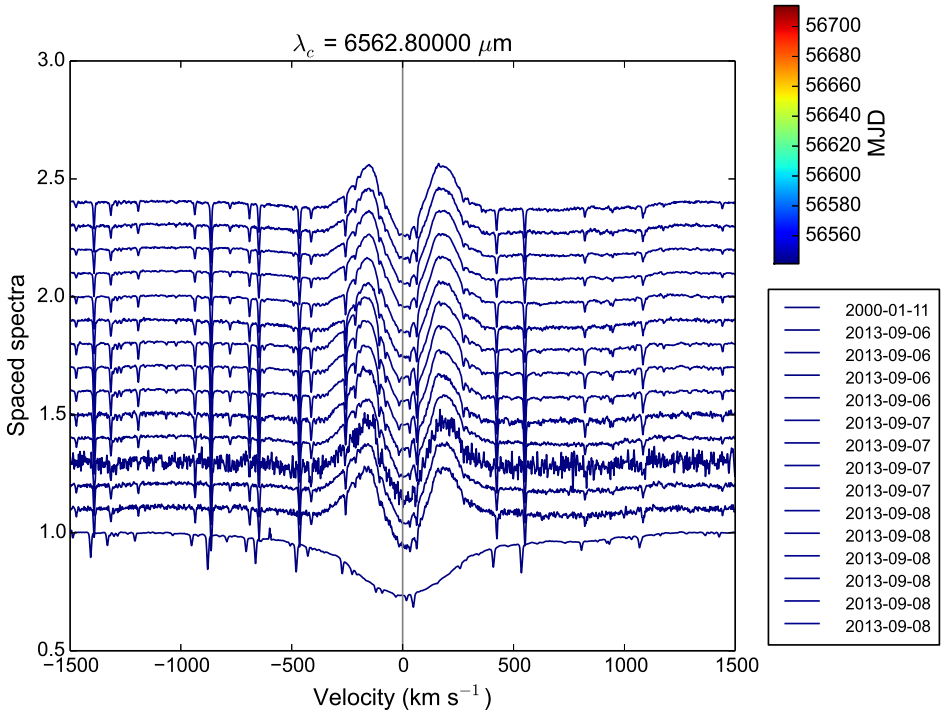

Figure F.5: Hα line profiles of Achernar during the 2013 outburst. The color corresponds to the observation date. The (pure) photospheric reference profile Rivinius et al. (2013) is also shown. It contains the observations from FEROS/ESO.

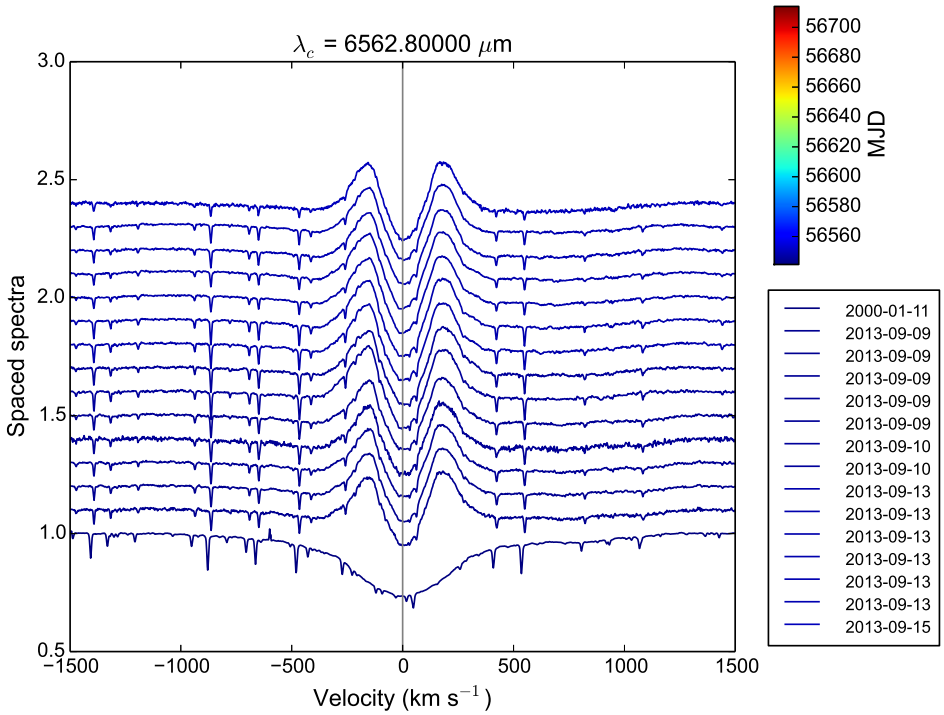

Figure F.6: The same as previous figure, for posterior observations.

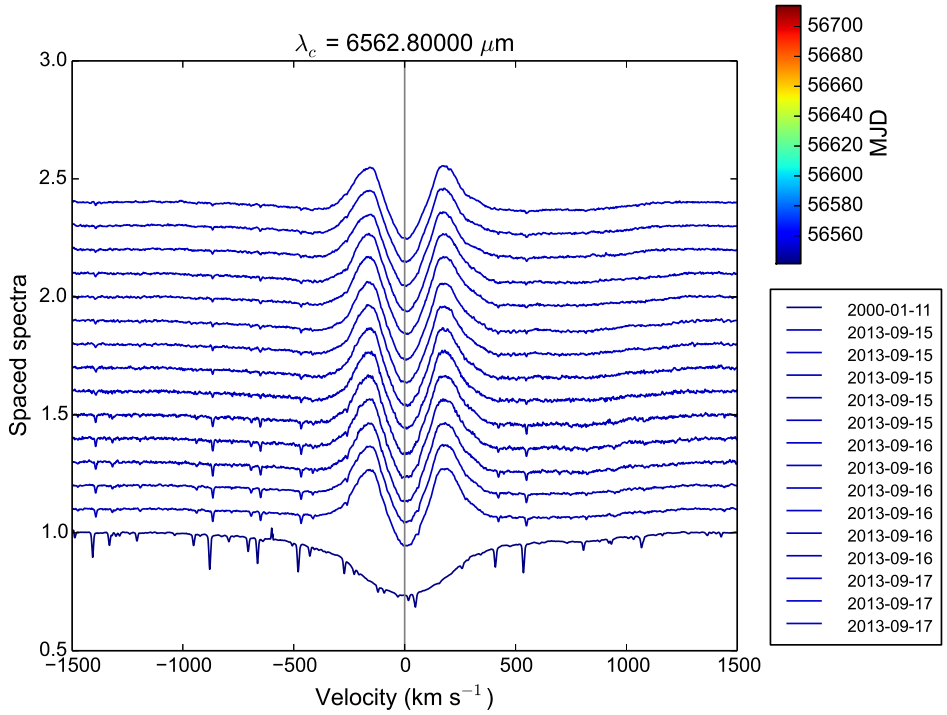

Figure F.7: The same as previous figure, for posterior observations.

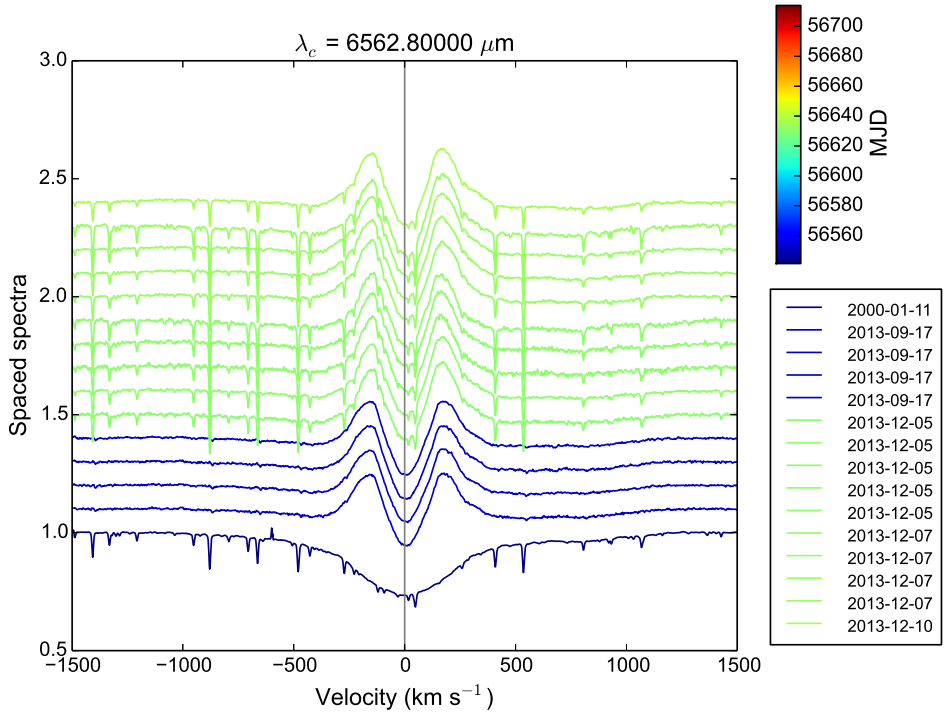

Figure F.8: The same as previous figure, for posterior observations.

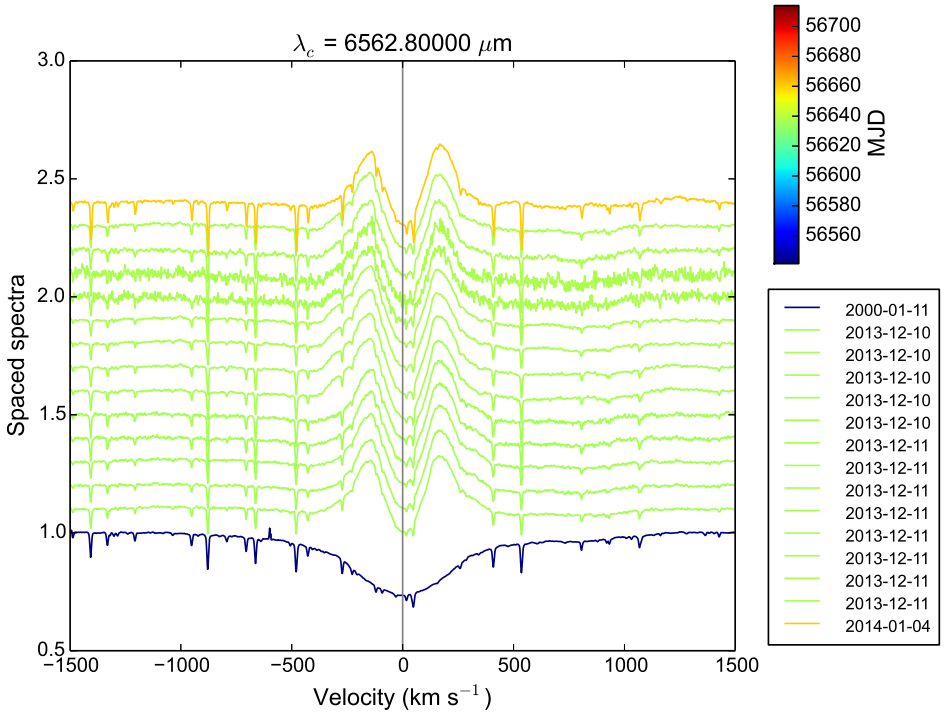

Figure F.9: The same as previous figure, for posterior observations.

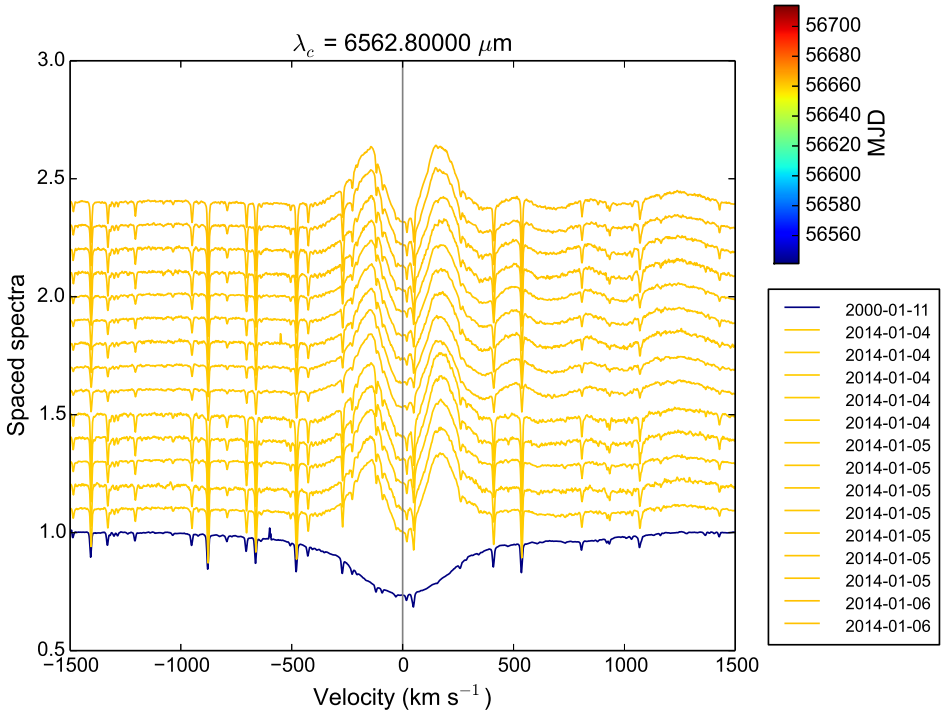

Figure F.10: The same as previous figure, for posterior observations.

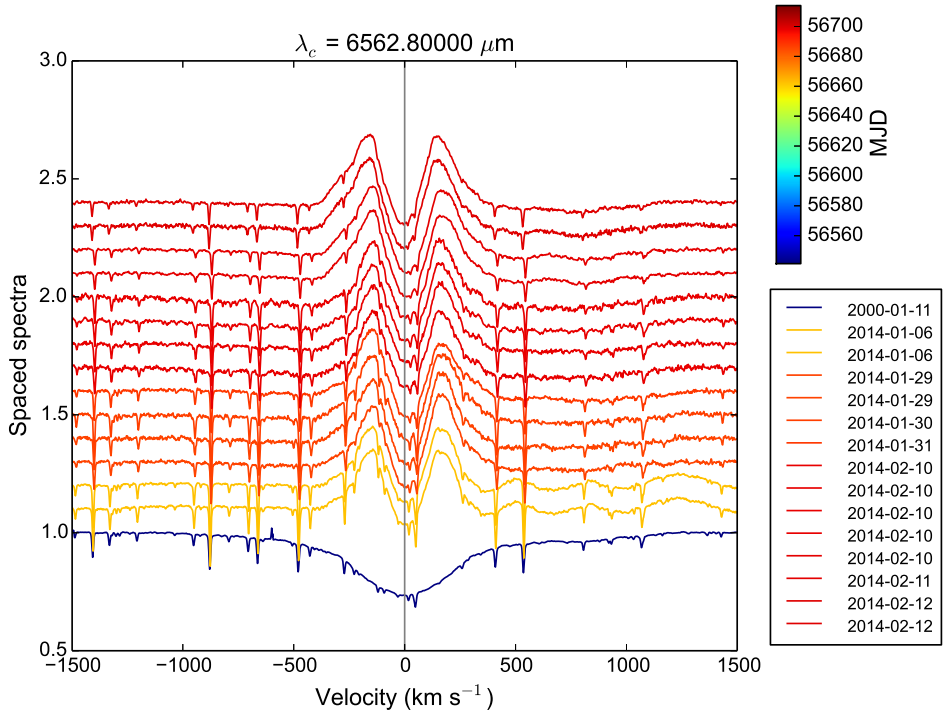

Figure F.11: The same as previous figure, for posterior observations.

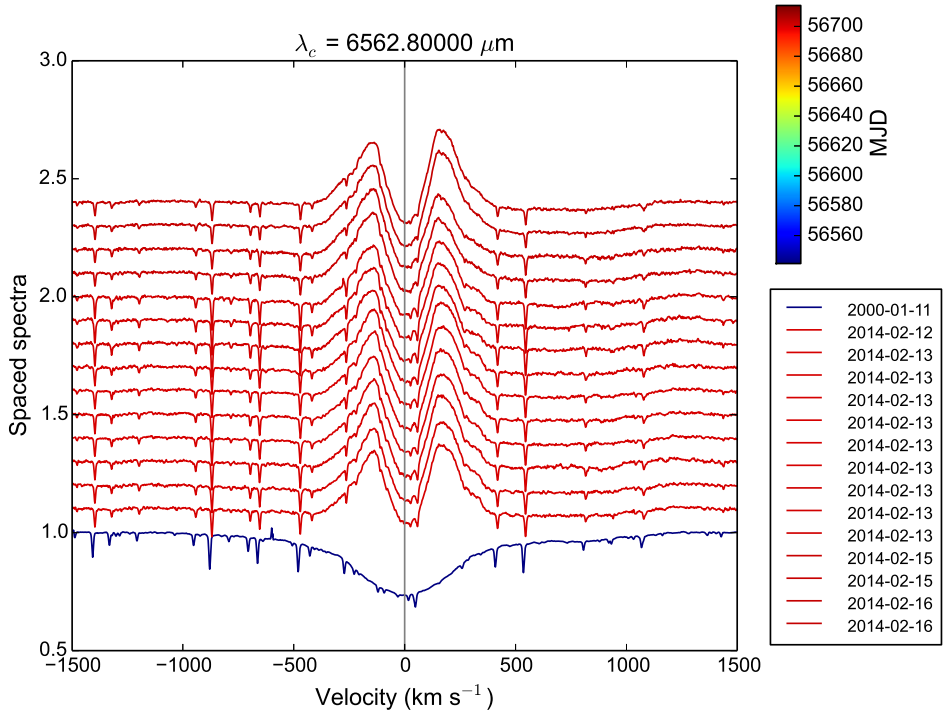

Figure F.12: The same as previous figure, for posterior observations.

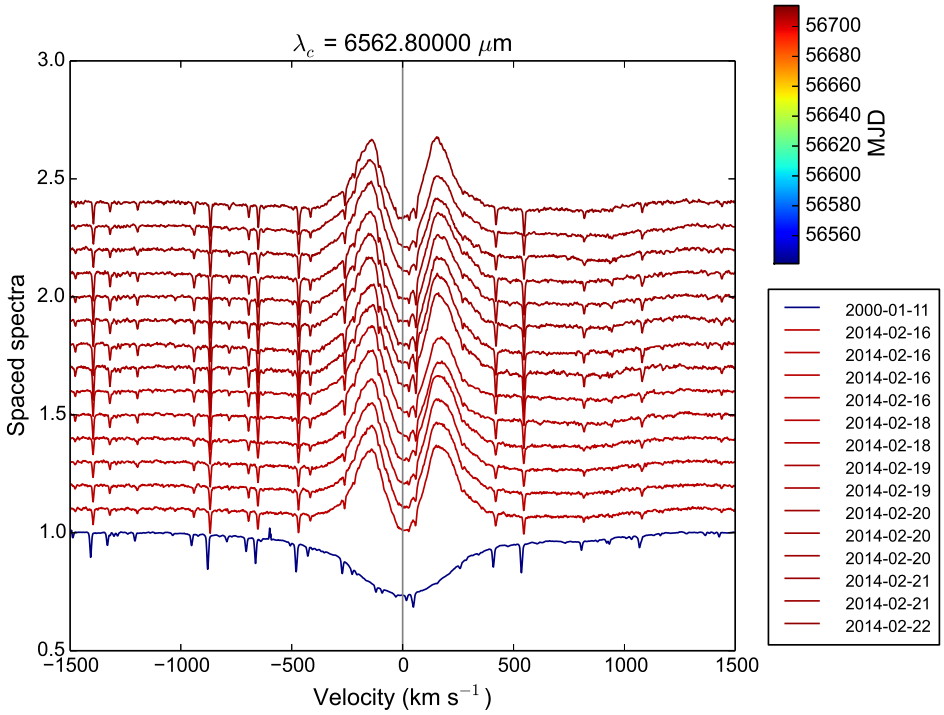

Figure F.13: The same as previous figure, for posterior observations.

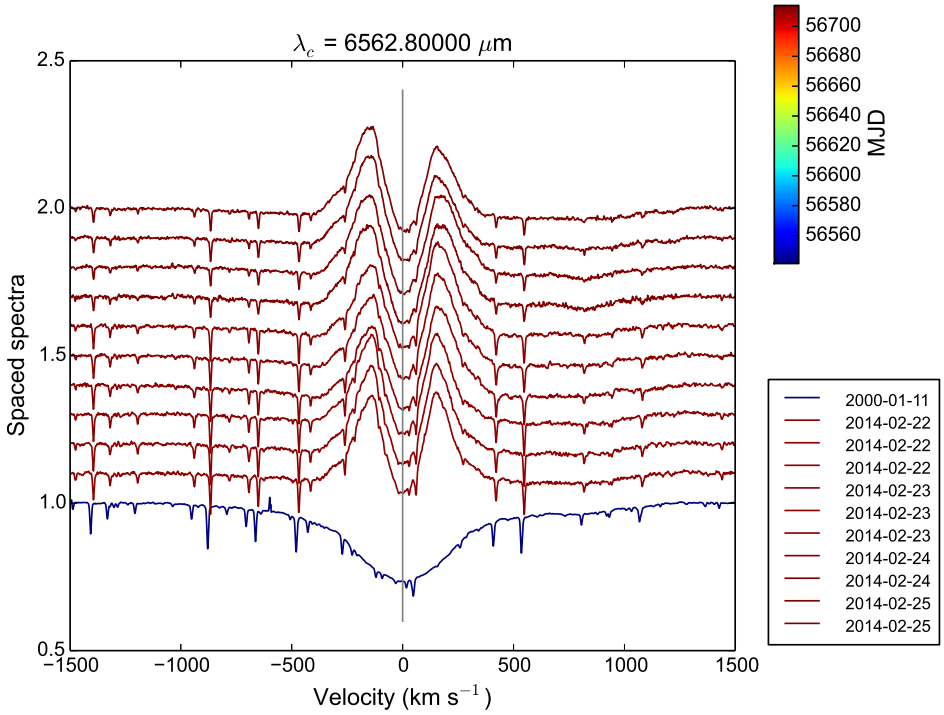

Figure F.14: The same as previous figure, for posterior observations.